Report No. FRA-ORD & D 74-51

RESEARCH TO IMPROVE TUNNEL SUPPORT SYSTEMS

S. L. Paul
E. H. Gaylord
A. J. Hendron
C. E. Kesler
B. Mohraz
R. B. Peck

University of Illinois
Urbana, Illinois

JUNE 1974

FINAL REPORT

Document is available to the public through the
National Technical Information Service
Springfield, Virginia 22151

Prepared for

Department of Transportation
FEDERAL RAILROAD ADMINISTRATION
Washington, D.C. 20590

NOTICE

1. This document is disseminated under the sponsorship of the Department of Transportation in the interest of information exchange. The United States Government assumes no liability for its contents or use thereof.

2. The United States Government and the University of Illinois at Urbana-Champaign do not endorse products or manufacturers. Trade or manufacturers' names appear herein solely because they are considered essential to the object of this report.

Technical Report Documentation Page

1. Report No.	2. Government Accession No.	3. Recipient's Catalog No.
FRA-ORD&D 74-51		

4. Title and Subtitle	5. Report Date
STUDIES TO IMPROVE TUNNEL SUPPORT SYSTEMS	June 1974
	6. Performing Organization Code

7. Author(s)	8. Performing Organization Report No.
S. L. Paul, C. E. Kesler, E. H. Gaylord, B. Mohraz, A. J. Hendron, R. B. Peck	UILU-ENG-74-2016

9. Performing Organization Name and Address	10. Work Unit No. (TRAIS)
Department of Civil Engineering University of Illinois at Urbana-Champaign Urbana, Illinois 61801	11. Contract or Grant No. DOT FR 30022

12. Sponsoring Agency Name and Address	13. Type of Report and Period Covered
Federal Railroad Administration Department of Transportation Washington, D. C. 20590	Aug. 72 - Aug. 73 Final Report
	14. Sponsoring Agency Code

15. Supplementary Notes

16. Abstract Studies are described that were directed toward improving the design of certain types of tunnel support systems.

Studies to predict the interaction of a circular liner with the medium performed with a linear finite element computer program and a closed form solution are described. Two construction techniques that give different interaction solutions and thus different liner loadings were simulated. Results are presented in the form of dimensionless plots from which moment, thrust, shear and deformation can be predicted.

Steel-fiber-reinforced regulated-set-cement concrete has been proposed for use in a slipformed tunnel liner system. Mix design, pumping characteristics and mechanical properties of this materal are described. Also, test results for two specimens which represent a portion of the slipformed liner are presented. Behavior of the liner and resisting mechanism was found to be highly nonlinear and to have a great deal of reserve strength beyond the linear range.

Eleven large-scale tests which simulate steel horseshoe sets in rock tunnels are described and the effects of connection characteristics, blocking stiffness, load distribution and load inclination on the set behavior are discussed.

Both the concrete liners and the steel sets that were tested, were simulated by a linear (STRUDL) and a nonlinear analysis (NASTRAN) and the results compared with those obtained from the tests.

17. Key Words	18. Distribution Statement
Tunnel Supports, Steel-Fiber Concrete, Regulated-Set Concrete, Tunnel Liners, Steel Sets, Tunnel Support Tests, Slipformed Liners.	Document is available to the public through the National Technical Information Service, Springfield, Virginia 22151

19. Security Classif. (of this report)	20. Security Classif. (of this page)	21. No. of Pages	22. Price
Unclassified	Unclassified		

Form DOT F 1700.7 (8-72) Reproduction of completed page authorized

PREFACE

The studies described in this report were performed by the Department of Civil Engineering of the University of Illinois at Urbana-Champaign, Urbana, Illinois from August 1972 to August 1973. The project was sponsored by the Federal Railroad Administration, Department of Transportation, through contract No. DOT FR 30022, under the technical direction of Mr. William N. Lucke. Considerable assistance was obtained in formulating goals for the research and directing the overall efforts from Profs. R. B. Peck, D. U. Deere, C. P. Siess and Mr. Lucke. Their help is greatly appreciated. Details of coordination of the project were carried out by Dr. S. L. Paul.

Persons responsible for preparation of each chapter of the report and direct supervision of the corresponding studies were :

Chapter 2: Rational Design of Tunnel Supports,
Profs. A. J. Hendron and B. Mohraz

Chapter 3: Concrete Materials - Evaluation and Behavior,
Prof. C. E. Kesler

Chapter 4: Steel Fiber Reinforced Concrete Monolithic Tunnel Liners, Prof. S. L. Paul and C. P. Siess

Chapter 5: Improvements to Steel Tunnel Supports,
Prof. Emeritus E. H. Gaylord

Professor Peck offered many helpful suggestions throughout preparation of the report. Part of the testing of large-scale steel supports described in Chapter 5 was conducted under the direction of Prof. P. C. Birkemoe before leaving the University of Illinois.

The research work described in this report is part of a continuing effort and therefore the studies are being extended in most cases. Results are presented for the work completed to date though final conclusions and recommendations are better left until studies are completed. However, where possible, tentative conclusions have been discussed to provide input to the tunnel industry concurrent with the research studies.

The topics selected for study are those which appear to be most promising in providing immediate and useful information to the designer of transportation tunnels. Also, the material studies for steel-fiber-reinforced regulated-set concrete and the tests of monolithic liners are directed toward providing information for the design of a slipformed liner system that has been described in a previous report. Both of these studies, however, will provide information which is useful for purposes other than the slipformed liner. Steel-fiber-reinforced concrete and regulated-set cement concrete is in use for many special-purpose applications and holds promise for many more. Many of the conclusions that can be drawn from the steel fiber-reinforced monolithic liner tests will be applicable to conventional liners.

TABLE OF CONTENTS

LIST OF TABLES

LIST OF FIGURES

LIST OF SYMBOLS

CHAPTER 2

C	compressibility ratio (Eq. 2.1)
D	diameter of the tunnel liner
ΔD	change in diameter of the tunnel liner
E_ℓ	modulus of elasticity of the tunnel liner
E_m	modulus of elasticity of the medium
F	flexibility ratio (Eq. 2.2)
H	depth from ground surface to center of tunnel
I_ℓ	effective moment of inertia of the tunnel liner cross section
K_o	coefficient of earth pressure at rest
M	bending moment
M_c	constrained modulus of the medium
P_i	pressure acting on the outside of the tunnel liner
P_o	pressure acting on the inside of the tunnel liner
R	radius of the tunnel liner
S	transverse shear force

T	thrust force
t	effective thickness of the tunnel liner
γ	unit weight of the medium
δ_L	deformation of a lined hole
δ_m	deformation of the medium
δ_T	total deformation
θ	angle defining position on the tunnel liner
ν_ℓ	Poisson's ratio of the liner
ν_m	Poisson's ratio of the medium
τ	shear stress at the liner-medium contact

CHAPTER 3

e	initial eccentricity measured from centroid of cross section
Δe	increment of eccentricity due to test specimen deflection
e/d	relative eccentricity
E_c	initial modulus of elasticity in compression
d	depth of cross section
S_D	specific heat of dry material

S_S	specific heat of steel fiber
S_W	specific heat of water
T	effective mix temperature
T_A	temperature of aggregate
T_C	temperature of cement
T_F	temperature of free moisture in aggregate
T_M	temperature of mixing water
W_A	weight of aggregate
W_C	weight of cement
W_F	weight of free moisture in aggregate
W_M	weight of mixing water
W_S	weight of steel fiber
ε_{cu}	ultimate concrete compressive strain
ε_{tu}	ultimate concrete tensile strain

CHAPTER 4

A_f	cross sectional area of a steel fiber
D	diameter of the monolithic liner specimen

ΔD	change in diameter of the monolithic liner specimen
E	initial modulus of the concrete
f'_c	compressive strength of the concrete
K_s	slope of load-deflection relationship for jacks that apply passive forces
M	moment on a section
n_w	number of fibers crossing a cross section per unit area
p	volume of fiber expressed as a percent of the total volume
P	active load applied to the liner
P_A, P_B	passive loads applied to the liner (see Fig. 4.31)
T	thrust on a section
ϕ	curvature at a section

CHAPTER 5

A	area
A_c	area of concrete in the concrete-filled structural steel tube
A_s	area of steel
e	eccentricity
E	modulus of elasticity (Young's modulus)

f'_c	ultimate compressive strength of concrete
I	moment of inertia
K	passive jack stiffness
L	length
M	moment
M_p	plastic moment
M_u	moment capacity of the concrete-filled structural steel tube
N	normal force
P	load
P_p	load at which the plastic moment is reached
P_u	ultimate load
P_y	yield load
S	elastic section modulus
Z	plastic section modulus
Δ	deflection
ϵ	unit strain
ϵ_y	yield strain

θ	angle of rotation in a specified length
σ	stress
σ_{PL}	proportional limit stress
σ_u	tensile strength
σ_y	yield stress

APPENDIX A

$\{C\}$	matrix relating the corner forces of the shear panel to the average shear flow along one edge of a shear panel
E_i	modulus of elasticity of increment i
E_o	initial modulus of elasticity
f	equivalent corner force on shear panel
$\{f_e\}$	vector of corner forces on shear panel
F	tangential edge force on shear panel
G_i	modulus of elasticity in shear (modulus of rigidity) in increment i
G_o	initial modulus of rigidity
$[K_{ee}]$	element stiffness matrix of shear panel
$[K_{gg}]$	structural stiffness matrix

$[K^{\ell}_{gg}]$	linear structural stiffness matrix
$[K^{n}_{gg}]$	nonlinear structural stiffness matrix
$[L_{\ell\ell}]$	lower triangular factor $[K_{gg}]$
$\{P_g\}$	structural load vector
$\{P_\ell\}$	load vector for the independent coordinates, modified by the imposed constraints
q	average shear flow along an edge of a shear panel
$\{q_s\}$	vector of forces of single point constraint
$[T]$	geometric transformation matrix relating element coordinate to global coordinates
$\{u_e\}$	vector of corner displacements of shear panel colinear with elements of $\{f_e\}$
$\{u_g\}$	structural displacement vector
$[U_{\ell\ell}]$	upper triangular factor of $[K_{gg}]$
Z	constant relating strain energy to the average shear flow on one side of a shear panel ($= \frac{A}{Gt}$ for rectangular shear panel, where t = thickness of panel)
α_i	load level factor of increment i
γ_i	ratio of load increment at increment i
δ	generalized displacement conjugate to q
ε_i	strain at increment i

CHAPTER 1

SUMMARY

Underground systems may provide a partial solution to many of the country's transportation problems. This possibility provides incentive for increased effort in research for improvement of tunnel design and construction. To meet future transportation needs, techniques which will increase the speed of tunneling and make it more economical and safe are needed. This report describes research on several topics among the most promising in improving the overall tunneling technology. The project is continuing, and work in some of the areas is incomplete. The objective in the long run of all the work is to improve either speed, safety, or economy of tunneling.

The second chapter describes studies designed to provide a better understanding of the interaction of tunnel liners with the medium in which they are placed. The loads on any ground support system depend on the relative stiffness of the support and medium, and on the construction and tunneling techniques. The effect of liner and medium material properties and geometry is considered by computing the liner moment, shear, thrust, and deformation as the compressibility and flexibility ratios of the linear-medium system are allowed to vary. These ratios are defined to provide a measure of the relative extensional and flexural stiffness of the liner and medium. A closed form solution and a discrete element computer program in which all material behavior is assumed to be linear were used, and the results from each are compared.

Two construction procedures were studied in which the sequence of material removal and support of the opening is different, resulting in different support loads. In the first, termed excavation loading, no deformation is assumed to occur at the face between the time the material is removed and support is provided. The full in situ stress condition acts on the completed liner at the start of the interaction. This loading can be developed on liners that have been constructed by advancing a series of adjacent drifts, backfilling each with concrete, and then excavating the material inside the completed ring. In the second, termed gravity loading, the opening is assumed to deform and support itself after the material is removed, and before the liner is constructed, but a load equal to the overburden load directly above the opening is subsequently applied to the liner. The liner then interacts with the surrounding medium in resisting this loading which results from the time-dependent deformation of the medium. This loading is most applicable to relatively shallow tunnels in which support is provided well behind the face. In these studies the depth of burial is varied, and the longitudinal stresses in the liner at the face are computed.

Thrust, moment, shear and diameter change are shown in graphical form as the relative stiffness of the liner and medium vary, and for the two construction procedures. The various solutions provide bounds on the liner behavior for the practical cases that exist in the field.

The third chapter is devoted to the description of properties of concrete made with a fast setting cement and containing randomly oriented steel fibers. In a previous report (Parker, et al., 1971), a system was described for slipforming a tunnel liner directly behind the face as

excavation proceeds. A rapid setting cement is required for this system so that the finished liner can support itself and the ground when the slipform has passed. For those situations that require more flexural strength for early support than the concrete alone can provide, randomly distributed steel fibers in the concrete were proposed. The experimental work described was undertaken to provide information about the materials for design of the slipform system.

The studies can be divided into problems associated with design of the mix and placement, and those associated with the long and short term properties of the hardened material. Placement is envisioned to be by pumping, which is made much more difficult by addition of the steel fibers. Thus, design of the mix must have the dual objective of obtaining a finished product with given properties and being pumpable for some given length of time. The effect of proportions of coarse and fine aggregate, cement and water on strength and pumpability have been studied. Experience in mixing and pumping steel fiber reinforced concrete and concrete made with a fast setting cement in the field under fairly typical construction conditions is described.

Design of the liner for short term and long term loads requires a knowledge of the material properties. Moment-thrust failure envelopes were obtained for the material at an early age and at 28 days with several steel fiber contents by testing a series of beam-columns. These tests help describe the load capacity and cracking behavior of a tunnel liner, and provide the mechanical properties of the liner material for analyses of the type described in Chapter 2. In addition, the section behavior is used in interpretation of large scale liner tests discussed in Chapter 4.

The slipformed liner provides the primary and secondary liners, and thus must furnish support throughout the life of the tunnel. Deterioration due to naturally occurring chemicals was investigated as well as long-term dimensional stability and creep under load.

Chapter 4 describes the testing of two specimens which were approximinately one-half scale models of sections of a steel-fiber-reinforced slipformed liner like that described above. The first specimen was made of concrete with a low strength and represented the liner shortly after the slipform had passed and before the concrete had gained full strength. The second represented more closely the long term strength of the liner. Radial loading of the specimen was provided by 24-60 ton hydraulic jacks spaced at 30 degree intervals. One-half the jacks were symmetrically placed around two sides of the specimen to represent active loads of the ground at the crown and invert. The remaining jacks at the other two sides represented the passive resistance of the ground around the springlines, and were controlled during the test to have a linear load-deflection behavior.

Instrumentation permitted determining the deformation and loads, and made possible the calculation of moments and thrusts in the liner. Capacity of the specimens was not reached due to failure of the loading system; nevertheless, the loading extended well beyond the linear range and allowed an evaluation of those characteristics of the system that allowed considerable redistribution of loads and moments. The moment-thrust path at the critical crown and invert sections followed the moment-thrust failure envelope, once it was reached, until the jacking system failed.

Linear (STRUDL) and nonlinear (NASTRAN) analyses are compared

with the test results, though the nonlinear analysis is in its early stages of use and only a few solutions are available. Poor agreement with the linear analysis was attributed to local anomalies in the test loading to which moments in the liner are sensitive. Maximum active loads in the tests were more than twice those predicted by the linear analysis. It is concluded that the linear analysis is an effective tool in predicting liner cracking, but is very conservative in its prediction of maximum load.

The nonlinear analysis allowed the moment-thrust path of the critical sections to follow the failure envelope, but did not predict the ultimate load accurately because the program will not allow the stress-strain diagram for the material to descend after reaching the peak stress. Further work is proposed with the nonlinear analysis.

Chapter 5 concerns ground support with steel sets, and describes tests on sets and analyses performed with linear and with nonlinear assumptions of material behavior. Several parameters which affect the set behavior are investigated in the tests and by analysis.

Horseshoe sets with a 5 ft (1.5 m) radius arch and 7 ft (2.1 m) straight legs were tested with concentrated loads applied at regular spacing around the arch. Eleven tests were performed of which five were carried to failure and the remainder were loaded in the linear range. The major variables in these tests were connection stiffness, blocking stiffness, load distribution, and section shape. Structure stiffness in terms of load--deflection relationships is compared for these variables and in some cases the load capacities can be compared. Seven load points evenly spaced around the arch segment represented either active loads from ground movement or

passive resistance of blocking points. Two configurations of active load were considered: three load points symmetrical about the crown, or three load points at the side of the arch. Two passive blocking stiffnesses that represent extreme cases of soft and hard blocking were considered. Two connections in the sets were used. One represented a standard connection for the smaller type set and had a low moment capacity whereas the other had a moment capacity almost equal to that of the set section. Sets made of a wide flange shape and a square structural tube were tested.

The parameters considered in the tests were varied over a much wider range by performing analyses on the sets with a linear analysis computer program. These studies indicate how the various parameters influence the set deflection, yield moments, and stiffness. In addition, a nonlinear analysis program is described and used to represent a simple beam to study its accuracy. It was then used to predict the behavior of a set test to show its applicability to studies of steel ground supports. Further studies are planned with this program.

Connections like those used in the set tests were subjected to combinations of moment and thrust to determine their stiffness and moment capacity for use in the computer programs. Mechanical properties of the material for correlation with the tests and for use in the analyses were obtained from tension coupon tests and stub column tests.

Short lengths of the structural tube section, filled with various strength of concrete and unfilled, were tested as beams, beam-columns and columns to determine the interaction diagrams. Calculations were made to predict these diagrams which will be used to study the behavior and load capacity of sets made of a concrete filled box.

Dual-unit format is employed in the presentation of all data, figures, and tables included in this report. Data and tables are presented in the English system, with International System of Units (SI) values included in parentheses. Figures are presented with auxiliary scales for SI units. In equations containing nonhomogeneous constants, the equation is given in English units followed by the SI form of the equation. For example, the English form of an equation may be designated Eq. 3.1 and the SI form designated Eq. 3.1-SI.

CHAPTER 2

RATIONAL DESIGN OF TUNNEL SUPPORTS

2.1 INTRODUCTION

Tunnel supports are designed on the basis of the anticipated magnitude and distribution of thrust, moment and shear. These forces are mobilized by the external pressures that act on the support. The magnitude and distribution of these external pressures are functions of many variables, two of which are the type of active loading to which the support is initially subjected and the interaction that follows between the supporting system and the surrounding medium. This medium-support interaction is a complex phenomenon that is in turn a function of the material properties of the support and the medium. This chapter evaluates certain aspects of this interaction for circular liners.

A circular tunnel support or liner can be designed without consideration of interaction if the assumption is made that it is either perfectly "rigid" or perfectly "flexible." A "rigid" liner does not deform under load and, thus, there can be no interaction and there is no change in the initial loading. A "flexible" liner is assumed to be incapable of carrying bending moments and, thus, deforms under the initial loading until equilibrium is reached under an external pressure that is nearly uniform. The design of tunnel liners based on either of the above assumptions is not affected directly by the material properties of the medium since the design parameters, such as moment and thrust, are functions only of tunnel

geometry and loading. However, the stiffness of the medium must be considered for liners of intermediate stiffness where interaction is taken into account to eliminate the conservatism associated with the "rigid" liner approach.

Realizing that most circular tunnel supports fall somewhere between the two limiting cases of perfectly "rigid" and perfectly "flexible," designers have attempted to account for interaction on an empirical basis. Some tunnel liners were designed for a uniform external pressure distribution (corresponding to the "flexible" case) and, to account for some rigidity, for bending moments resulting from an assumed diameter change that is based on some field measurements of liners which have behaved satisfactorily. Other liners have been designed for an external pressure distribution corresponding to a modified coefficient of earth pressure at rest (corresponding to the "rigid" case). This modified K, which amounts to the actual K_o adjusted so as to be more nearly equal to 1.0, accounts for some interaction between the soil and the liner. In both approaches given above the extent of the deviation from the limiting case was determined from consideration of the material properties of the medium and the liner.

Recent developments resulting from the study of interaction have provided more rational methods of analysis that consider not only tunnel geometry and loading, but also the material properties of the medium and the liner. This chapter presents results from both closed form and discrete element methods for the determination of forces and deformations used in the design of tunnel liners embedded in an elastic medium. The effects of medium material properties on forces and deformations, the effects of various loading conditions, and finally the longitudinal effects

for cases where the liner is advanced near the face of the tunnel are evaluated. Finally, the practical application of these techniques to the design of tunnel liners is discussed.

2.2 MATERIAL PROPERTIES: THE COMPRESSIBILITY AND FLEXIBILITY RATIOS

The properties of the surrounding medium have a pronounced effect on the behavior of the tunnel support. The forces and deformations in a liner in soft ground are quite different from those in an identical liner, subject to the same loading conditions, in a stiff ground.

Analytical soil-structure interaction studies by Burns and Richard (1964) and by Höeg (1968), define two parameters, the compressibility and flexibility ratios, which give a quantitative assessment of the relative stiffness of the liner and the medium. The compressibility ratio is defined as the extensional stiffness of the medium relative to that of the liner, while the flexibility ratio is a measure of the flexural stiffness of the medium relative to that of the liner. The two ratios are given below:

$$C = \frac{\dfrac{E_m}{(1+\nu_m)(1-2\nu_m)}}{\dfrac{E_\ell t}{(1-\nu_\ell^2)}\,\dfrac{1}{R}} \qquad (2.1)$$

$$F = \frac{\dfrac{E_m}{(1+\nu_m)}}{\dfrac{6\,E_\ell I_\ell}{(1-\nu_\ell^2)}\,\dfrac{1}{R^3}} \qquad (2.2)$$

where

C, F = compressibility and flexibility ratios, respectively,

E_m, E_ℓ = modulus of elasticity of the medium and the liner, respectively,

ν_m, ν_ℓ = Poisson's ratio of the medium and the liner, respectively,

R, t = radius and effective thickness of the liner, respectively,

I_ℓ = effective moment of inertia of the liner cross section.

A detailed derivation of these two parameters is given by Peck, Hendron and Mohraz (1972). For tunnel supports consisting of built-up sections such as the channel and wide-flange, the effective thickness, t, is the cross sectional area of the section divided by the spacing between ribs in the direction of the tunnel axis. Similarly, the effective moment of inertia, I_ℓ, of such supports is the standard moment of inertia of the section divided by the rib spacing. Guidelines for the determination of E_m are given by Krizek and Kay (1972).

The variation of compressibility and flexibility ratios with a non-dimensional parameter reflecting the liner's dimensions and the medium and liner moduli (modulus ratio) is given in Figs. 2.1 and 2.2. The plots are for a circular liner of uniform cross section with Poisson's ratio values of 0.15 and 0.30 which are typical of concrete and steel, respectively. On account of a linear relationship between the compressibility and flexibility ratios and the modulus ratio, the plots are straight lines with a 45 degree slope. The plots indicate that Poisson's ratio of the medium has

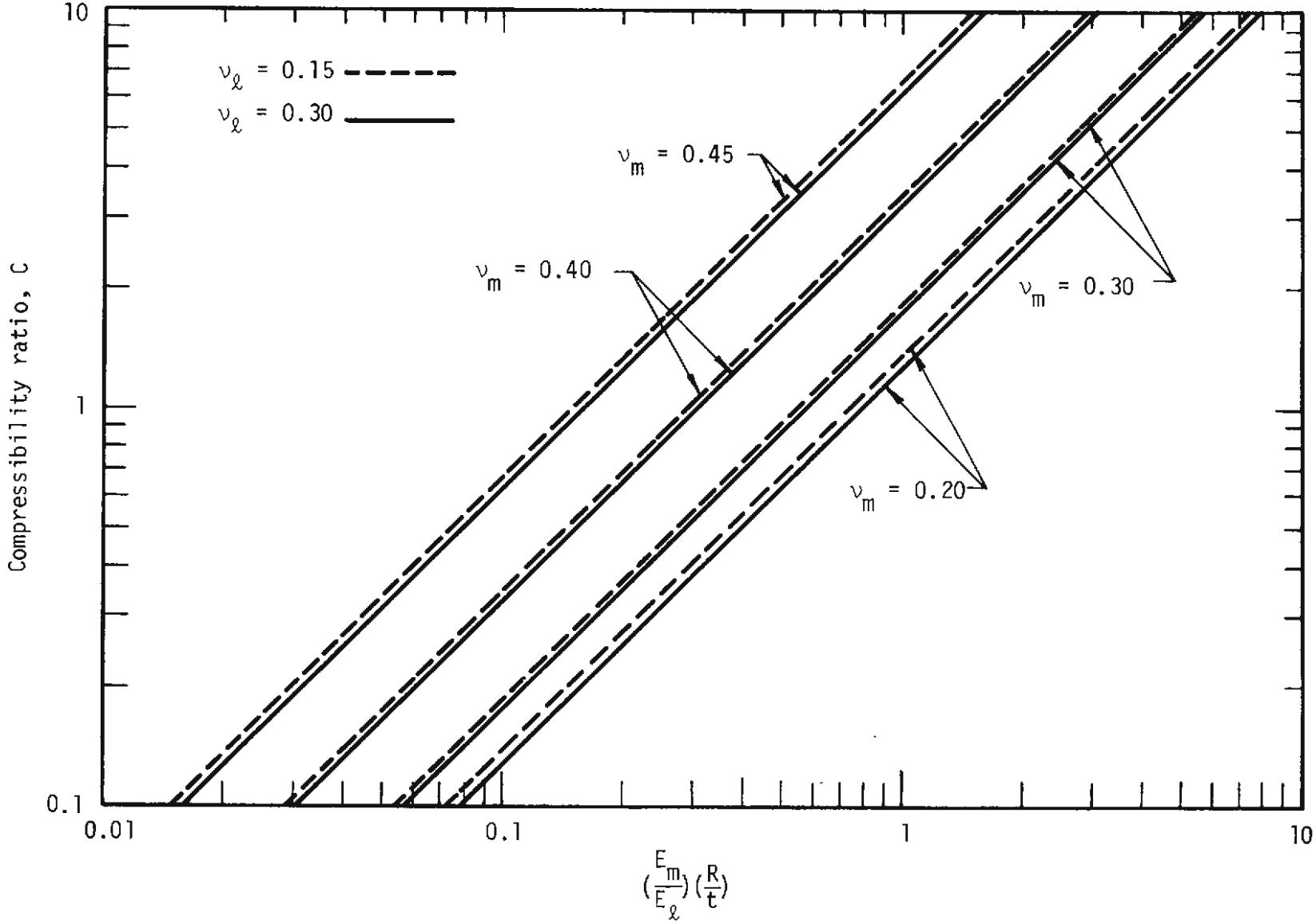

FIGURE 2.1 VARIATION OF COMPRESSIBILITY RATIO WITH MODULUS RATIO

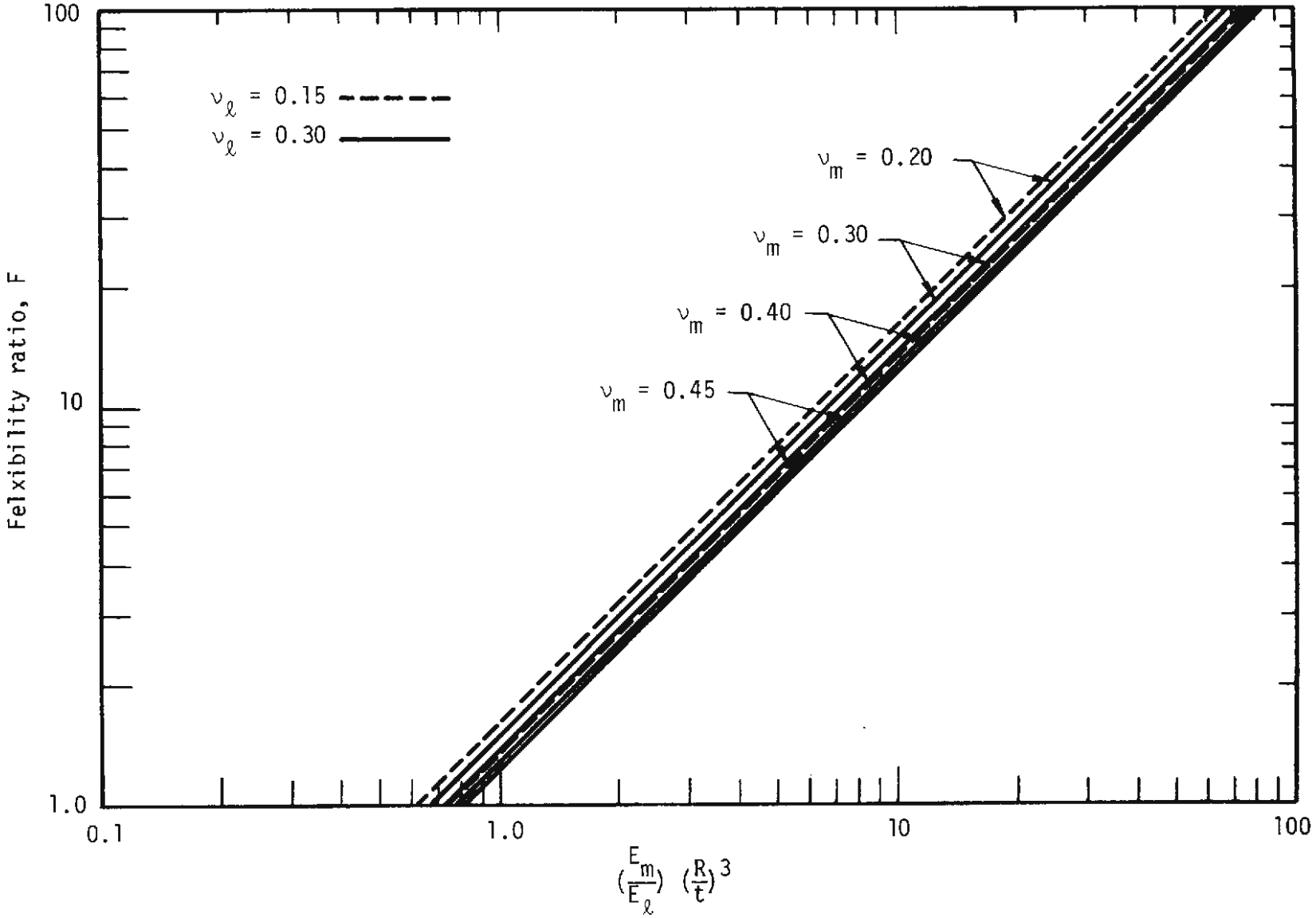

FIGURE 2.2 VARIATION OF FLEXIBILITY RATIO WITH MODULUS RATIO

a pronounced effect on the compressibility ratio but not on the flexibility ratio, where as the Poisson's ratio of the liner has negligible effect on both ratios.

2.3 CLOSED FORM SOLUTIONS

2.3.1 GENERAL

Burns and Richard (1964) have shown that, because of the interaction of the liner and the medium, the thrust and moment in the liner are functions of both the compressibility and flexibility ratios. In addition, the condition at the interface of the liner and medium (full or no slippage) affects the thrust and moment in the liner. The no-slippage case is more realistic for liners in rock while the behavior of liners in cohesive and granular soils can be considered to be between the no-slip and full-slip cases.

2.3.2 EXPRESSIONS FOR THE DESIGN PARAMETERS

The expressions for thrust, moment, transverse shear, and deformations in the liner are obtained by considering the appropriate pressure distribution on the liner or by modifying the equations formulated by Burns and Richard (1964). Nondimensionalized coefficients for thrust, moment, transverse shear, deformations and shear stress at the interface as functions of compressibility and flexibility ratios for both full slippage and no slippage conditions are given below:

For full slippage at the interface

$$\frac{T}{\gamma HR} = \frac{1}{2}\left[(1 + K_o)(1 - a_1) + \frac{1}{3}(1 - K_o)(1 + 3a_2 - 4a_3)\cos 2\theta\right] \tag{2.3a}$$

$$\frac{M}{\gamma HR^2} = \frac{1}{6}(1 - K_o)(1 + 3a_2 - 4a_3)\cos 2\theta \tag{2.4a}$$

$$\frac{S}{\gamma HR} = -\frac{1}{3}(1 - K_o)(1 + 3a_2 - 4a_3)\sin 2\theta \tag{2.5a}$$

$$\frac{\Delta D/D}{\gamma H/M_c} = \frac{1}{2}\left[(1 - \nu_m)(1 + K_o)(1 - a_1)\, C - \frac{2}{3}\left(\frac{1 - \nu_m}{1 - 2\nu_m}\right)(1 - K_o)(1 + 3a_2 - 4a_3)\, F \cos 2\theta\right] \tag{2.6a}$$

$$\frac{\tau}{\gamma H} = 0 \tag{2.7a}$$

and for no slippage at the interface

$$\frac{T}{\gamma HR} = \frac{1}{2}\left[(1 + K_o)(1 - b_1) + (1 - K_o)(1 + b_2)\cos 2\theta\right] \tag{2.3b}$$

$$\frac{M}{\gamma HR^2} = \frac{1}{4}(1 - K_o)(1 - b_2 - 2b_3)\cos 2\theta \tag{2.4b}$$

$$\frac{S}{\gamma HR} = -\frac{1}{2}(1 - K_o)(1 - b_2 - 2b_3)\sin 2\theta \tag{2.5b}$$

$$\frac{\Delta D/D}{\gamma H/M_c} = \frac{1}{2}\left[(1 - \nu_m)(1 + K_o)(1 - b_1)\, C - \left(\frac{1 - \nu_m}{1 - 2\nu_m}\right)(1 - K_o)(1 - b_2 - 2b_3)\, F \cos 2\theta\right] \tag{2.6b}$$

$$\frac{\tau}{\gamma H} = \frac{1}{2}(1 - K_o)(1 - 3b_2 + 2b_3) \sin 2\theta \qquad (2.7b)$$

in which

$$a_1 = b_1 = \frac{(1 - 2\nu_m)(C - 1)}{(1 - 2\nu_m)(C) + 1}$$

$$a_2 = \frac{2F + 1 - 2\nu_m}{2F + 5 - 6\nu_m}$$

$$a_3 = \frac{2F - 1}{2F + 5 - 6\nu_m}$$

$$b_2 = \frac{(1 - 2\nu_m)(1 - C)\,F - \frac{1}{2}(1 - 2\nu_m)^2\,C + 2}{[(3 - 2\nu_m) + (1 - 2\nu_m)\,C]F + (\frac{5}{2} - 8\nu_m + 6\nu_m^2)\,C + 6 - 8\nu_m}$$

$$b_3 = \frac{[1 + (1 - 2\nu_m)\,C]\,F - \frac{1}{2}(1 - 2\nu_m) - 2}{[(3 - 2\nu_m) + (1 - 2\nu_m)\,c]\,F + (\frac{5}{2} - 8\nu_m + 6\nu_m^2)\,C + 6 - 8\nu_m}$$

where

T, M, S = thrust, moment, and transverse shear in the liner, respectively

τ = shear stress at the interface

R, D, ΔD = radius, diameter and the change in diameter of the liner, respectively

H = distance from the ground surface to the center of the tunnel

γ = unit weight

M_c = constrained modulus of the medium surrounding the liner = $\frac{E(1 - \nu_m)}{(1 + \nu_m)(1 - 2\nu_m)}$

θ = angle defining position on the liner; measured counter clockwise from the right springline, Fig. 2.3

The above equations are for a deeply buried, circular tunnel liner embedded in an elastic, homogeneous and isotropic medium. The expressions are for a portion of the medium containing the liner and loaded by external pressures as shown in Fig. 2.3. It is assumed that the liner is placed into the opening without disturbing the medium and that the medium and the liner are unstressed before any loads are applied.

2.3.3 MOMENT AND TRANSVERSE SHEAR

The expressions for moment and transverse shear in the liner, Eqs. 2.4 and 2.5, indicate that the moment and transverse shear are proportional to $(1 - K_o)$, which is a measure of the difference between the major and minor free-field principal stresses in the medium. For the full slippage condition the moment and transverse shear coefficients are independent of the compressibility ratio. Even though both the flexibility and compressibility ratios appear in expressions for b_2 and b_3 which are used in the moment and transverse shear coefficients for the no slippage condition, computations indicate that these coefficients are primarily functions of the flexibility ratio only. The condition at the liner-medium interface has

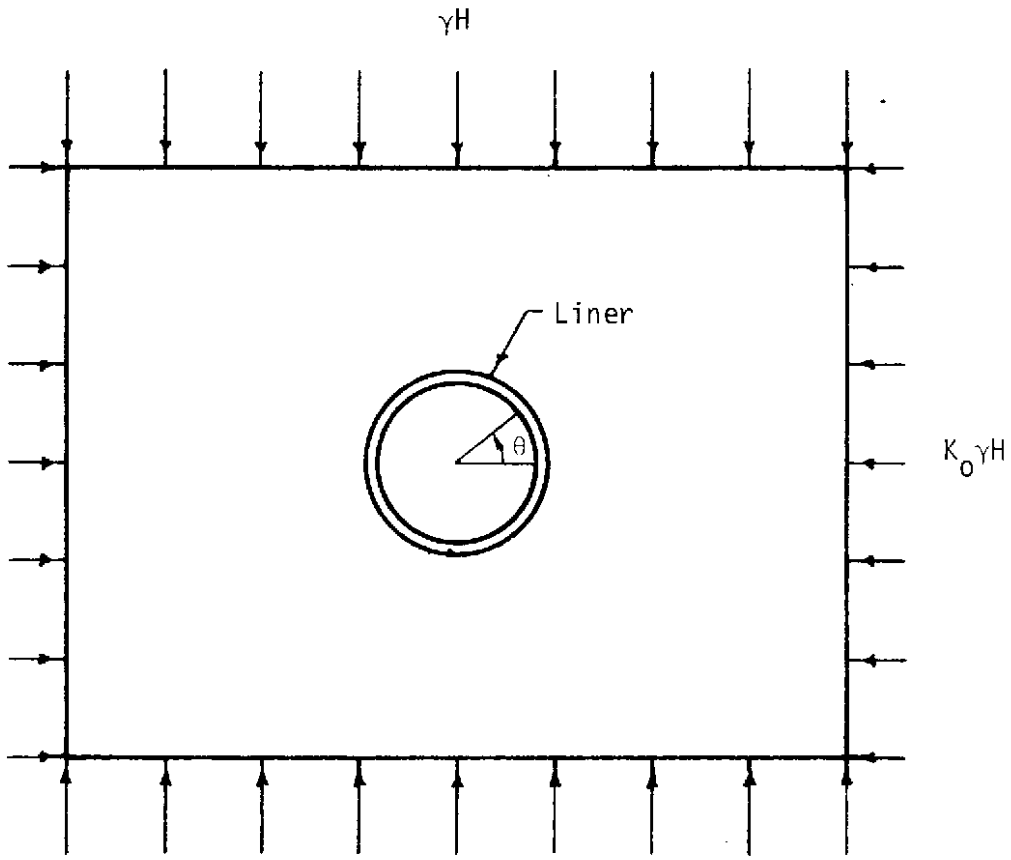

FIGURE 2.3 LOADING CONDITION USED IN THE CLOSED FORM SOLUTION

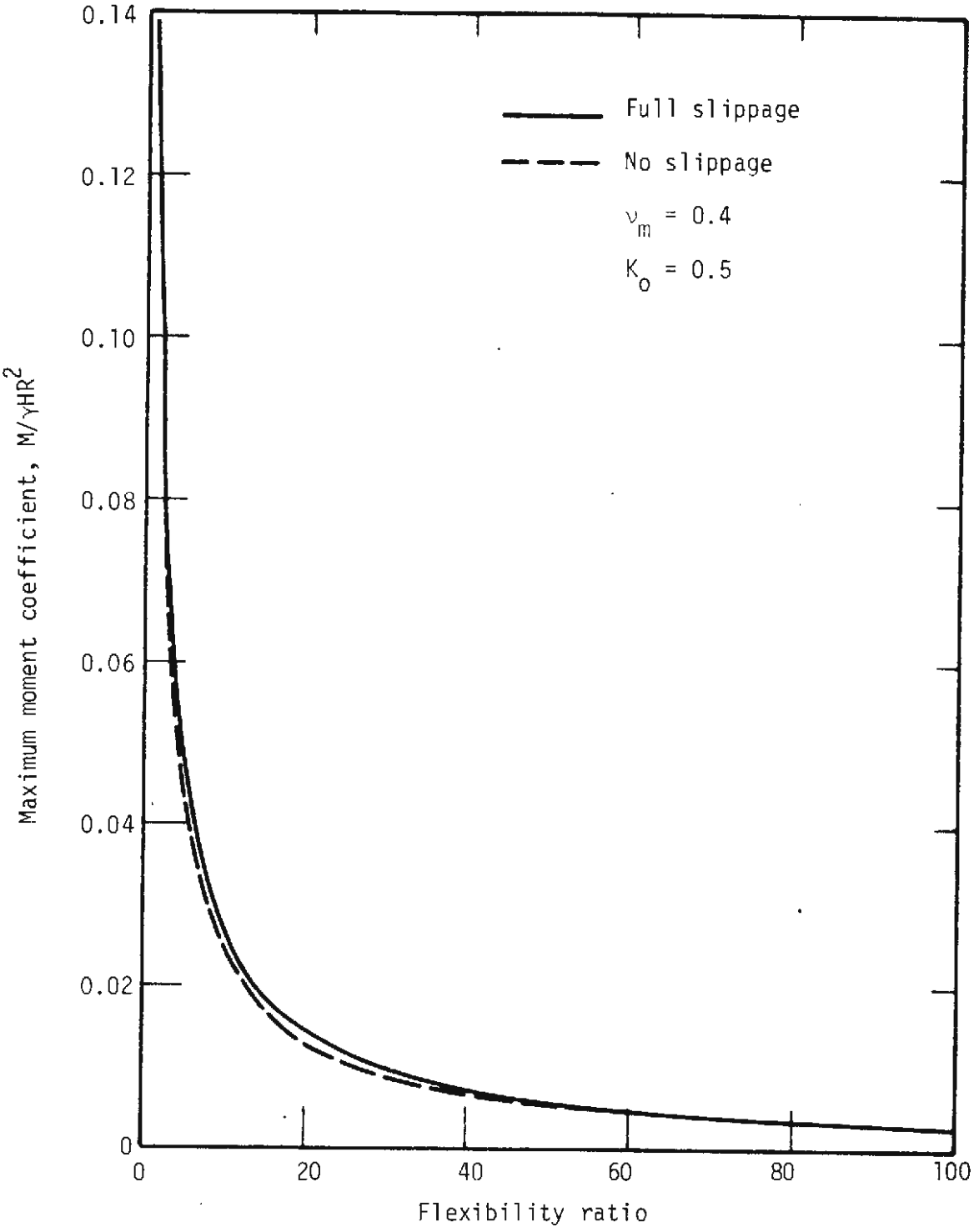

FIGURE 2.4 VARIATION OF MAXIMUM MOMENT COEFFICIENT WITH FLEXIBILITY RATIO

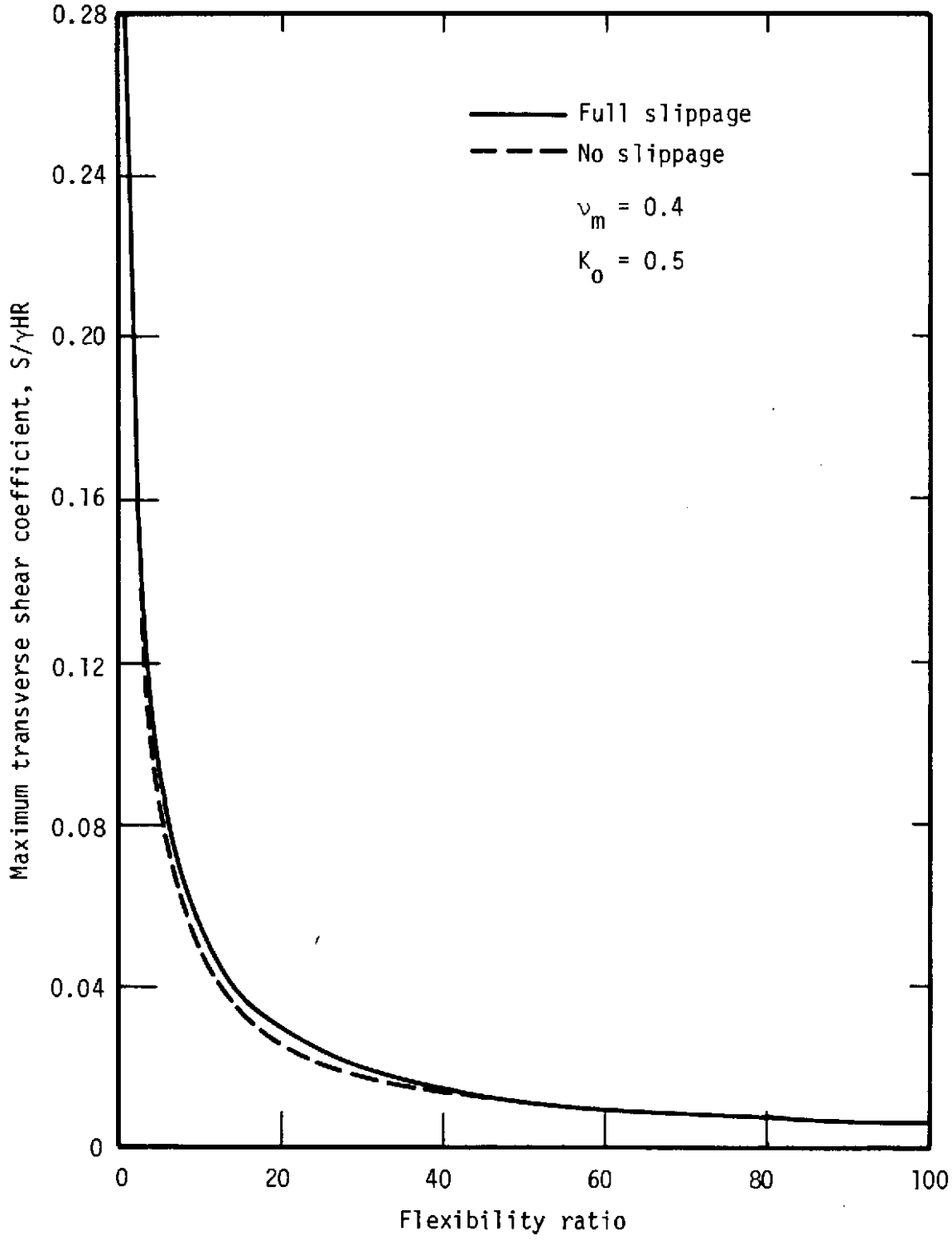

FIGURE 2.5 VARIATION OF MAXIMUM TRANSVERSE SHEAR COEFFICIENT WITH FLEXIBILITY RATIO

little influence on the moment and transverse shear coefficients, Figs. 2.4 and 2.5. These curves indicate that the maximum moment and transverse shear coefficients decrease very rapidly with an increase in the flexibility ratio. For flexibility ratios greater than about 10, the liner can be said to behave flexibly (moments in the liner are not significant) with respect to the medium. Although the plots are for a $K_o = 0.5$ and $\nu_m = 0.4$, plots for other values of coefficient of earth pressure and Poisson's ratio are easily obtained from Eqs. 2.4 and 2.5.

2.3.4 THRUST

Plots of the thrust coefficient as functions of flexibility and compressibility ratios are given in Figs. 2.6 and 2.7, respectively. The plots indicate that the thrust coefficient is insensitive to the flexibility ratio, especially for high flexibilities. However, the thrust coefficient is strongly affected by the condition at the interface. The difference between the thrust coefficients at the crown and springline in the "no slippage" case is due to the presence of shear stresses at the interface. The magnitude of these shear stresses can be obtained from Eq. 2.7b. Thrust coefficients for other Poisson's ratio and coefficients of earth pressure are easily obtained from Eqs. 2.3a and 2.3b.

2.3.5 INTERFACIAL SHEAR STRESS

Figure 2.8 indicates that the maximum interfacial shear stress coefficient is constant for all flexibility ratios except for very low flexibilities. The shear stress at the interface is a function of the coefficient of earth pressure K_o. For flexible liners, the magnitude of this

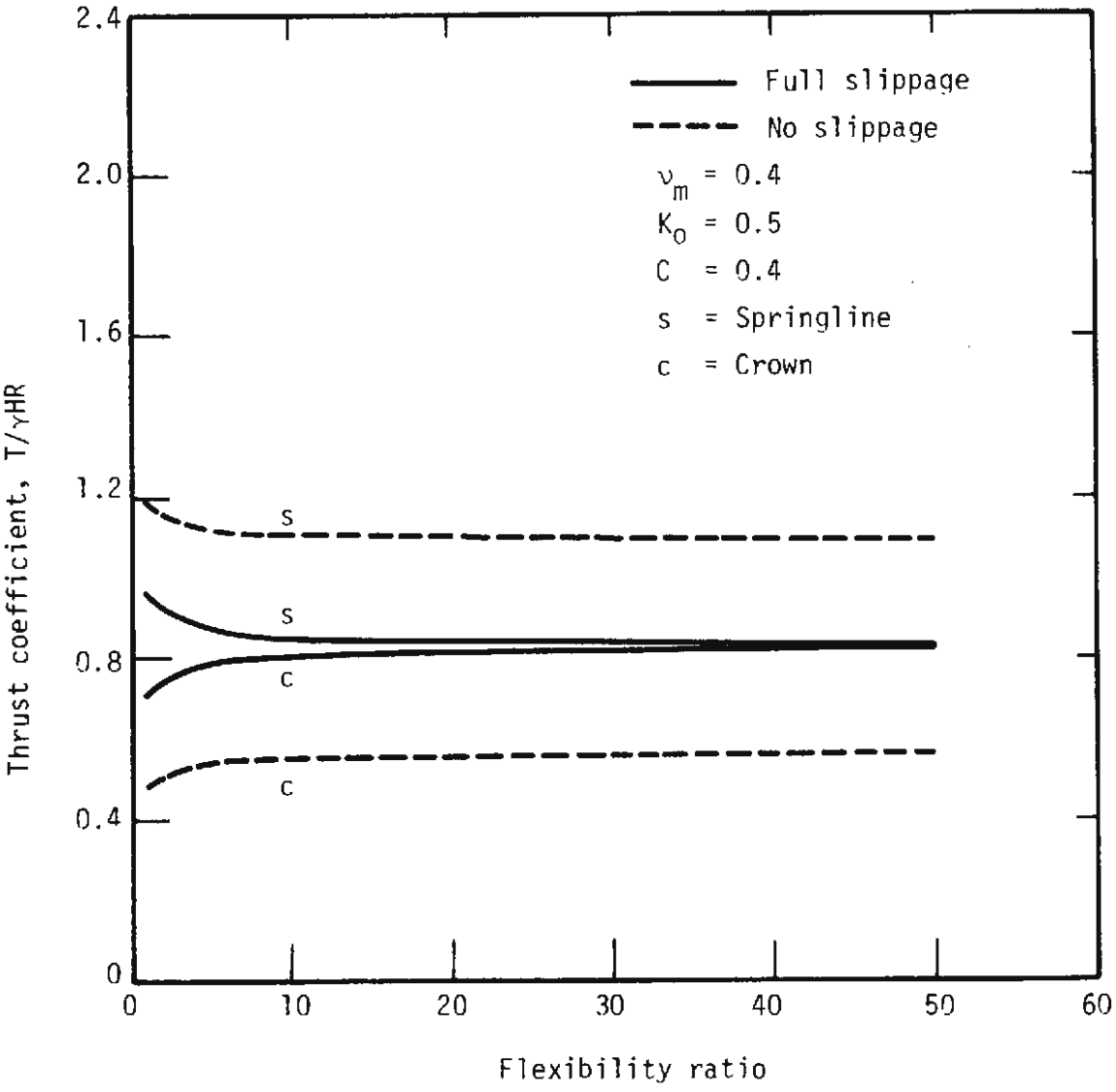

FIGURE 2.6 VARIATION OF THRUST COEFFICIENT WITH FLEXIBILITY RATIO

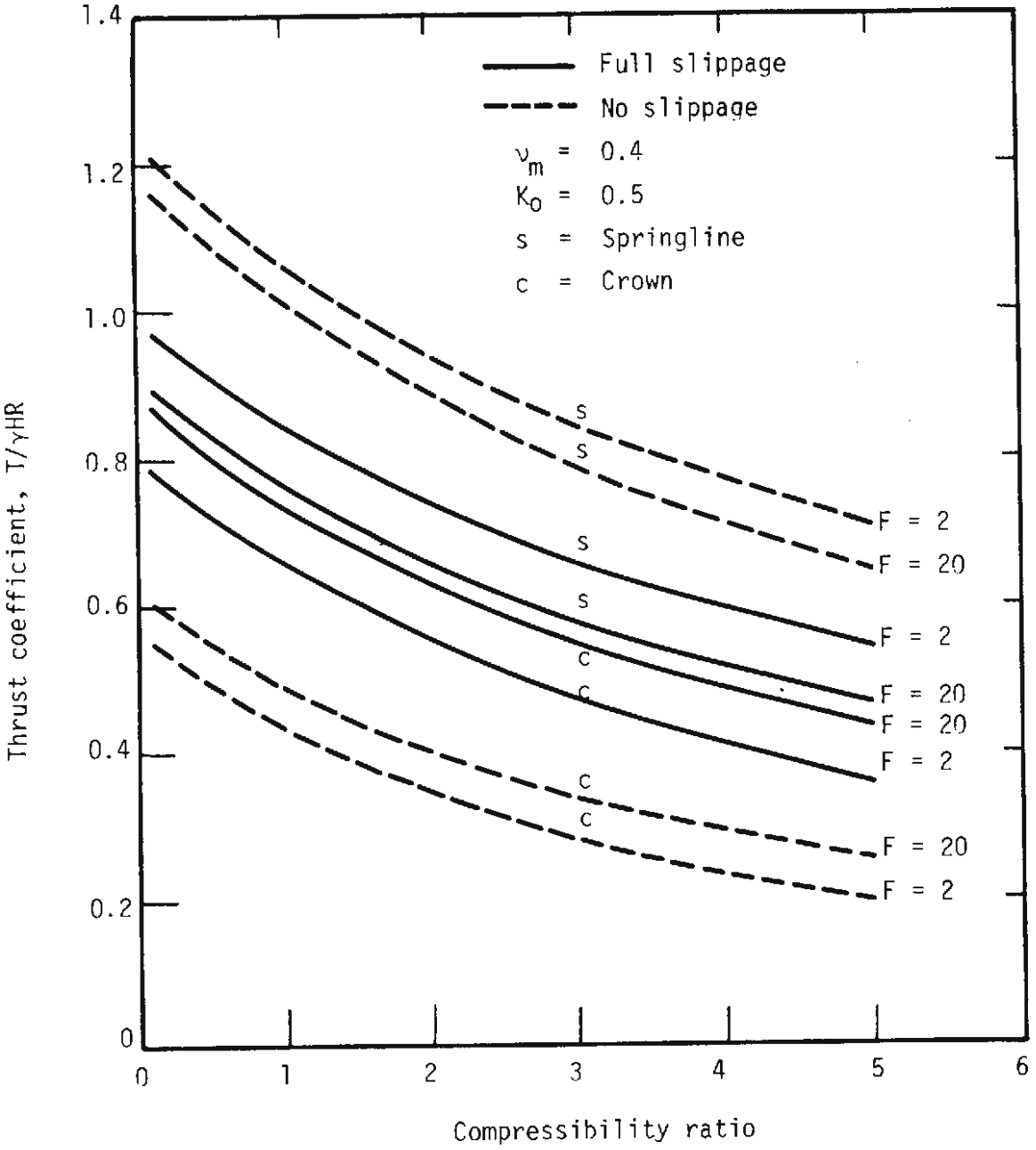

FIGURE 2.7 VARIATION OF THRUST COEFFICIENT WITH COMPRESSIBILITY RATIO

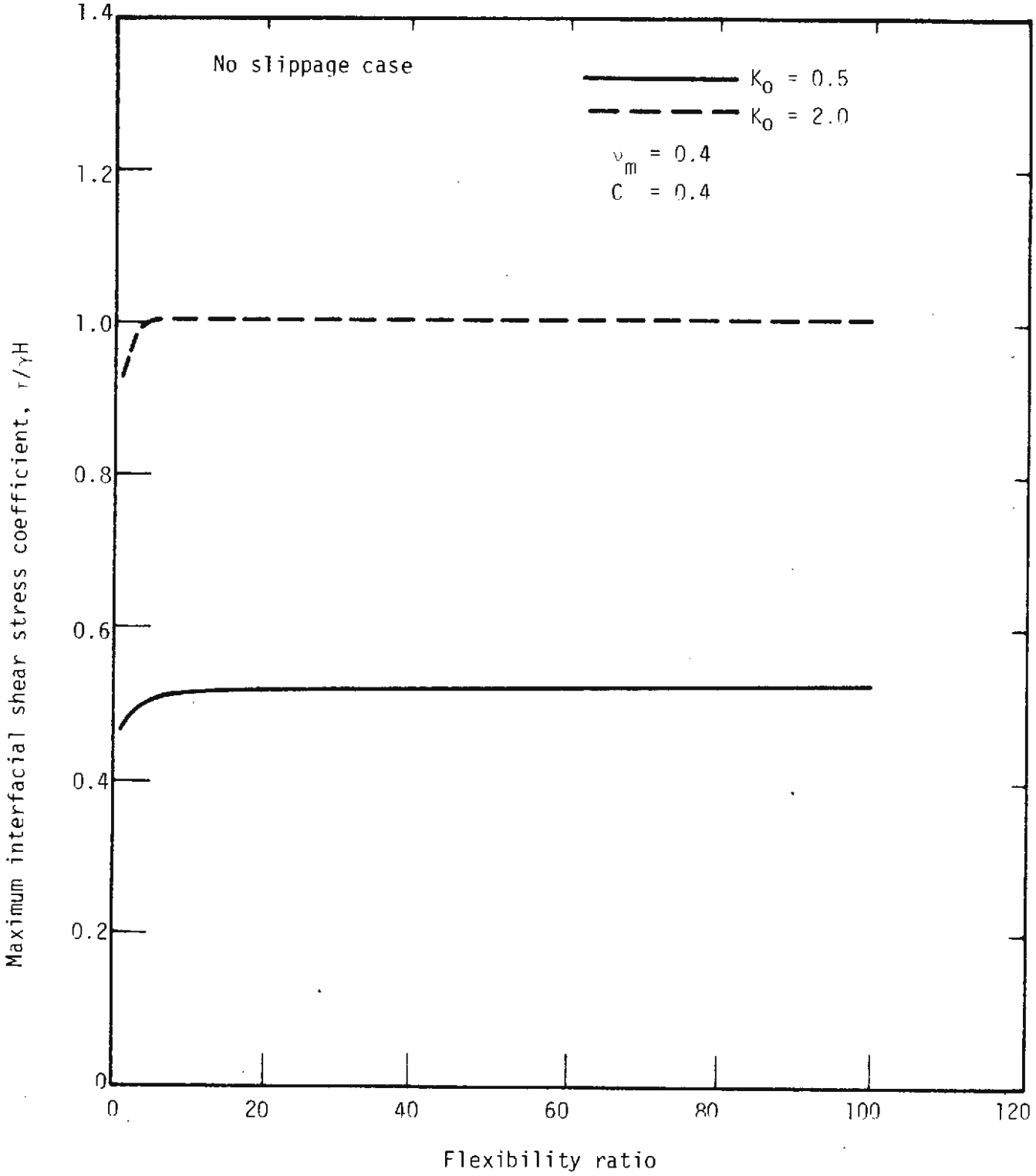

FIGURE 2.8 VARIATION OF MAXIMUM INTERFACIAL SHEAR STRESS COEFFICIENT WITH FLEXIBILITY RATIO

maximum shear stress can be approximated by $(1 - K_o)\gamma H$. When the no slippage condition is assumed for obtaining the forces and deformations in the liner, the interfacial shear stress should not exceed the shear strength of the medium.

2.3.6 DIAMETER CHANGE

The expressions for diameter changes, Eqs. 2.6a and 2.6b, give the total deformation that results when an unstressed medium containing a lined hole is subjected to the applied stress shown in Fig. 2.3 (i.e., the lined hole is present before the stresses are applied). The total deformation, δ_T, is the sum of the deformation of the medium, δ_M, due to the applied stress and the deformation of the lined hole, δ_L. In reality the medium is subjected to the applied stress before the lined hole is placed. Thus, δ_M has occurred prior to the existence of the lined hole and should not be considered as part of the deformation of the liner which occurs due to tunneling. The approximate deformation of the liner due to excavation is given by

$$\delta_L = \delta_T - \delta_M$$

where δ_T corresponds to the closed form expressions given by Eqs. 2.6a and 2.6b and δ_M is given by the following medium deformations:

$$\left(\frac{\Delta D/D}{\gamma H/M_c}\right)_{\text{vertical}} = \frac{1 - \nu_m}{1 - 2\nu_m}\left[(1 - \nu_m) - K_o\nu_m\right] \qquad (2.8a)$$

$$\left(\frac{\Delta D/D}{\gamma H/M_c}\right)_{\text{horizontal}} = \frac{1 - \nu_m}{1 - 2\nu_m}\left[K_o(1 - \nu_m) - \nu_m\right] \qquad (2.8b)$$

The variation of the liner diameter change with flexibility ratio is shown in Fig. 2.9. The plot indicates that, for flexibility ratios greater than 10, the diameter changes are nearly constant. Since the moment in the liner is almost the same for both full slippage and no slippage conditions (see Fig. 2.4), the difference between the two deformations is due to the difference in thrusts in the liner.

2.4 DISCRETE METHOD SOLUTIONS

2.4.1 GENERAL

Due to the many simplifying assumptions required to obtain an exact solution (see Sect. 2.3.2), the closed form analysis is not applicable to many real tunneling conditions. A large number of tunnels being built today are located at shallow depths of cover where the surface boundary and the increase in in situ stresses with depth affect the behavior of the tunnel. Although one can obtain closed form expressions for unlined shallow tunnels (Mindlin, 1940), closed form solutions for lined shallow tunnels are not available. In addition, the closed form solutions do not simulate the actual loading conditions on the liner. For example, in most cases when the tunnel is excavated, some deformations occur before the liner is placed. The magnitude and distribution of this initial deformation affect the magnitude and distribution of the pressures that act on the liner. If a high percentage of the deformation due to excavation occurs before the liner is placed, the primary source of loading is the force of gravity which acts to pull the overburden down onto the liner with time due to the undrained creep characteristics of cohesive materials.

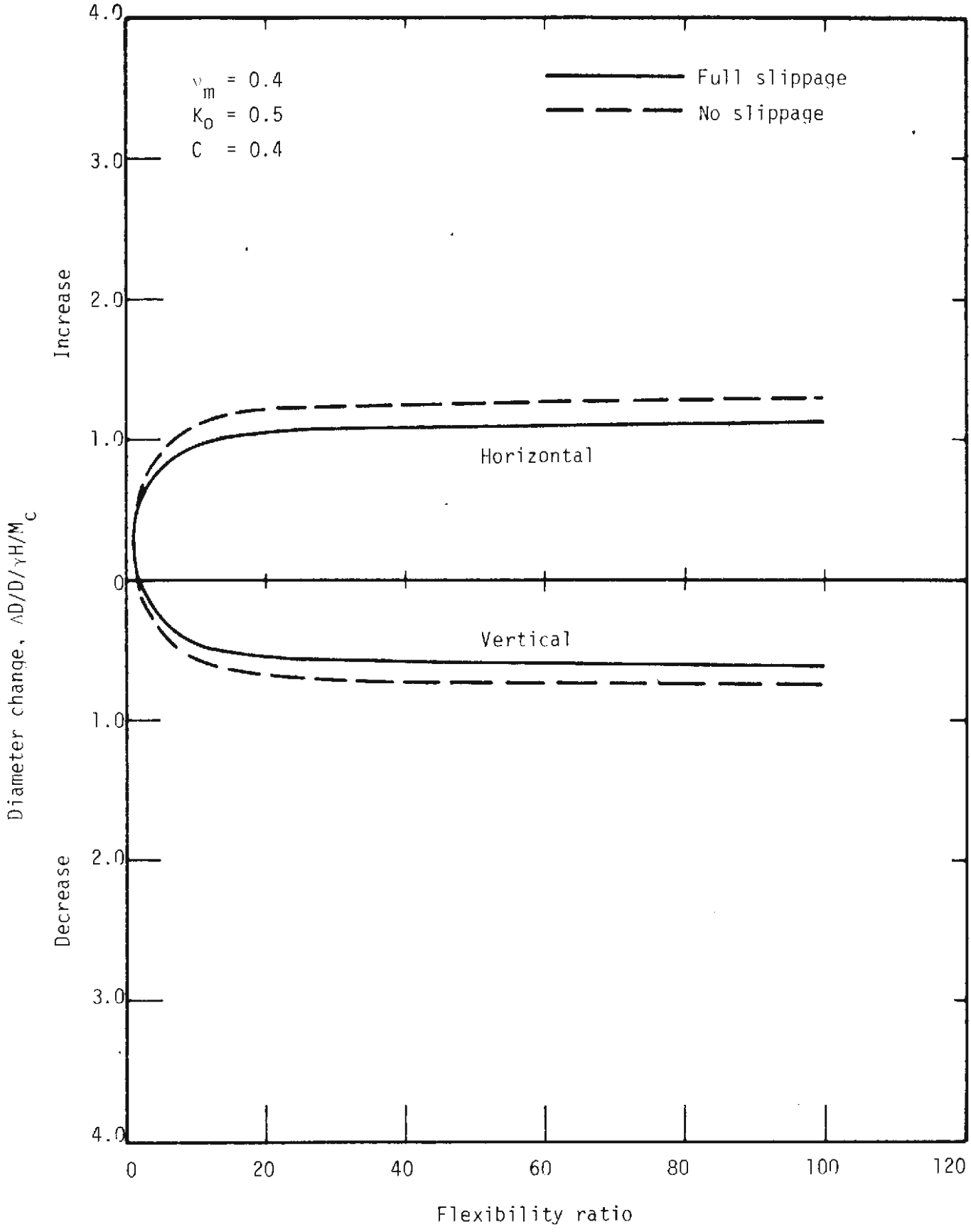

FIGURE 2.9 VARIATION OF DIAMETER CHANGE COEFFICIENT WITH FLEXIBILITY RATIO

For cases such as those mentioned above, the discrete methods of analysis such as the finite differences or the finite element method can be used to approximate the forces and deformations in the liner. Nevertheless, the closed form solutions can be used to identify significant dimensionless parameters such as the flexibility and compressibility ratios and dimensionless thrust, moment, and shear coefficients for the forces in the liner.

The finite element method has been widely used for problems in geotechnical engineering. This method is versatile with respect to various loading and boundary conditions and is adaptable to computer programming.

2.4.2 LOADING CONDITIONS

Two loading conditions were investigated in this study by means of the finite element procedure. Both of these solutions are elastic solutions that assume no slippage between the liner and the medium. The first, referred to as "excavation loading," would, in principle, be developed if the lining could be inserted into the medium without strain or deformation and the medium inside the lining then excavated. This condition can be approximated in practice on tunnel liners constructed by advancing a series of adjacent drifts around the perimenter of the proposed tunnel, backfilling each with concrete, and then excavating the material inside the completed ring, Fig. 2.10a. This type of construction technique might be used for large diameter tunnels driven through weak materials that would not tolerate conventional full-face or heading and bench driving methods. The deformations and disturbance of the surrounding medium due to this method of construction are small relative to those that would result if conventional

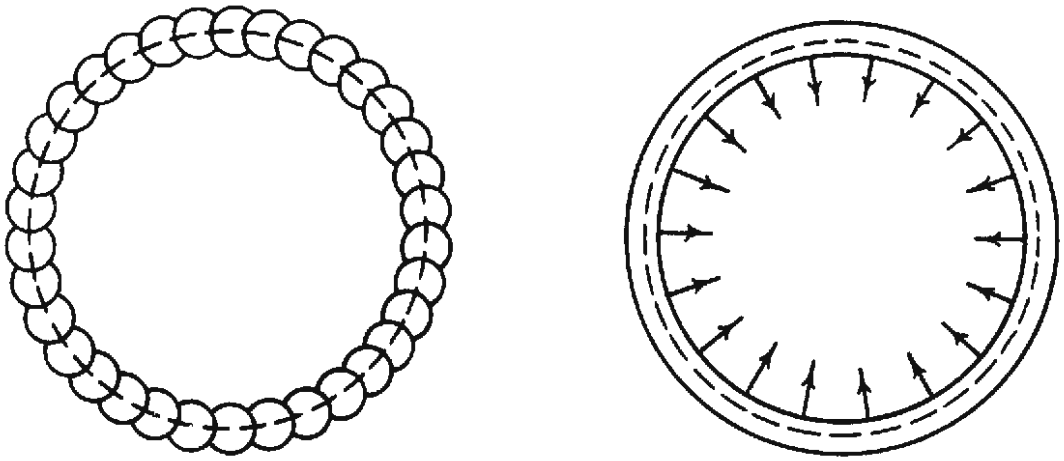

a) Actual condition

b) Used in solution

FIGURE 2.10 EXCAVATION LOADING

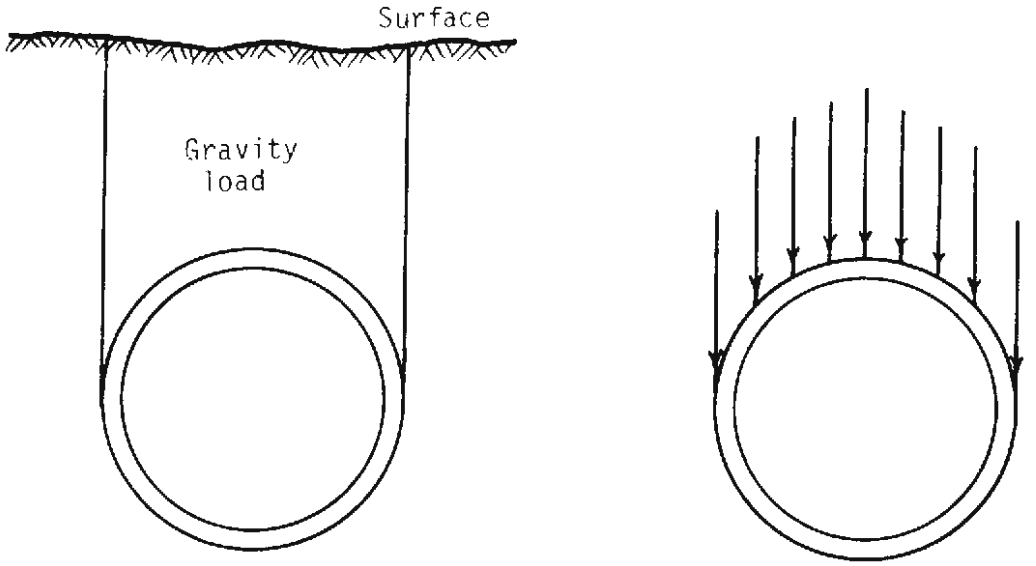

a) Actual condition

b) Used in solution

FIGURE 2.11 GRAVITY LOADING

full-face or top heading and bench methods of driving were used. Thus, it is conservative to assume that the full in situ stress condition acts on the completed liner.

In this mathematical model, prior to excavation of the material inside the completed ring of drifts, a pressure, $P_o = f(\gamma, H, K_o)$, is exerted radially inward on the outer surface of the liner and, due to the material inside the liner, an equal pressure distribution, $P_i = P_o$, is exerted radially outward on the inner surface of the liner, Fig. 2.12a. Under the action of these equal but opposite pressures the liner is in equilibrium and no deformations occur. It is assumed that the stress at any point in the liner corresponds to the stress that would exist in the medium at that same point if the liner were not present. These stresses result in an initial force distribution in the liner.

Excavation of the material within the liner removes the inner pressure and leaves only the outer pressure which then acts to deform the liner and mobilize thrusts, shears and moments in the liner.

Excavation of the material from inside the liner can be modeled in a finite element analysis by applying a stress, $- P_i$, to the inner surface of the embedded liner, Fig. 2.12b. The finite element solution yields the forces and deformations due to this excavation. Total force values in the completed liner are obtained by adding the forces given by the finite element solution and those calculated from the in situ stresses, Fig. 2.12c.

The other loading condition, referred to as "gravity loading," occurs when the tunnel is excavated and deformations due to this excavation take place before the liner is advanced. Once the liner is placed, time-dependent deformations of the medium induce forces and deformations in the

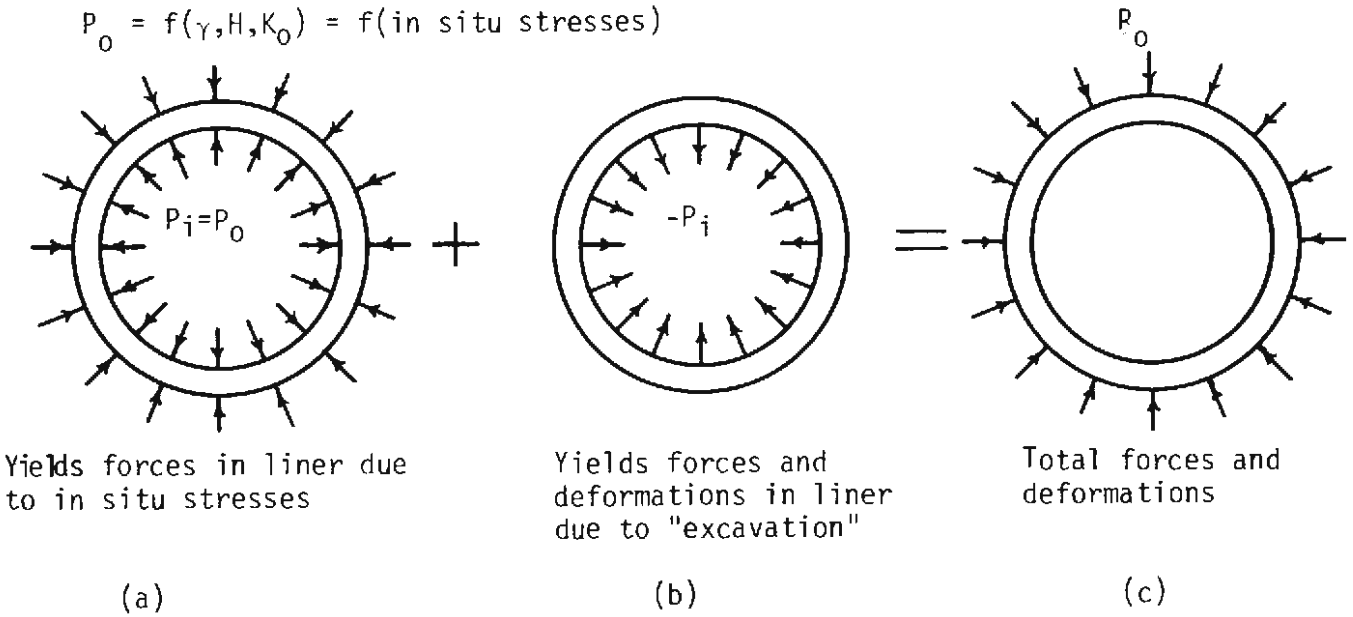

FIGURE 2.12 ASSUMED PRESSURE DISTRIBUTIONS AND METHOD USED FOR CALCULATION OF LINER FORCES AND DEFORMATIONS-EXCAVATION LOADING

liner. An accurate assessment of these forces and deformations could be obtained only by a nonlinear and time-dependent analysis. In the absence of such a computer program, an estimate of the forces and deformations in the liner may be obtained by assuming that only the medium above the opening actively exerts pressures on the liner due to the force of gravity. Although the magnitude of the gravity load on the liner is not known, an upper limit is the weight of an entire column, or a fraction of a column, of soil or rock, having a width equal to the diameter of the tunnel, is applied to the liner, Fig. 2.11. Interaction of the liner and the medium is initiated by this vertical gravity load. The crown is forced down and the springlines are forced out, resulting in a shortened vertical diameter and a lengthened horizontal diameter. As the springlines are forced out against the medium, lateral loads are mobilized. The amount of distortion of the liner and the final magnitude and distribution of the radial pressure acting on the liner and the forces in the liner are functions of the gravity loading and the material properties of the liner and the medium. The solution for this loading condtion, which is independent of the coefficient of earth pressure at rest, gives the liner deformation and forces directly.

The full gravity loading condition, loading due to the entire column of material above the tunnel, is more applicable for shallow tunnels than for deep ones. For deeply buried tunnels the weight of the full column may not be supported entirely by the liner since the medium itself may support some of this weight through the mechanism of arching around the tunnel.

Solutions were obtained for the excavation and full gravity loading

conditions for three different depths of cover and properties of the medium representative of soft ground. Solutions were also obtained for full gravity loading and medium properties with much larger Young's modulus, representative of rock or very stiff clay (larger compressibility and flexibility ratios). It was assumed that there is no slippage at the liner-medium interface.

2.4.3 THRUST

The maximum thrust coefficient ($T/\gamma HR$) for various loading conditions together with the closed form solution is given in Fig. 2.13. While the thrust in the liner increases with depth, the figure shows that the effect of depth of cover on the dimensionless thrust coefficient is very small. However, the manner in which the liner is subjected to the applied medium loads affects the thrust coefficient significantly. The thrust coefficient for the gravity loading condition is approximately half of that for the excavation loading. The thrust coefficient is lowest for the case simulating the rock condition (high flexibility and compressibility). This is consistent with the results from the closed form solution. The closed form solution gives a thrust coefficient which can be considered an upper bound.

2.4.4 MOMENT

A plot of the maximum moment coefficient ($M/\gamma HR^2$) for various loading conditions is given in Fig. 2.14. Unlike the thrust coefficients, the moment coefficient for the gravity loading condition is higher than

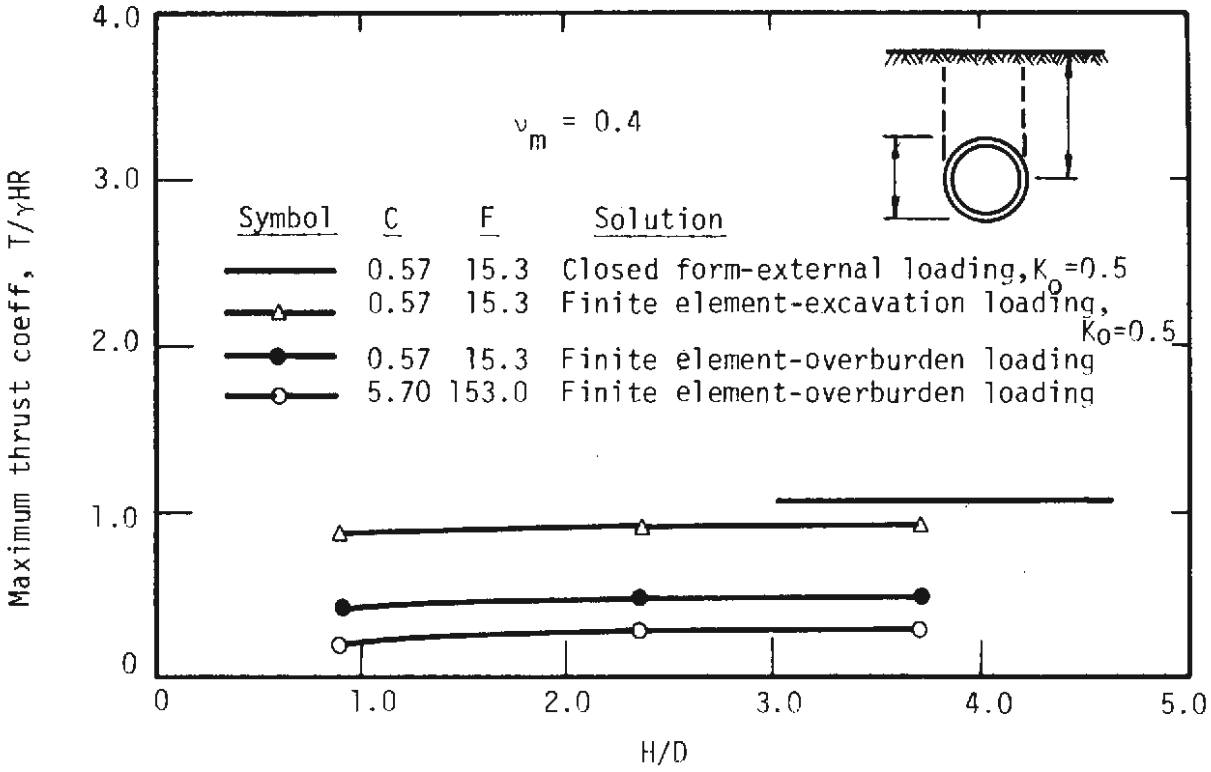

FIGURE 2.13 VARIATION OF THRUST COFFFICIENT WITH DEPTH OF COVER

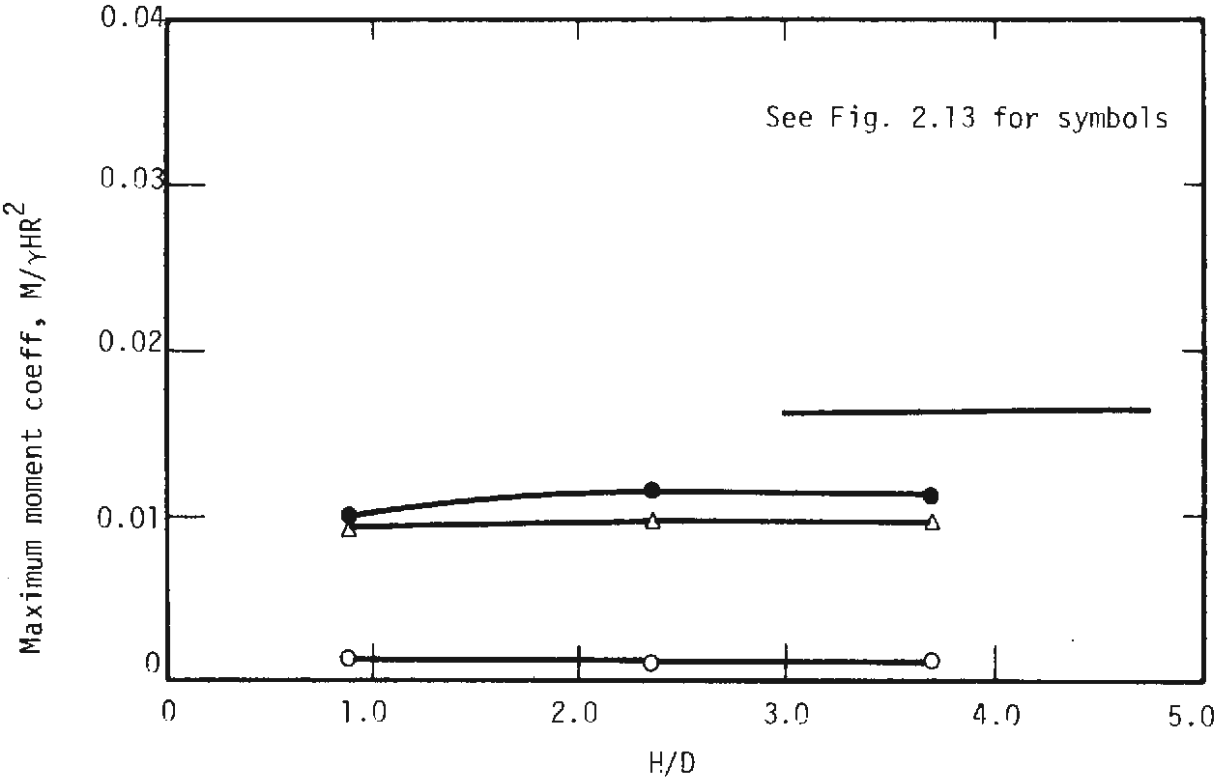

FIGURE 2.14 VARIATION OF MOMENT COEFFICIENT WITH DEPTH OF COVER

that for excavation loading. The moment coefficient obtained from the closed form solution is higher than those for the other two loadings. However, even the highest moment coefficient is less than about 2 percent. This is to be expected since the moment coefficient is considerably reduced for flexibilities higher than 10.

2.4.5 TRANSVERSE SHEAR

The plot of the maximum transverse shear coefficients ($S/\gamma HR$) for various loading conditions is shown in Fig. 2.15. Unlike the thrust and moment coefficients, the transverse shear coefficient for the excavation and gravity loadings is higher than that obtained from the closed form solution. This is due to the additional degree of nonuniformity of loading for the excavation and gravity loading conditions over that assumed for the loading in the closed form solution. The more nonuniform the external pressure distribution, the more nonuniform will be the moment distribution. The more nonuniform the moment distribution, the greater is the change in moment with position around the liner ($dM/d\theta$) and, thus, the greater is the transverse shear. For the excavation loading condition the additional nonuniformity is introduced by the increase of in situ stresses with depth, which was not considered in the closed form solution. The pressure distribution is even more nonuniform for the gravity loading condition where loads are actively applied only on the upper half of the liner. The distribution of applied pressure also affects the circumferential position of the maximum values of the forces in the liner (see Sect. 2.4.7). For concrete liners, the strength of the liner in shear should be checked and shear reinforcement should be provided if needed to resist the shear force.

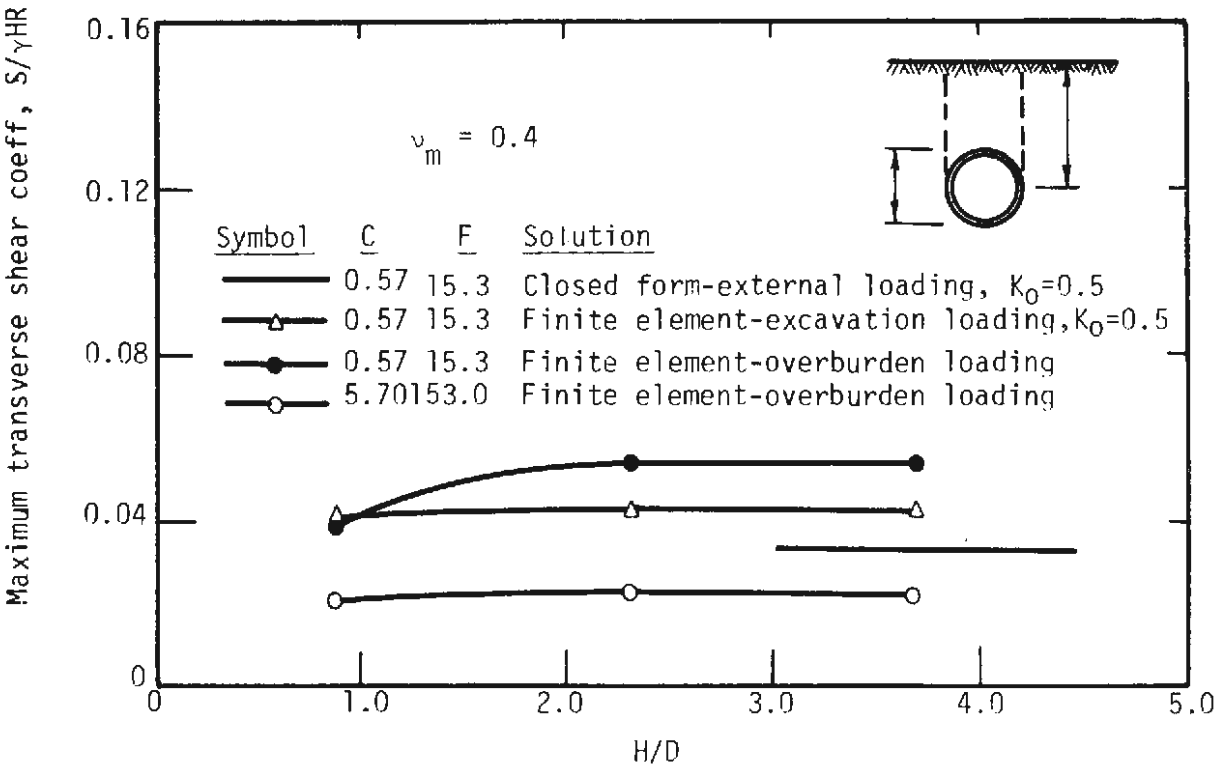

FIGURE 2.15 VARIATION OF TRANSVERSE SHEAR COEFFICIENT WITH DEPTH OF COVER

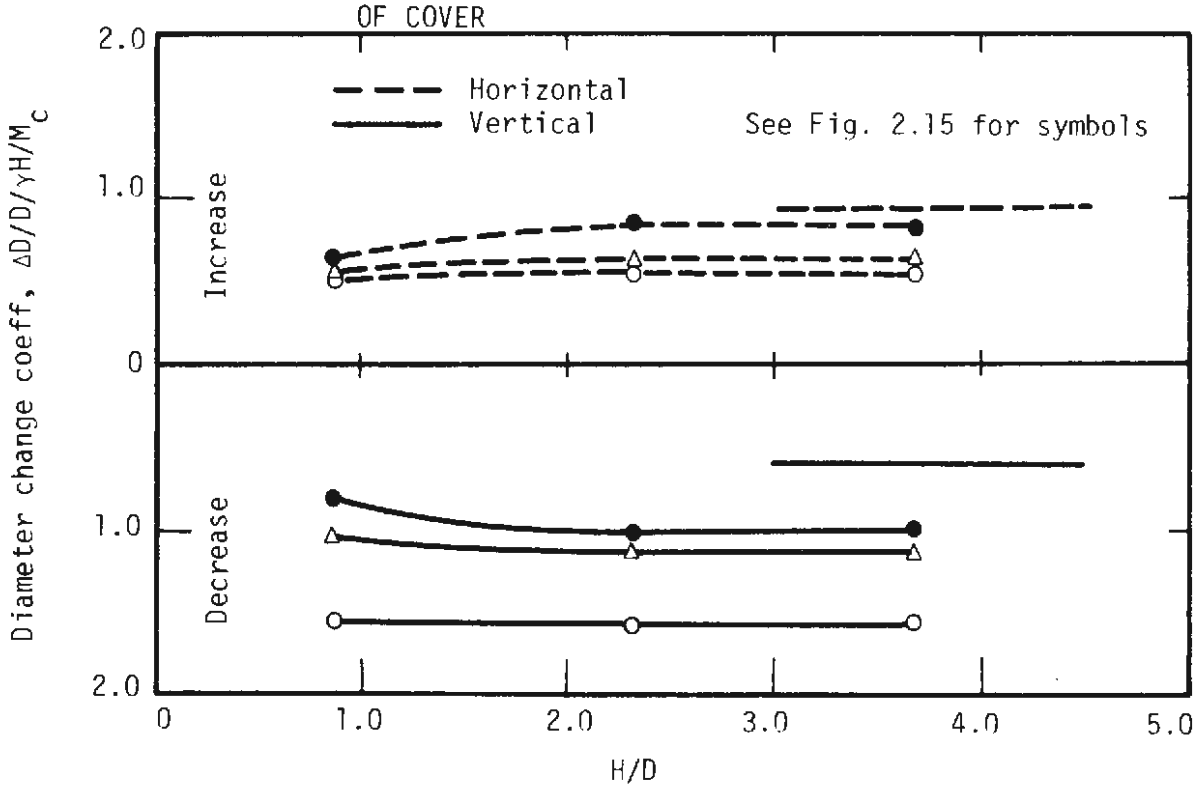

FIGURE 2.16 VARIATION OF DIAMETER CHANGE COEFFICIENT WITH DEPTH OF COVER

2.4.6 DIAMETER CHANGE

Vertical and horizontal diameter changes are given in dimensionless form in Fig. 2.16 for various solutions. The diameter changes are fairly insensitive to the depth of cover. It is important to note, however, that the closed form solution underestimates the diameter change in the vertical direction. It should be noted that, although the diameter change coefficient for the case simulating the rock condition is the same order of magnitude as that for a soft medium, the actual diameter change is much smaller since the normalization is made to the constrained modulus of the medium.

2.4.7 CIRCUMFERENTIAL DISTRIBUTION OF FORCES

Typical distributions of liner thrust, moment, and transverse shear in the circumferential direction for various loading conditions are given in Fig. 2.17. The distributions indicate that the maximum thrust, moment, and shear occur at different locations in the liner for any one loading condition. This is important when an interaction diagram is used for proportioning the liner. The location of the maximum value of thrust, moment or transverse shear is a function of loading condition and, for the excavation loading case, also the depth of burial.

The closed form solution assumes an external pressure distribution that is symmetrical about both the horizontal and vertical diameters. Thus, the maximum, absolute value of moment occurs at the springlines, crown and invert. For K_o = 0.5 the maximum thrust is located at the springlines.

C = 0.57

F = 15.3

H/D = 3.7

ν_m = 0.4

Scale:

$T/\gamma HR$: 1.000

$S/\gamma HR$: 0.100

$M/\gamma HR^2$: 0.0100

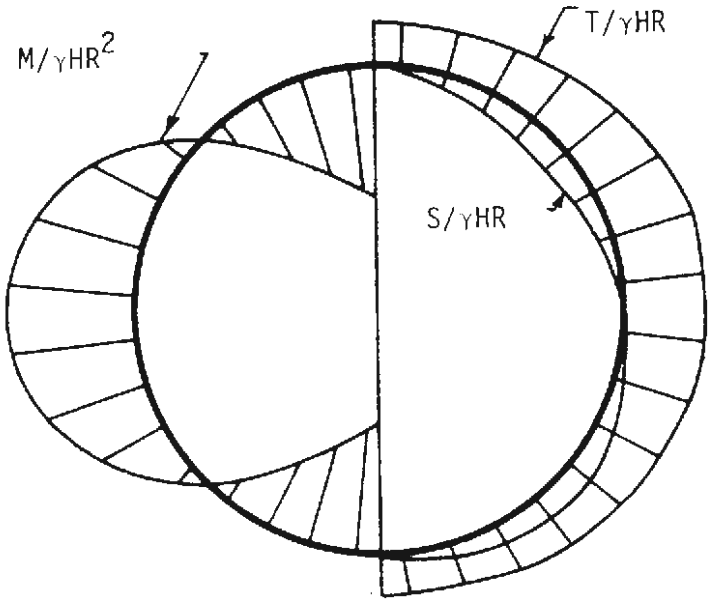

Closed form solution
External loading, K_o=0.5

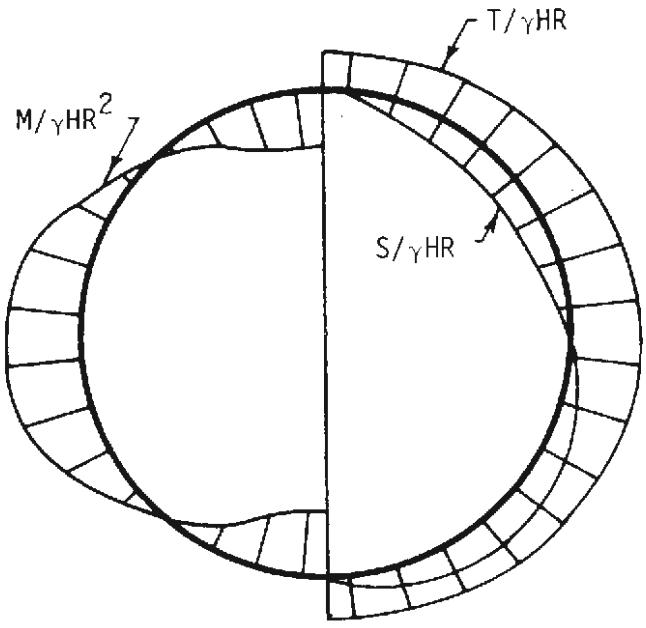

Finite element solution
Excavation loading, K_o=0.5

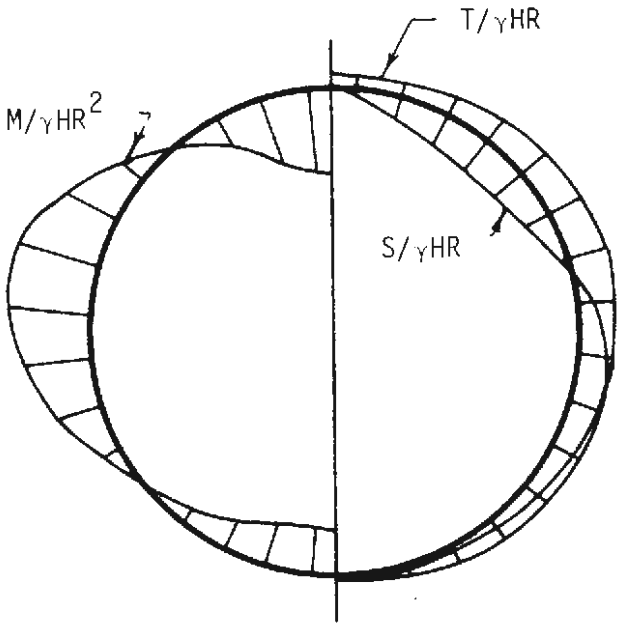

Finite element solution
Gravity loading

FIGURE 2.17 DISTRIBUTION OF FORCES AROUND THE LINER FOR VARIOUS SOLUTIONS

The maximum absolute value of transverse shear occurs at points 45 degrees above and below the springlines.

The excavation loading condition includes the increase with depth of the in-situ stresses. Thus, the in situ stress in the medium at the invert exceeds that at the crown and the applied pressure distribution is no longer symmetrical about the horizontal axis. This lack of symmetry affects the force distributions in the liner and, thus, the positions of the maximum forces. As the depth of burial decreases, the stress difference between the crown and invert becomes more pronounced relative to the average stress. For H/D values of 3.7, 2.35 and 0.84 the maximum thrust appeared to be located at points 5°, 5° and 28° below the springlines, respectively. For the same order of H/D values the maximum moments occurred at points 5°, 5° and 10° below the springlines, respectively; and the maximum shears were located at points 50°, 50° and 62° below the springlines, respectively.

These values indicate that the locations of the maximum force values are functions of the depth of burial. It appears that the shift of location is more pronounced at shallow depths of cover (H/D < 1.5-2.0). Due to the limited amount of data available it is not clear whether the 5° shift values at H/D of 3.7 and 2.35 are due to the depth of burial or the result of the lack of exactness of the solution technique.

Due to the fact that the gravity loading condition imposes active loads on the top half of the liner only, the pressure and force distributions are not symmetrical about the horizontal axis. For this loading condition the maximum thrust occurred at points 17° above the springlines.

For most of the cases considered, the maximum moment was located at the crown. However, for some of those cases in which the much stiffer medium was considered, the maximum moment was located at points 17° above the springlines. The maximum transverse shears occurred at points 51° above the springlines.

2.5 LONGITUDINAL EFFECTS

The thrust, moment, transverse shear, and displacement coefficients presented in the previous sections were obtained from two-dimensional, plane strain solutions. Although the solutions are applicable for a section far away from the face of the tunnel, they do not give an estimate of the forces and deformations near the face nor the variation of forces and displacements along the axis of the tunnel. Generally, however, the variation of forces and displacements along the axis of the tunnel away from the face is not significant unless the properties of the surrounding medium change from one section to another. It is near the face that the longitudinal variations become significant.

The longitudinal effects can be investigated using a three-dimensional finite element solution. However, such solutions can be costly and difficult to use because of the large number of elements needed to model the tunnel system adequately. A two-dimensional, axisymmetric solution represents a reasonable alternative. Although such a solution is restricted to conditions where the coefficient of earth pressure at rest, K_o, is equal to one, it nevertheless provides a qualitative feel for the variation of forces and deformations in the longitudinal direction.

As was mentioned in Section 2.4.2, the forces and deformations in a tunnel support are affected by the amount of deformation of the medium that occurs before the support is installed. Figure 2.18, which shows the elastic displacements of an unlined tunnel due to excavation, was obtained using a two-dimensional axisymmetric finite element solution. The displacements in the medium at the face of the tunnel and at several points behind the face are given in the figure. The figure indicates that approximately 50 percent of the elastic deformation due to excavation occurs within a distance of one-fourth the tunnel radius behind the face, and that essentially all the elastic deformation occurs within a distance of one to one-and-a-half diameters behind the face.

2.6 DISCUSSION OF RESULTS

2.6.1 DISCUSSION OF THE ASSUMPTIONS

The results from the foregoing analytical studies should be evaluated by comparing the assumptions with real tunnel conditions and by consideration of the measured performance of tunnels in similar materials and conditions. Though many of the assumptions may seem idealistic, they can provide bounds on anticipated behavior. In many cases, a rational treatment with idealistic assumptions may be better than continued use of traditional methods such as the design of soft ground tunnels for an arbitrary, unchanging set of loads based on an assumed earth pressure at rest. It has been shown that the use of the analytical soil-structure interaction methods results in small numerical values for the design parameters even with the most conservative loading assumptions. It has been recognized that the primary

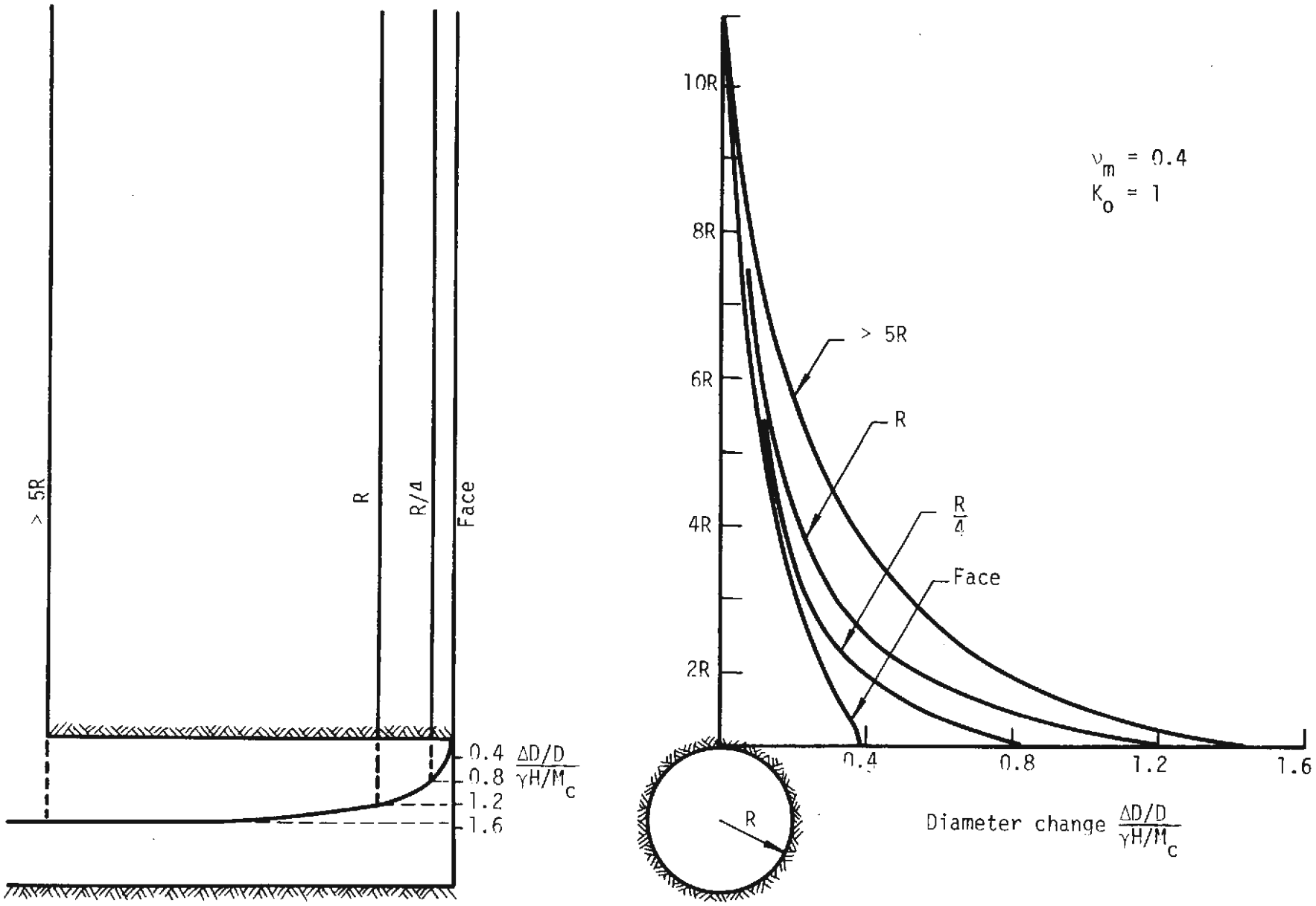

FIGURE 2.18 LONGITUDINAL VARIATION OF ELASTIC DISPLACEMENTS DUE TO EXCAVATION

load-carrying member is the medium itself (Peck, 1969). The following paragraphs discuss some of the assumptions common to the three methods described in this chapter; comments about assumptions that apply to each of the methods are given in Section 2.6.2.

The loading conditions in all three methods are valid only for the loads attributed to the excavation of the tunnel itself and thus they are not appropriate for the design of secondary liners installed after considerable deformation of the medium has occurred with a temporary support system. In the form shown, the methods described are valid for liners which are installed with intimate contact between the medium and the entire perimeter of the liner. Thus, the methods apply to segmented liners which are grouted or expanded after leaving a shield or to concrete liners placed close to the face, but not to supports such as steel sets with discrete blocking. The general principles could be used to develop an analytical technique to analyze supports such as steel sets, however.

Since the methods presented in this chapter are linear, elastic solutions, they should be used with appropriate limitations in mind. Furthermore, the closed-form and the excavation loading cases assume that the liner not only was installed but became a fully effective support system before the face was excavated. Liners are usually installed some distance from the face and the ground moves before they become fully effective. The effect of these departures from the assumptions are discussed in Section 2.5 and in the following sections. Only the gravity-load case is not restricted by this assumption.

2.6.2 IMPORTANT ASPECTS OF EACH ANALYTICAL METHOD

CLOSED-FORM METHOD

For the range of flexibility, F, and compressibility, C, discussed in this chapter, the closed form solution provides the highest numerical values for maximum moment and thrust coefficients. The maximum thrust is especially dependent on the assumption of full slippage at the interface between the liner and the medium and on the compressibility parameter, C. The maximum moment and transverse shear coefficients are relatively insensitive to the slippage assumption.

One advantage of the closed-form method is that results are relatively easy to obtain with ordinary office equipment; a computer is not required. The closed-form method can be used as a qualitative measure of the behavior of the system for other loading conditions since the same trends are evident as for the more complex methods. Burns and Richard (1964) also give equations for stresses and displacements in the medium.

The boundary conditions however apply only to tunnels at depths greater than three diameters. Furthermore, with the boundary and loading conditions assumed in the solution, the final displacements include the elastic displacements associated with excavation of the tunnel and the in situ stresses. Since as much as one-half of these elastic displacements can occur before the liner is installed, the assumption is conservative.

Guidelines for correcting the value of the deformation of the liner to account for the unrealistic treatment of in situ stresses are given in Section 2.3.6. Unfortunately, the equations for thrust, moment and shear

are not as easy to correct and the corrections are not included. Thus, the equations for moment, thrust, and stress are rather conservative. A second correction for longitudinal effects is also appropriate but not included in the solution; this correction is discussed in Sections 2.5 and 2.6.3.

EXCAVATION LOADING METHOD

This method most closely simulates the case of individual drifts around the perimeter of the proposed tunnel. It is a finite element solution, and takes into account the tunnel depth. The boundary conditions and treatment of the in situ stresses are such that the computed deformations are theoretically correct (the correction of Section 2.3.6 is not required) yet still conservative since the longitudinal effects of Section 2.5 are not included.

For the assumptions of the comparative study in Section 2.4, the excavation loading case, the thrust coefficient is only slightly less than that from the closed-form solution while the other coefficients were closer to those from the gravity loading condition.

GRAVITY LOADING METHOD

The gravity loading finite element solution is the most realistic of the three methods because the assumptions more closely approximate actual tunnel conditions. Theoretically, the diameter changes as well as the other coefficients do not need correction for in situ stresses nor for longitudinal effects and the method is appropriate for shallow tunnels. Furthermore, the results are independent of K_o.

More importantly, the gravity load is versatile since the load can be selected to be equivalent to the full overburden or to a percentage of full overburden. This allows the designer to exercise judgment over the size of the load or the time-dependent nature of the load.

The thrust coefficient is about one-half of that given by the other two methods. The transverse shear coefficient however was highest for the gravity load case.

2.6.3 PRACTICAL APPLICATION OF MEDIUM-STRUCTURE INTERACTION METHODS

Medium-structure interaction methods type discussed can be applied to practical tunnel design. The flexibility, F, and the compressibility, C, can be calculated easily if the material and medium properties are estimated. By referring to the dimensionless plots given in this chapter or those by Peck, Hendron, and Mohraz (1972) or by using the equations given, the dimensionless parameters F and C provide a qualitative assessment to the anticipated overall interaction of the liner-medium system.

The gravity loading solution provides the most realistic approximation of the loads on tunnel supports installed close to the face by conventional tunnel construction methods.

The evaluation of thrust, however, need not require a computer solution. It is suggested that linings be designed for thrust on the basis of the full overburden pressure equal to γha and an appropriate factor of safety. The minimum practical thickness necessary for construction of most linings, especially concrete linings, results in a thrust capacity equal to or greater than this recommended design thrust so a design on the basis of full overburden pressure is easily and economically achieved.

For typical tunnels in other than exceptional ground, the gravity loading method of analysis is recommended for the evaluation of moment, transverse shear and diameter changes, however, and substantial economy can result from such an analysis. For preliminary analysis the recommended magnitude of gravity load term, γh may be taken as the pressure exerted by a column of rock or soil either 2-diameters high or the full overburden height, whichever is less. Again, appropriate factors of safety should be used and the design engineer may exercise judgement in choosing allowable stresses exceeding traditional working stresses on the critical section.

For tunnels in squeezing ground at depths greater than about 150 ft (33 m), creep design techniques such as those described by Semple, Hendron, and Mesri (1973) should be used.

Because of the assumptions and the consequent corrections required, the closed-form solution and the excavation loading solution are not as desirable as the gravity loading solution. Although the results from the closed-form and the excavation loading solutions are directly related to K_o, the measurement of K_o is not practical or possible in problems in real in situ soils. The closed-form solution however has the advantage of providing a conservative "ball park" estimate without the need of a computer or design charts.

Construction conditions must also be evaluated. If it is expected that grout may be placed nonuniformly and intimate contact with the medium is unlikely, the low moment coefficients are unjustified as the analysis is unrepresentative. Furthermore, the liner must also be proportioned for handling and installation stresses.

2.7 CONCLUSIONS

Three powerful analytical methods to evaluate the liner-medium interaction have been presented and compared. They permit a designer to analyze cases intermediate between the extreme "rigid" and "flexible". The application of these methods as part of the overall tunnel design procedures is encouraged. They are being used as part of the analysis for the design of the slipformed tunnel liners of the Extruded Liner System described in Chapter 1. Even with conservative and idealistic assumptions, rational treatment including interaction should result in a safe design having substantial savings over traditional methods of design. In most cases, rational treatment of idealistic assumptions is expected to be far superior to the continued use of traditional methods which are completely inappropriate both in the selection and treatment of the assumptions. A classic example of an inappropriate traditional method is the design of soft ground tunnels as a rigid lining for an arbitrary unchanging set of loads based on K_o.

The most significant conclusion drawn from this study is the fact that if the lining is flexible (F greater than 10) the absolute value of the maximum moment coefficient obtained from these solutions is an order of magnitude lower than that obtained from the traditional method of analysis for "rigid" liners irrespective of the loading conditions assumed. Although the actual loading conditions are unknown, a safe design can be achieved by proportioning the liner for the maximum thrusts, moments and shears without sacrificing economy.

Comparison of results from similar studies with field measurements and the extension and refinement of these techniques to incorporate nonlinear behavior, and to account for nonuniform conditions associated with the construction sequence are strongly encouraged.

CHAPTER 3

CONCRETE MATERIALS - EVALUATION AND BEHAVIOR

3.1 INTRODUCTION

The major objective of these studies in concrete materials is to determine and interpret their behavior in a useful manner for tunnel designers and constructors. In particular, the materials required for the extruded tunnel liner system (Parker, et al., 1971) are studied in detail. To determine the effect of possible deleterious environments on this behavior is of utmost importance. Cost is always a consideration. In addition, new materials are sought in an attempt to improve the performance of concrete in place.

Consideration is given to fiber reinforced concretes made with quick setting cements. Concretes reported here are made with steel fiber reinforcement and regulated-set cement unless noted otherwise.

Topics given particular attention are:

1. Studies of material properties and mix proportioning for the improvement of workability and handling time.
2. Studies of the behavior of hardened concrete in response to different types and combinations of loadings.
3. Studies of volume stability under various stimuli.
4. Determination of the ability to function in adverse environments.

The program of research is in no way complete and the results reported here, while believed to be correct, are only tentative.

3.2 MIX DESIGN

3.2.1 INTRODUCTION

The purpose of this study is to develop mix designs for steel fiber reinforced, quick setting cement concretes which will meet the criteria necessary for use in an extruded tunnel liner system. The concrete must be pumpable with a handling time on the order of 30 min. Strength requirements are dependent on ground conditions. By the time the slipform has passed sufficient strength must have been attained for the liner to perform the necessary support function.

The mix designs developed are valid only with the regulated-set cement used in this project. Regulated-set cements vary considerably in composition from company to company, and from burn to burn. These cements can be produced so as to possess setting times and early strengths within certain limits. In addition, setting time and early strength can be further altered by admixtures and temperature changes.

3.2.2 PROPORTIONS

Mix designs selected for detailed study are shown in Table 3.1. Each mix used mixing water cooled with ice and containing citric acid to obtain handling times of 30 min. These mixes respectively contain 0.9, 1.2, and 1.5 percent, by volume, of fibers. Aggregate and cement proportions vary with each mix depending upon the fiber content. Mixes with higher fiber contents require a higher paste content and a lower ratio of coarse to fine aggregate in order to produce a workable mix with uniform distribution of fibers.

TABLE 3.1

PRELIMINARY MIX DESIGNS--STEEL FIBER REINFORCED,
REGULATED-SET CEMENT CONCRETE

Volume of fiber, percent of total volume	0.9	1.2	1.5
Material, lbm/cu yd (kg/m^3)			
Cement	650 (385.5)	725 (430.0)	800 (474.5)
Water	325 (193.0)	326 (193.5)	360 (213.5)
Fine aggregate*	1610 (955.0)	1610 (955.0)	1670 (991.0)
Coarse aggregate*	1130 (670.5)	1080 (640.5)	870 (516.0)
Steel fiber	120 (71.0)	160 (95.0)	200 (118.5)
Citric acid			
percent by weight of cement	0.2	0.2	0.2
lbm (kg)	1.53 (0.90)	1.39 (0.80)	1.25 (0.75)
Water temperature, F (C)	32 (0)	32 (0)	32 (0)
Ice, percent by weight of mixing water	60	60	60
Water-cement ratio	0.50	0.45	0.45
Air, percent	4.1	3.7	3.5
Unit weight, lbm/cu ft (kg/m^3)	144.5 (2314)	144.0 (2306)	142.2 (2278)

*Saturated, surface dry.

For each mix 60 percent of the mixing water was in the form of crushed ice. The ice melted three to five minutes after introduction to the mixer, providing the cooling necessary to delay hydration. The initial slump of all mixes was about 8 in. (205 mm). After 30 min the slump reduced to 1 to 3 in. (25 to 75 mm). The percentages of entrapped and entrained air and the unit weights listed in Table 3.1 are typical but vary with the mixing time and the amount of vibration.

Coarse aggregate used in these mix designs was 3/8-in. (10 mm) maximum size pea gravel. Gradations, unit weights, bulk specific gravities and absorption capacities for the sand and gravel are shown in Tables 3.2 and 3.3.

The fibers used in these mixes were 0.010 in. by 0.022 in. by 1 in. (250 μm by 560 μm by 25 mm) USS Fibercon steel fibers.

3.2.3 ADMIXTURES

Various admixtures were evaluated with regard to controlling the setting time and improving the workability of the regulated-set cement concrete. Several were found to be somewhat effective but the most efficient appeared to be citric acid, which may be added in crystalline form or as a solution in the mix water.

When used in appropriate concentrations in regulated-set cement concrete, citric acid increased handling time and entrained air. The increased entrained air improved workability. Generally, higher concentrations of citric acid resulted in mixes with lower early strengths.

A pumping agent called Flo-Dense, produced by Halliburton Services,

TABLE 3.2

SIEVE ANALYSIS - SAND AND PEA GRAVEL

Sieve	Sand, percentage		Pea gravel, percentage	
	retained	passing	retained	passing
3/8 in. (10 mm)			0	100
No. 4	0	100	88	12
No. 8	6	94	98	2
No. 16	29	71	99	1
No. 30	60	40	100	0
No. 50	83	17	100	0
No. 100	95	5	100	0
Fineness modulus	2.73		5.85	

TABLE 3.3

PROPERTIES OF SAND AND PEA GRAVEL

Property	Sand	Pea gravel
Unit weight, lbm/cu ft (kg/m^3)	107.6 (1724)	100.6 (1612)
Bulk specific gravity, SSD	2.56	2.55
Absorption capacity, percent	1.8	2.2

Inc., extended the handling time of regulated-set cement concrete to about 15 min and improved workability. In concentrations up to 0.5 percent by weight of cement it did not reduce ultimate strength.

3.2.4 WORKABILITY AND HANDLING TIME

The fresh concrete must have sufficient workability so that it can be pumped into place and consolidated. It is desired that at least 30 min of handling time be available for placing the material. This will allow some time to dispose of mixed concrete in the event of a breakdown. It is also desired that the mix remain pumpable throughout as much of the 30 min as possible.

Although the precise pumping requirements of steel fiber reinforced, quick setting cement concretes are unknown, a vane shear test provides a tentative measure of pumpability (Parker, et al., 1973, Appendix B). A preliminary study has indicated that the threshold of pumpability for steel fiber reinforced concrete occurs when the shearing resistance is approximately 0.6 psi (4 kPa), measured by the vane shear test. This shearing resistance corresponds to about a 3-in. (75 mm) slump.

Handling time, as opposed to pumping time, has been taken as the length of time from addition of mixing water until the mix has reached a vane shearing resistance of 0.9 psi (6 kPa), about a 1/2-in. (15 mm) slump.

3.2.5 EFFECT OF TEMPERATURE

In order to control the setting and handling times of the regulated-set cement concrete, it is convenient to take advantage of the

sensitivity of the cement hydration reaction to temperature. High temperatures accelerate cement hydration while low temperatures retard it. Data indicate that hydration of regulated-set cement is virtually nil when mix temperatures are below about 47 F (27 C). Above this temperature the rate of hydration increases with increasing temperature. Figure 3.1 shows the time variance of vane shear resistance and concrete temperature. Since shearing resistance increases as hydration progresses, the rate of change of shearing resistance can be assumed to mirror the rate of hydration.

By maintaining the mix temperature below the critical temperature it is possible to delay hydration. This has been done successfully for up to 30 min. In this way the desired handling time can be attained.

The effective mix temperature is a function of material quantities, specific heats, and temperatures. The following equation is an extension of that found in ACI 605-59:

$$T = \frac{S_D(W_A T_A + W_C T_C) + S_S W_S T_S + S_W(W_M T_M + W_F T_F)}{S_D(W_A + W_C) + S_S W_S + S_W(W_M + W_F)} \qquad (3.1)$$

where

S_D = specific heat of dry material = 0.2 BTU/lbm•F (836J/kg•C)

S_S = specific heat of steel fiber = 0.1 BTU/lbm•F (418J/kg•C)

S_W = specific heat of water = 1.0 BTU/lbm•F (4.18kJ/kg•C)

T = effective mix temperature, F (C)

T_A = temperature of aggregate, F (C)

T_C = temperature of cement, F (C)

T_F = temperature of free moisture in aggregate, F (C)

T_M = temperature of mixing water, F (C)

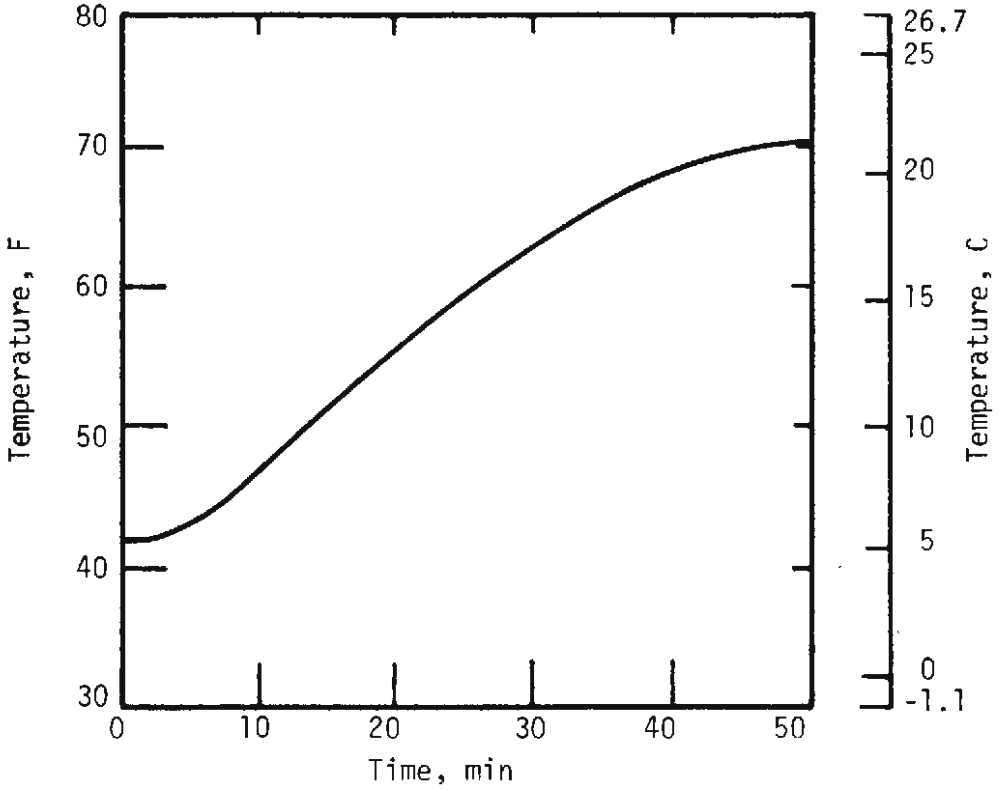

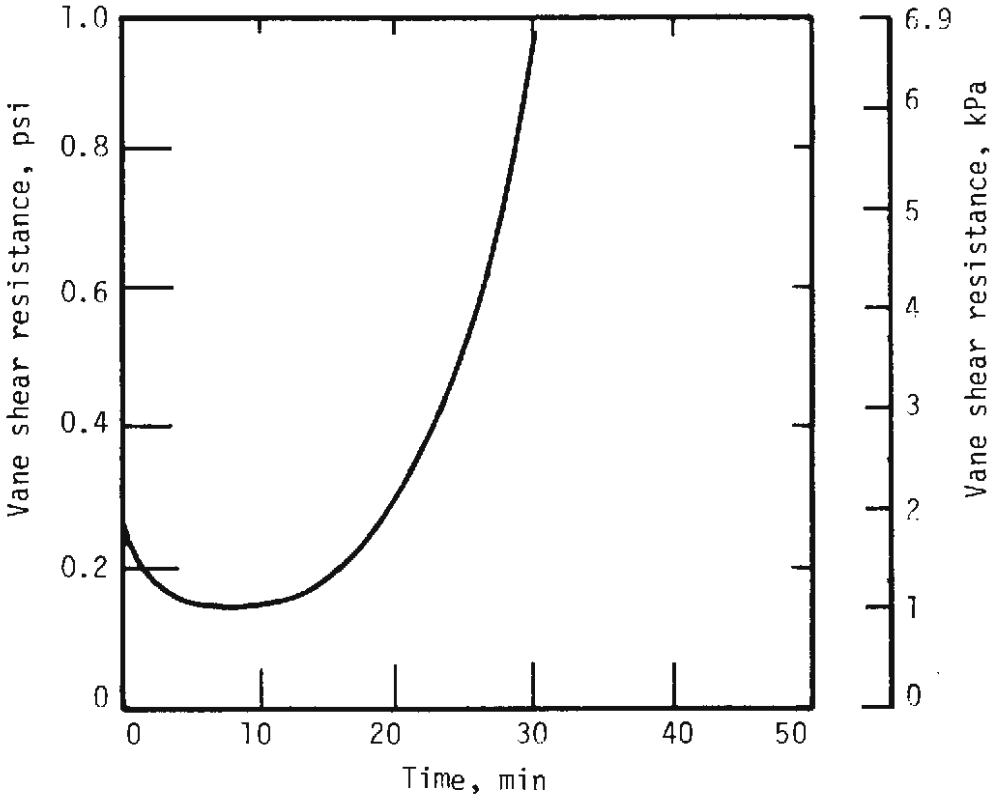

FIGURE 3.1 TIME VARIANCE OF MIX TEMPERATURE AND VANE SHEAR RESISTANCE

W_A = weight of aggregate, lbm (kg)

W_C = weight of cement, lbm (kg)

W_F = weight of free moisture in aggregate, lbm (kg)

W_M = weight of mixing water, lbm (kg)

W_S = weight of steel fiber, lbm (kg)

The effect of individual quantities on the effective mix temperature may be seen by substituting the quantities from the 1.2 percent fiber mix reported in Table 3.1 into Eq. 3.1, with the result:

$$T = \frac{T_A}{2.0} + \frac{T_C}{7.4} + \frac{T_M}{2.8} + \frac{T_S}{66.8} \qquad (3.2)$$

In Eq. 3.2 the denominator of each term indicates the required temperature change of the constituent material to cause a change of one degree in the effective mix temperature. Since this is a homogeneous equation, the result is valid for both English and SI units.

The most important materials for determining effective mix temperature are aggregate and water. Aggregate is important from considerations of total quantity, while water is the most effective material per unit quantity.

In the laboratory ice has been used in two ways for reduction of the effective mix temperature. Ice may be used to cool mix water to a reduced temperature but is removed prior to introduction into the mix. Alternately, a mixture of water and crushed ice may be introduced directly into the mix. In this case heat of cement hydration supplies the heat of fusion for the ice.

If ice is introduced directly into the mix, T_M should be determined on the basis of ice and water temperatures and proportions at the time of mixing. It is important to note that this effective mix temperature will not be the exact mix temperature as the ice does not melt instantaneously.

The effective mix temperature should be regarded as an index property inasmuch as it does not account for time effects, heats of wetting and hydration of cement, mechanical work of mixing, or heat exchange with the environment.

Figure 3.2 illustrates the relationship between handling time and effective mix temperature for two mixes, similar except for citric acid content.

Figures 3.3 and 3.4 show strength-time curves for mixes with different ice and citric acid contents. Times given on each curve are pumping times. Handling times are approximately ten minutes longer. Both times are dependent on heat exchange with the environment. The laboratory environment for the mix design work reported herein was 72 F (22.0 C), 50 RH.

3.3 BEHAVIOR OF HARDENED CONCRETE

3.3.1 INTRODUCTION

PURPOSE

The use of steel fiber reinforced, quick setting cement concrete is relatively new, with little information readily available as to its physical properties. To date, only a few tests have been made on members of large dimension.

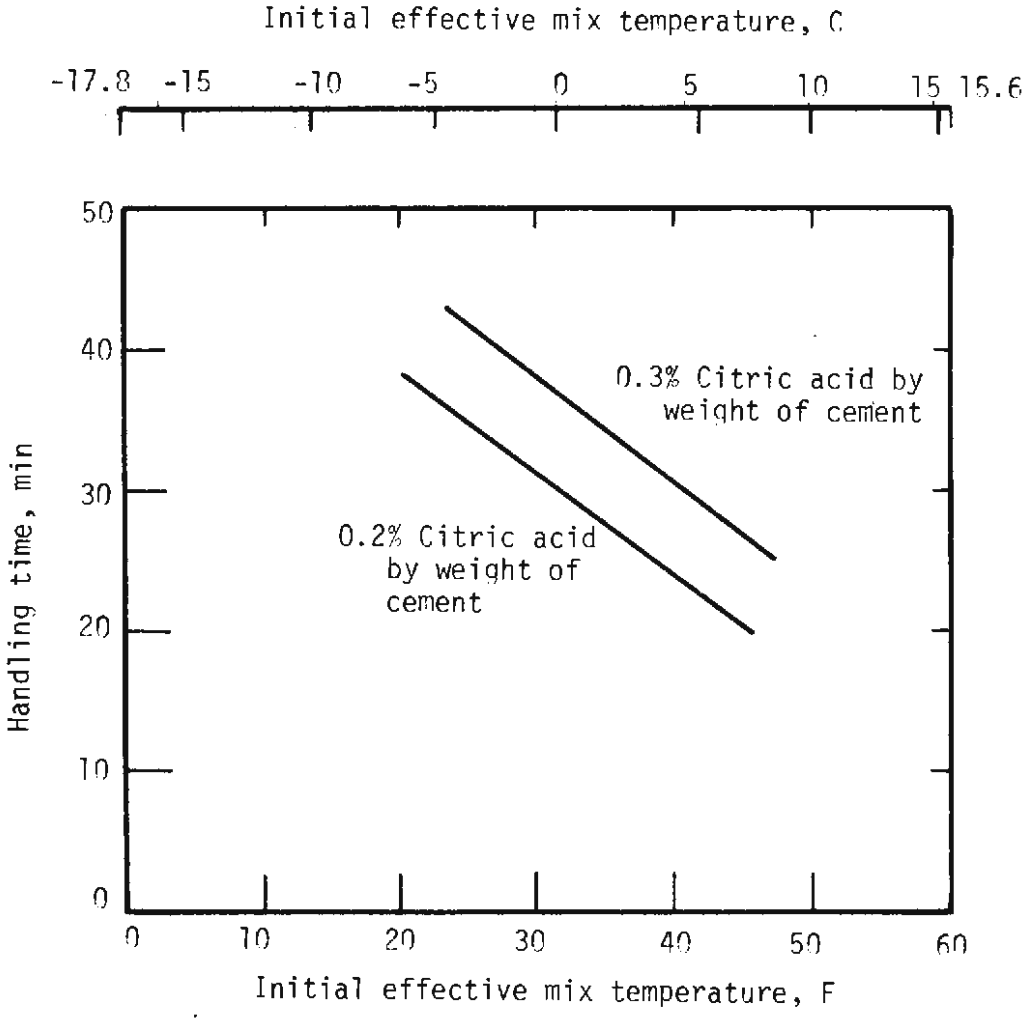

FIGURE 3.2 HANDLING TIME VS. INITIAL EFFECTIVE MIX TEMPERATURE FOR DIFFERENT CITRIC ACID CONTENTS

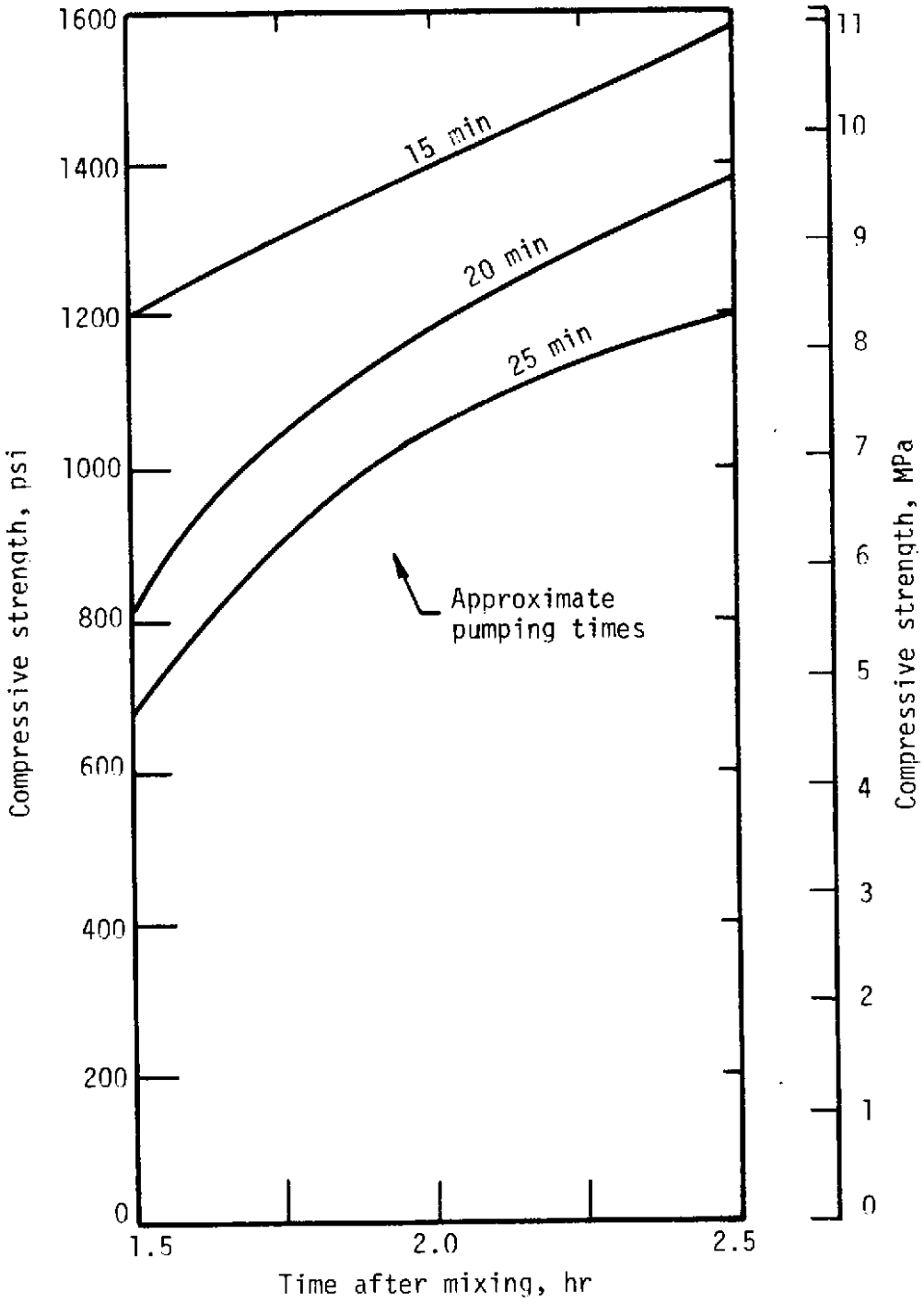

FIGURE 3.3 COMPRESSIVE STRENGTH VS. TIME FOR CONCRETE CONTAINING 0.2 PERCENT CITRIC ACID (BY WEIGHT OF CEMENT)

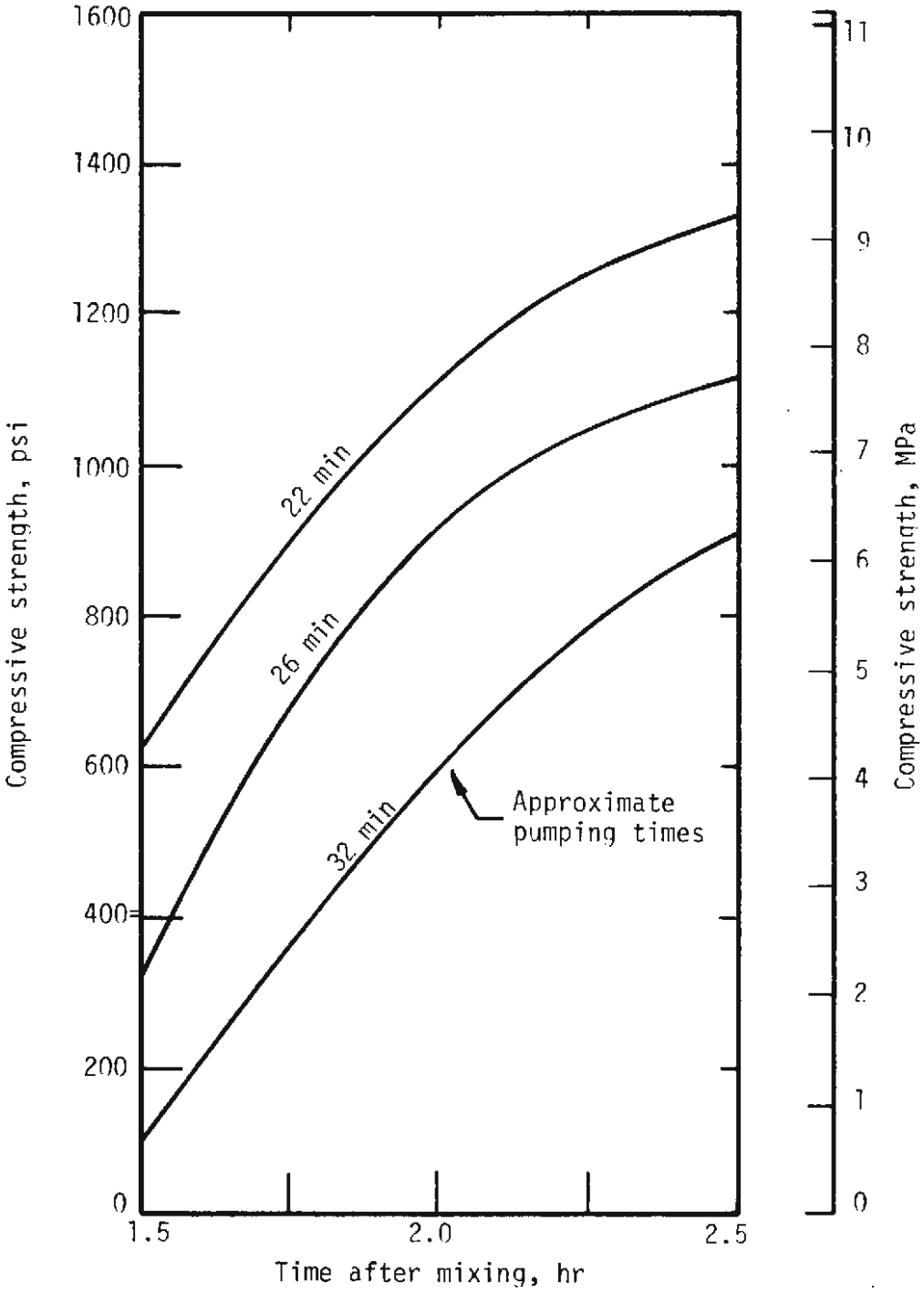

FIGURE 3.4 COMPRESSIVE STRENGTH VS. TIME FOR CONCRETE CONTAINING 0.3 PERCENT CITRIC ACID (BY WEIGHT OF CEMENT)

This phase of the study was undertaken to develop an understanding of the behavior of steel fiber reinforced concrete members subjected to axial compression, pure flexure, and bending combined with axial load. Emphasis was placed on strength properties but tests were initiated to determine creep behavior. This section describes the basic behavior of this material under these loadings and interprets the behavior in terms that can be extended for use in design.

OUTLINE OF TESTS

The mix designs given in Table 3.1 were used. Beam-columns of 6 in. (150 mm) square cross section were tested to determine the behavior of steel fiber reinforced, regulated-set cement concrete under bending combined with axial load. For each beam-column, three 4 in. by 8 in. (100 mm by 200 mm) cylinders were tested in compression and three 3 in. by 3 in. by 15 in. (75 mm by 75 mm by 380 mm) beams were tested in third-point flexural loading as control specimens. Similar cylinders and beams were tested at 1.5 hr, 8 hr, 1 day, 7 days, and 28 days to obtain further information on stress-strain characteristics.

Test apparatus for compressive and flexural specimens are shown in Figs. 3.5 and 3.6, respectively. Both devices can be connected to automatic plotters and stress-strain or load-deflection curves obtained. Compression specimens were gaged to measure longitudinal strain over a 5 in. (125 mm) gage length. A C-gage was employed to measure midspan deflection of flexural specimens.

A beam-column undergoing a test is shown in Fig. 3.7. Load was

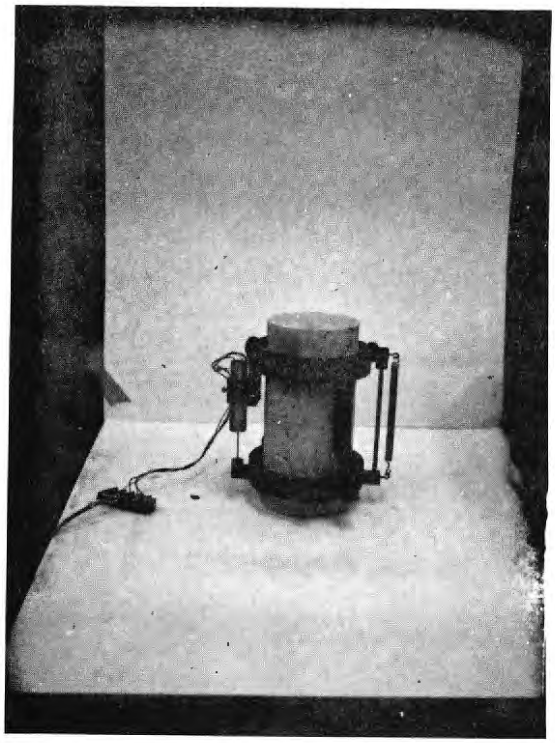

FIGURE 3.5 INSTRUMENTATION FOR COMPRESSION TESTS

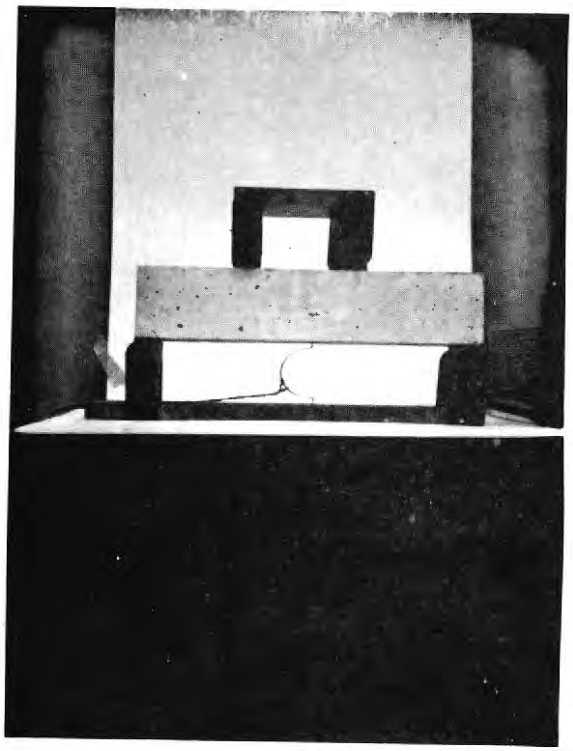

FIGURE 3.6 TESTING ARRANGEMENT FOR MODULUS OF RUPTURE SPECIMENS

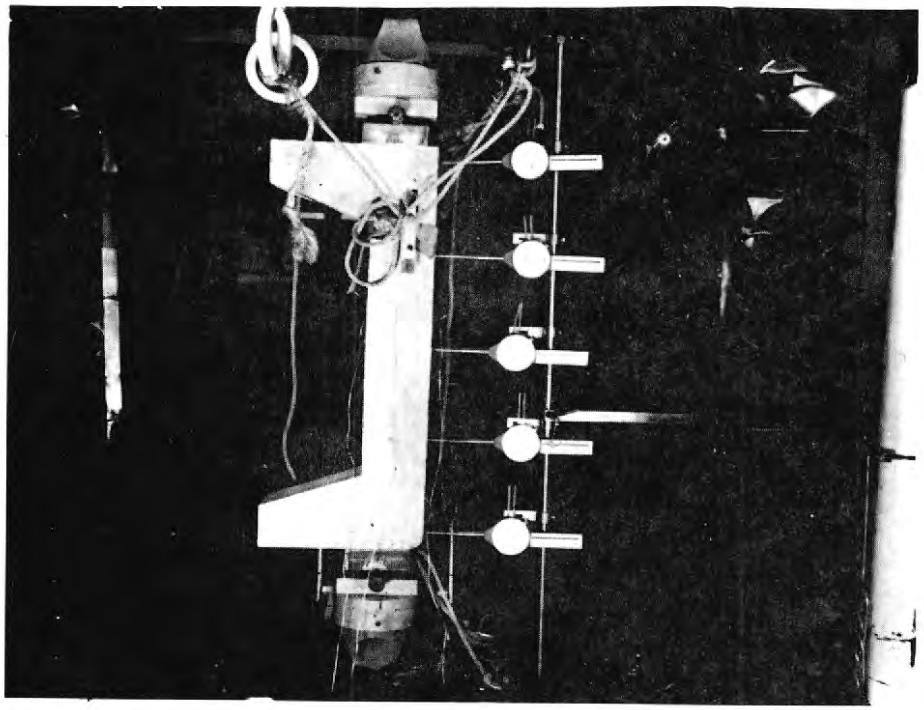

FIGURE 3.7 VIEW OF BEAM-COLUMN UNDER LOAD

applied to the specimen through cylindrical bearings. A deflection bridge with five dial indicators allowed measurement of deflection in the plane of eccentricity.

Nineteen beam-columns were tested; 11 with 1.2 percent fiber content and 4 each with 0.9 percent and 1.5 percent fiber. An outline of the test results is given in Table 3.4. The major variables were volume percentage of steel fiber reinforcement and eccentricity of load. All beam-columns were tested in 12 to 15 increments of load to failure; the total testing time varied from 30 to 45 min. Strains and deflections were measured after each increment of load was applied.

FABRICATION AND CURING

Details of the beam-column specimen are shown in Fig. 3.8. Bar reinforcement was provided only in capitals to transfer the eccentric load to the prismatic shaft of the beam-column.

Beam-columns were cast and vibrated in a horizontal position to avoid a differential in concrete quality along the length of the specimen.

The beam-columns and specimens used in the stress-strain studies were removed from the forms 1.5 to 2 hr after casting and stored in a fog room at 75 to 80 F (24.0 to 26.5 C). Cylinders and beams tested at 1.5 hr, 8 hr, or 1 day were cured in laboratory conditions, 72 F (22.0 C), 50 RH, until time of testing to facilitate application of strain gages. Cylinders and beams tested at 7 or 28 days were cured in the fog room until the day before they were to be tested. They were then removed and gaged.

Beam-columns and control specimens were normally cured in the

TABLE 3.4

RESULTS OF BEAM-COLUMN TESTS

Specimen	Age at testing, days	Strength, psi (MPa)		e	Δe	Maximum load	ε_{cu}	Mode of failure[3]
		compressive	flexural	in. (mm)	in. (mm)	10^3 lbf		
MI-0.9-1	30	6160 (42.5)	1030 (7.1)	0.0 (0)	0.03 (0.8)	185.1 (823.5)	0.0025	C
MI-0.9-2	33	6160 (42.5)	1030 (7.1)	3.0 (76)	0.22 (5.6)	20.1 (89.4)	--	T
MI-0.9-3	33	6160 (42.5)	1030 (7.0)	0.5 (18)	0.08 (2.0)	140.2 (623.5)	0.0026	C
MI-0.9-4	32	5830 (40.2)	1090 (7.5)	1.75(44)	0.12 (3.0)	79.2 (352.5)	0.0028	CT
MI-1.2-1[1]	31	6400 (44.1)	1250 (8.6)	0.0 (0)	0.03 (0.8)	150.0 (667.0)	0.0032	C
MI-1.2-2	29	6640 (45.8)	1330 (9.2)	0.0 (0)	0.03 (0.8)	187.0 (832.0)	0.0032	C
MI-1.2-3	35	5990 (41.3)	990 (6.8)	0.5 (18)	0.08 (2.0)	140.5 (625.0)	0.0026	C
MI-1.2-4[2]	34	5830 (40.2)	1230 (8.5)	1.0 (25)	0.12 (3.0)	139.5 (620.5)	0.0032	C
MI-1.2-5	34	6180 (42.6)	1250 (8.6)	3.0 (76)	0.21 (5.3)	28.1 (125.0)	--	T
MI-1.2-6	31	6690 (46.1)	1130 (7.8)	1.5 (38)	0.13 (3.3)	96.8 (430.5)	0.0034	C
MI-1.2-7	31	5560 (38.3)	1090 (7.5)	2.0 (51)	0.15 (3.8)	67.8 (301.5)	--	T
MI-1.2-8	33	6020 (41.5)	1090 (7.5)	3.5 (88)	0.25 (6.4)	18.8 (83.5)	--	T
MI-1.2-9	31	6230 (43.0)	1070 (7.4)	2.5 (64)	0.17 (4.3)	48.2 (214.5)	--	T
MI-1.2-10	29	6170 (42.5)	1080 (7.4)	1.0 (25)	0.10 (2.5)	116.9 (520.0)	0.0032	C
MI-1.2-11	28	6630 (45.7)	1080 (7.4)	1.75(44)	0.16 (4.1)	80.0 (359.4)	0.0032	CT
MI-1.5-1	28	6830 (47.1)	1310 (9.0)	0.0 (0)	0.05 (1.3)	187.0 (831.2)	0.0025	C
MI-1.5-2	32	6710 (46.3)	1160 (7.8)	0.5 (18)	0.08 (2.0)	153.4 (682.5)	0.0024	C
MI-1.5-3	32	6910 (47.7)	1540 (10.6)	1.75(44)	0.16 (4.1)	92.5 (411.5)	0.0028	CT
MI-1.5-4	32	7420 (51.2)	1150 (7.9)	3.0 (76)	0.20 (5.1)	35.8 (159.0)	--	T

[1] Local failure due to use of thin loading plate, not included in Figs. 3.21 to 3.23.

[2] Not included in Figs. 3.21 to 3.23.

[3] C = Compression failure
T = Tension failure
CT = Balanced or near-balanced failure.

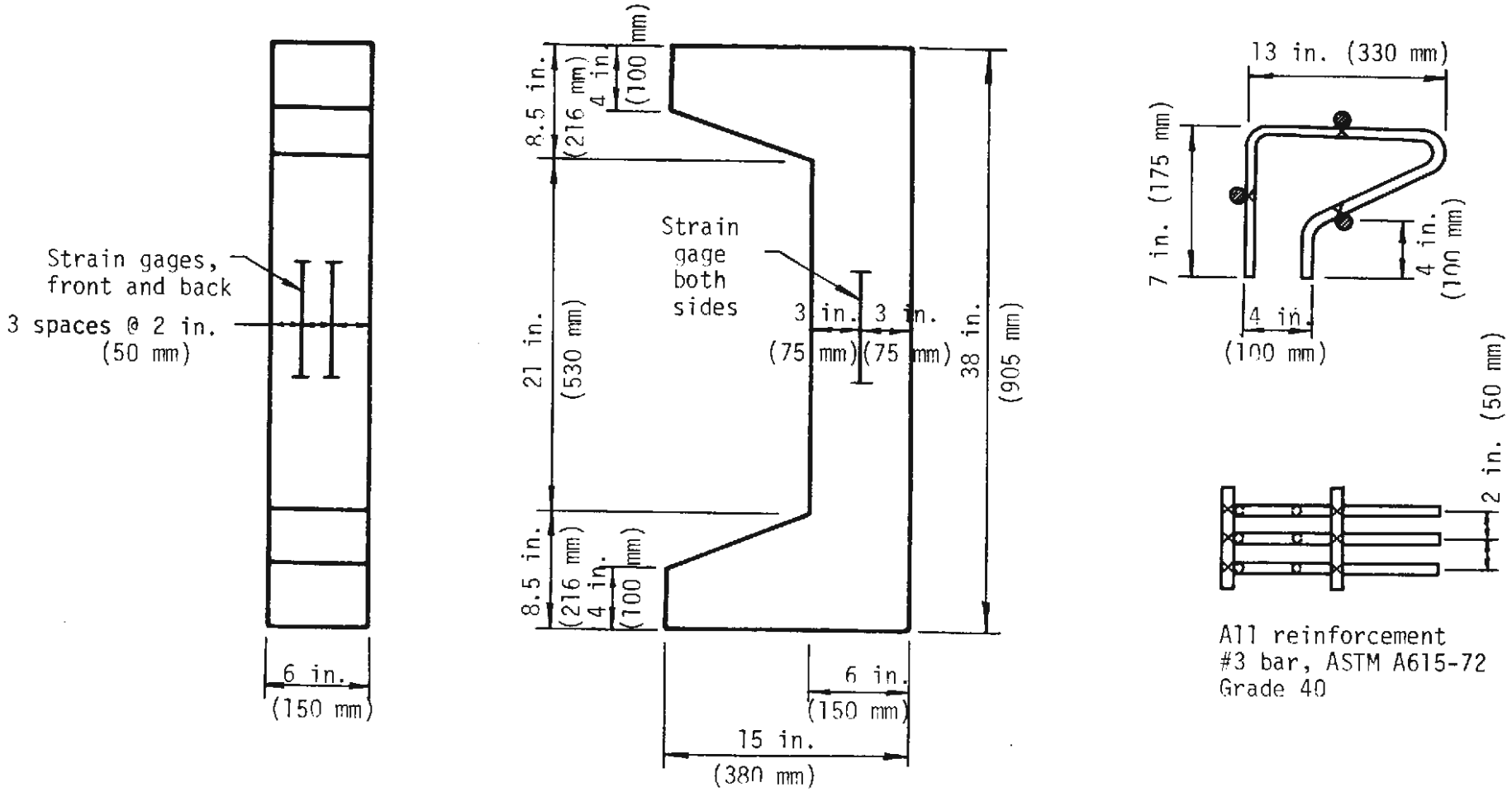

FIGURE 3.8 DETAILS OF BEAM-COLUMN AND CAPITAL REINFORCEMENT

fog room for 21 days, after which time they were removed and strain gages mounted. The specimens were then stored in the laboratory environment until tested.

3.3.2 STRESS-STRAIN PROPERTIES

COMPRESSIVE STRESSES IN THE CONCRETE

The compressive stress-strain relationship for steel fiber reinforced concrete is of primary interest. Typical stress-strain curves at various ages are shown in Fig. 3.9. The curves shown are for concrete with 1.2 percent fiber by volume, and would change somewhat with different fiber contents.

The 28-day compressive stress-strain relationships of steel fiber reinforced concrete cylinders are shown in Fig. 3.10 for the three fiber percentages used in this study. These curves show that the fibers enable the specimen to carry loads and strains well beyond the point at which the maximum load is reached. The strain at the maximum load observed in these tests was found to be on the order of 0.0025 at low fiber contents and about 0.003 at the higher fiber contents. In most cases the maximum compressive strains observed in the beam columns at maximum loads were about the same or slightly higher than the strain corresponding to the maximum stress in concentric compression. The tendency for stress redistribution in the compression zone as extreme fibers become highly strained is less pronounced than is observed for conventionally reinforced sections.

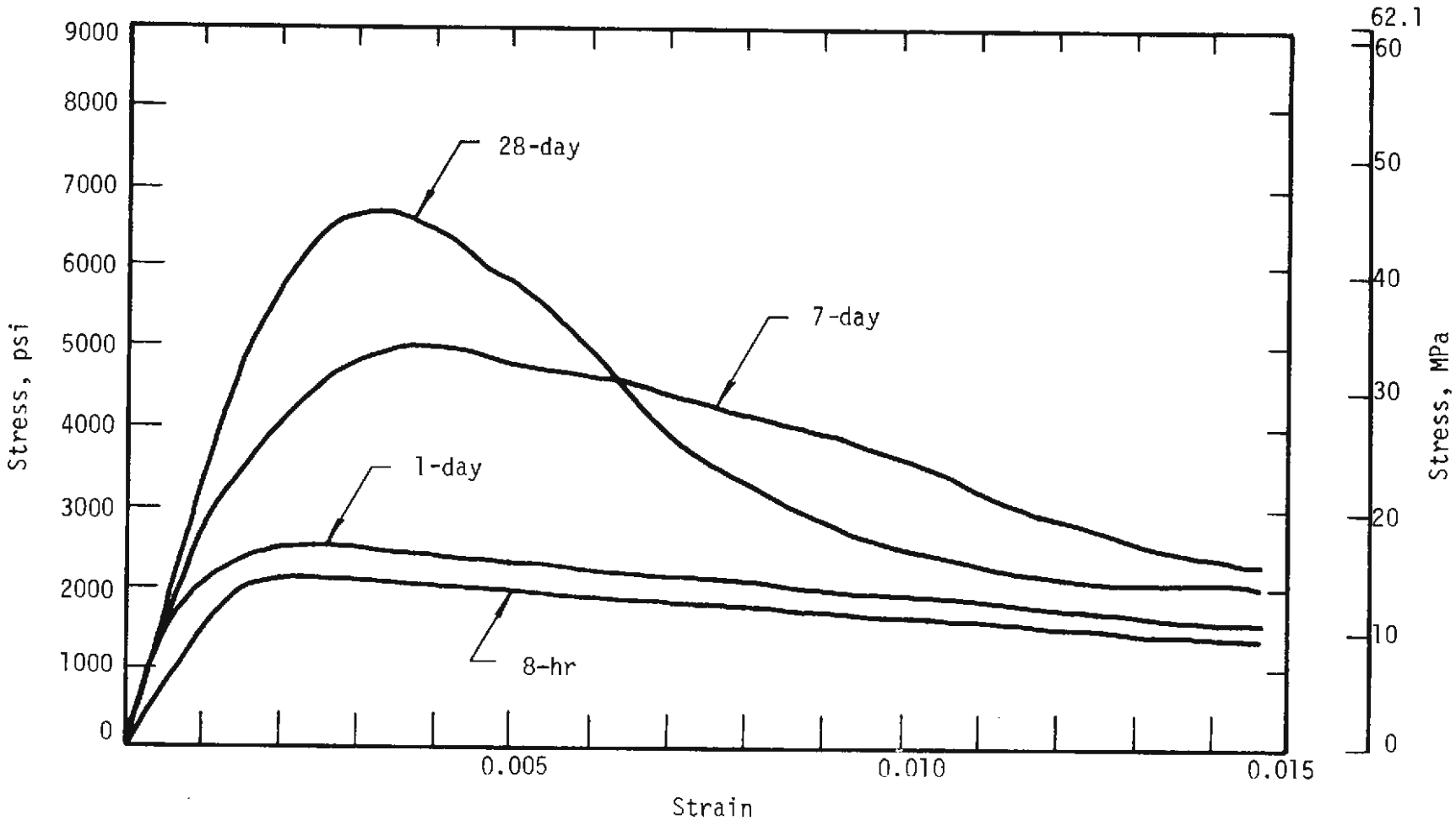

FIGURE 3.9 COMPRESSIVE STRESS-STRAIN CURVES WITH AGE FOR 1.2 PERCENT STEEL FIBER

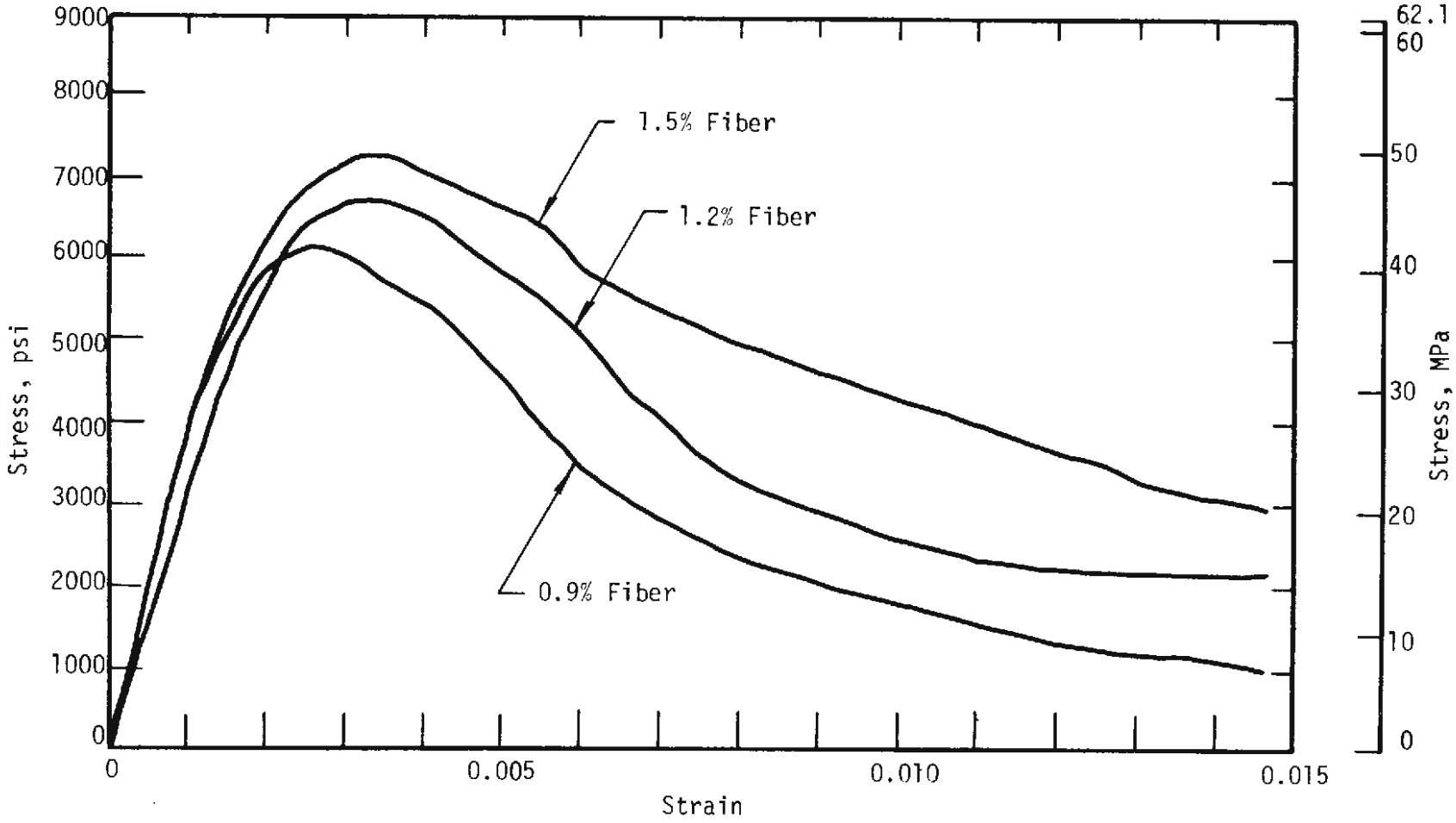

FIGURE 3.10 TYPICAL 28-DAY COMPRESSIVE STRESS-STRAIN CURVES FOR THREE FIBER CONTENTS

TENSILE STRESSES IN THE CONCRETE

The significant tensile strength of fibrous concrete has been well established by numerous previous investigators. An extensive bibliography has been reported by ACI Committee 544 (1973). Average load-elongation curves for steel fiber reinforced concrete in direct tension have been recently reported by Naaman, Moavenzadeh and McGarry (1974).

From experimental measurement of load, deflection, and strain distribution, a moment-curvature relationship may be determined for the failure section of beams and beam-columns. An average stress-strain relation may be computed for the failure section by application of numerical methods. These techniques are currently being employed in the generation of the tensile stress-strain relation from test results for beams and beam-columns. At this time results have not been verified and are not included in this report.

Typical load-deflection curves 3 in. by 3 in. by 15 in. (75 mm by 75 mm by 380 mm) steel fiber reinforced regulated-set cement concrete beams tested at different ages are shown in Fig. 3.11. The curves shown are for concrete with 1.2 percent fiber by volume, and would change somewhat with different fiber contents.

MODULUS OF ELASTICITY

The initial modulus of elasticity, E_c, for steel fiber reinforced regulated-set cement concrete was obtained from cylinder tests. Results are reported in Fig. 3.12 where modulus of elasticity is plotted against compressive strength.

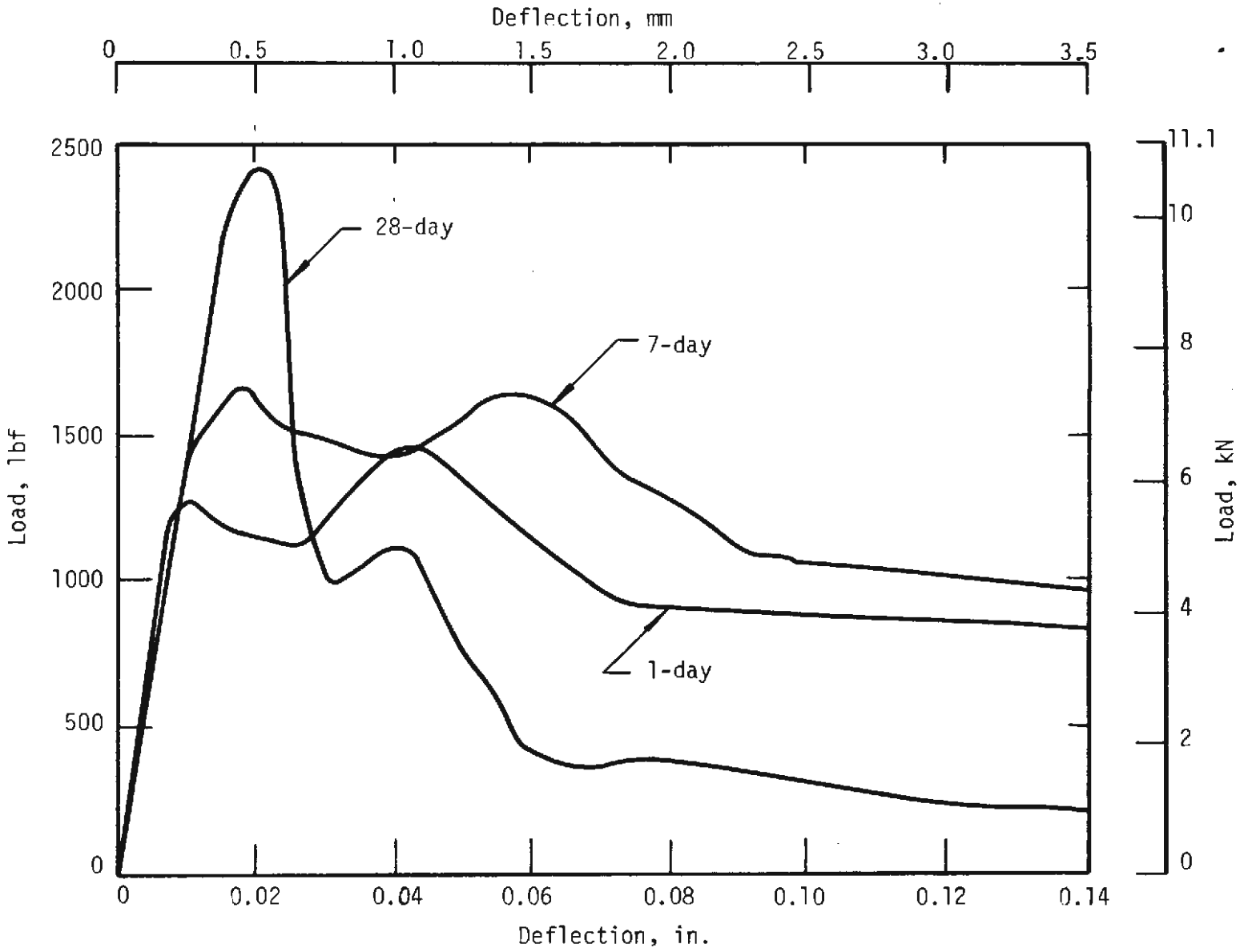

FIGURE 3.11 LOAD-DEFLECTION CURVES IN FLEXURE WITH AGE FOR 1.2 PERCENT STEEL FIBER

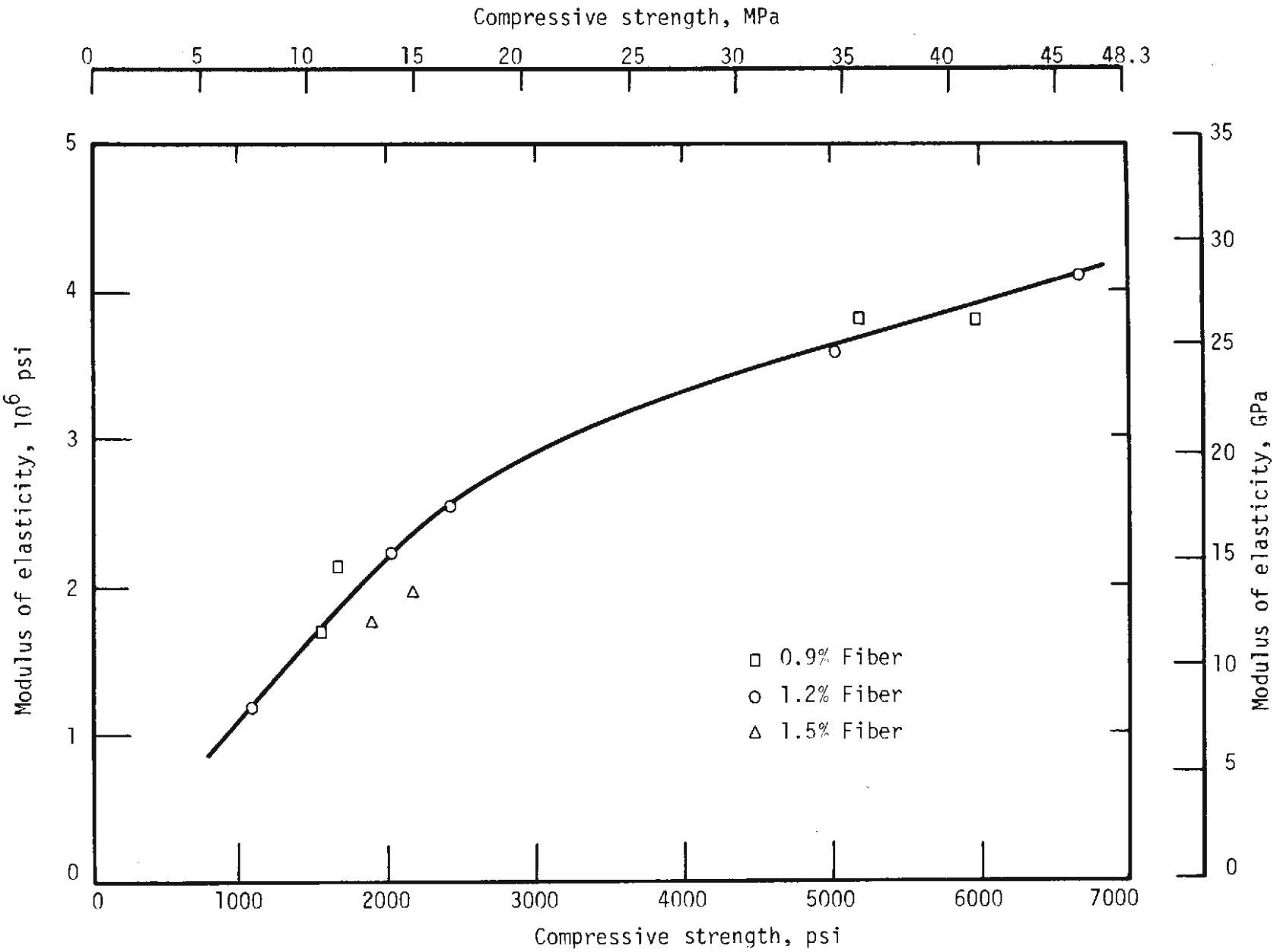

FIGURE 3.12 VARIATION OF MODULUS OF ELASTICITY WITH COMPRESSIVE STRENGTH

3.3.3 VARIATION OF STRENGTH WITH TIME

For a given fiber content, both the compressive and flexural strengths of steel fiber reinforced, regulated-set cement increase with age, as illustrated by Figs. 3.13 and 3.14.

The ratio of ultimate flexural strength to ultimate compressive strength varies considerably, decreasing from about 0.30 for lower strengths to 0.20 for high strengths.

3.3.4 STRAIN MEASUREMENTS IN BEAM-COLUMN TESTS

The ultimate strains in tension and compression, ε_{tu} and ε_{cu}, were determined from the tests of eccentrically loaded beam-columns reported in Table 3.4. The ultimate strain in this report is defined as the strain measured at the maximum load of the specimen. Except where the eccentricity was very low the load on the specimen normally dropped to a low value just past the maximum load. This was especially characteristic of tension failure at high eccentricity.

Strain gages were attached at the midheight of all specimens as indicated in Fig. 3.8. For specimens failing in compression crushing noemally occurred across the gages. The tension failures normally occurred slightly above the gages, making it difficult to interpret the strain readings.

Although the compression failures occurred normally at the location of gages, it appears that the apparent strain at a given high load is not a well defined quantity. This is because the measurement of strains is dependent on time, strain gage characteristics, and the concentration of strain is in a small region near the zone of crushing. However, it was felt that

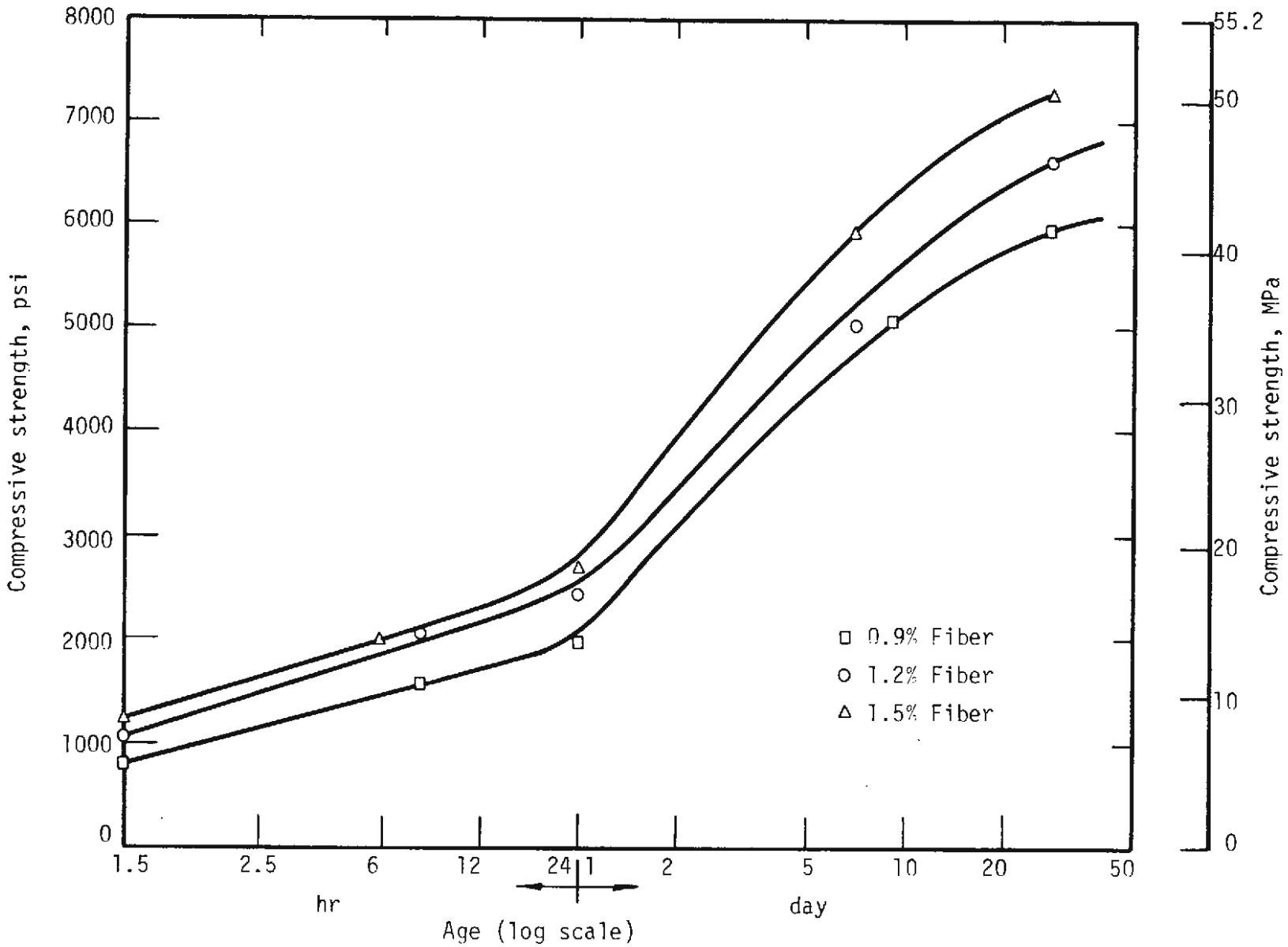

FIGURE 3.13 STRENGTH-TIME CHARACTERISTICS IN COMPRESSION FOR THREE FIBER CONTENTS

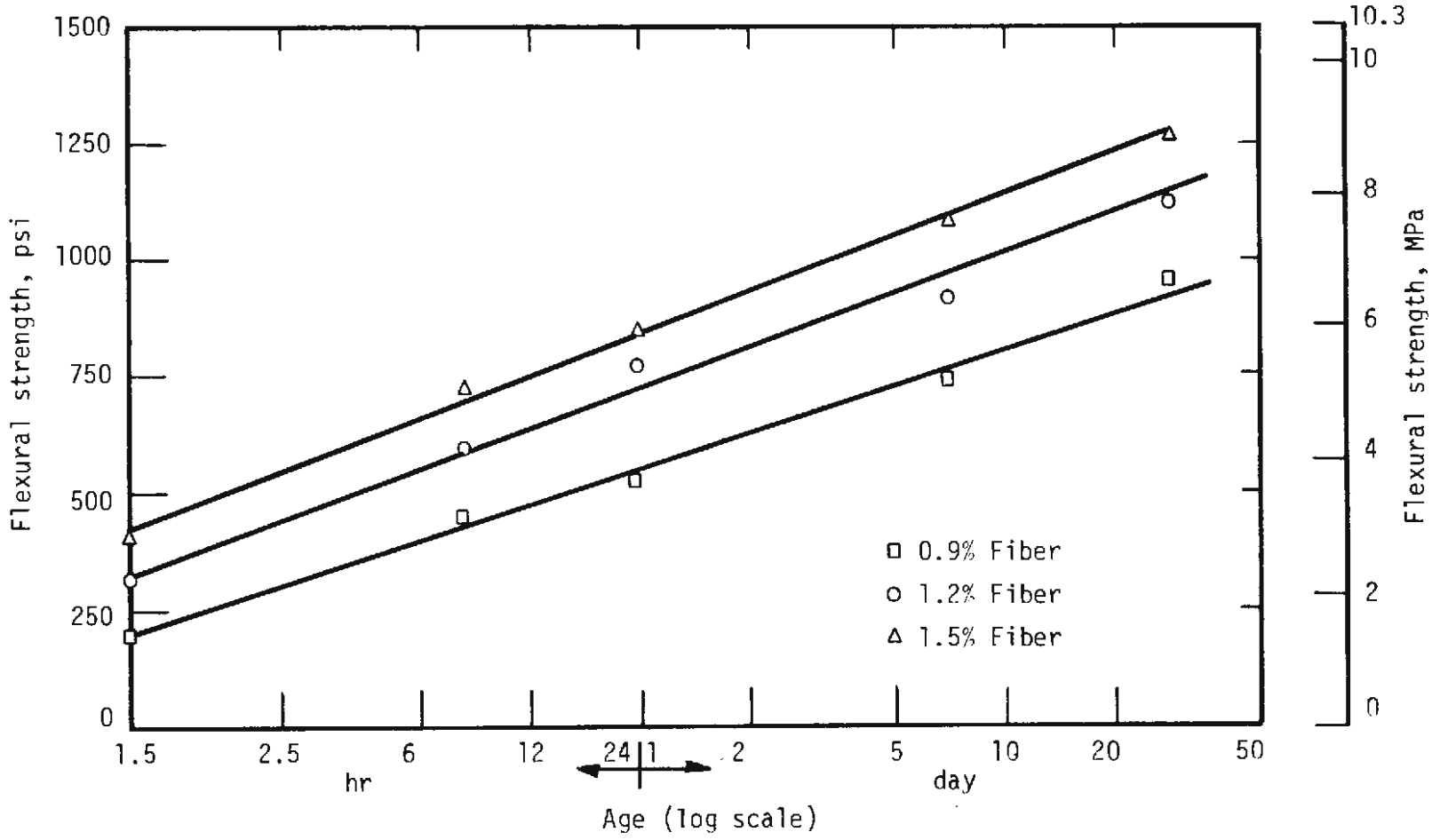

FIGURE 3.14 STRENGTH-TIME CHARACTERISTICS IN FLEXURE FOR THREE FIBER CONTENTS

a strain measured over a reasonably long gage length, 6 in. (150 mm) in the failure region, would be useful in a flexural analysis.

Values of compressive strain measured during testing are shown in Fig. 3.15 for several beam-columns. The dotted lines represent an extrapolation of the strain to a known ultimate load. In Fig. 3.16 are shown typical examples of the measured strains at both the tension and compression faces for three specimens as loading progressed. This information is used to determine the moment-curvature relationship of a beam-column loaded at a given eccentricity.

The compression and tension strains at ultimate load varied considerably with mean values of 0.003 in compression and 0.0021 in tension.

A potentially useful assumption for the analysis of any structural element is the linear variation of strain between the outer fibers of a cross section. Some evidence for this is provided in Figs. 3.17 to 3.19.

3.3.5 INTERACTION DIAGRAMS

Ultimate interaction and load-curvature diagrams obtained from the tests of steel fiber reinforced concrete beam-colums reported herein are shown in Figs. 3.20 to 3.22 for the three fiber contents. The moments shown are calculated as the maximum load times the total eccentricity at this load as measured during the tests. The total eccentricity is the original eccentricity plus the deflection at the midheight of the specimen.

Strains measured at the outer fibers of the specimen at ultimate load are shown adjacent to corresponding points on the interaction diagram.

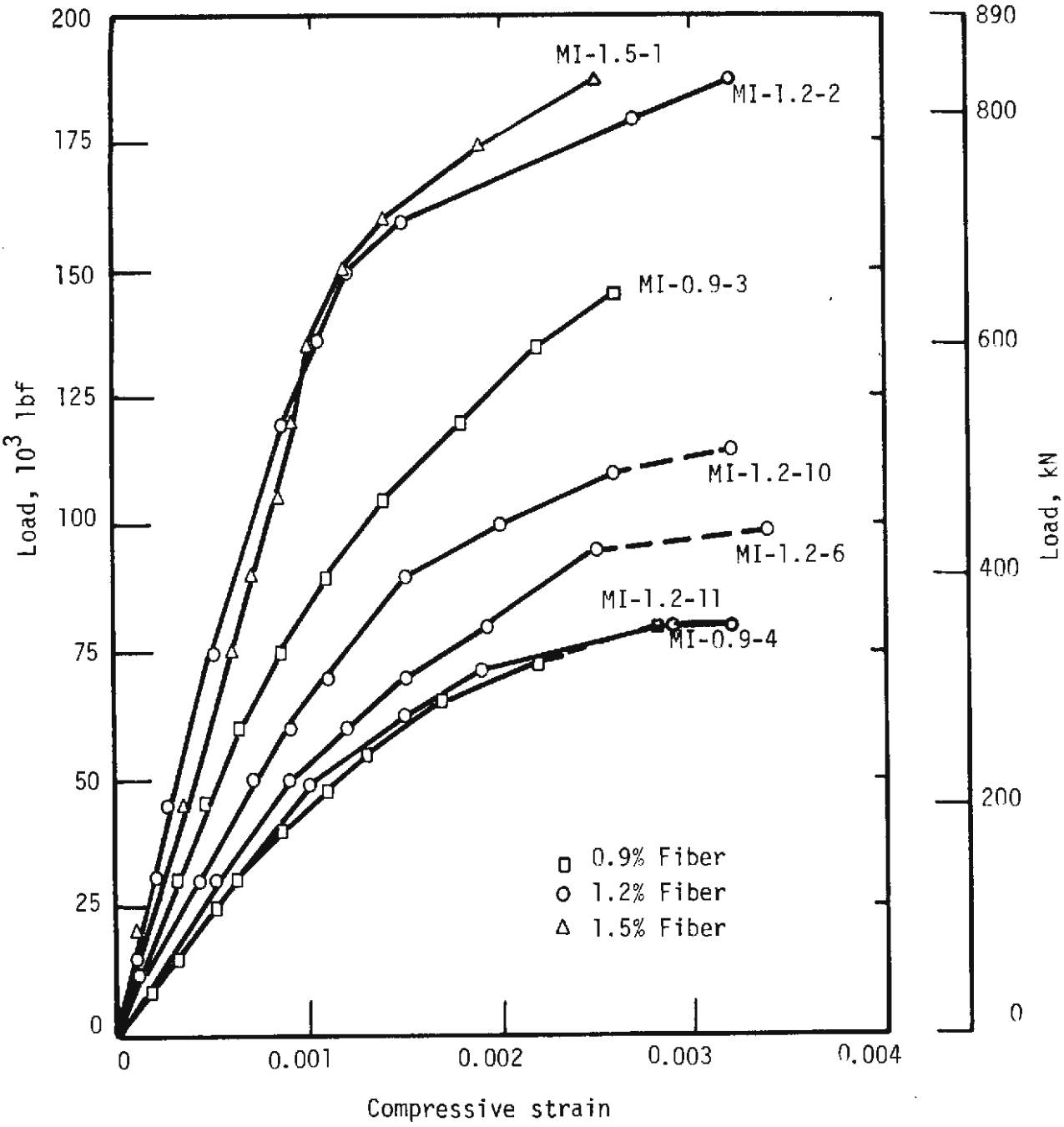

FIGURE 3.15 TYPICAL LOAD VS. STRAIN CURVES AT BEAM-COLUMN CENTERLINE

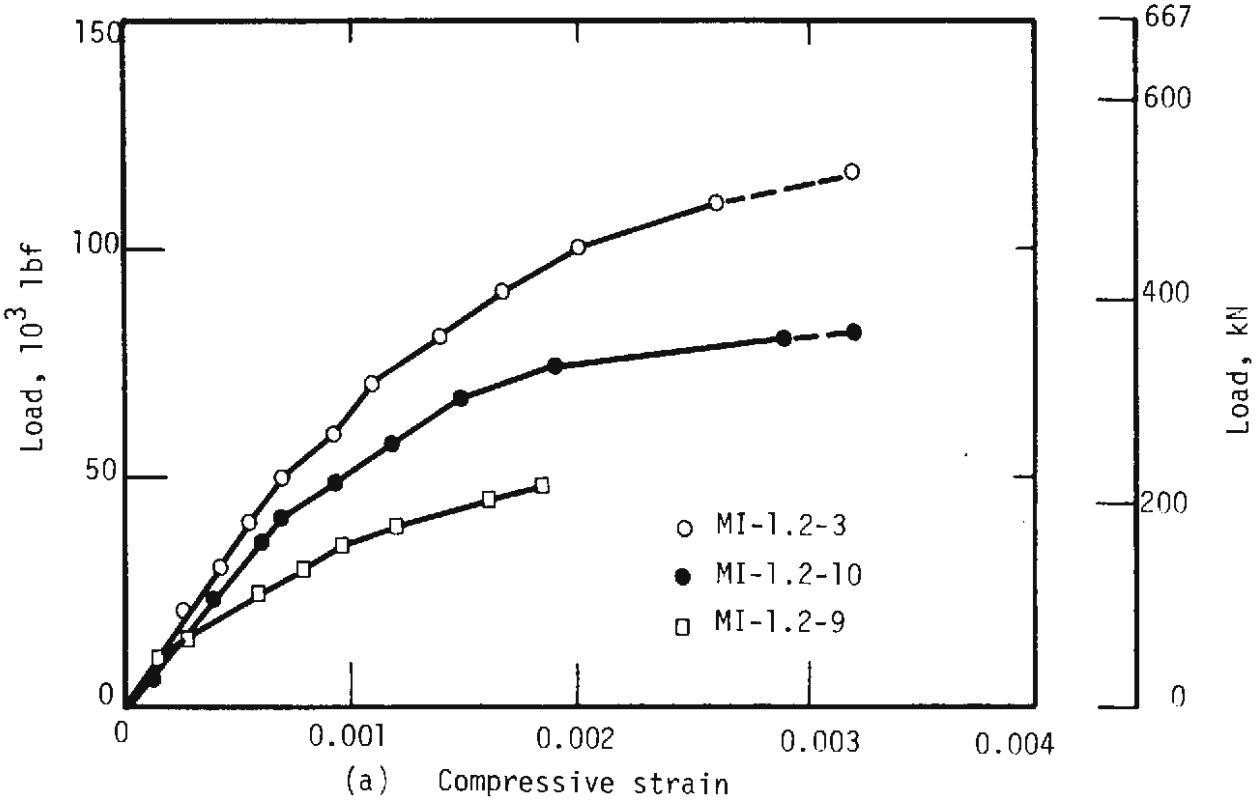

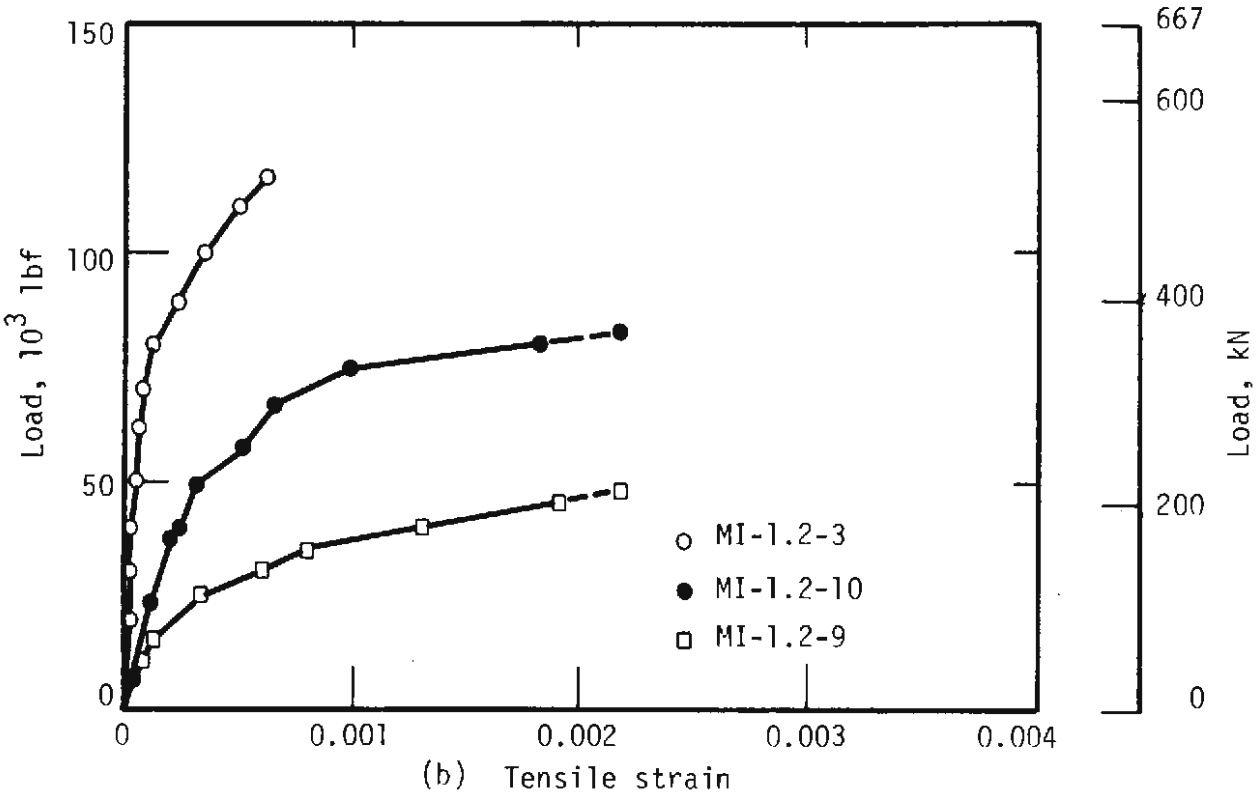

FIGURE 3.16 LOAD VS. STRAIN AT COMPRESSION AND TENSION FACES FOR TYPICAL BEAM-COLUMNS

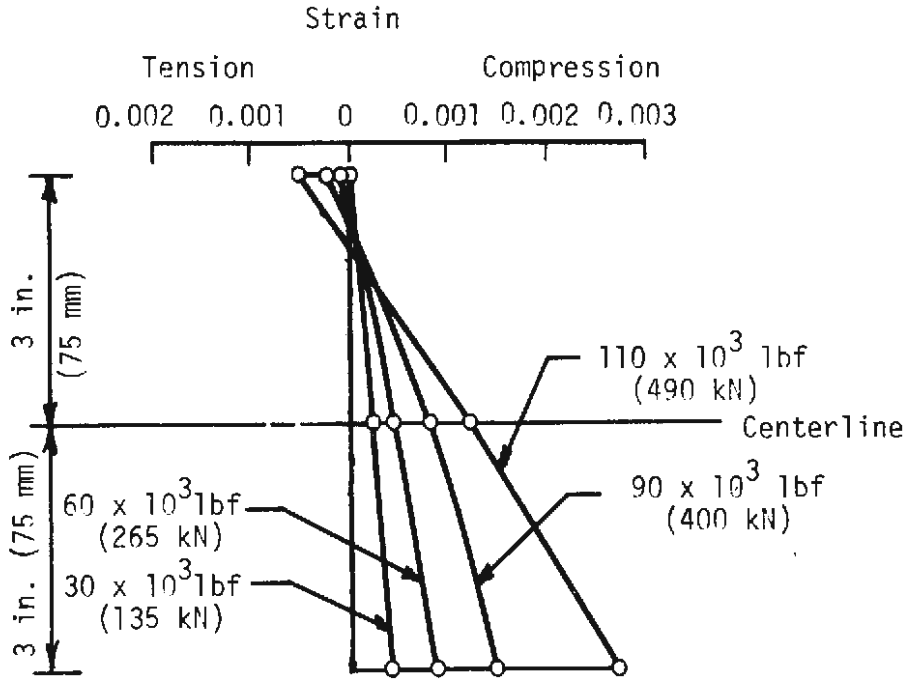

FIGURE 3.17 STRAIN DISTRIBUTION WITH INCREASING LOAD FOR COMPRESSION FAILURE MI-1.2-10

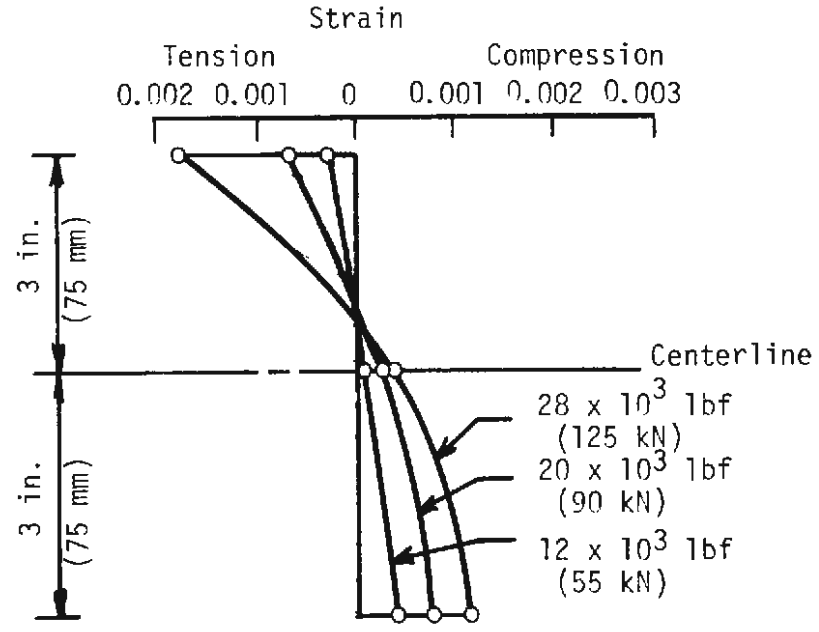

FIGURE 3.18 STRAIN DISTRIBUTION WITH INCREASING LOAD FOR TENSION FAILURE MI-1.2-5

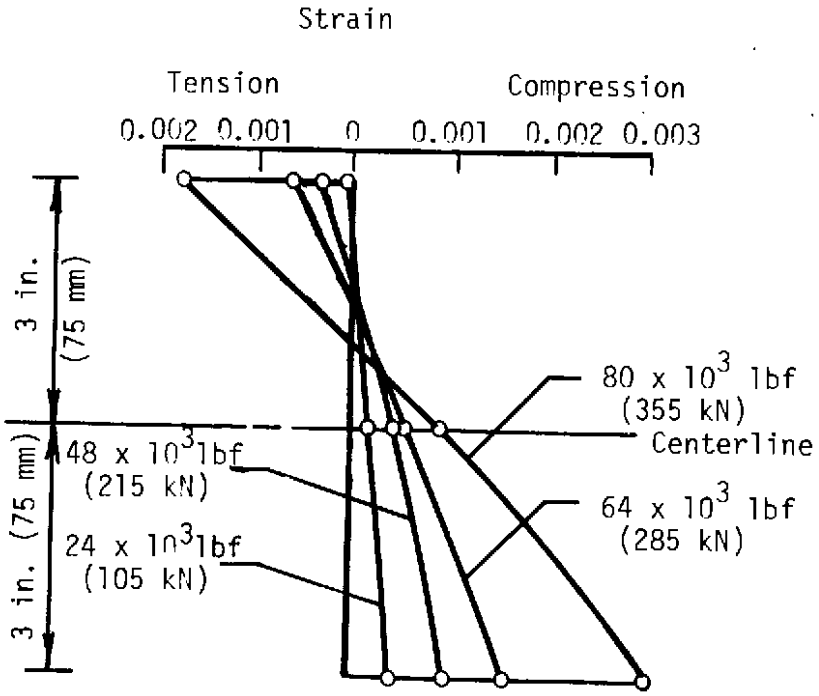

FIGURE 3.19 STRAIN DISTRIBUTION WITH INCREASING LOAD FOR BALANCED FAILURE MI-1.2-11

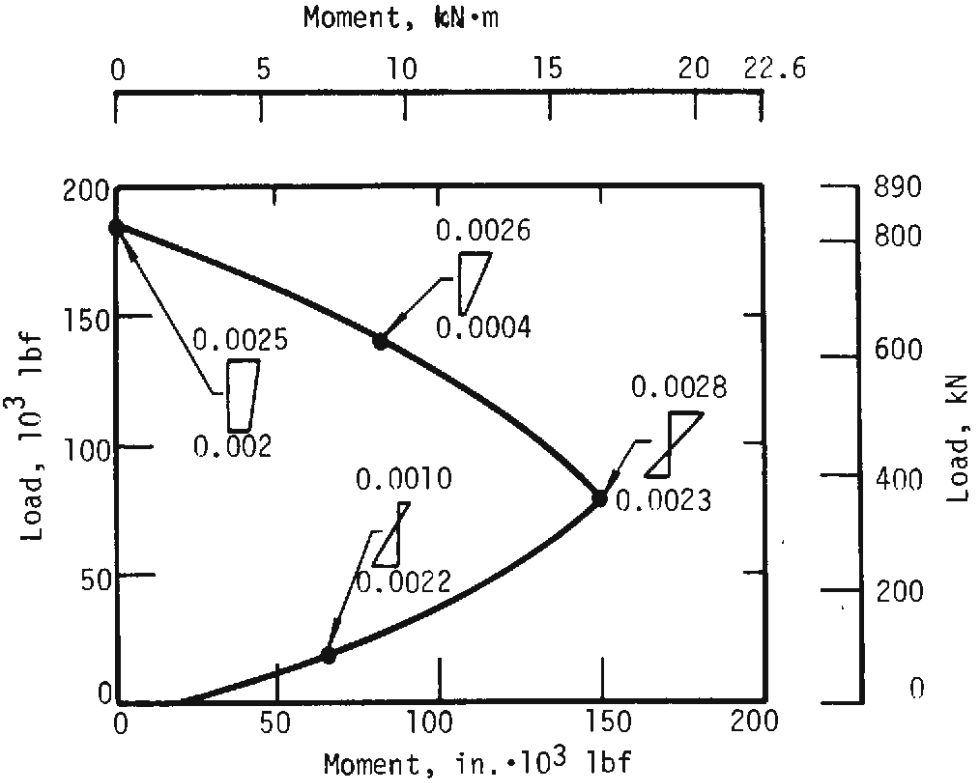

(a) Interaction diagram

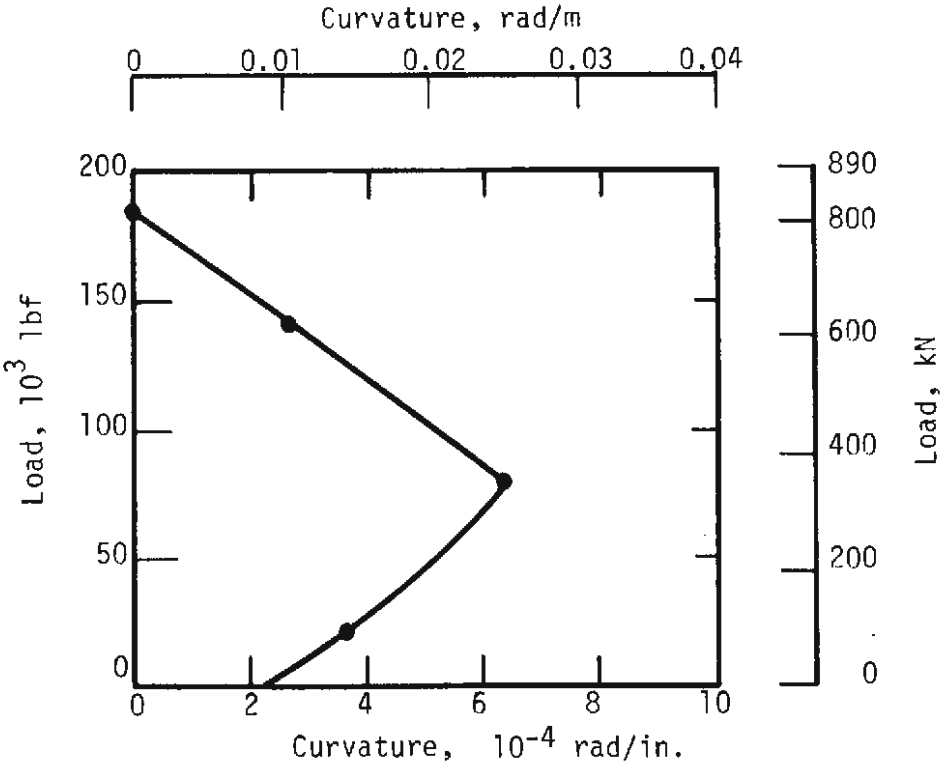

(b) Load-curvature diagram

FIGURE 3.20 ULTIMATE INTERACTION AND LOAD-CURVATURE DIAGRAMS FOR 0.9 PERCENT FIBER

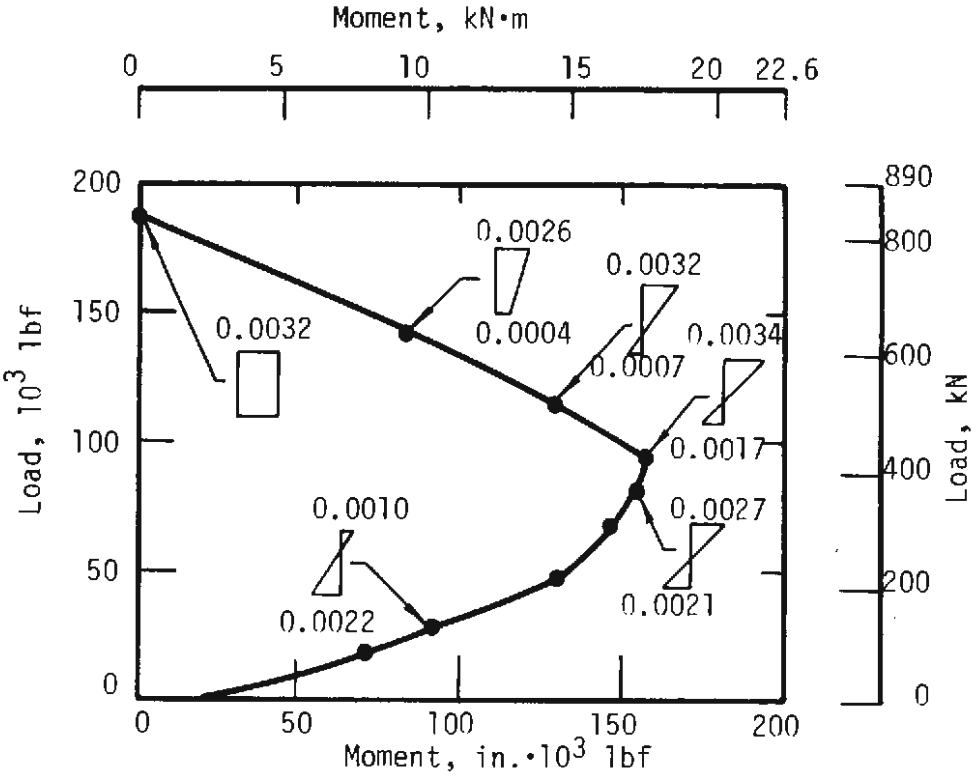

(a) Interaction diagram

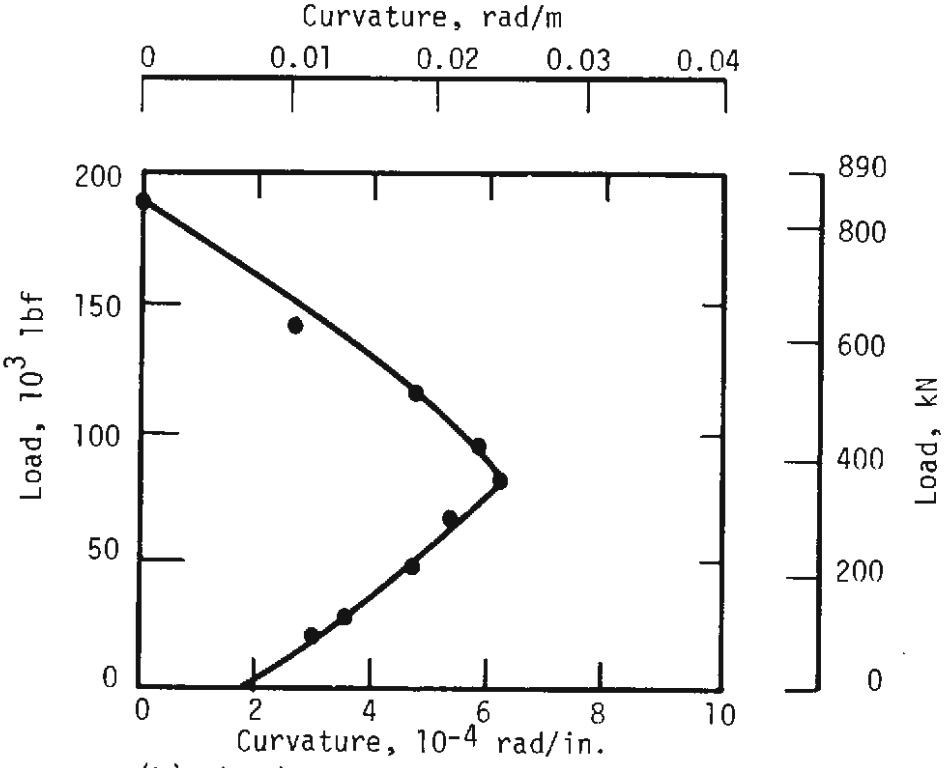

(b) Load-curvature diagram

FIGURE 3.21 ULTIMATE INTERACTION AND LOAD-CURVATURE DIAGRAMS FOR 1.2 PERCENT FIBER

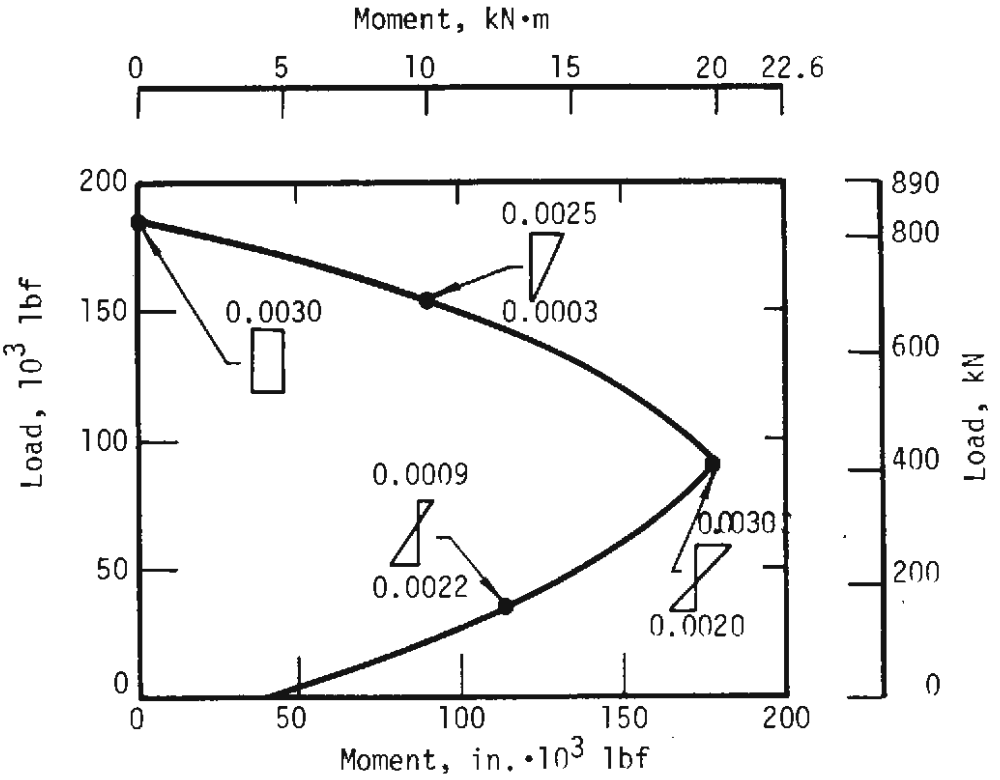

(a) Interaction diagram

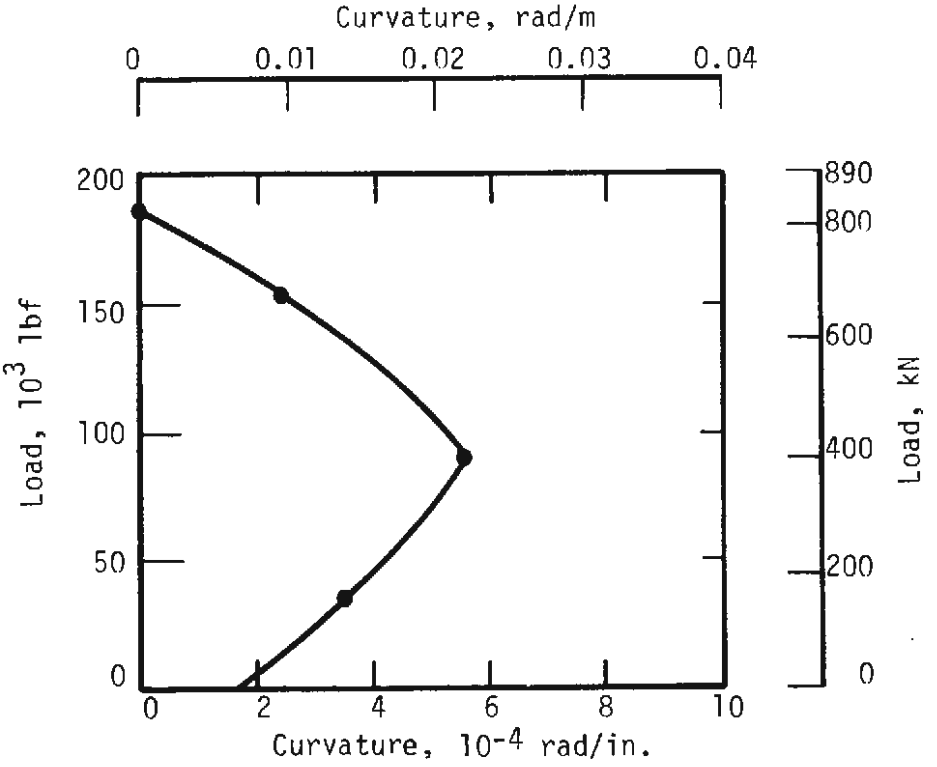

(b) Load-curvature diagram

FIGURE 3.22 ULTIMATE INTERACTION AND LOAD-CURVATURE DIAGRAMS FOR 1.5 PERCENT FIBER

3.3.6 GENERAL BEHAVIOR AND MODES OF FAILURE FOR BEAM-COLUMNS

The behavior and modes of failure of steel fiber reinforced concrete beam-columns can be described in terms similar to those of conventionally reinforced members.

In this report, ultimate conditions refer to the attainment of maximum load or the conditions at the peak of the load-deflection curve. Three curves of load vs. head deflection of the testing machine, Fig. 3.23, obtained during the beam-column tests, will be used to help explain the conditions described in the following paragraphs. In the following discussion the ratio of initial eccentricity to the depth of the section is given by e/d. The observed mode of failure of each beam-column, described in the terms of conventionally reinforced concrete, is reported in Table 3.4.

The general behavior and modes of failure of steel fiber reinforced concrete beam-columns can be summarized as follows:

1. At low eccentricities, e/d less than 0.25, the failure of the specimens was by crushing of the concrete at the ultimate strain of about 0.003. Shortly after crushing occurred, the load carrying capacity of the member dropped suddenly to a low value. For this mode failure was less brittle than a compression failure in conventional reinforced concrete. Typical examples of this failure mode are MI-1.2-2 in Figs. 3.24 and 3.25 and MI-1.2-6 in Fig. 3.25.
2. For intermediate eccentricities, e/d from 0.25 to 0.33, failure was by crushing of the concrete and rapid propagation of the tension crack. In conventional terms, this is the balanced

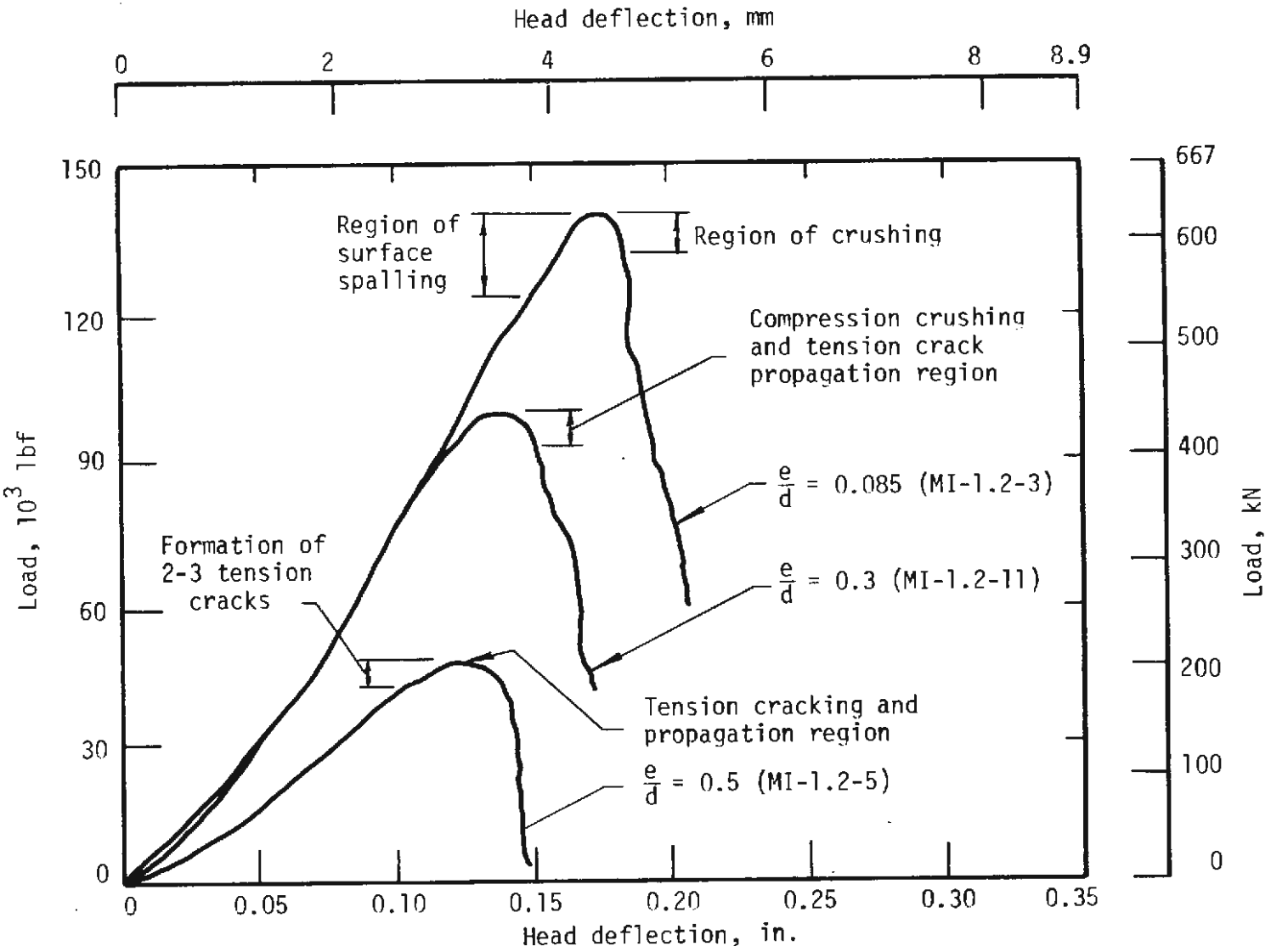

FIGURE 3.23 LOAD VS TESTING MACHINE HEAD DEFLECTION WITH VARIOUS INITIAL ECCENTRICITY

FIGURE 3.24 DETAIL OF TYPICAL COMPRESSION FAILURE, MI-1.2-2, e/d = 0.0

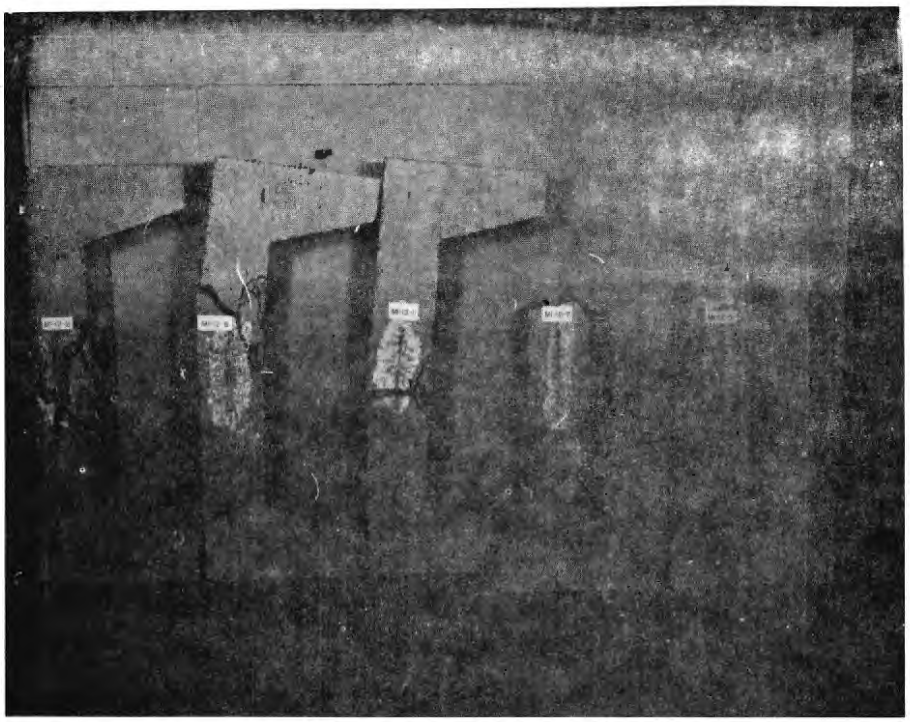

MI-1.2-2 MI-1.2-6 MI-1.2-11 MI-1.2-7 MI-1.2-5

FIGURE 3.25 BEAM-COLUMN FAILURES WITH INCREASING ECCENTRICITY

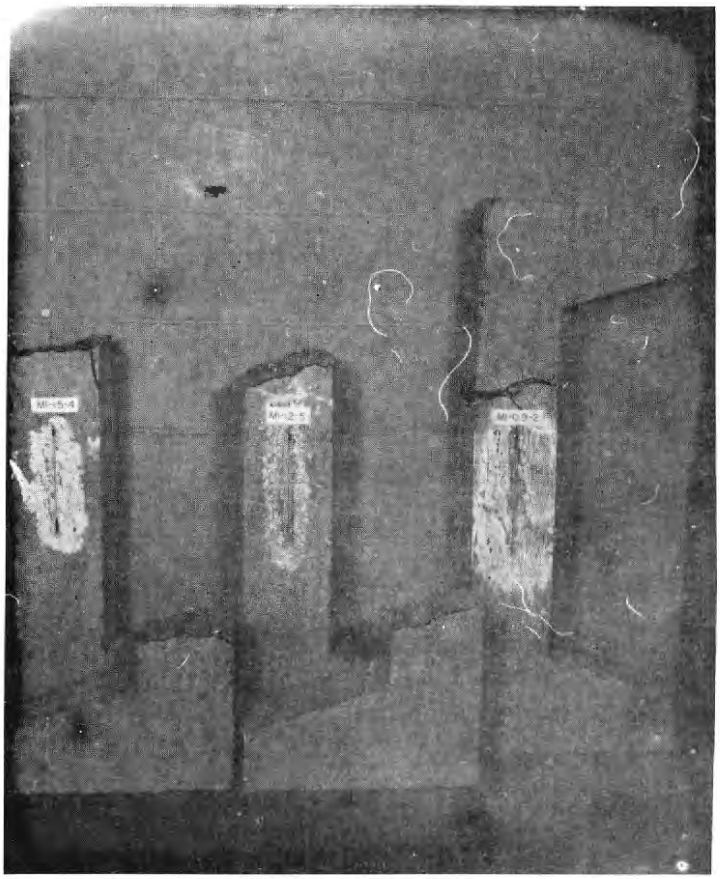

FIGURE 3.26 DETAILS OF TYPICAL TENSION FAILURES

failure mode. Examples of this type of failure are found in Fig. 3.26.

3. For eccentricities with e/d greater than about 0.33, failure was characterized by rapid propagation of the tension crack through the specimen with no crushing at the compression face. Normally two or three tension cracks could be observed just before the maximum load. One of these cracks propagated through the member at or shortly after the maximum load. Beam-columns failing in tension developed much larger deflections than those failing in compression. A typical example of this failure mode is MI-1.2-11 in Fig. 3.25.
4. The location of the neutral axis moved toward the compression face of the specimen as the initial eccentricity of load increased. This can best be seen in Figs. 3.17 to 3.19.
5. The load carrying capacity of all beam-columns normally dropped to very low values just after ultimate. With very small additions of load considerable increase in deformation occurred.
6. The increase in load capacity with increase in fiber content is greatest in the region of tension failure.
7. In no instance did a failure occur by yielding of the fibrous reinforcement.

3.3.7 CREEP

Creep tests are currently underway to develop additional information on the behavior of hardened, steel fiber reinforced, regulated-set

cement concrete. The test procedures and curing, followed the criteria set forth in "Standard Method of Test and Creep of Concrete in Compression," (ASTM C512-69). Eight 6 in. by 12 in. (150 mm by 300 mm) cylinders were cast vertically, using the 1.5 percent fiber mix appearing in Table 3.1. The slump of the mixture was 4-1/4 in. (105 mm) with an air content of 3.9 percent at 145.4 pcf (86.3 kg/m^3).

One cylinder was cut in half for use as a plug in the creep rack; two cylinders were tested for compressive strength prior to the loading of creep specimens. The strengths were 7900 psi and 7550 psi (54.45 MPa and 52.05 MPa). Steel gage points for use with a mechanical strain gage were affixed with epoxy cement to each specimen so as to permit measurement on three longitudinal axes per cylinder. Two gaged specimens are serving control purposes and are not loaded. The remaining three specimens have been placed into a spring-loaded creep rack and loaded to 1000 psi (6.90 MPa). Strain readings on control and loaded specimens are taken on a regular schedule.

3.3.8 SUMMARY

GENERAL

The object of this study was to further the understanding of the behavior of steel fiber reinforced concrete members subjected to axial compression, flexure, and bending combined with axial load.

Nineteen eccentrically loaded beam-columns were tested to failure in short-term tests. Behavior during loading was recorded by measurement of load, strain, and deflection.

A study of the material behavior under sustained loads was initiated. The standard test for creep in compression is currently underway.

STRESS-STRAIN RELATIONSHIPS

Typical stress-strain curves in compression for steel fiber reinforced, regulated-set cement concretes were obtained for various fiber contents and ages.

A stress-strain relation for tension is being derived from experimentally obtained load, deflection, and strain information.

The ratio of ultimate flexural strength to ultimate compressive strength varies inversely as compressive strength. Average ultimate strains experimentally obtained in beam-column tests were 0.0021 in tension, and 0.003 in compression.

FAILURE MODES

Ultimate interaction diagrams have been obtained for fiber contents of 0.9, 1.2, and 1.5 percent by volume. Three failure modes have been observed:

1. A compression failure characterized by crushing of concrete in the compression zone.
2. A tension failure characterized by rapid propagation of a tensile crack through the specimen with no crushing of concrete.
3. A balanced failure in which both failure modes are exhibited in part.

For beam columns of 6 in. by 6 in. (150 mm by 150 mm) cross section, each failure mode corresponds to a particular range of eccentricities: compression failure, e/d from 0 to about 0.25; balanced failure, e/d varying from 0.25 to 0.33; and tension failure, e/d greater than 0.33, where e is total eccentricity of the maximum load, and d is the depth of the cross section.

No failures have been observed which can be attributed to yielding of fibrous reinforcement.

CONCLUSION

The work reported herein has established strength-time characteristics, ultimate strains, and ultimate interaction diagrams for steel fiber reinforced, regulated-set cement concrete. Beam-column tests have established failure modes for steel fiber reinforced regulated-set cement concretes and have provided information for use in the rational design of concrete tunnel liners. Strength-time information is of direct interest to constructors and designers. Ongoing research attempts to supplement current information in both of these aspects.

3.4 DURABILITY

3.4.1 INTRODUCTION

Concrete used in tunnels may be subjected to various deteriorating environments which it must resist and still retain the strength necessary to continue its support function. Typical of such environments are sulfate waters, corrosive liquids or gases, and high temperatures which may result from a fire. In addition, after fresh concrete is placed in a tunnel wall

it may be disturbed during the setting period as additional new concrete is vibrated into place.

Since both sulfate attack and corrosion are affected by the porosity of the concrete some knowledge of the permeability is needed.

Preliminary information on the disturbance of the young concrete and the effect of high temperature are reported, though information on the other possible deteriorating factors is too meager to report.

3.4.2 DISTURBANCE OF YOUNG CONCRETE

When concrete is placed by slipforming it is possible for the concrete that is setting to be disturbed by the vibration of newly placed concrete. An estimate of the potential for possible damage to early strength was made by revibrating cylinders and beams for short intervals until testing. These tests were performed using 4 in. by 8 in. (100 mm by 200 mm) cylinders and 3 in. by 3 in. by 15 in. (75 mm by 75 mm by 380 mm) beams. Control and experimental specimens were cast from a single batch of the 1.5 percent fiber mix described in Table 3.1.

For purposes of control, three cylinders and three beams were given a 5 sec compactive vibration, allowed to set for 2 hr, and tested in compression. The remaining specimens were given a comparable 5 sec initial vibration followed by revibrations of 15 sec at 15 min intervals for either 1.5 hr or 2 hr, then tested at the age of 2 hr in compression. Results are reported in Table 3.5. Vibration frequency was 167 Hz.

Results from the tests indicate revibration of the concrete did not induce harmful effects. All specimens were cut in half longitudinally and inspected for segregation of coarse aggregate or fiber. Segregation was not observed in either the test or control specimens.

TABLE 3.5

EFFECT OF EXTENDED VIBRATION ON EARLY STRENGTH

Strength of control, psi (MPa)		Strength of vibrated, psi (MPa)	
Compression	Flexure	Compression	Flexure
Vibrated at 15 min intervals for 1.5 hr			
740 (5.10)	220 (1.52)	970 (6.69)	270 (1.86)
Vibrated at 15 min intervals for 2 hr			
790 (5.45)	240 (1.65)	1000 (6.89)	300 (2.07)

3.4.3 EFFECT OF HIGH TEMPERATURE

The influence of high temperature on steel fiber reinforced, regulated-set cement concrete depends on the time-temperature history. Series of strength tests were made on concrete that had been subjected to 350 F (175 C) and 600 F (315 C), respectively. Cylinders, 6 in. by 12 in. (150 mm by 300 mm) and beams, 3 in. by 3 in. by 15 in. (75 mm by 75 mm by 380 mm), were cast for each temperature using the mix given in Table 3.2.1 for 1.5 percent fiber.

All specimens were air dried for two days prior to high temperature exposure. If this precaution was not taken the specimens tend to explode from vaporization of entrapped water. For each high temperature the specimens were broken down into groups of three cylinders and three beams; one group of each series was subjected to its respective high temperature

for one day, the other was subjected to the high temperature for seven days. In Table 3.6 results are compared to a series of specimens which were air dried and kept continuously at 73 F (23 C). All specimens were at 73 F (23 C) when tested for strength.

TABLE 3.6

EFFECT OF HIGH TEMPERATURES ON STRENGTH

Length of Exposure, days	Strength of control, psi (MPa)		Strength when subject to high temperature, psi (MPa)			
	73 F (23 C)		350 F (175 C)		600 F (315 C)	
	Compression	Flexure	Compression	Flexure	Compression	Flexure
1	5600 (38.60)	880 (6.05)	2940 (20.25)	850 (5.86)	1970 (13.60)	400 (2.75)
7	5890 (40.60)	1080 (7.45)	2270 (15.65)	410 (2.85)	1160 (8.00)	210 (1.45)

Considerable strength decreases are apparent with an increase in high temperature and with increased time of exposure to the high temperature.

3.4.4 SUMMARY

Preliminary data for the particular steel fiber reinforced, regulated-set cement concrete tested indicate that early strength may not be adversely affected if the concrete is revibrated during the setting period. Further, heating the concrete to 350 F or 600 F (176.5 C or 315.5 C), as might occur in fire does decrease the strength.

3.5 FIELD PUMPING STUDY

Pumping tests of steel fiber reinforced concrete have been previously reported (Parker, et al. 1973, Appendix C). Further pumping trials of steel fiber reinforced concretes were conducted at the plant of National Concrete Machinery Company, Lancaster, Pennsylvania. Although some of the mixes were pumpable the results were less than satisfactory. This was in large part due to the poor gradation of the sand which was deficient in fines. However, the results were sufficiently encouraging that some confidence was developed that a proper mix of fiber reinforced concrete can be pumped.

The fibers were 0.010 in. by 0.022 in. by 1 in. (250 μm by 560 μm by 25 mm). Type 1, regulated-set and Duracal cements were used. The water was kept at 32 F (0 C) by ice. The concrete was mixed in a Concrete Mobile and a Daffin pump was used.

Concrete which contained 0.9 percent fiber and had slumps above 4 in. (100 mm) appeared to be pumpable. Difficulties were observed in the reducer from the pump, which in three sections went from 10 in. (250 mm) to 4 in. (100 mm), and in the 90 degree turns in the line beyond the reducer. The fibers strongly resisted reworking of the concrete which occurred as the concrete passed through the reducer and elbow sections. When one section of the reducer was removed, leaving the discharge opening 6 in. (150 mm) in diameter instead of 4 in. (100 mm), most of the concretes pumped through it. Another source of difficulty was leaks at joints which allowed the mix water to escape, leaving behind solids which could not be forced through the line.

Failures of concrete to pump may be described as segregation

failures or friction failures. The failures reported here were due to segregation by having the water forced through the mix at high pressure or the water leaking out through a loose joint.

Three solutions are suggested. One is to increase the fines content so that the higher pump pressures required for fiber reinforced concretes can be resisted without segregation. The second is to eliminate the reworking required as the concrete leaves the pump by eliminating the reducer or reducing as little as possible, and by using large radii for any changes in direction of the line. Third, pumpability may be improved by increasing the fluidity of the mix. New admixtures have recently become available which may significantly increase fluidity without segregation.

The cement, type 1, regulated-set or Duracal, was not a distinguishing factor in these tests.

3.6 EMERGENCY PROCEDURES IN CASE OF EQUIPMENT FAILURE OR STOPPAGE

It is recognized that construction does not always proceed smoothly and continuously. Sudden unavoidable work stoppages may occur at any time, and it is necessary to have some emergency procedures to implement when the time comes.

The quick setting nature of regulated-set cement concrete requires that it be placed within a fixed time after mixing. It is possible, however, to extend the placement time by 10 to 15 min by adding the pumping agent Flo-Dense in concentrations of 0.5 percent by weight of cement. Adding this agent in dry form will increase mix workability for a short time during which it may be possible to place the concrete. The use of Flo-Dense

will not cause significant loss of strength. If for some reason mixed regulated-set cement concrete cannot be placed within this extended period it must be discarded.

Disposal of the mixed concrete may be aided by the addition of citric acid in water solution. A concentration of 0.3 percent by weight of cement will retard hydration to allow a few more minutes in which to dump the concrete. This material cannot be used as regulated-set cement concrete for slipforming after additional citric acid solution has been added since its early strength properties will have been altered adversely.

Other uses for this rejected concrete may be found, however, as its 28-day compressive strength will be on the order of 4500 psi (31 MPa), depending upon what change in water-cement ratio occurs when the citric acid solution is added. Twenty-five gallons of 1.5 percent citric acid solution per cubic yard (0.12 m^3/m^3) of concrete added to the 1.2 percent fiber mix will produce concrete with a 0.48 water-cement ratio. This concrete may be suitable for use in the tunnel invert or elsewhere, but it must be used promptly.

The addition of more crushed ice to the regulated-set cement concrete will slow hydration in the event of an emergency. This method is also destructive as it alters the water-cement ratio.

3.7 ESTIMATED COST OF CONCRETE MATERIALS

The steel fiber and regulated-set cement used in this concrete are both still in the experimental stage of development. Market production is on a small scale and is not well established. Costs are therefore considerably higher than those predicted for the future. The figures given in

Table 3.7 are based on 1974 prices. They exclude the cost of shipping, batching, and handling. Costs per cubic yard (m^3) of concrete are based on a fiber content of 1.2 percent. For purposes of comparison, the average material cost of plain concrete can be assumed to be $20.00 per cubic yard ($26.00 per cubic meter).

TABLE 3.7

1974 MATERIAL COSTS FOR STEEL FIBER REINFORCED, REGULATED-SET CEMENT CONCRETE

Item	Cost, U.S. dollars	
	Per pound (kg) of material	Per cubic yard (m^3) of concrete
Regulated-set cement	0.027 (0.012)	19.57 (25.60)
Steel fiber	0.23 (0.104)	36.80 (48.13)
Aggregates	0.002 (0.0009)	5.38 (7.04)
Citric acid	0.50 (0.23)	0.70 (0.92)
		62.66 (81.69)

3.8 SUMMARY

While the various studies regarding concrete materials for tunnel linings are obviously incomplete, much useful information has been obtained to date and many further considerations identified.

Steel fiber reinforced, regulated-set cement concretes can be proportioned to meet design criteria for the extruded tunnel liner systems. The mix designs studied in detail were proportioned for a handling time of approximately 30 min and a minimum compressive strength of 500 psi (3.5 MPa) 1.5 hr after water was added to the mix. Since strength requirements vary with ground conditions, the technology of controlling strength gain must be fully developed. The search continues for an admixture which will provide the requisite handling behavior at a feasible temperature and without adverse effects. Citric acid has been used to extend workability; however, when used in sufficient amount to meet handling criteria, the material strength is adversely affected.

Strength-time curves for compression and flexure have been determined for the particular concretes reported herein.

Testing of steel fiber reinforced, regulated-set cement concrete beam-columns has provided information relative to strain distribution during loading and ultimate flexural strains in both the tension and the compression regions. Ultimate interaction and load-curvature diagrams have been obtained for concretes containing three different percentages of steel fiber reinforcement. The behavior and failure modes of fiber reinforced concrete have been described in terms used for conventionally reinforced concrete. In particular, failure becomes more ductile as relative eccentricity increases and the failure mode progresses through compression, balanced, and tension modes. A creep test was initiated to determine the behavior of steel fiber reinforced, regulated-set cement concrete to sustained loads in concentric compression.

Durability studies included the effect of disturbance during the setting period, and exposure to high temperatures. For the particular steel fiber reinforced, regulated-set cement concretes tested, there appear to be no harmful effects from revibration such as might occur in the extruded liner system. Temperatures of 350 F and 600 F (175 C and 315 C) were found to decrease ultimate strength with increases in both temperature and length of exposure.

Field pumping studies were less than satisfactory, although insight was gained into important factors of aggregate gradation, fiber content, and the effect of reducer and elbow sections present in pump lines.

Although the setting nature of a cement is not a distinguishing factor in its pumping performance, the setting characteristics are of primary importance in the event of equipment malfunction. This situation should be critically examined prior to employment of any system utilizing quick setting concretes.

At present, the cost of steel fiber reinforced, regulated-set cement concrete is from two to four times that of plain concrete made with type 1 cement. The fiber is the major factor in the cost differential, but regulated-set cement is substantially more expensive than type 1 or type 3 cement. The cost differential of steel fiber reinforced, regulated-set cement concretes over conventional concretes must be qualified by noting that fibrous reinforcement and quick setting cements are still in the developmental stages. In any event, fibrous quick setting concretes are superior for certain applications for which the cost differential would be justified.

Research continues regarding the properties of steel fiber reinforced, quick setting cement concretes and their suitability for use in

tunnel support systems. Much information has already been acquired regarding short term behavior. Continuing studies will serve to extend this knowledge and expand its basis with regard to durability in adverse environments; performance under sustained loads; the interpretation of experimental results for the prediction of behavior and application to design; and methods for placing fiber reinforced concrete by pumping.

It is necessary to complete these studies which are underway, and expand their scope, to assure that satisfactory and reliable concretes are available for use in tunnel liner systems.

CHAPTER 4

STEEL FIBER REINFORCED CONCRETE MONOLITHIC TUNNEL LINERS

4.1 INTRODUCTION

The testing and evaluation of two circular monolithic concrete tunnel liners cast with random steel fiber reinforcement is described in this chapter. The specimens were 10 ft (3.05 m) outside diameter and 6 in. (152 mm) thick. Each specimen was loaded several times with a nonuniform radial loading consisting of active loads on two opposite sides and passive loads oriented 90 degrees from these. The passive load-deformation characteristics were varied in each loading case.

In a previous report (Parker, et al., 1971) a system for slip forming a continuous liner behind a tunnel boring machine is described. In this system a fast setting cement is used so that the liner is strong enough at any point behind the slipform to support itself and the ground. Steel fiber reinforcement is used to provide flexural strength, especially at this early age. The liner continues to gain strength after the slip-form has passed, and the loading changes on account of the effect of time on the ground, progress of the tunnel, and changes in the liner-medium interaction. The primary objective of these tests was to model the material properties of the slipformed liner at an early time, say, shortly after the slipform has passed, and at a much later time when it has gained full strength. An understanding of the structural behavior is necessary in order to determine the thickness and concrete properties for the slipform system. The results also will be helpful in understanding the behavior of other types of liners.

It was impractical to use fast setting cement and test it at an early age, since the specimen could not be prepared for testing quickly enough. Thus it was decided to use ordinary Type 1 cement and design a mix with low strength. The structural behavior would be similar to that of a liner made with quick-setting cement concrete and tested at an age for which the strength is the same.

The emphasis in selecting the loading was that it should be one which can be modeled when studying structural behavior and which can be conviently applied and controlled in the laboratory, rather than one which accurately represents the ground loading. Hence, 12 concentrated, radial loads equally spaced around the liner were elected. In a gross way the active loads represent the overburden pressure and the reaction below the tunnel. These loads are all equal. The remaining six loads, three on each side, represent the passive resistance of the ground on the sides. A linear load-deformation behavior of these "passive" loads was selected to facilitate the analysis.

The basic section behavior of a steel fiber reinforced concrete member subjected to a full range of moment-thrust combinations is described in Chapter 3. This information is adequate to define the behavior of a very simple structure. A circular continuous tunnel liner is indeterminate to the third degree if all the loads are known, and is even more complex when it is in the ground where the loads are not well defined. Also, as sections within the liner reach their moment capacity, but still have thrust capacity, the moments are redistributed and additional load can be resisted. These tests will help to improve the understanding of the mechanism of moment redistribution, determine the deformations and amount of cracking associated with it, and aid in the development of a means of predicting the ultimate capacity and appro-

priate service loads for the structure.

It was found in these tests that a circular liner subjected to loadings similar to ground loadings behaves in a ductile manner; it redistributes moments readily as the moment capacity is reached at critical sections, and it will sustain deformations of the order generally required in the ground without severe cracking which would limit the serviceability of the structure. The load-deformation behavior was highly dependent on the stiffness of the passive forces. The initial linear behavior can be predicted reasonably well with a linear analysis, but such an analysis is of little value in computing the moment redistribution or ultimate capacity of the liner.

The first specimen tested is designated C-1 and represents the early strength of a slipformed liner with a concrete compressive strength of 1640 psi (11.31 MPa). The second, designed C-2, represents the slipformed liner at a considerably later time with a compressive strength of 9300 psi (64.12 MPa).

4.2 FABRICATION AND MATERIAL PROPERTIES OF THE SPECIMENS

4.2.1 FABRICATION

The forms used to cast the specimens consist of two corrugated sheet metal cylinders (ARMCO) 123 in. OD (3.12 m) and 105 in. ID (2.67 m) shown in Fig. 4.1. The corrugated forms were lined in order to provide a smooth concrete surface and control the liner thickness. The covering material was 1/4 in. (6.35 mm) thick masonite for specimen C-1. After removing the forms it was found that the masonite at the bottom of the forms had buckled due to expansion as it absorbed water. For the second specimen 1/4 in. (6.35 mm)

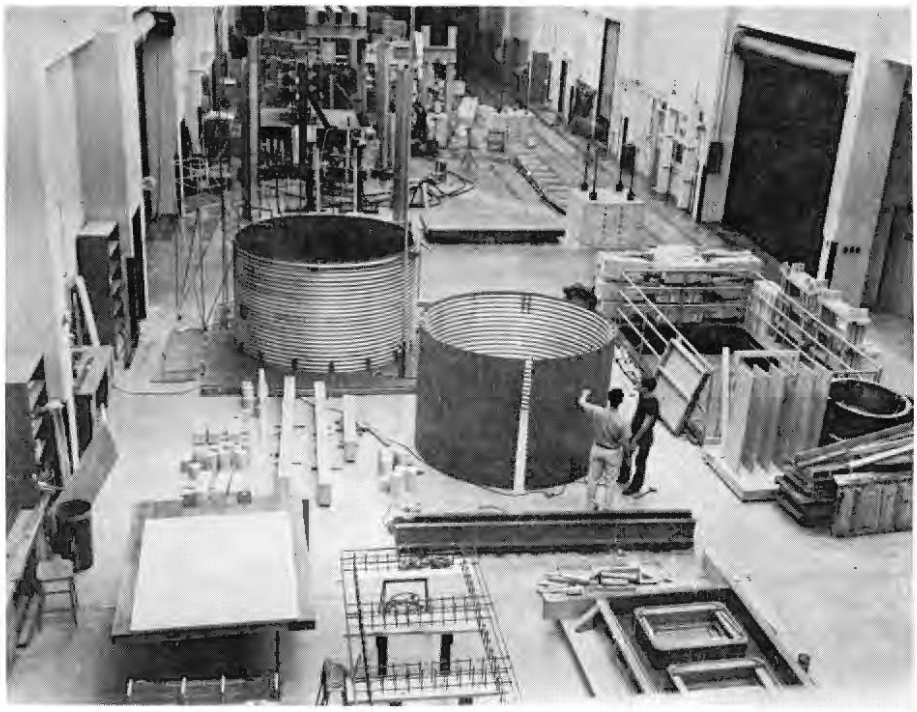

FIGURE 4.1 FORMS USED FOR CASTING MONOLITHIC LINERS

thick exterior grade plywood coated twice with waterproofing paint was used.

A vertical cut in each cylinder and a suitable connection facilitated the removal of the forms from the specimen. The connection was constructed so that it would resist the moment and could be adjusted to give geometric continuity to the form.

The two cylinders were positioned concentrically and were attached to a wood platform by clip angles welded to the cylinders and bolted to the platform. Pipes with 3/8-in. (9.53 mm) outside diameter and 6-in. (152 mm) length were placed between the two forms at midheight and near the top to maintain a constant thickness of the specimen. A rod between the forms and through the pipe held the forms together and kept the spacers in place.

The concrete was purchased from a local ready-mix plant and transported to the laboratory in a transit mix truck. The steel fiber was mixed with the aggregate before the cement and water were added. This was done by feeding the fiber by hand into the chute as the aggregates were metered into the truck. The fibers were removed from the shipping boxes and separated by hand to reduce the possibility of fiber balling during mixing. At the laboratory the slump was measured and additional water added until the desired workability was obtained. The air content, density, and control specimens were then taken.

The concrete was placed in the forms in three lifts of 2 ft (0.61 m) each. Each lift was vibrated at its midheight with two form vibrators attached to the inside form opposite one another. When the vibrators were raised for each lift, they were also rotated 90 degrees from the previous position.

The lower lift was vibrated approximately 30 seconds and the top lift about 45 seconds in specimen C-1. The top lift of specimen C-2 required about 60 seconds of vibration as the concrete was becoming stiff. An overview of the casting operation and form vibrators is shown in Fig. 4.2.

4.2.2 MATERIAL PROPERTIES

For both specimens, 4-1/4 cy (3.25 m^3) of concrete was mixed with Type I cement and 1.5 percent steel fiber by volume or 200 lb/cy (119 kg/m^3). The basic mix is shown in Table 4.1. A summary of the properties of the resulting concrete is shown in Table 4.2. The same basic mix was used for two specimens; however, a considerable amount of air-entraining agent was added to specimen C-1. This successfully reduced the strength and the

TABLE 4.1

MIX PROPORTIONS FOR MONOLITHIC LINER SPECIMENS*

Pea gravel, lb (kg)	=	1075	(488)
Sand, lb (kg)	=	1580	(717)
Cement type (1), lb (kg)	=	800	(363)
Water, lb (kg)	=	342	(150)
Steel fibers, lb (kg) (1.5% by volume)	=	199	(90)

*Quantities for 1 cu yd batch (0.765 m^3)

modulus of elasticity in approximately the correct proportion and resulted in a satisfactory mix. The ratio of modulus of rupture to $\sqrt{f'_c}$ based on the maximum load on the flexure specimen is about 14.5 for the low-strength

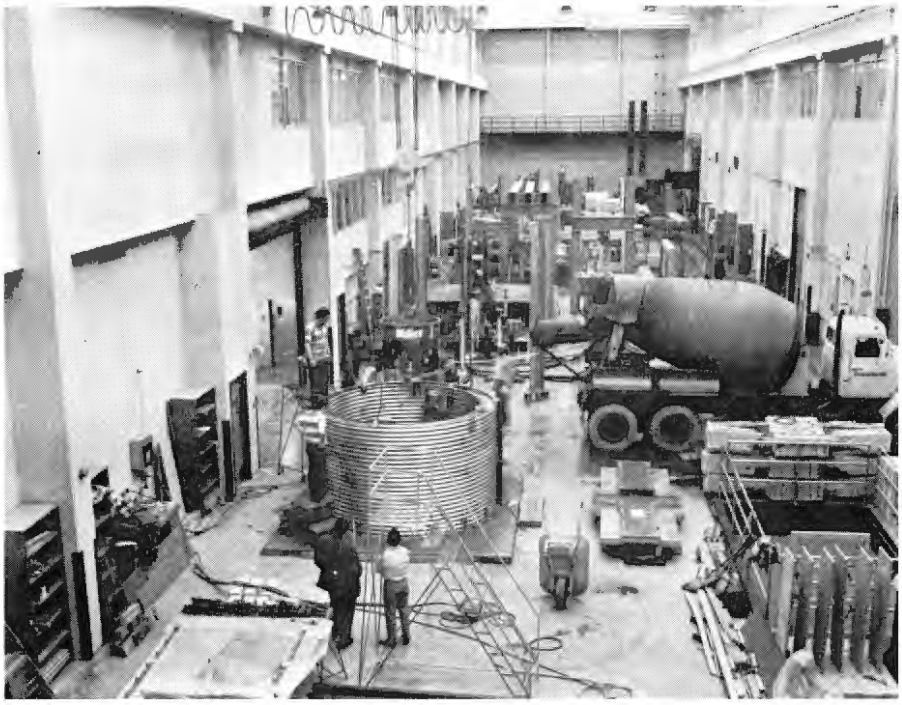

(a) Mixing and Placing of the Concrete

(b) Filled form with one of the form vibrators

FIGURE 4.2 PHOTOGRAPH OF CASTING OPERATION

TABLE 4.2

SUMMARY OF MATERIAL PROPERTIES FOR SPECIMENS C-1 AND C-2

Specimen	Slump, in. (mm)	Entrained air, percent	Unit weight, lb/cu ft (kg/m^3)	Compressive strength, psi (kPa)	Modulus of elasticity, ksi (MPa)	Modulus of rupture[1] psi (kPa)	Splitting tensile stress[2] psi (kPa)
C1	5-3/4 (146)	13.2	not taken	1640 (11307)	1500 (10342)	585 (4033)	300 (2068)
C2	4-3/4 (121)	1.4	150 (2400)	9300 (64121)	3900 (26890)	1590 (10963)	1000 (6895)

[1] Taken as the average of six tests on beams 6 x 6 x 21 in. (152 x 152 x 533 mm).
[2] Taken as the average of six tests on 6 x 6 in. (152 x 304 mm) standard cylinders.

concrete and 16.5 for the high-strength concrete; this represents roughly a 100 percent increase in modulus of rupture over plain concrete. The modulus of elasticity of the low-strength mix has a value 40 to 50 percent lower than that given by the ACI formula. However, it does agree rather well with the modulus of elasticity obtained for a regulated-set cement concrete at an early age. Compression tests on regulated-set cement concrete at a compressive strength of about 1600 psi (11.03 MPa) show a modulus of elasticity of 1700 ksi (11.72 GPa) (Peck, et al., 1973). The model mix had a modulus of 1500 ksi (10.34 GPa) and a compressive strength of 1640 psi (11.31 MPa).

A strength-time curve for the materials in the two specimens is shown in Fig. 4.3. Each point represents the average of two compression tests on 6x12-in. (152x304 mm) standard concrete cylinders, except for the last point which is the average of six specimens. Specimen C-1 was tested at 86 days (control cylinders at 100 days) and C-2 at 120 days. At the time of the test the curve is rather flat and therefore the strength obtained is probably reasonably representative of the strength in the specimen. Curing of the specimen and the cylinders should have been similar, as the thickness of the specimen was comparable to the size of the cylinders. In both cases the forms were removed after one day and the specimens were covered with burlap and vinyl sheeting and kept moist for seven days, after which the cover was removed and further curing was in the air of the laboratory which is maintained at approximately 50 percent relative humidity. From Fig. 4.3, it can be observed that the strength increase for specimen C-2 changed after the wet burlap was removed at seven days. There is not adequate data at seven days to see the effect of this change in the curing rate for specimen C-1. Representative stress-strain curves for 6 x 12-in. (152 x 304 mm) standard cylinders for

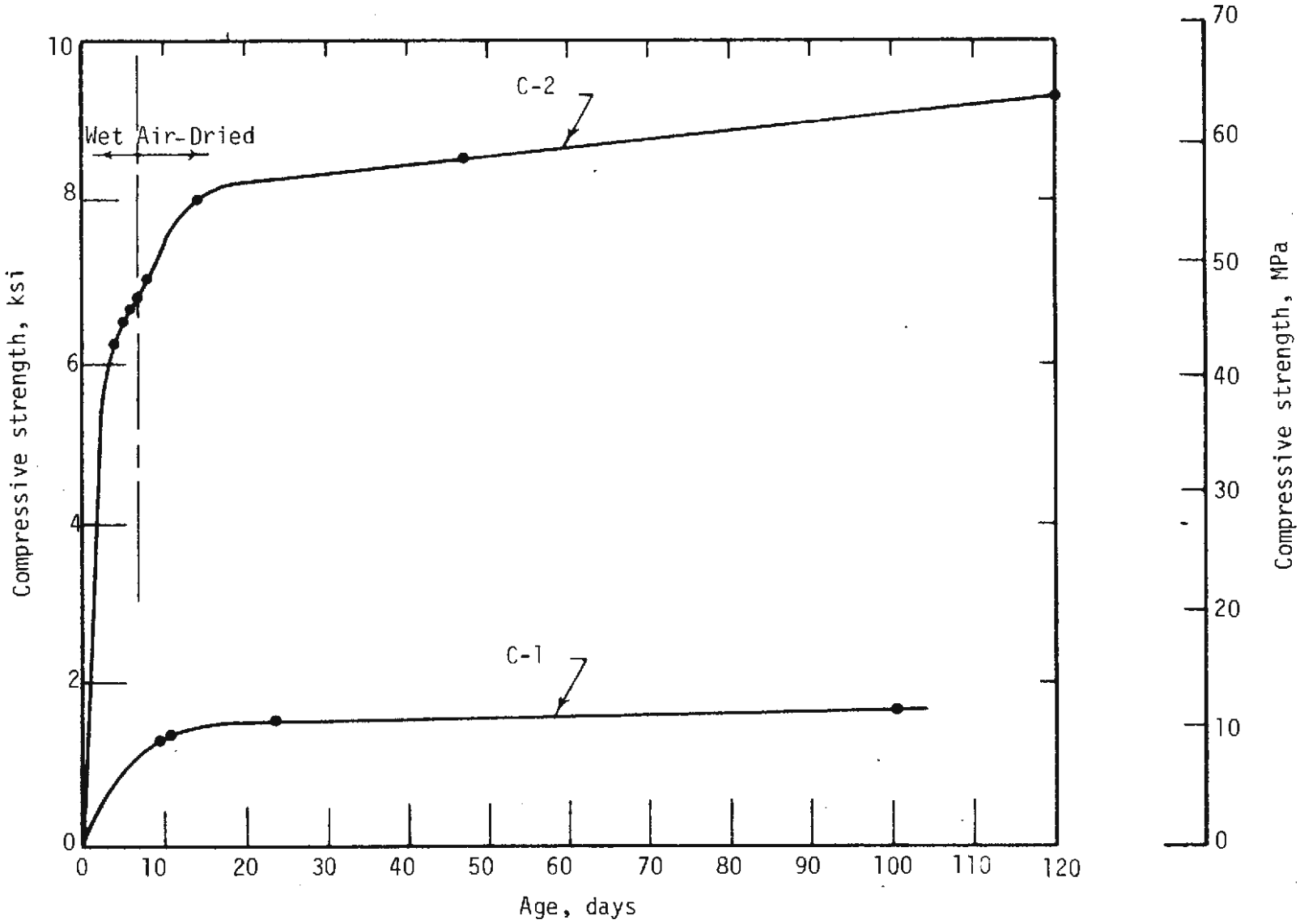

FIGURE 4.3 STRENGTH-TIME RELATION FOR THE CONTROL CYLINDERS FOR SPECIMENS C-1 AND C-2

the two mixes are shown in Fig. 4.4. The low-strength concrete has a much more ductile curve. The initial modulus values are shown on the curve, and it may be observed that the curve is linear up to somewhat less than one-half f'_c for the high-strength mix and somewhat more than that value for low-strength mix. These particular curves were obtained from continuous recording of load-deformation on an X-Y recorder. The strain was measured over a four-inch (102 mm) gage length at the center of the specimen using a compressometer with a linear variable differential transformer to obtain the deformation. Also, it was obtained with a rather low rate of strain (0.00083/min) and with a very stiff testing machine placed on controls which kept the head movement constant. It was only in this way that the downward slope of the stress-strain curve for the stronger concrete could be obtained. It should be noted that this part of the curve is quite variable and depends upon the strain rate used and the stiffness of the testing machine.

In order to investigate the fiber distribution in the specimens, vertical and horizontal saw cuts were made near the bottom, midheight, and top of the specimen after the tests were completed. Fibers were counted in a 1 by 1-in. (25.4 mm) grid 4 in. (102 mm) wide and 6 in. (152 mm) through the specimen thickness or over 24 $in.^2$ (15484 mm^2). The results of these fiber counts are shown in Fig. 4.5 where the fiber counts per square inch are the average of the four square-inches (2581 mm^2) counted at each depth through the thickness.

The volume of fibers in the matrix is related to a theoretical fiber spacing which can also be related to the average number of fibers counted on a cut across the matrix (Romualdi and Mandel, 1964). A comparison of the actual fibers counted on several cut faces is an indication of

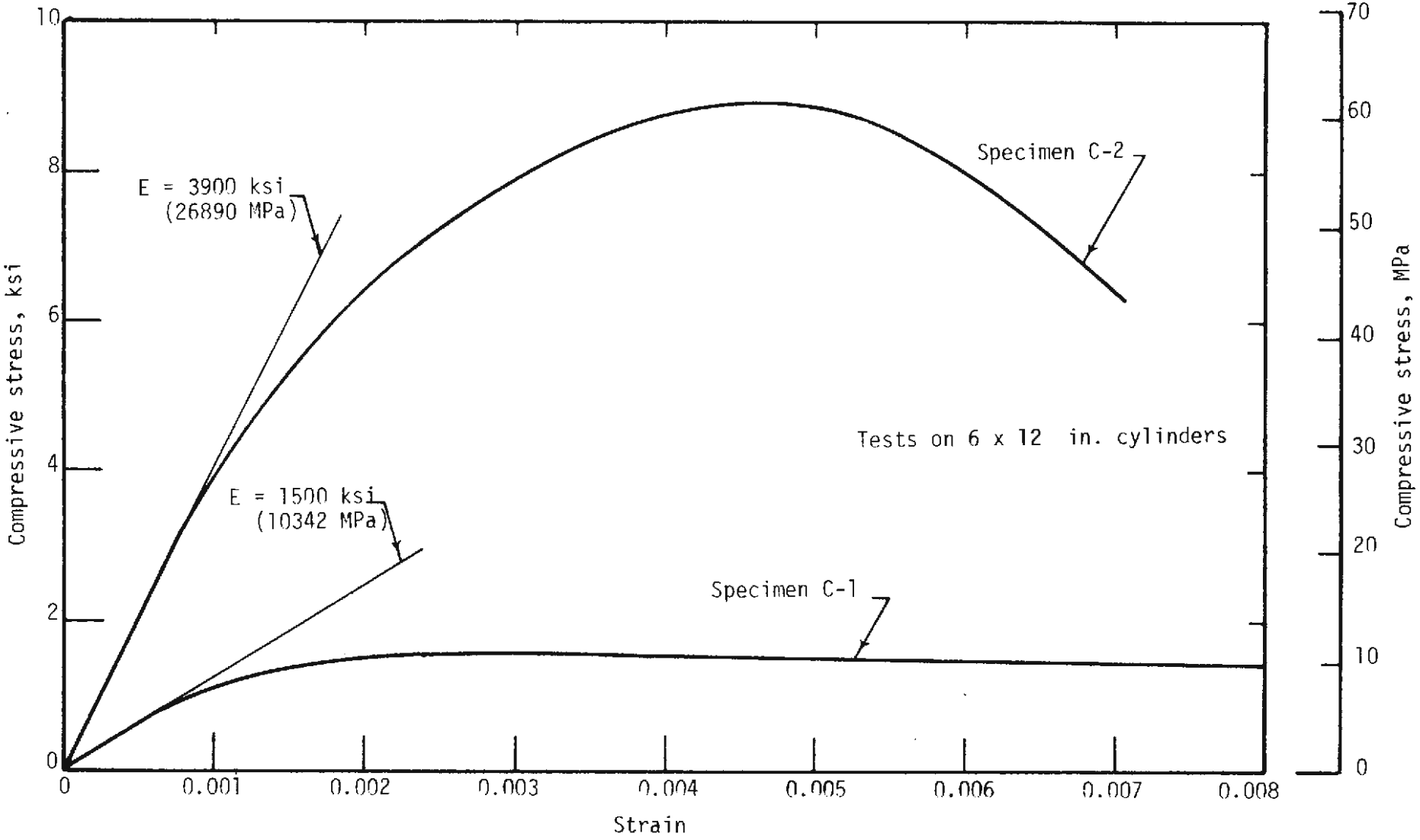

FIGURE 4.4 COMPRESSIVE STRESS-STRAIN CURVES FOR CONTROL CYLINDERS

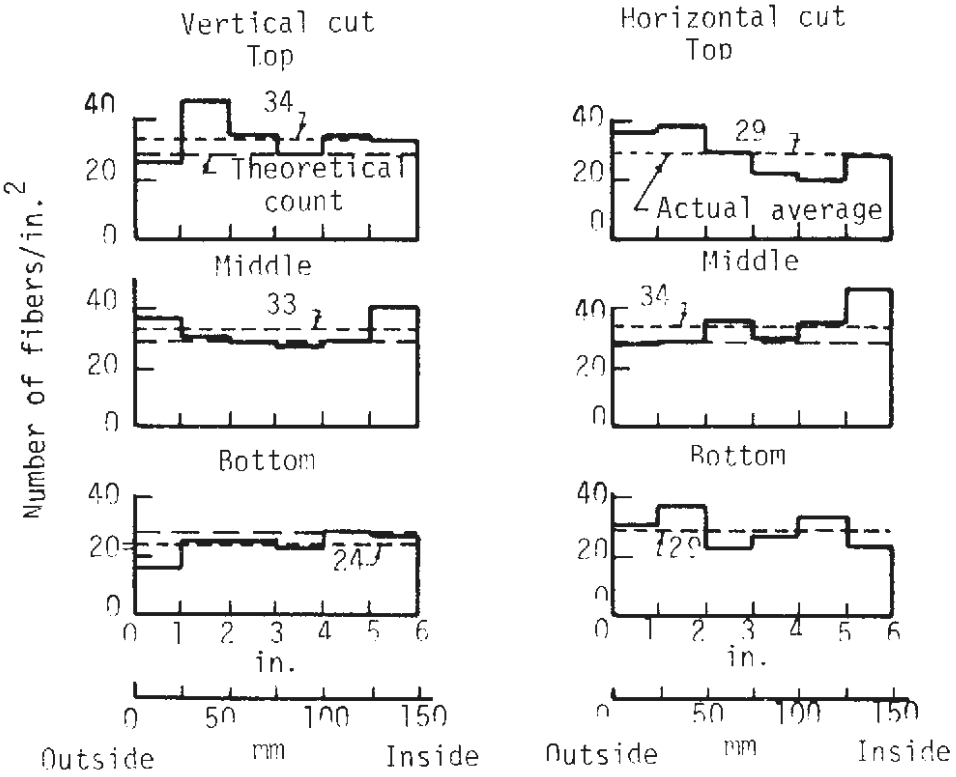

(a) Fiber counts on the cut surface for specimen C-1

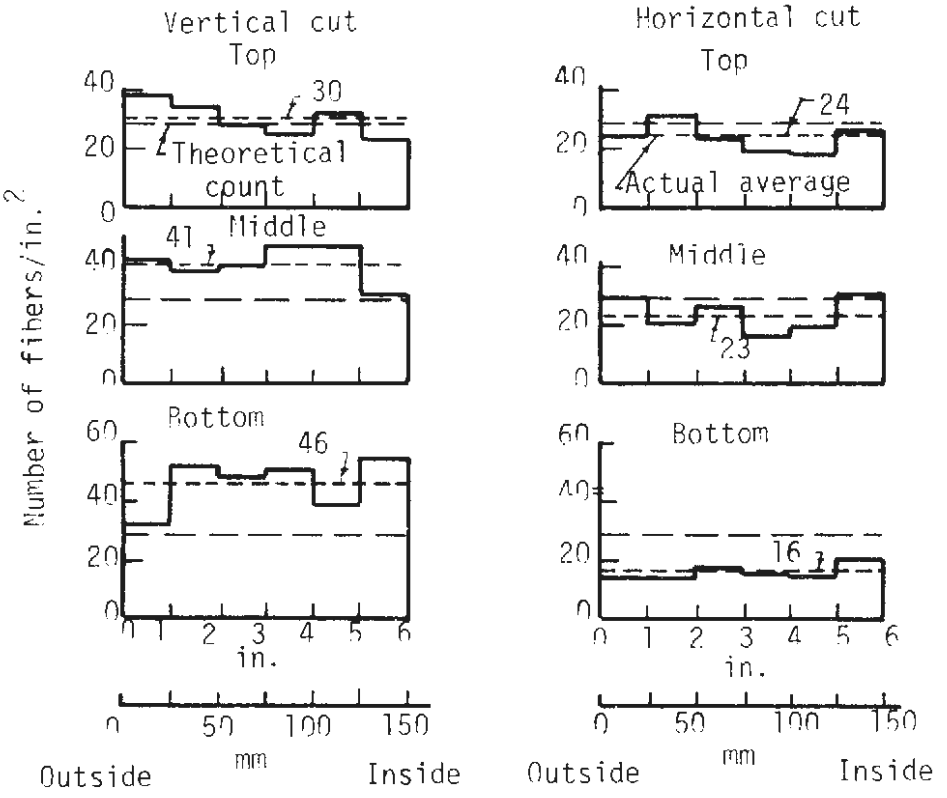

(b) Fiber counts on the cut surface for specimen C-2

FIGURE 4.5 FIBER DISTRIBUTION IN THE MONOLITHIC LINER SPECIMENS

the homogeneity of the specimen. A comparison of these counts with the theoretical counts provides an estimate of the overall uniformity, because the proper total weight of the fiber was placed in the mix and a greater-than-theoretical count in one region must result in a lower count elsewhere. In addition, comparing the fibers counted on adjacent vertical and horizontal cuts gives an indication of preferred orientation. If there is a preferred vertical orientation, a large number of fibers will be counted on a horizontal cut. The horizontal and vertical cuts refer to the as-cast position of the specimen.

The theoretical average fiber count is given by the formula (Romualdi and Mandel, 1964):

$$n_w = 0.0041\ p/A_f \qquad (4.1)$$

where n_w = number of fibers on a cross section per unit area; p = volume of fiber expressed as a percent of the total volume; A_f = cross sectional area of the fiber in units that determine the unit area for n_w. In this formula only 41 percent of the fibers are considered to be effective, and for 1.5 percent fibers the theoretical count per $in.^2$, n_w, is found to be 28 and the theoretical spacing is 0.19 in. (4.83 mm).

There was no definite trend in distribution of fibers for specimen C-1, either through the height of the specimen or through the thickness. All average fiber counts are within a reasonable range of variation, and without a large number of counts no definite statement can be made on a statistical basis. Through the thickness, the largest range from highest to lowest counts is 21 and the smallest is 12. Previous fiber counting of cuts on 4x8-in. (102x204 mm) cylinders has shown a tendency for fibers to

concentrate near the externally vibrated form. The large specimens were vibrated only on the inside form. There is no definite indication that the form vibration caused concentration of fibers in C-1. Also, there does not appear to be a preference in orientation, as the counts on vertical and horizontal cuts were rather close at each level.

The fiber counts in specimen C-2, however, show some trends. This specimen required a longer time to cast and the last lift required much more vibration due to loss of slump; this may explain the trends. There are more fibers counted on vertical cuts than horizontal cuts for the bottom and midheight sections indicating a preference to horizontal orientation. The concrete at these levels received more vibration than the top level which does not show this marked difference. If this trend is typical around the specimen it would indicate an increased tensile strength of the concrete in the circumferential direction. From Eq. 4.1, the average equivalent fiber content is 2.1 percent by volume for the fiber count on a vertical cut, as compared to the average distribution of 1.5 percent. The distribution appeared to be uniform from top to bottom as the high counts on vertical cuts are offset by low counts on horizontal cuts. The theoretical sum of counts on adjacent vertical and horizontal cuts is 58, and the sums for specimen C-2 varied between 54 and 62.

After the liners were tested, prisms were cut from them for compression and flexure tests. Two prisms approximately 6x6x12 in. (152x152x304 mm) were tested from each specimen and gave average compressive strengths of 1650 psi (11.38 MPa) for C-1 and 9610 psi (66.26 MPa) for C-2. These values compare quite well with the compressive strengths given by the control cylinders. The corresponding average Young's modulus values were 1.38×10^6 psi (9.51 GPa)

and 4.35×10^6 psi (30.0 GPa). The prisms for compression and flexure tests were cut vertically from the specimens which is not the direction in which the liner specimens resisted load. In compression this is not important, but in flexure the strength is more sensitive to the fiber orientation. One flexure test from each specimen gave values of modulus of rupture of 115 psi (793. klp) for specimen C-1 and 705 psi (4.68 MPa) for C-2. These strengths are much lower than those obtained from control beams, possibly because of fiber orientation as discussed above. The strength of the beams tested would depend on the fiber count on a horizontal cut. Another possible reason was that the concrete was damaged when the liner was tested, though the prisms were cut from the liner near the quarter point where the least damage would have occurred.

4.3 TESTING PROCEDURE

Loads were applied to the specimens at 12 equally spaced locations 30 degrees apart with two 60-ton (54.55 metric tons) jacks at each location as shown in Fig. 4.6. The jacks were located 1-1/2 ft (0.46 m) and 4-1/2 ft (1.37 m) above the bottom of the specimen and applied load to the test specimen through a ball joint to a spread beam as shown in Fig. 4.6. The jack reactions were resisted by concrete abutments bolted to the test floor as shown in Fig. 4.7. The spread beam was an W8X48 with length equal to the height of the specimen. A cylindrical bearing was placed between the jack and abutment to prevent transfer of tangential force to the specimen. This cylindrical seat was removed at the N, S. E and W locations when specimen C-2 was tested. The spread beam was grouted to the specimen to assure uniform bearing.

The weight of the specimen rested on nests of rollers between steel plates located 90 degrees apart and oriented to roll in the radial direction.

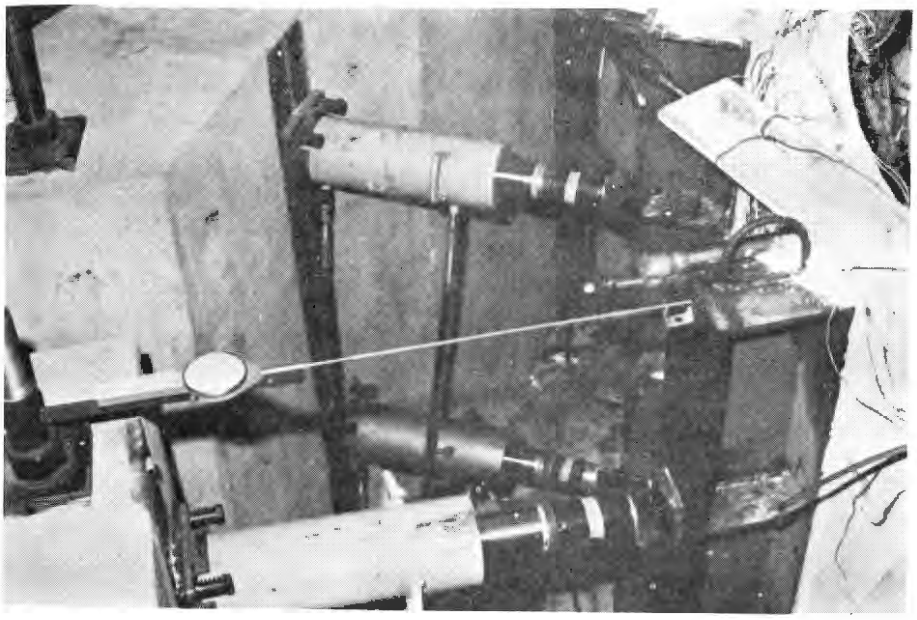

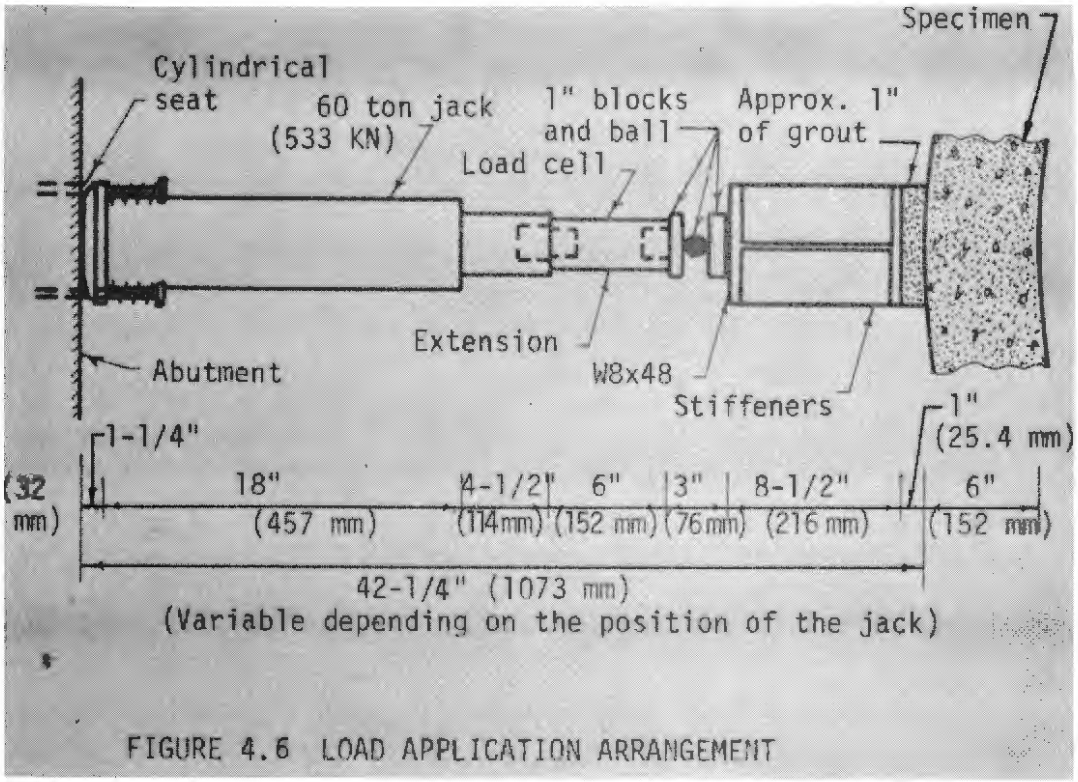

FIGURE 4.6 LOAD APPLICATION ARRANGEMENT

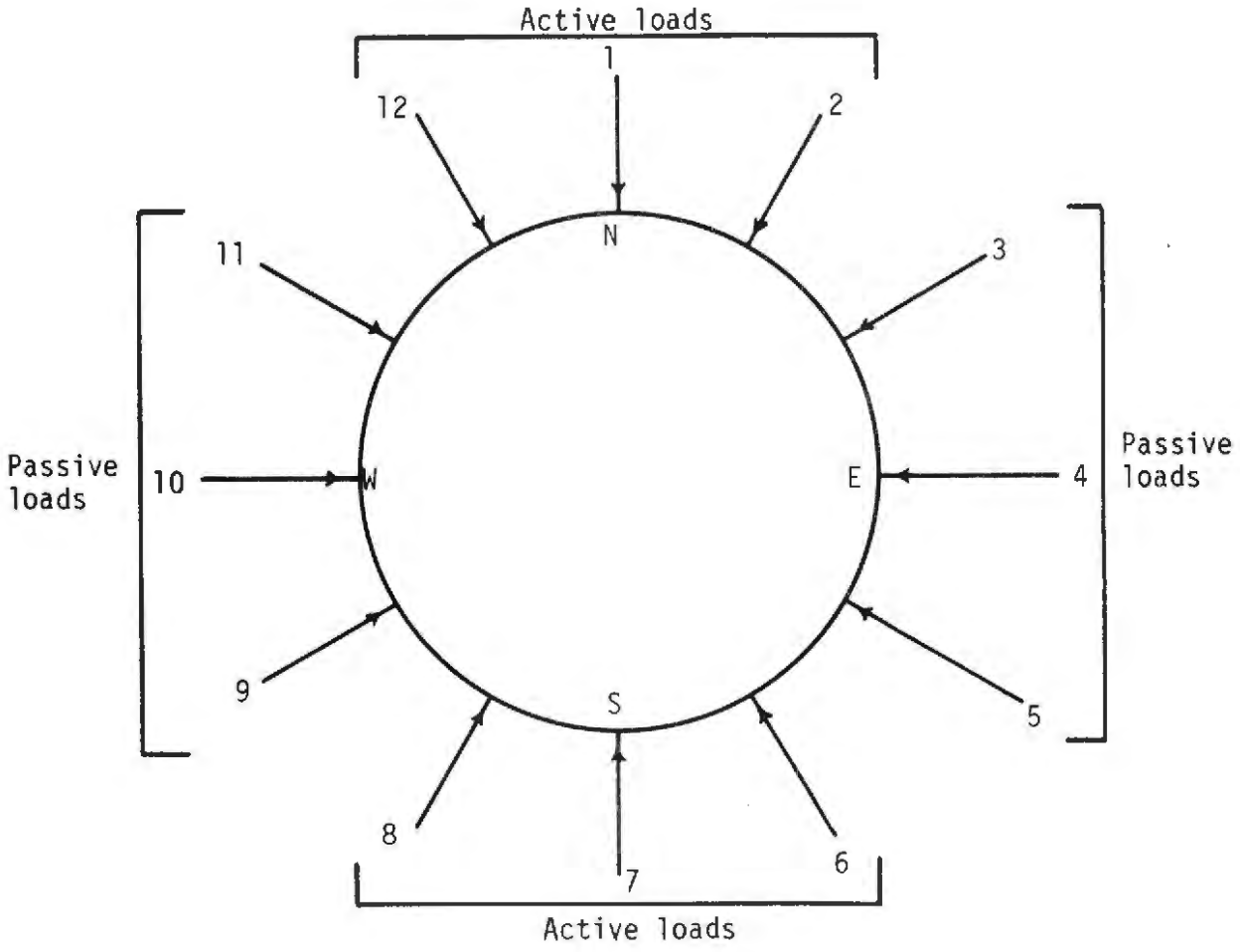

FIGURE 4.7. OVERALL LOADING SYSTEM WITH SPECIMEN

These rollers were quite free, but in both tests the specimen lifted off the rollers slightly so that the friction at the bottom was completely eliminated. This occurred because of a slight upward component of force by the jacks as they rotated because of a small displacement of the abutments. This had the disadvantage that the weight of the specimen was applied vertically (laterally) to the jacks and increased the friction in them between the piston and cylinder. This probably contributed to a small nonsymmetry of the loading.

Three loads centered around the north direction and three around the south, consisting of 12 jacks, applied active loads to the specimen (Fig. 4.7) and were connected hydraulically so they had the same load except for friction between the piston and cylinder of the jacks. The loads on one side may be considered the active overburden load at the crown while those on the opposite side are the reaction at the invert. The six loads on the remaining two sides, consisting of 12 jacks, were adjusted to represent the passive resistance of the ground on the sides of the tunnel liner specimen. The load positions have been numbered as shown in Fig. 4.7 for purposes of discussion. The figure also contains a photograph of the overall loading system.

All passive loads in both tests were adjusted so that they would have a linear load-deflection relationship. This control was accomplished by connecting the load point displacement to the X axis and the jack load to the Y axis of an X-Y recorder so that the load and displacement could be continuously monitored. The load-deflection relationship desired was drawn on the graph paper of the recorder and during application of active load the passive load was adjusted so that the pen of the recorder followed the predetermined line. The loads were adjusted by manipulating

the jack pressure with a manual pump and a microflow hydraulic valve. This procedure was followed in both tests, but the details of the execution varied slightly.

For the first loading of specimen C-1 deflection was measured relative to the floor for each passive load point, and each passive load-deflection relationship was controlled separately. This required six X-Y recorders and 6 hydraulic control systems. Slight inaccuracies in the control on opposite sides of the specimen disturbed the equilibrium of the specimen and caused it to move around excessively. In subsequent loading of specimen C-1 passive jacks 4 and 10 were connected hydraulically as were 3, 5, 9 and 11 (Fig. 4.7). Also, the opposite displacement measuring devices were connected electronically so the measured displacements would be added, although the measurements were still made relative to the floor. This procedure eliminated the error in passive jack control from rigid body motion of the specimen, but some error still occurred because the specimen movement allowed the core of the LVDT to bind in its housing. Deflections at locations 4 and 10 were used to control the load in the corresponding jacks, while locations 3 and 9 were used to control the load in the other four positions. This was equivalent to assuming that the displacement on the diameter 5-11 was the same as for 3-9. This is reasonable since the loads at those locations were the same. By this method only two X-Y recorders were required, and load control was much easier.

The rigid body movement of specimen C-1 during loading was not eliminated by the change in passive jack controls or by more accurate alignment of the jacks. A tendency to rotate seemed to be the most severe problem. Prestressed restraining cables were attached to the pick-up anchors in the

top of the specimen 120 degrees apart, and to the hold-down bolts on top of the abutments. They were oriented approximately tangent to the specimen so the radial component of load applied to the specimen was relatively small, but they resisted the unbalance of forces in the tangential direction. A small misalignment of any jack caused a tangential component of force which caused a small rotation of the specimen. This resulted in a small tangential component of force from all the jacks. If the movement could be prevented, only the original small force must be resisted. The forces in the cables were not measured. It was possible to compensate for rigid body movement of the specimen by restricting the movement of certain jacks with the valving system, so the movement could be kept to a minimum, but there was no way to compensate for rotational movement.

The hydraulic loading system and jack alignment were arranged so that the specimen should be in equilibrium. Thus the forces resisted by the restraining cables result from unequal friction in opposing jacks and slight misalignment of the jacks. Some of the loadings of the specimen were terminated because of breaking of cables, but the cable capacity was relatively small compared to the loads on the specimen.

When specimen C-2 was tested the hydraulic connections and the displacement controls remained the same, but the diameter changes were measured directly with one LVDT rather than adding the measurements at the ends of the diameter from 2 LVDT's. In this way the error from rigid body movement was completely eliminated.

The loading arrangement used in these tests ideally should cause only radial movement of the crown, invert and springlines. Thus the test arrangement for specimen C-2 was changed by placing brackets at these loca-

tions to allow movement only in the proper direction. A bracket, shown in Fig. 4.8, was placed at midhieght of the specimen to prevent tangential movement of the load spread beam. Rollers between the bracket and spread beam allowed radial movement. Also, a system was devised for more accurate radial orientation and placement of the jacks. Once the jacks were properly aligned and movement was not allowed to begin, the brackets were required only to resist unbalance of forces caused by friction in the jacks.

Load increments were applied by pumping the active jacks while the passive jacks were adjusted. Once the load was attained all hydraulic valves were closed while instrumentation readings were taken. This required from 15 to 30 minutes and, at high load levels, the creep of the specimen and loss of hydraulic fluid in some cases allowed some loss of load. Loads were therefore read at the start and at the end of the instrumentation readings, and, in general, the average of these load readings was used.

4.4 INSTRUMENTATION

STRAIN MEASUREMENTS

Surface strain measurements on both specimens were concentrated at midheight of the specimen and in the northeast quadrant. Additional strains were measured near the top and at other locations around the specimen. These strains provided a means of determining the internal forces within the specimen by using the strain at the quarter points, that is, northeast (NE),

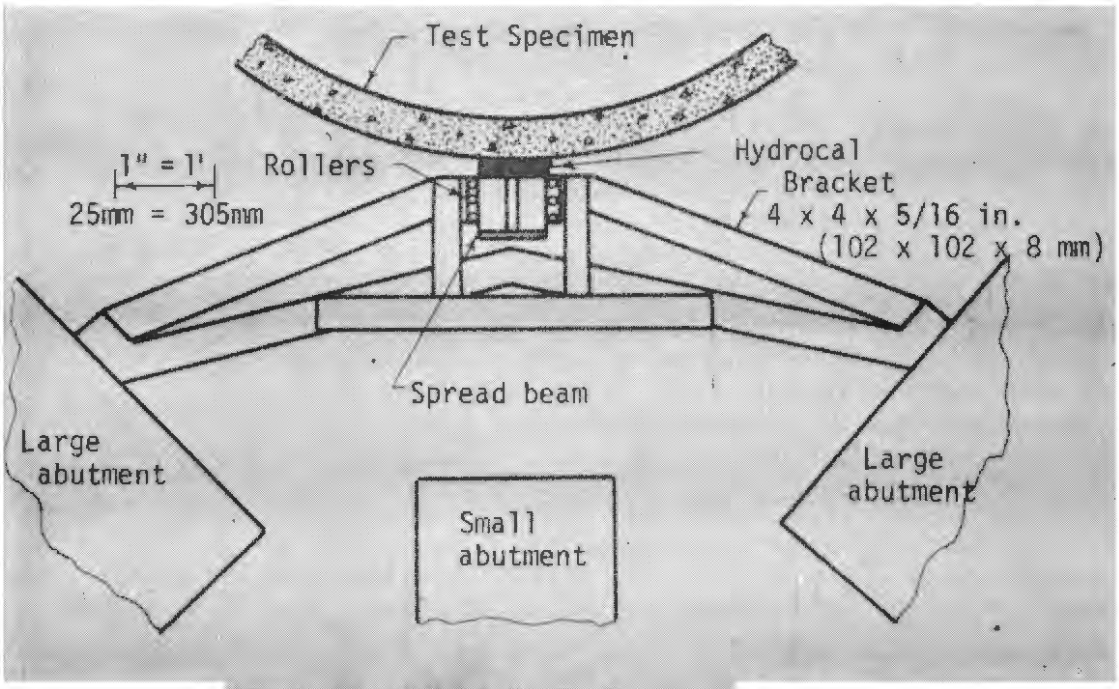

Brackets used at N, S, E and W

FIGURE 4.8 BRACKETS USED TO RESTRAIN MOVEMENT OF SPECIMEN C-2

southeast (SE), etc., to compute the moment and thrust at these sections. It was then possible to compute the internal moments and thrusts at other sections within the specimen from equilibrium. The quarter points were selected for the measurements because they are near the inflection points and therefore have small bending stresses; also it was expected that the strains due to axial thrust would be small. There would be no cracking at these sections, and the strains would probably remain within the linear stress-strain range.

In specimen C-1 it was found that there was considerable variation in the strains measured at the quarter points; therefore, in specimen C-2 a considerably larger number of strain gages was placed at these locations in order to increase the reliability of the computed moments and thrusts. In specimen C-2, six strain gages were placed on the outside surface and six on the inside surface at each quarter point distributed vertically along the specimen. One-inch electrical resistance paper-backed gages were used.

DEFORMATION MEASUREMENTS

For the testing of specimen C-1, 12 linear variable differential transformers (LVDT's), one at each load point, were attached to stands grouted to the test floor. As discussed in Section 4.3, this was changed for specimen C-2 to six LVDT's to measure diameter change directly at all six loaded diameters with the arrangement shown in Fig. 4.9.

Mechanical dial gages were used on the outside of the specimen to measure deformation of the liner relative to the abutments at the load spread beams. These gages were placed at the top of the spread beam at all load

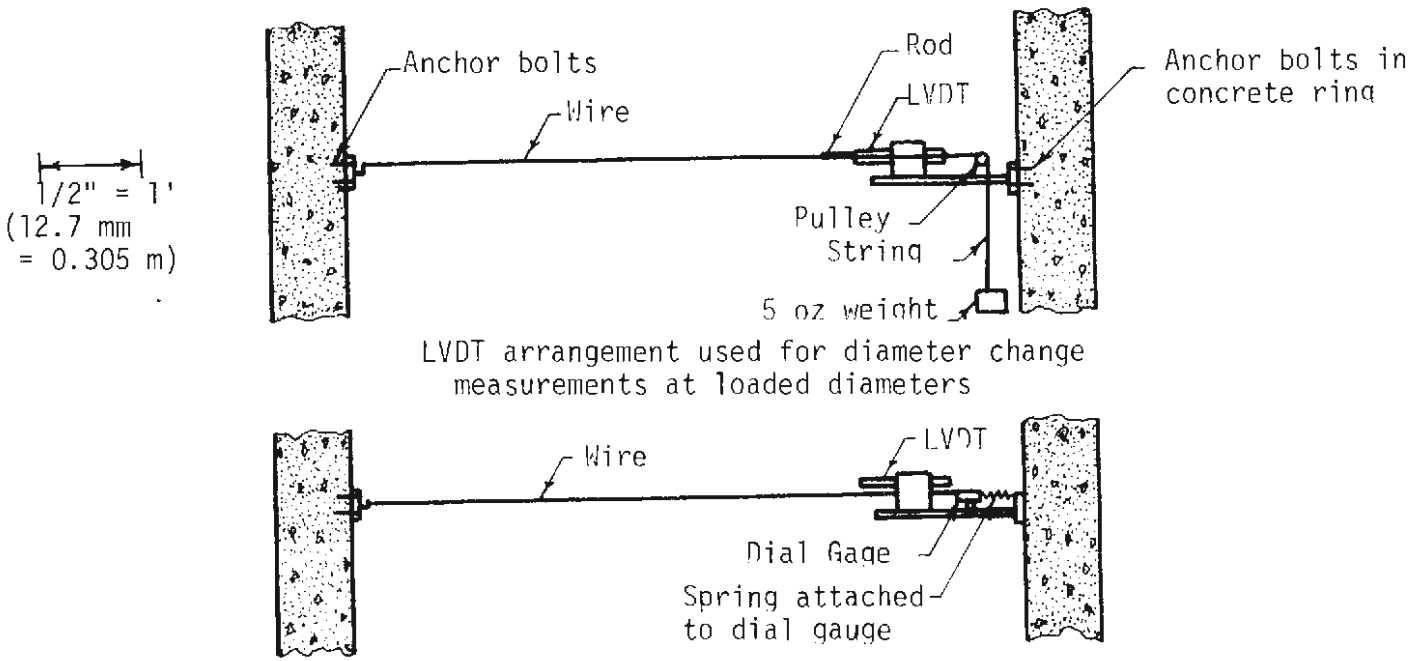

FIGURE 4.9 DEVICE USED TO MEASURE INTERNAL DIAMETER CHANGE

points in specimen C-1, and additional gages were placed at the bottom for specimen C-2. In addition, mechanical dial gages were placed inside the specimen to check the measurements made by the LVDT's. On specimen C-2 dial gages were placed in parallel with the LVDT's to measure diameter change in the NS and EW directions with the arrangement shown in Fig. 4.9. Because of the tendency of the specimen to rotate, tangential movement of several points around the specimen were also monitored with dial gages.

Dial gages were used to measure the deflection of the top of two abutments relative to the test floor during the testing of specimen C-2. These gages were placed on the west and northwest abutments near the top. This was done to determine the abutment deflection in order to correct the external specimen deflection measurements which were relative to the abutments.

These dial gages were used to measure the bending deformation of one of the loading spread beams in specimen C-2 by attaching a bar to the beam at the load points and measuring the deformation of the beam relative to the bar. The purpose was to determine the spread beam deflection which affects the distribution of force along the height of the specimen. Gages were placed at the center and one foot (0.305m) from each end of the 6 ft (1.83m) beam. It was determined that the deformation of the spread beams was negligible.

LOAD MEASUREMENT

The loads applied by each of the 24 jacks was measured by load cells placed between jacks and the spread beams as shown in Fig. 4.7. The loads were recorded at each increment by automatic reading equipment, and

loads on selected passive jacks were used to control the load-deformation characteristics of the jacks. The sensitivity of the load measurements is indicated by the calibration factors which averaged 68 microinches of strain per kip of load (388 micromilimeters of strain per kN of load).

PROCESSING OF DATA

All measurements were taken at each load increment. The output of the LVDT's, strain gages and load cells were connected to automatic switching and balancing equipment. The sequence of reading consisted of first the load cells, then the LVDT's and strain gages and finally the load cells again. The changes in voltage read by the balancing and reading equipment were automatically recorded by a teletype which produced a punched paper tape and typed copy. The data were then transmitted to a computer where the raw data were converted to more usable information and transmitted back to the test site immediately. In this way the information obtained for one loading increment could be used to plan the next. The returned information consisted of the deformations measured by the LVDT's, jack loads, and the strains measured at the quarter points converted to moments by using a predetermined modulus of elasticity for the material. The program then automatically calculated the thrust and moment at the crown and springline by isolating free-bodies from the structure and summing forces and moments.

Since the program did not reject strains which might result from poor measurements or bad strain gages at the quarter points. Some error resulted in the calculation of moments. For this reason the strains were later visually scanned and those values which were obviously in error were

rejected. These strains were again used in the computer program to obtain final values of the internal moments and thrusts.

4.5 TEST RESULTS

In this section results of the tests are presented; the next section contains a comparison of the results and a discussion of the behavior. Six tests were performed on specimen C-1 with different passive jack stiffnesses; only the last three were considered useful because of the problems of loading discussed in Section 4.3. Specimen C-2 was also loaded 6 times, and in this case, data from 4 tests with different passive stiffness will be discussed. The tests are summarized in Table 4.3.

4.5.1 SPECIMEN C-1

The first loading of specimen C-1 ended with the sudden movement of the specimen to the NE. A nonuniform loading resulted that caused slight cracking of the specimen. The locations of these initial cracks are shown in Fig. 4.10. The second test also ended because of instability of the specimen, and the third because of a leak in the active jack system.

There was a tendency for rotation in the clockwise direction during test T-4 that increased in rate during the last two increments of load. At an active jack load of about 58 kips (258 kN) the specimen became unstable and rotated clockwise.

For loading T-5, the test proceeded smoothly and without significant movement of the specimen until an active load of 128 kips (569·kN) at which time the specimen rotated.

TABLE 4.3

SUMMARY OF MONOLITHIC LINER TEST RESULTS

Specimen	Test	Average passive jack stiffness, K/in. (MN/m)	Maximum average active load, kip, (kN)	Maximum diameter change, in. (mm)	
				E-W	N-S
C-1	T-4	1300 (228)	38 (169)	0.071 (1.88)	0.080 (2.03
	T-5	620 (109)	128 (569)	0.388 (9.86)	0.485 (12.3)
	T-6	50 (8.76)	45 (200)	4.08 (104)	4.17 (106)
C-2	T-1	20000 (3503)	70 (311)	0.011 (0.28)	0.054 (1.37)
	T-2	1300 (228)	141 (627)	0.131 (3.33)	0.211 (5.36)
	T-5	2500 (438)	113 (503)	0.207 (5.26)	0.268 (6.81)
	T-6	510 (89.3)	206 (916)	1.05 (26.7)	2.74 (69.7)

A low passive jack stiffness was used for test T-6, and the specimen was loaded to failure. There was some rotation and translation which continued throughout the test, and the presence of additional forces from the restraining cables due to this movement should be kept in mind. At the end of increment 5 which corresponded to an average load of 25 kips (111 kN), at each active load point considerable cracking became visible. Prior to this load no cracking could be seen from 5 (1.53 m) to 10 ft (3.05 m) away although there may have been some present. Because of the high loads, and the possibility of sudden movement of the specimen, breaking of cables, and the jacks kicking out, it did not seem advisable to search for cracks close to the specimen. The specimen continued to resist additional load to an average load of 44 kips (196 kN) at each active load point with a change in diameter greater than 4 in. (102 mm).

The cracks which developed in loading T-6 continued to open until failure. An overall view of the failed specimen is shown in Fig. 4.10 (a), where the crack locations and final deformation is shown. The drawing in Fig. 4.10 (b) gives greater detail of crack locations. In general, tension cracking occurred on the inside near the N and S sections and outside near the E and W sections as shown in Figs. 4.11 and 4.12. Also, there was crushing of the concrete on the inside opposite the major tension cracks at the W section as shown in Fig. 4.12 (c). The E and W cracks are about 10 degrees N of the E and W load spread beams. This resulted from high loads in the E and W jacks which reduced the moment at these locations due to overall bending and shifted the maximum curvature toward the quarter point.

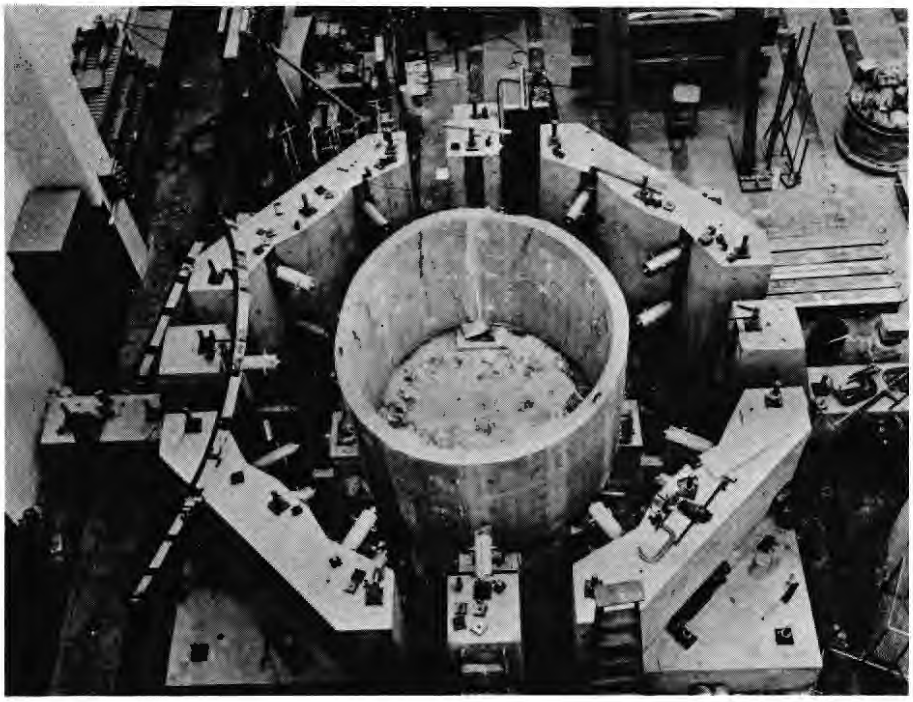

(a) General view of failed specimen

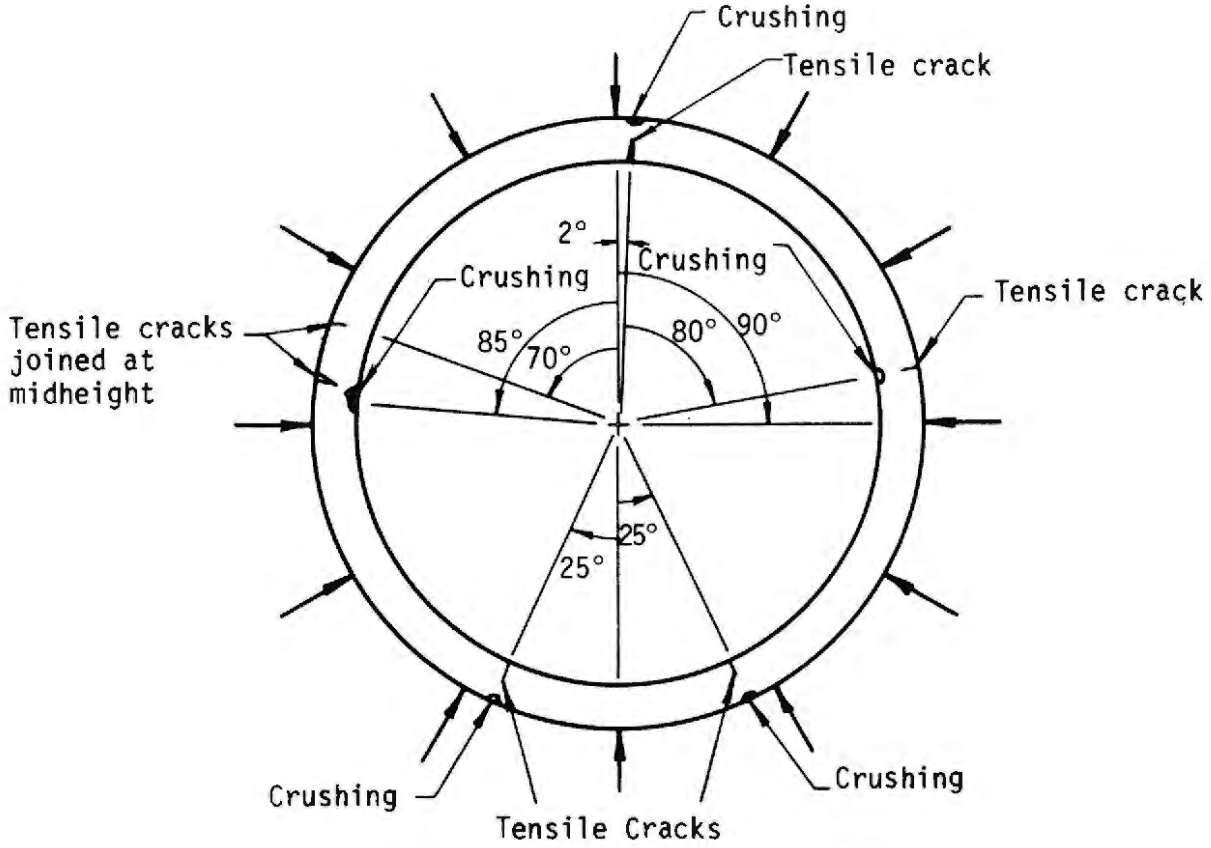

(b) Crack locations after failure

FIGURE 4.10 CRACK LOCATIONS AND PHOTOGRAPH OF SPECIMEN C-1 AFTER FAILURE

(a) North side

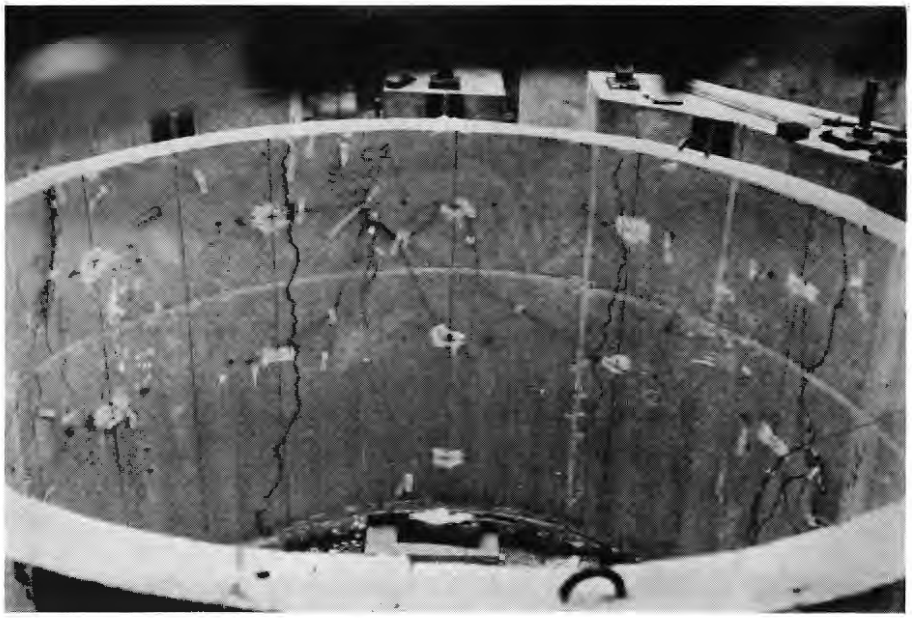

(b) South side

FIGURE 4.11 PHOTOGRAPHS OF CRACKS INSIDE SPECIMEN C-1 AFTER FAILURE

(a) North-east outside

(b) North-west outside

(c) West inside

FIGURE 4.12 PHOTOGRAPHS OF CRACKS IN SPECIMEN C-1 AFTER FAILURE

At the N section cracking occurred near the spread beam, while there were two cracks near the S section which were 20 to 30 degrees on each side of the S spread beam (Fig. 4.10). This occurred because the active loads on the N side were fairly uniform at the initial cracking load while the center active load on the S side was smaller.

The actual stiffness of the passive jacks was determined after the test by plotting the passive loads against their corresponding deflections, drawing a straight line through the points and averaging the slope of these lines. These stiffnesses were 1300 kips/in. (228 MN/m), 620 kips/in (109 MN/m), 50 kips/in. (8.76 MN/m) for T-4,T-5 and T-6 respectively.

A common measure of behavior, which is useful for comparison with other tests and analyses, is load-deformation. The average active load vs. change in diameter in the N-S and E-W directions are shown in Figs. 4.13 and 4.14. The deformations depend strongly on the passive jack stiffness. For the loading to failure (T-6) the behavior is quite ductile. After an average load of 40 kips (187 kN) at each active load point, the change in N-S and E-W deflection doubled at essentially constant load. Even at failure the load fell off slowly as deformations became very large until the section in the NE quadrant became geometrically unstable. Hinges formed at the major cracks and crushing occurred on the compression side near the E and W sections.

An important element in the understanding of the structural behavior and the prediction of failure is the relation between moment and thrust on critical sections in the liner as load was increased. This cannot be measured directly, but must be computed from other measurements. This computation required a knowledge of Young's modulus of the material in the test speci-

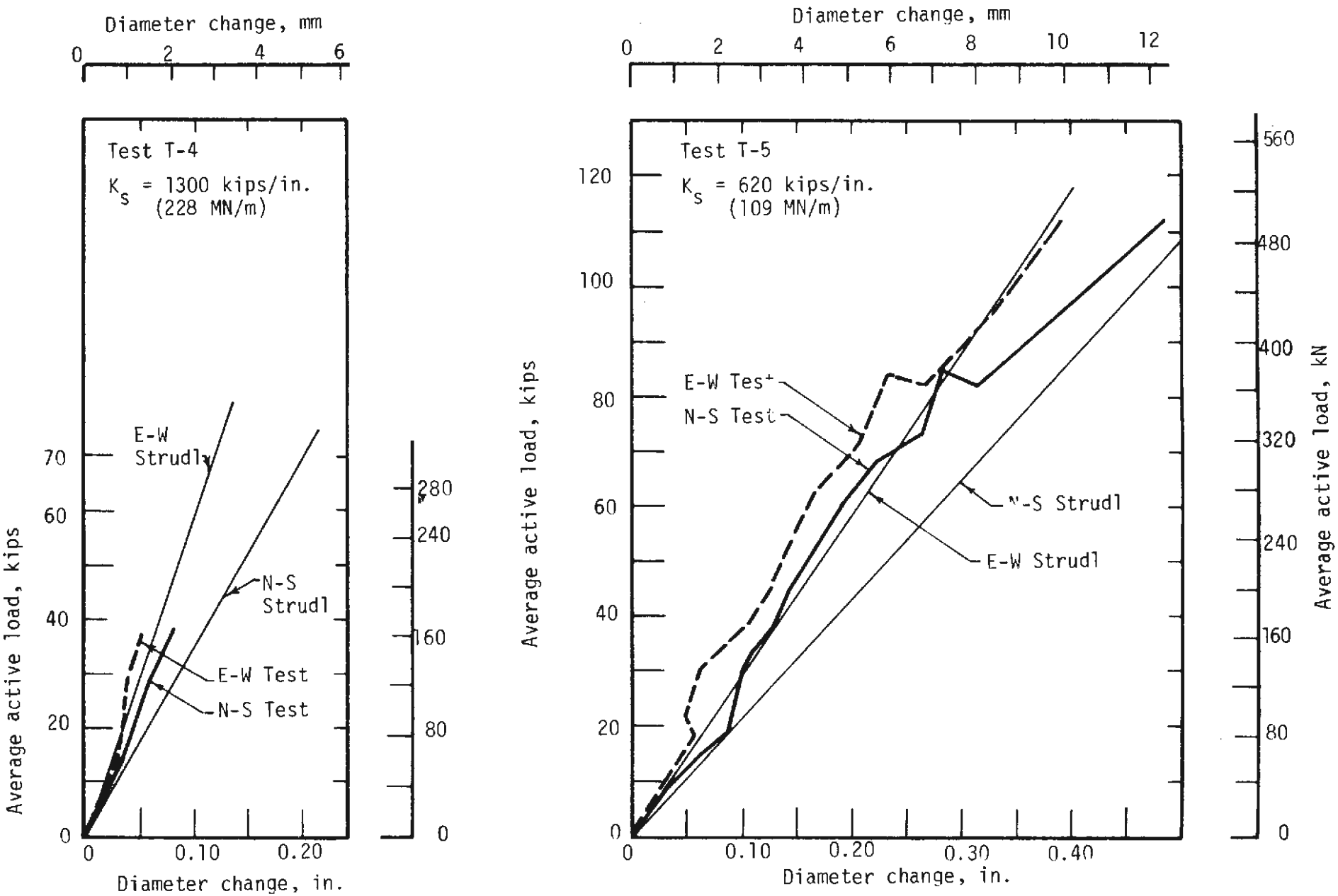

FIGURE 4.13 LOAD-DEFORMATION FOR SPECIMEN C-1 TESTS T-4 AND T-5

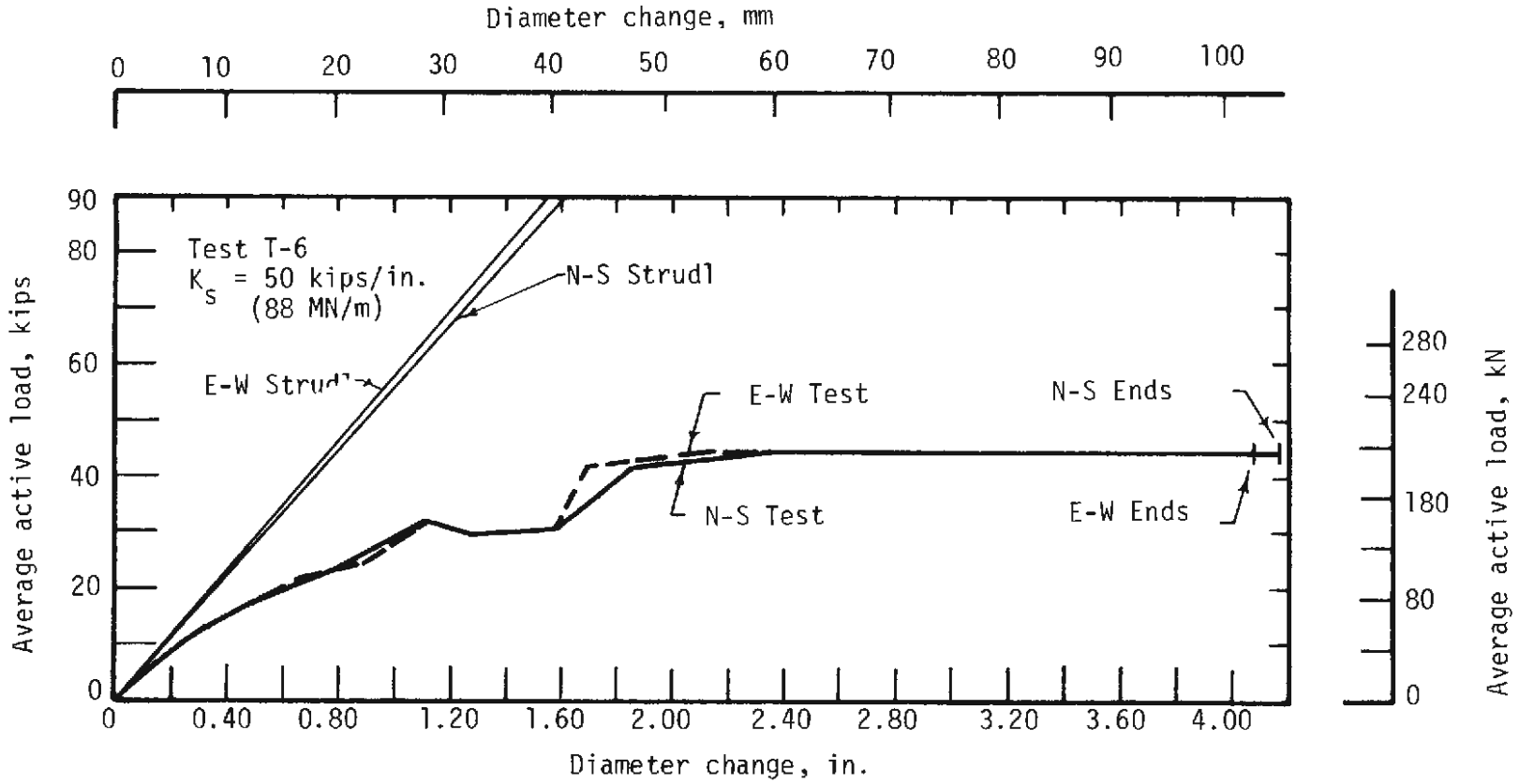

FIGURE 4.14 LOAD-DEFORMATION FOR SPECIMEN C-1 TEST T-6

men, which was predicted from measurements on the control cylinders.

Once the moments and thrusts at each quarter point were found, a free-body of the segment of the specimen from the quarter point to the N, S, E or W sections could be isolated, and the unknown quantities on the sections found by summing forces and moments on the free-body. This approach was modified somewhat, as it was found that the thrusts at the N and S sections were more consistent and reliable if the structure was cut in half and the external force components perpendicular to the cut summed to give the thrusts in the sections at each cut. By assuming symmetry the thrust on each of the cut faces was one-half this total force. The procedure described above was then used to obtain the moment on the section. Symmetry was also assumed in the moment calculation as the shear on the cut section at the N and S sections was taken as zero. Some inconsistencies resulted from this procedure since the N section moment was different when computed from the free bodies to the E and to the W of the N section. In this case, the moments from each of these computations were averaged.

Figs. 4.15-4.17 show the moment-thrust paths for critical sections as obtained by the procedure described above for loadings T-4, T-5 and T-6. The moment-thrust paths are much more sensitive to the loading distribution and irregularities in it than are the deformations discussed above. They contain and are sensitive to the errors in the computed moments at the quarter points and to the errors resulting from inability to maintain the proper load distribution around the specimen during the test. The jumps and non-smooth behavior can be traced back to irregularities in the load distributions.

Distribution of the passive loads on the specimen strongly influence

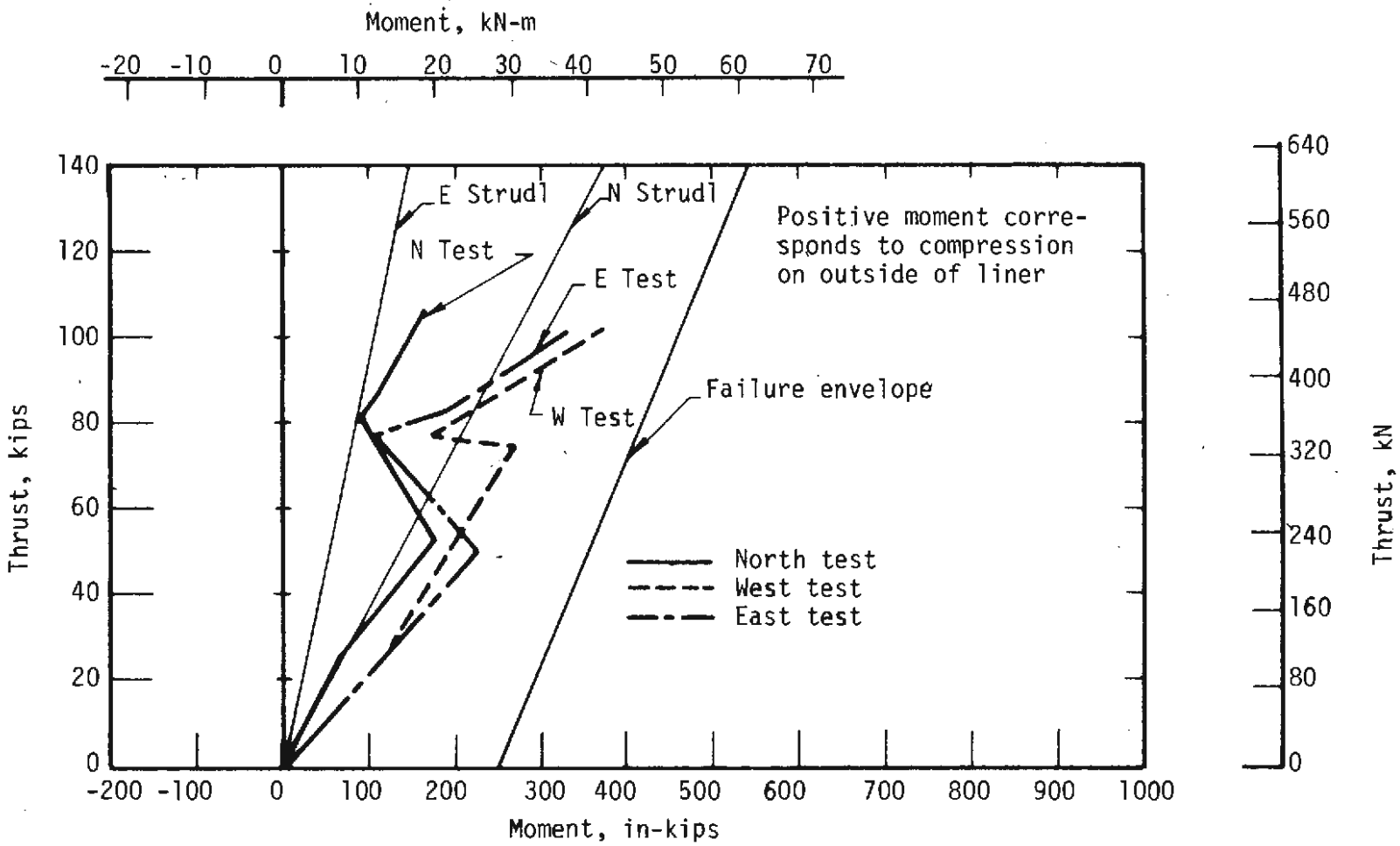

FIGURE 4.15 MOMENT-THRUST FOR SPECIMEN C-1 TEST T-4

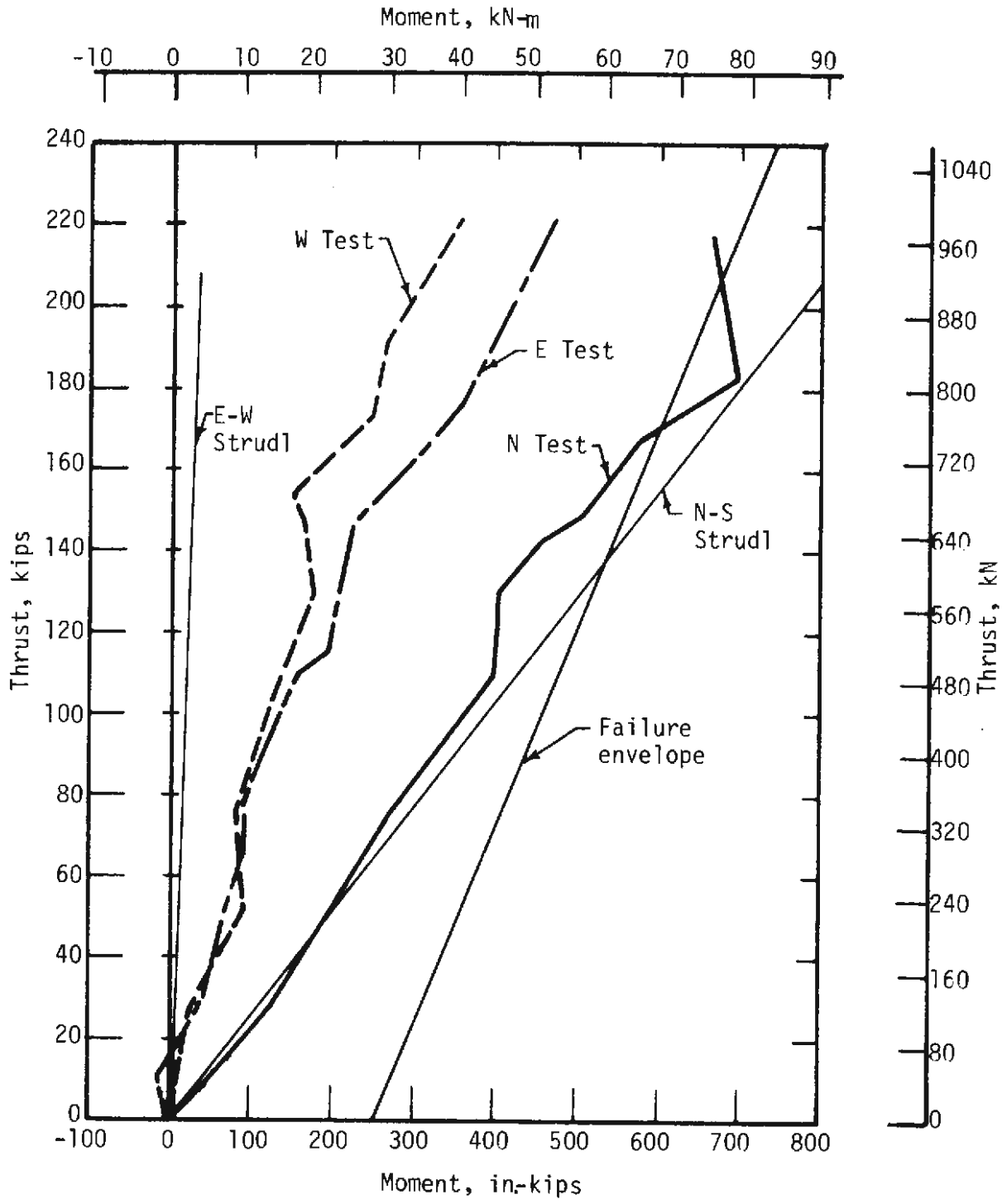

FIGURE 4.16 MOMENT-THRUST FOR SPECIMEN C-1 TEST T-5

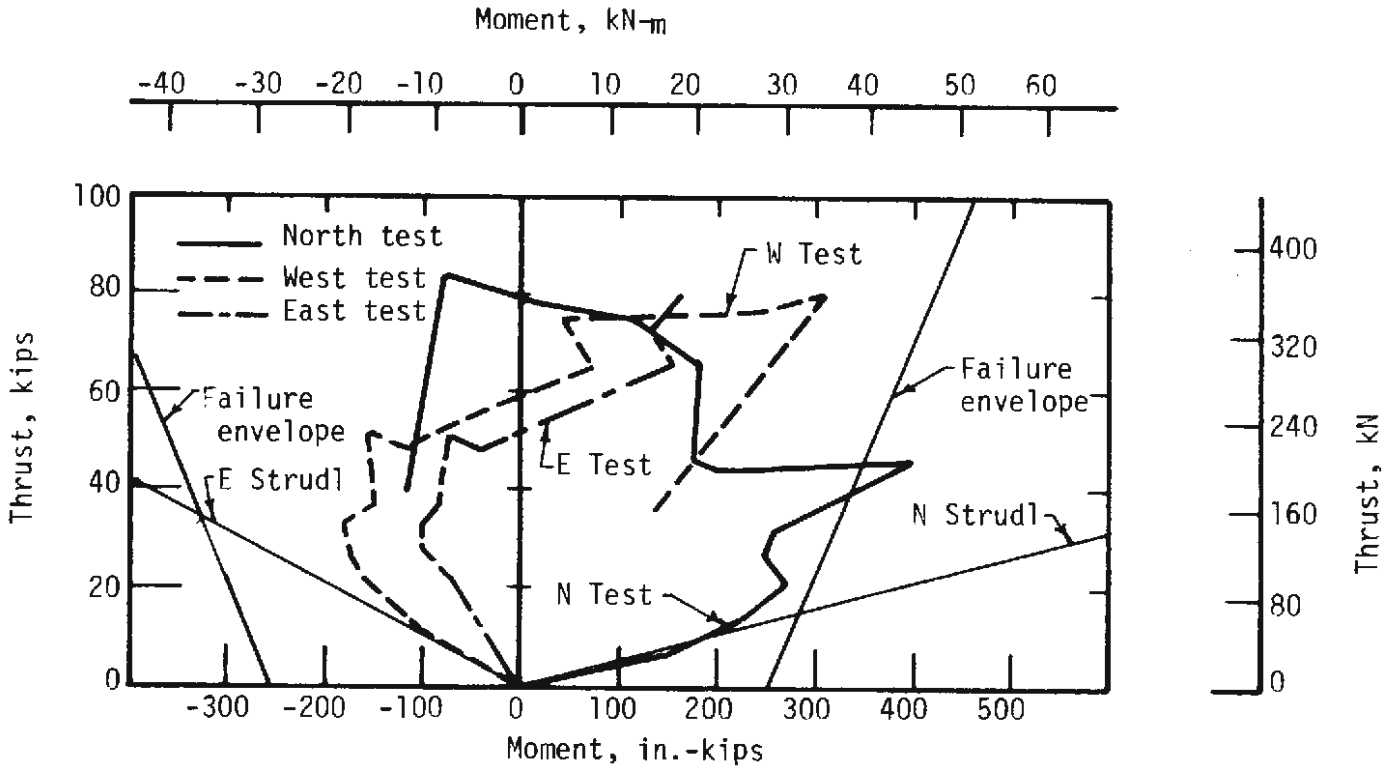

FIGURE 4.17 MOMENT-THRUST FOR SPECIMEN C-1 TEST T-6

its overall behavior and the internal forces. The passive loads are also a measure of the interaction between the specimen and passive jacking system in resisting the active loads. Perfectly linear behavior and correct regulation of passive loads would result in a linear relationship between the active and passive loads. As hinges form during the test due to cracking, this relationship became nonlinear and the passive loads begin to increase more rapidly. This relationship is shown in Fig. 4.18-4.20 for the three tests. The errors in passive jack control occurred primarily at high loads after considerable movement of the specimen, and caused the irregular behavior shown by these curves.

The overall load-deformation behavior can be explained by observing the curves presented in Figs. 4.18-4.20. For example, in test T-5, the passive load P_A shown in Fig. 4.18 was too large; thus the deformations of Fig. 4.13 are too small as compared with the initial linear behavior. At a load of 31 kips (138 kN), the specimen in Test T-6 deformed considerably without additional load (Fig. 4.14). At this same load, P_A remained constant (Fig. 4.20).

The reason for the failure of specimen C-1 in test T-6 was difficult to determine since the passive jack system was not functioning properly. The specimen failed in a ductile manner at an average load of 44 kips (196 kN) at each active load point with considerable tensile cracking and some crushing in compression. With proper passive jack behavior the failure load may have been higher. Most of the curves describing the behavior have an initial linear section which will be useful in some of the comparisons that will be made later. Also the overall response of the specimen to failure in test T-6 is comparable to that of specimen C-2 described

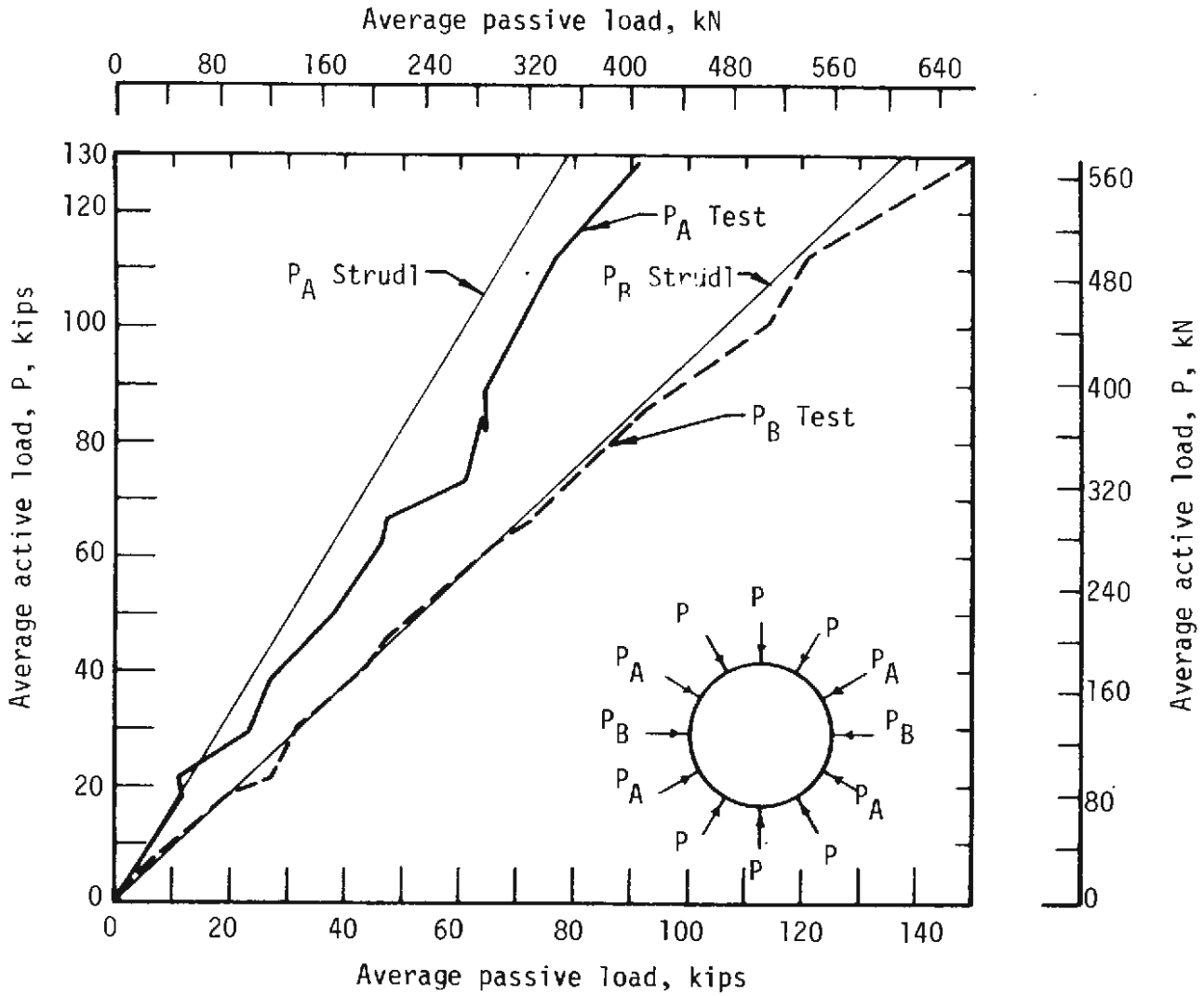

FIGURE 4.18 ACTIVE-PASSIVE LOADS FOR SPECIMEN C-1 TEST T-5

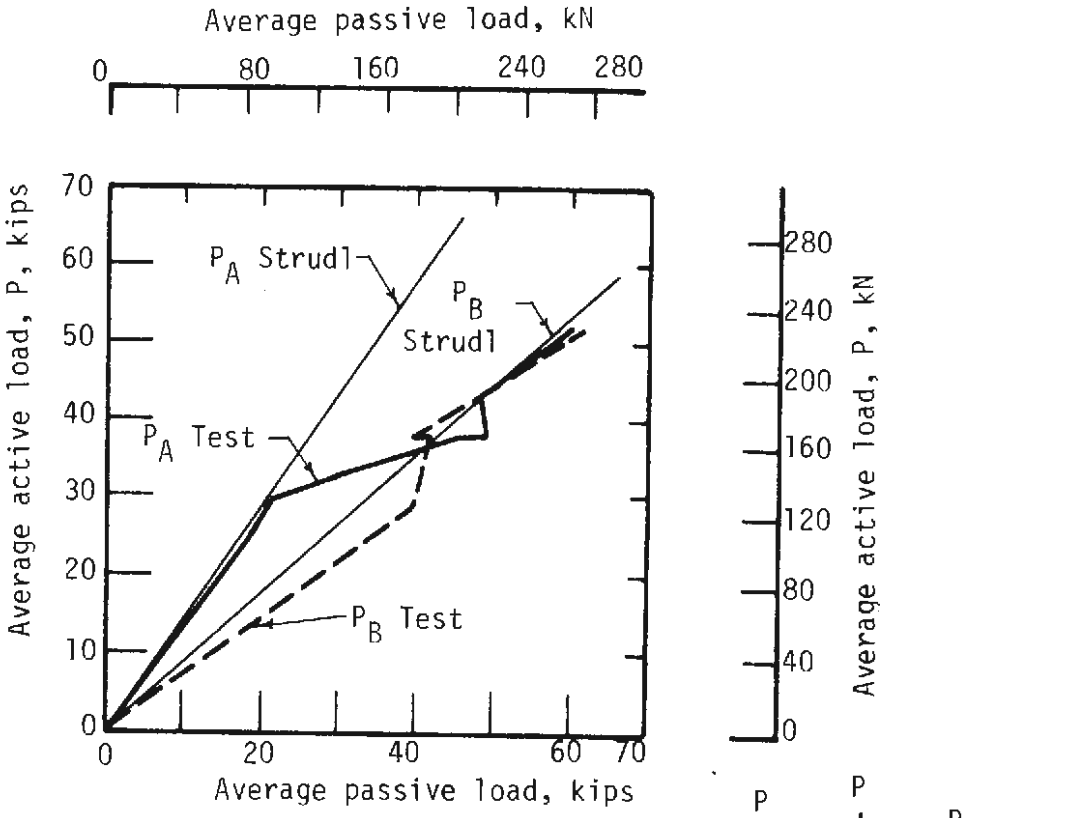

FIGURE 4.19 ACTIVE-PASSIVE LOADS FOR SPECIMEN C-1 TEST T-4

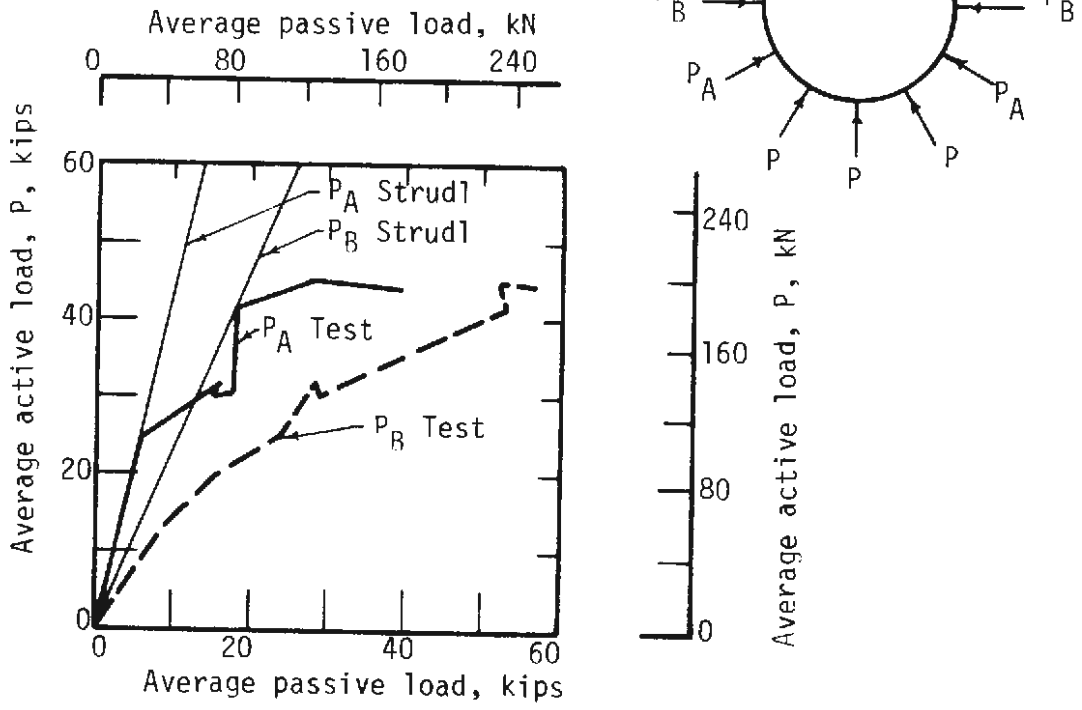

FIGURE 4.20 ACTIVE-PASSIVE LOADS FOR SPECIMEN C-1 TEST T-6

in the next section. In general, the results from specimen C-1 will be used only to compare overall behavior since it is recognized that some of the measurements were inaccurate and the passive jacks exhibited irregular behavior.

4.5.2 SPECIMEN C-2

The loading arrangement for the testing of specimen C-2 was changed as described in Sect. 4.3 to prevent rigid body movement and rotation of the specimen. With this arrangement, the tests proceeded smoothly. A more accurate method was used for radial alignment of the hydraulic jacks and load spread beams. As a result, small forces were developed in the restraining brackets; this could be shown by the fact that the sums of the external load components in various directions resulted in equilibrium of forces within the accuracy of the load measurements. Deformation of the specimen caused some small realignment of the jacks, which resulted in tangential components of force on the specimen, but these forces did not result in an unbalance of forces on the specimen as long as the deformation was symmetrical.

A sketch of the crack locations and photographs of the specimen after the final test (T-6) are shown in Figs. 4.21 and 4.22, respectively. The distribution of load at representative load increments in test T-6 is shown in Figs. 4.23, and provides an indication of the magnitude of the lack of symmetry that existed at various loads, and will help to explain the behavior of the specimen.

The overall stiffness of the specimen is shown by the load-diameter change plots of Figs. 4.24 and 4.25. Results of the linear analysis shown on these figures will be discussed later. Two points may be noted. The

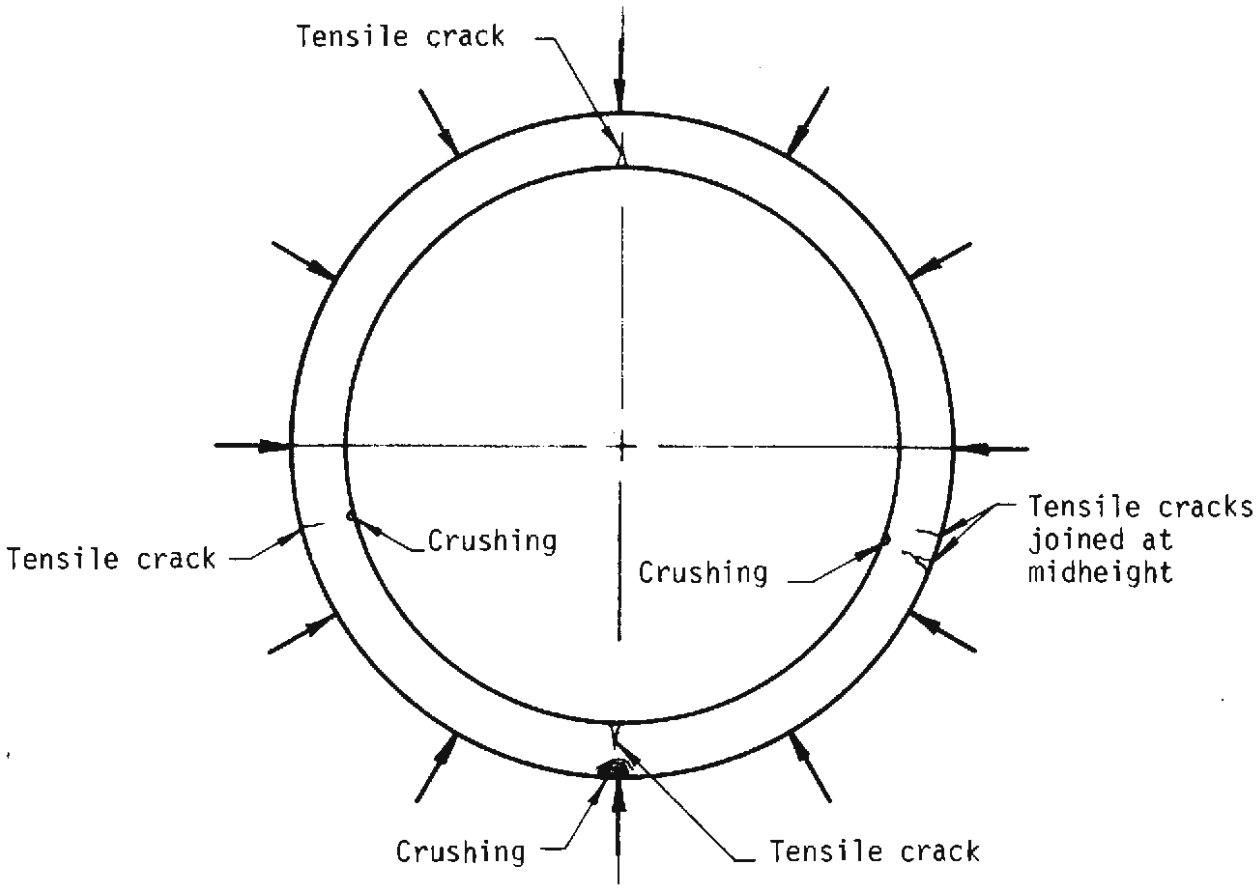

FIGURE 4.21 CRACK LOCATIONS IN SPECIMEN C-2 AFTER TEST T-6

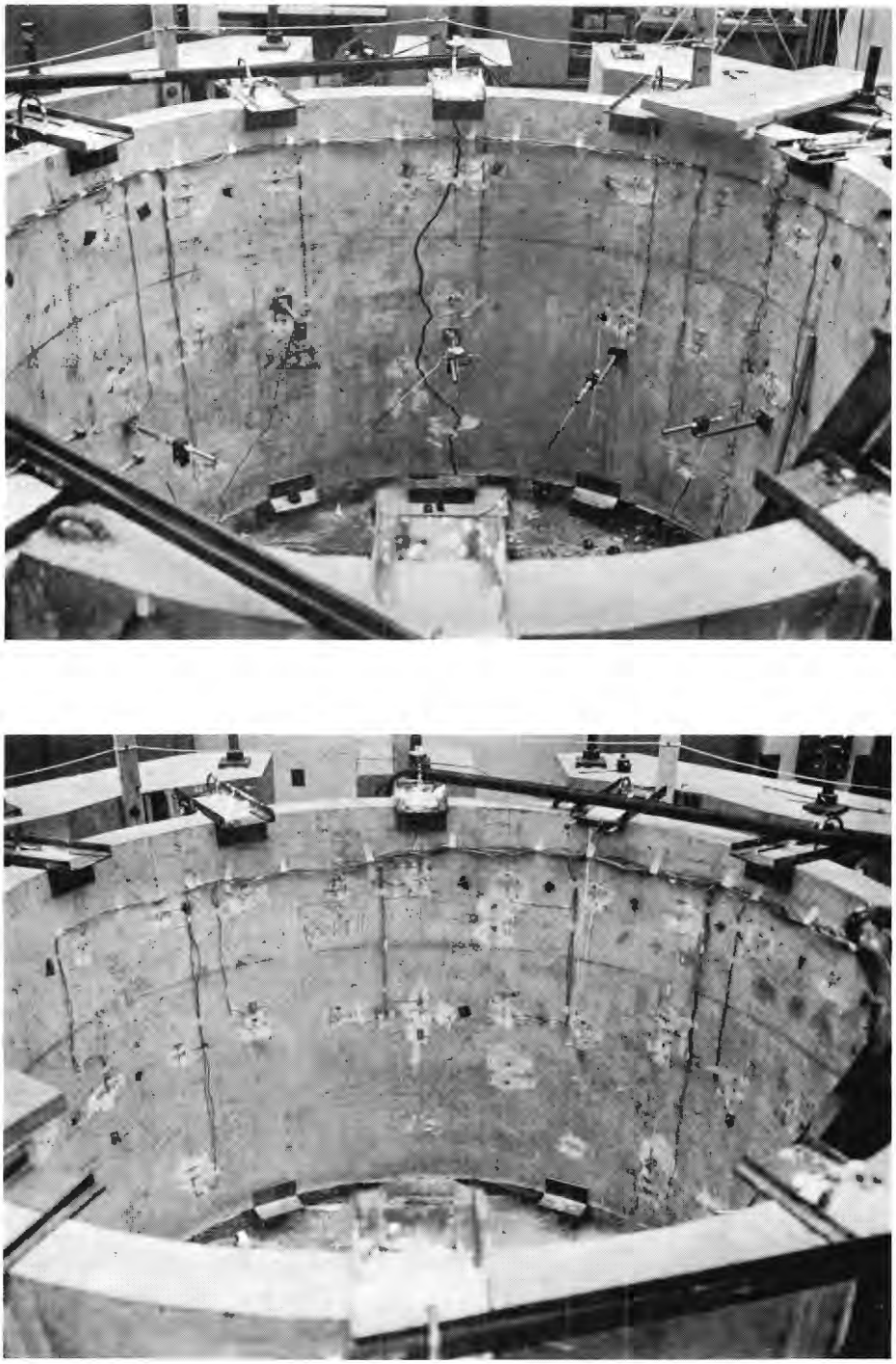

FIGURE 4.22 PHOTOGRAPHS OF SPECIMEN C-2 AFTER TEST T-6
(South side at top North at bottom)

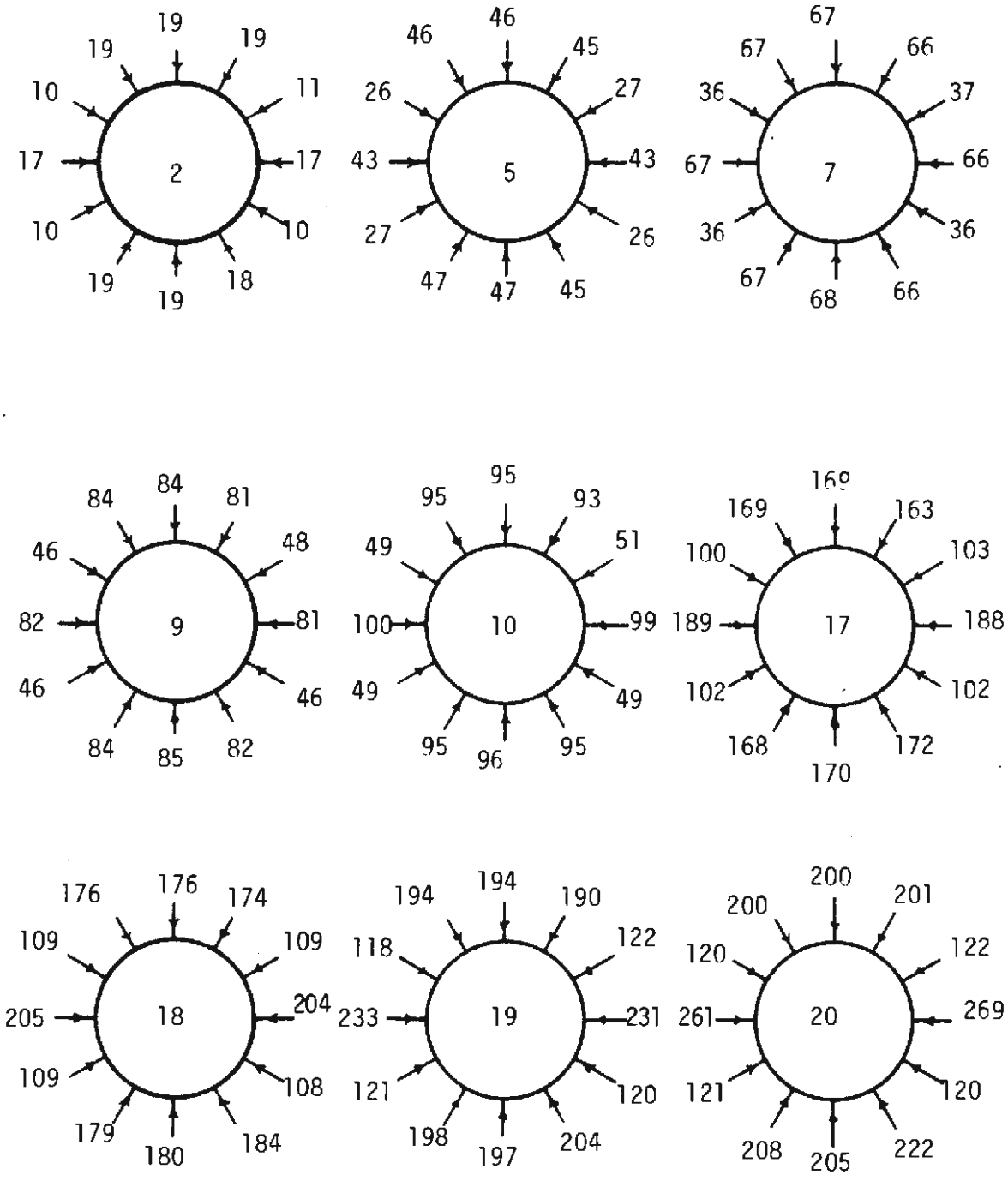

Loads given in kips

1 kip = 4.45 kN

FIGURE 4.23 LOAD DISTRIBUTION FOR SPECIMEN C-2 TEST T-6

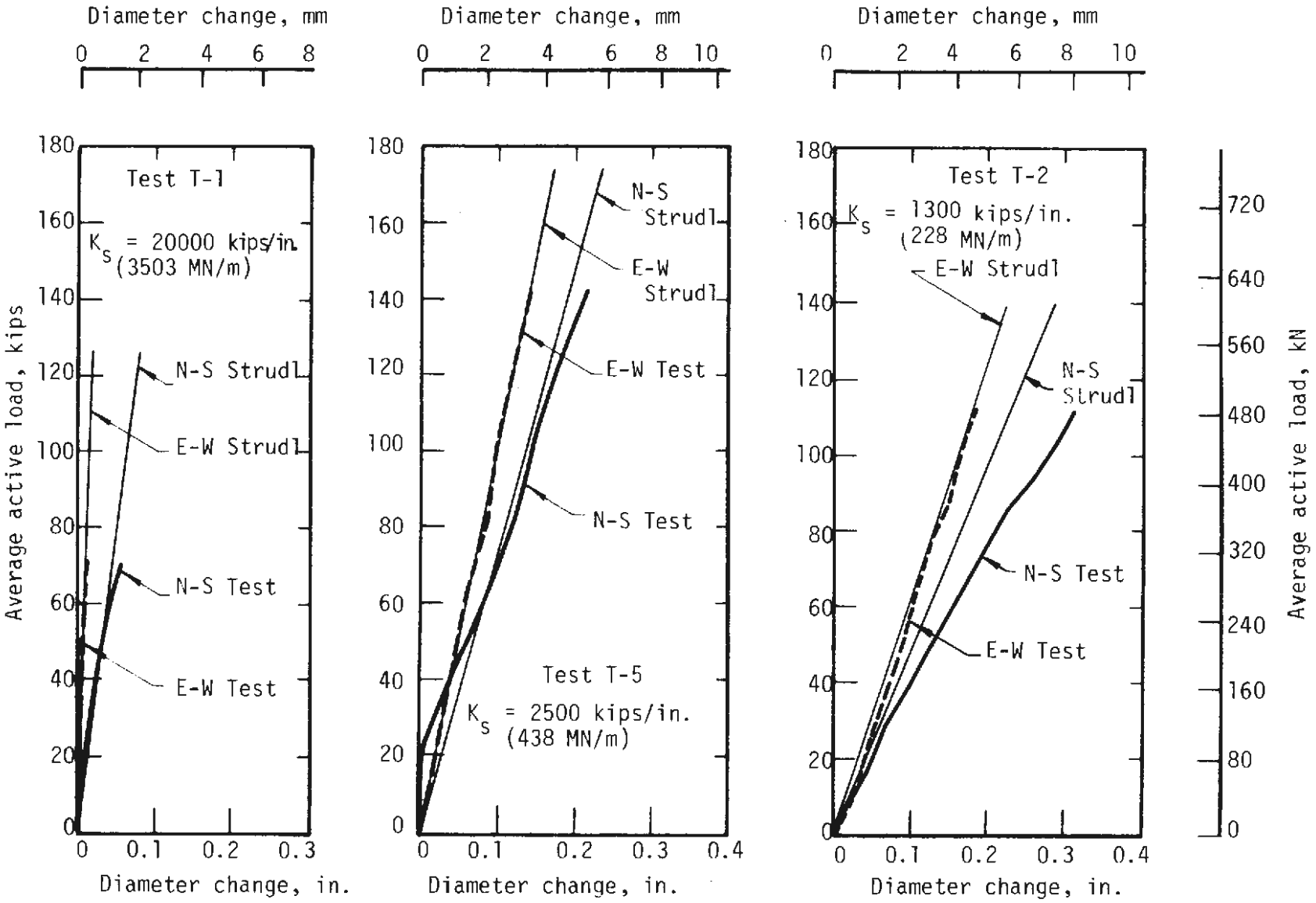

FIGURE 4.24 LOAD-DEFORMATION FOR SPECIMEN C-2 TESTS T-1, T-5 AND T-2

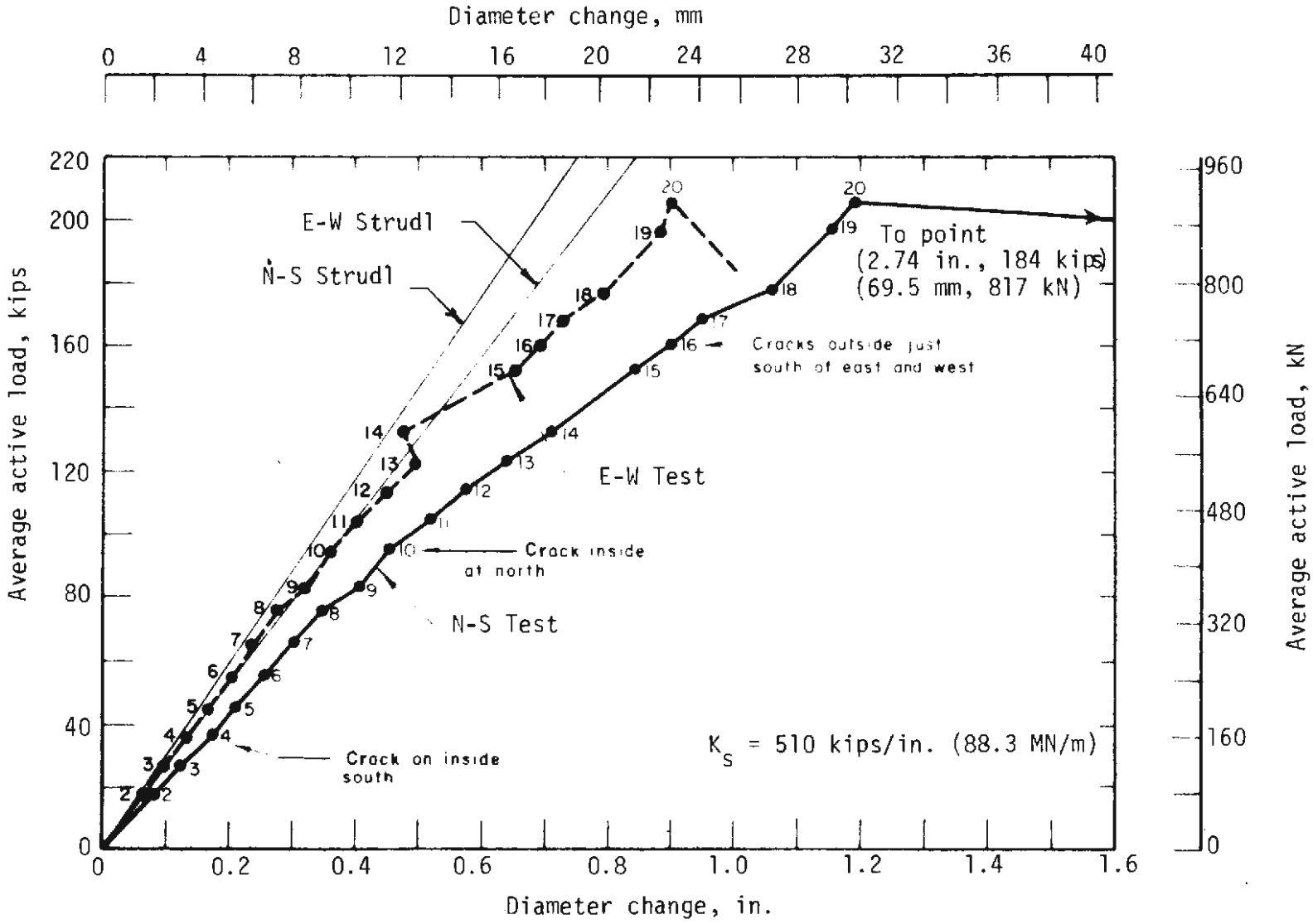

FIGURE 4.25 LOAD-DEFORMATION FOR SPECIMEN C-2 TEST T-6

structure stiffness is influenced greatly by the passive jack stiffness, and the N-S diameter change is always larger than that of the E-W. The difference in N-S and E-W diameter change results primarily from shortening of the circumference because of axial compression of the ring. The difference is approximately constant at any particular active load for each test; this is shown by the difference between the N-S and E-W diameter change curves in Figs. 4.24 and 4.25, which is approximately equal in each case.

The moment-thrust relationship at critical sections is an effective measure of the internal behavior of the specimen and is shown in Figs. 4.26 to 4.29. These curves are less smooth than the load-deformation curves as discussed in the previous section. This is important because failure occurs due to these internal forces and may occur prematurely if the loading has local anomalies. The calculated moment-thrust failure envelope is shown on each graph. This envelope was obtained by changing the one obtained in Chapter 3 for a 6x6-in. (152x152 mm) beam column to a 6x72-in. (152x1829 mm) section by direct proportion, and then making an appropriate adjustment for the difference in compressive and flexural strength. Only in test T-6 was the envelope reached, and the moment-thrust path for the north section paralled it closely. The shape of this curve shows a change in behavior which represents a change in the way the specimen resisted the load when the moment-thrust path reached the failure envelope. The moment at the N and S sections was reduced while thrust increased rapidly at the E and W sections. A redistribution of moments and greater tendency to resist load by thrust is indicated. The same behavior was noted in specimen C-1 test T-6 as shown in Fig. 4.17. This behavior is quite

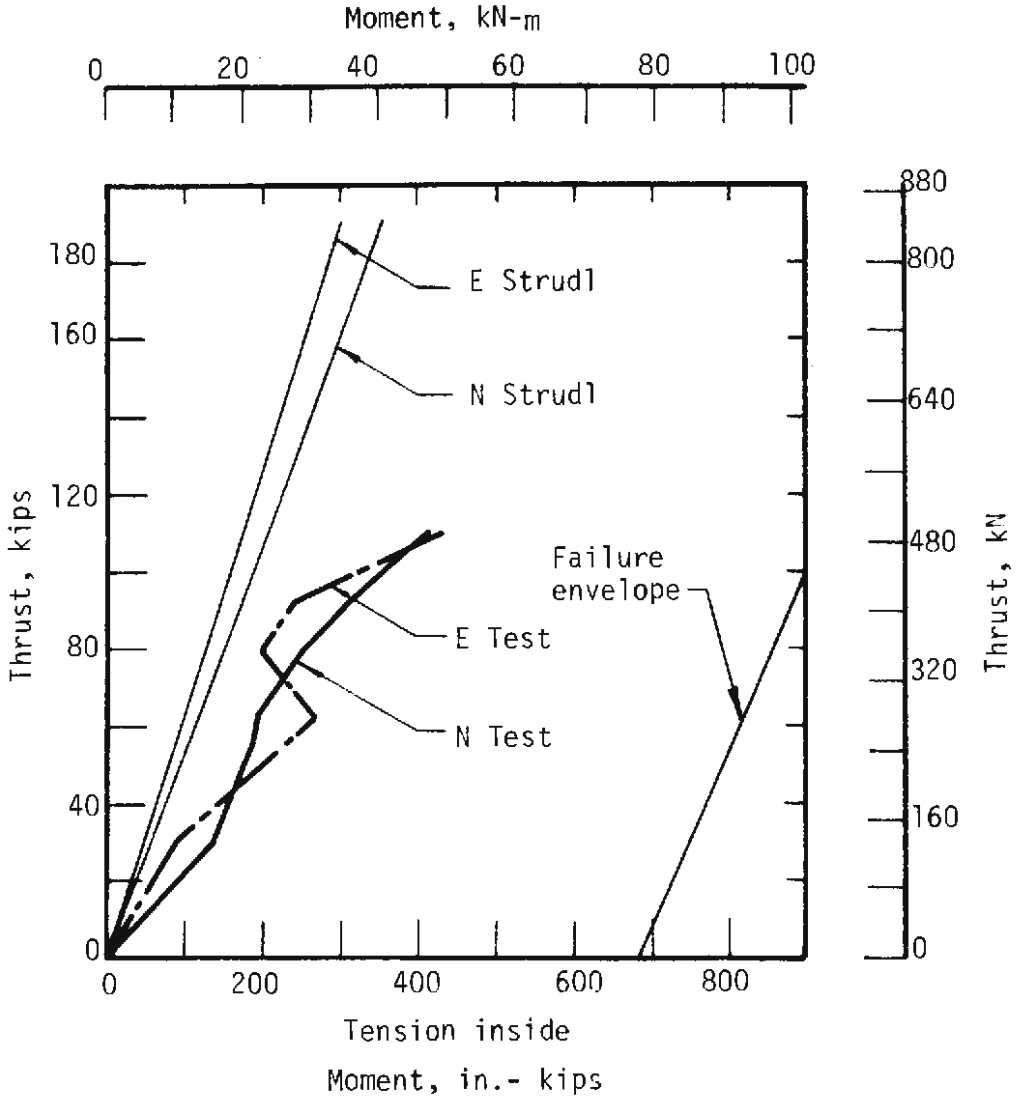

FIGURE 4.26 MOMENT-THRUST FOR SPECIMEN C-2 TEST T-1

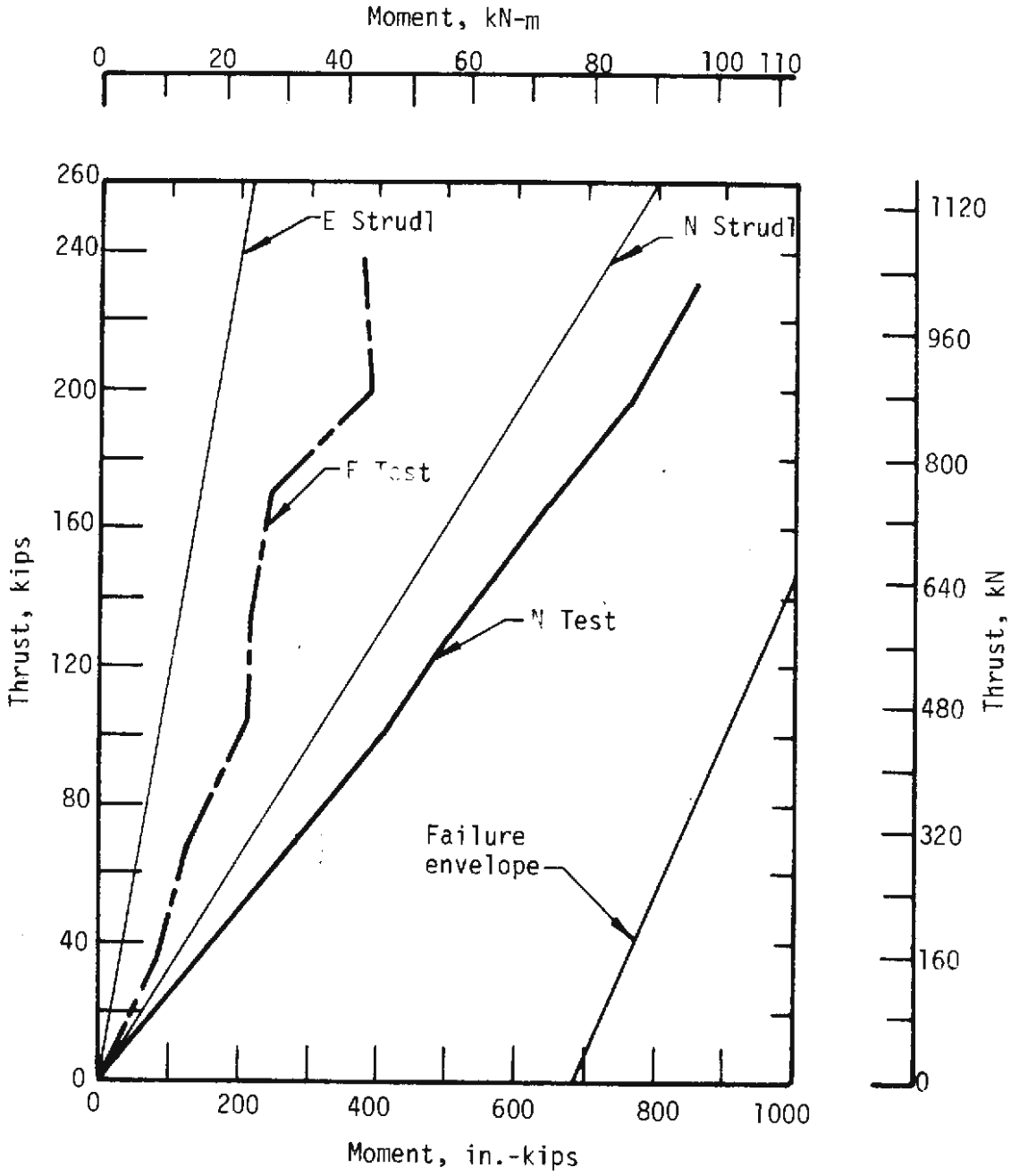

FIGURE 4.27 MOMENT-THRUST FOR SPECIMEN C-2 TEST T-5

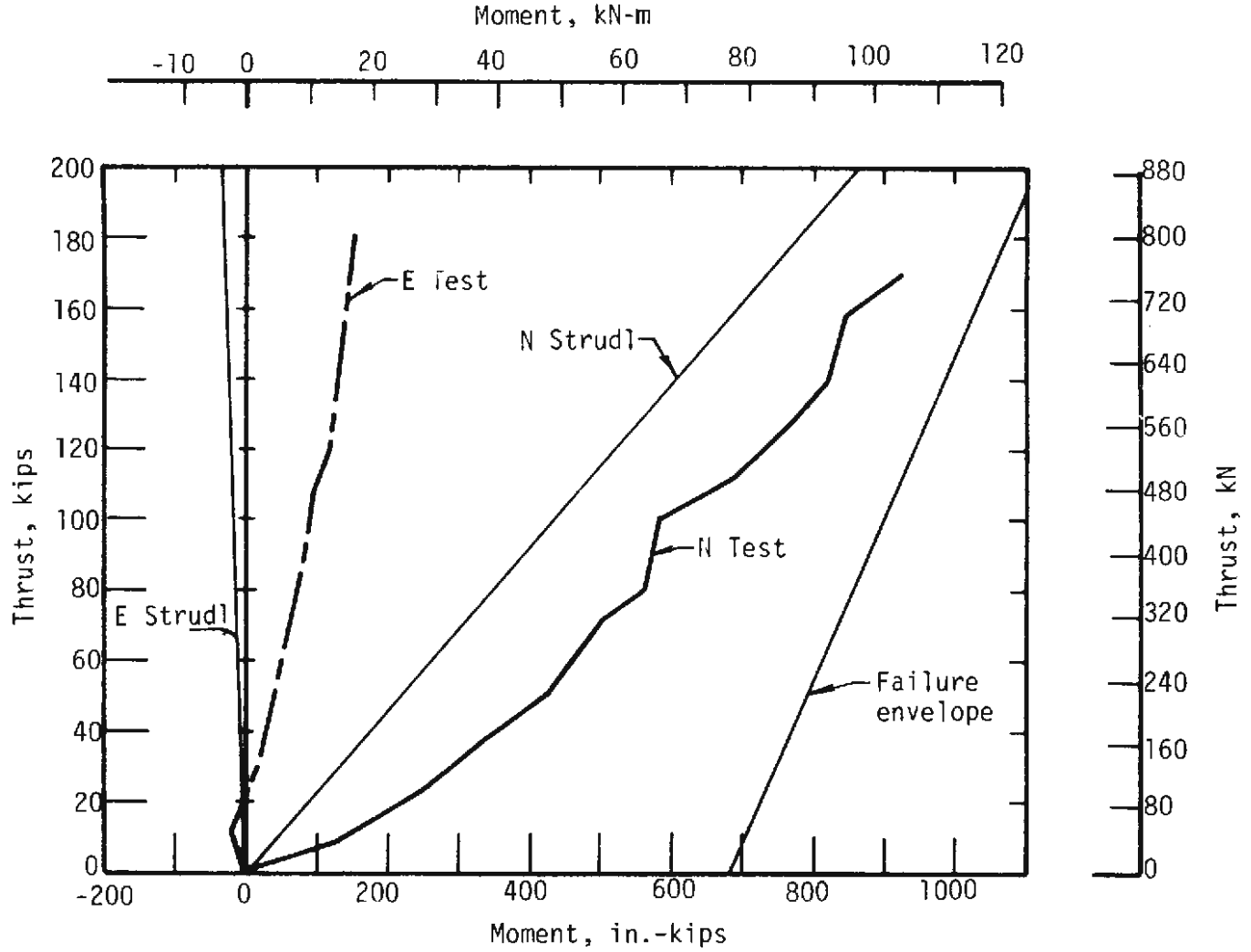

FIGURE 4.28 MOMENT-THRUST FOR SPECIMEN C-2 TEST T-2

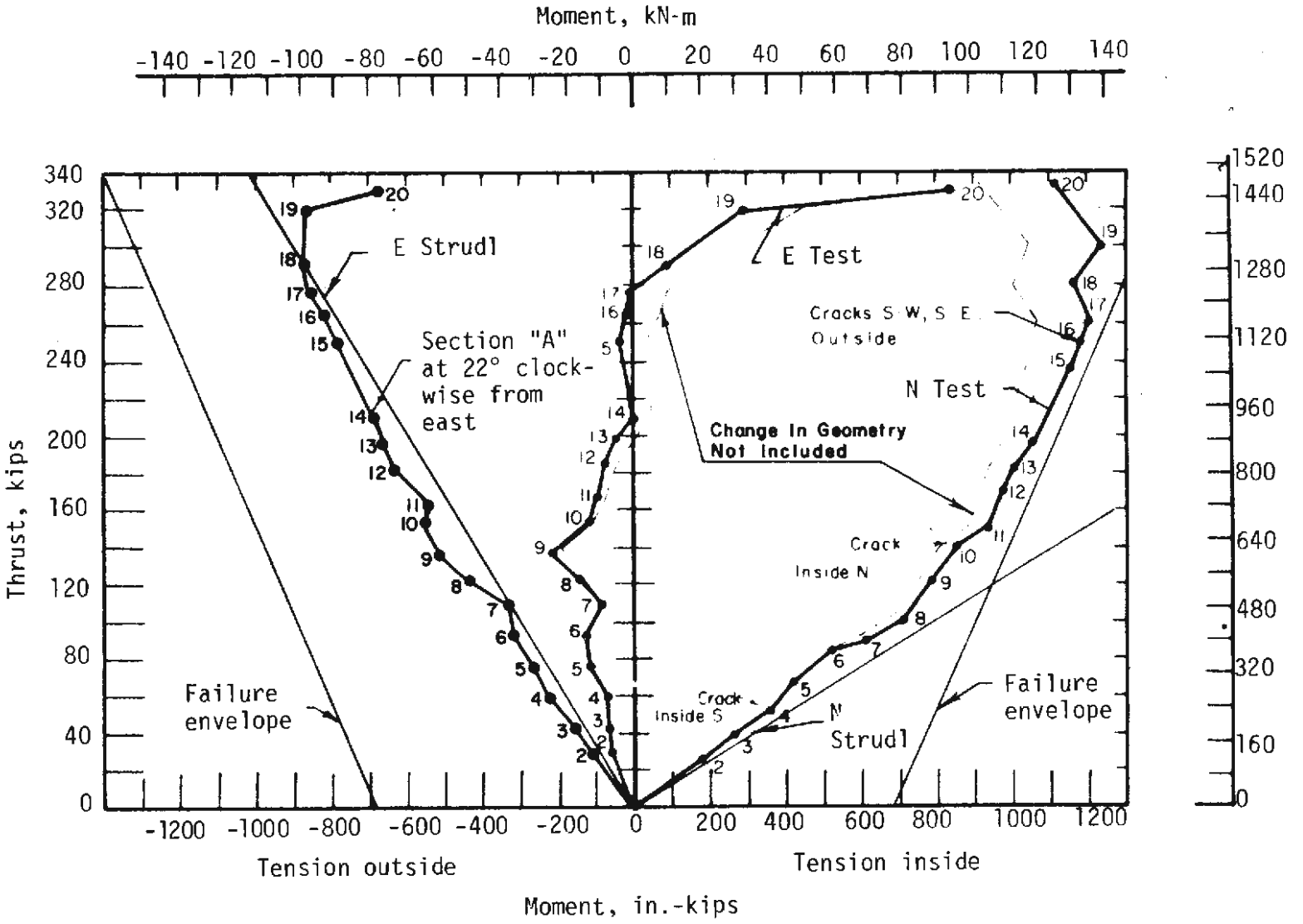

FIGURE 4.29 MOMENT-THRUST FOR SPECIMEN C-2 TEST T-6

important and will be discussed in more detail later.

Two moment-thrust curves for the N and E sections are shown in Fig. 4.29. One was calculated by ignoring the effect of specimen deformation and the other by including it. The curve found by taking deformation into account is obviously more accurate, but both curves are shown to demonstrate the magnitude of the difference, which depends on the magnitude of both the thrust and the deformation. Consideration of the deformation is shown to have appreciable effect on the moment and thrust.

Distribution of the passive loads is related to the deformation of the specimen. The E and W sections of the passive load points deflected most and therefore have the largest passive loads as shown in Figs. 4.30 - 4.32. In each case the average of the loads P_A and P_B is shown. These curves are closely related to those of Figs. 4.33 and 4.34 which show the passive loads plotted against their corresponding deformation (one-half the diameter change). The curves indicate the accuracy obtained in the passive jack controls and show that good linearity and smoothness were obtained in these tests until the last increment of test T-6. The slopes of the curves are the passive jack stiffness.

Cracking in specimen C-2 was negligible until loading increment 4 of test T-6 (Fig. 4.29) when a crack, extending from top to bottom of the specimen, was first detected at the S section. The crack on the inside at the N section developed during increment 10 and outside cracking just S of the E and W spread beams developed during increment 16, as shown on Figs. 4.25 and 4.29. In the discussion which follows, the load increments are numbered on the figures that are involved.

Fig. 4.25 shows that the specimen started to deform without increase

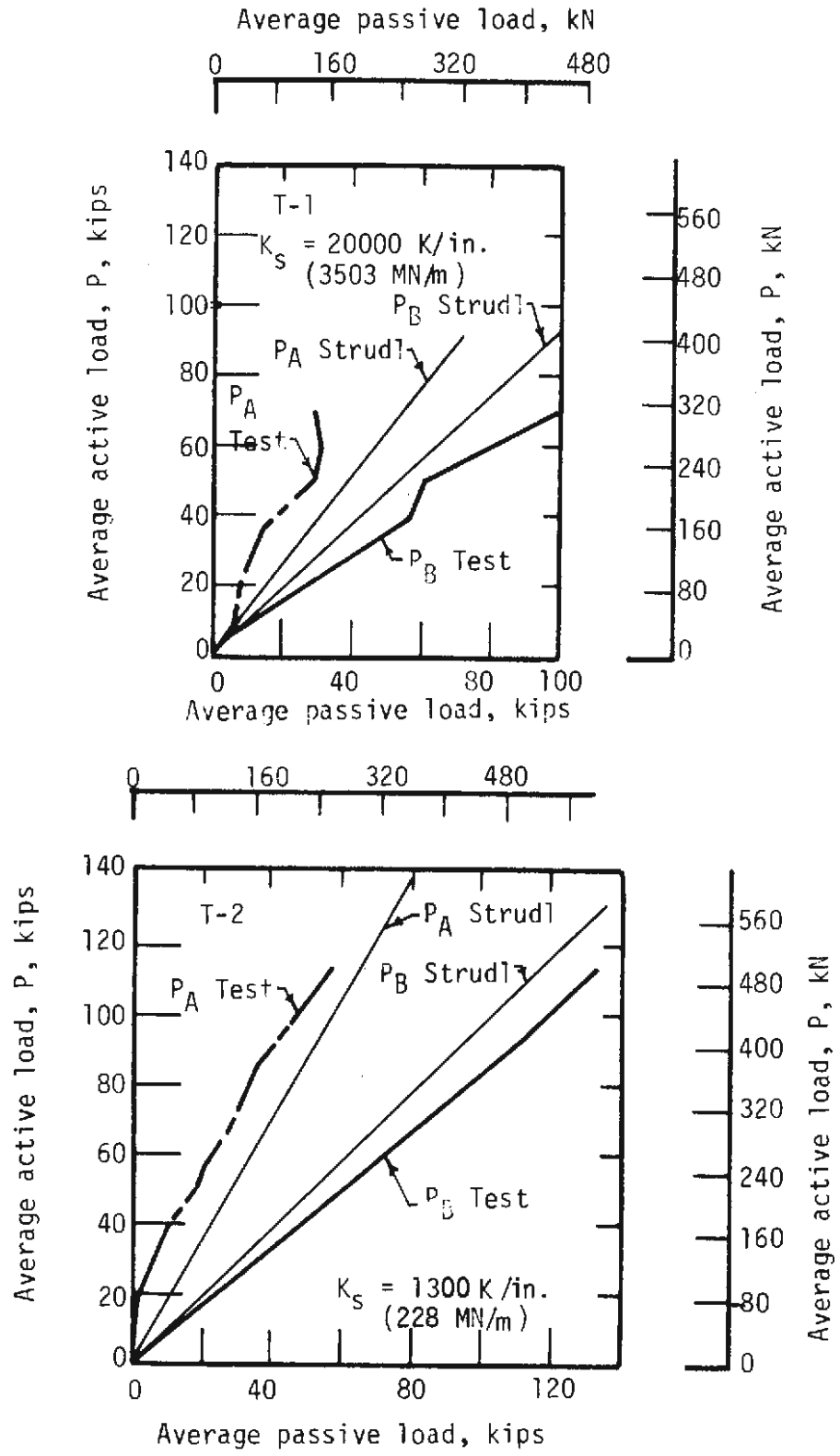

FIGURE 4.30 ACTIVE-PASSIVE LOADS FOR SPECIMEN C-2 TEST T-1 AND T-2

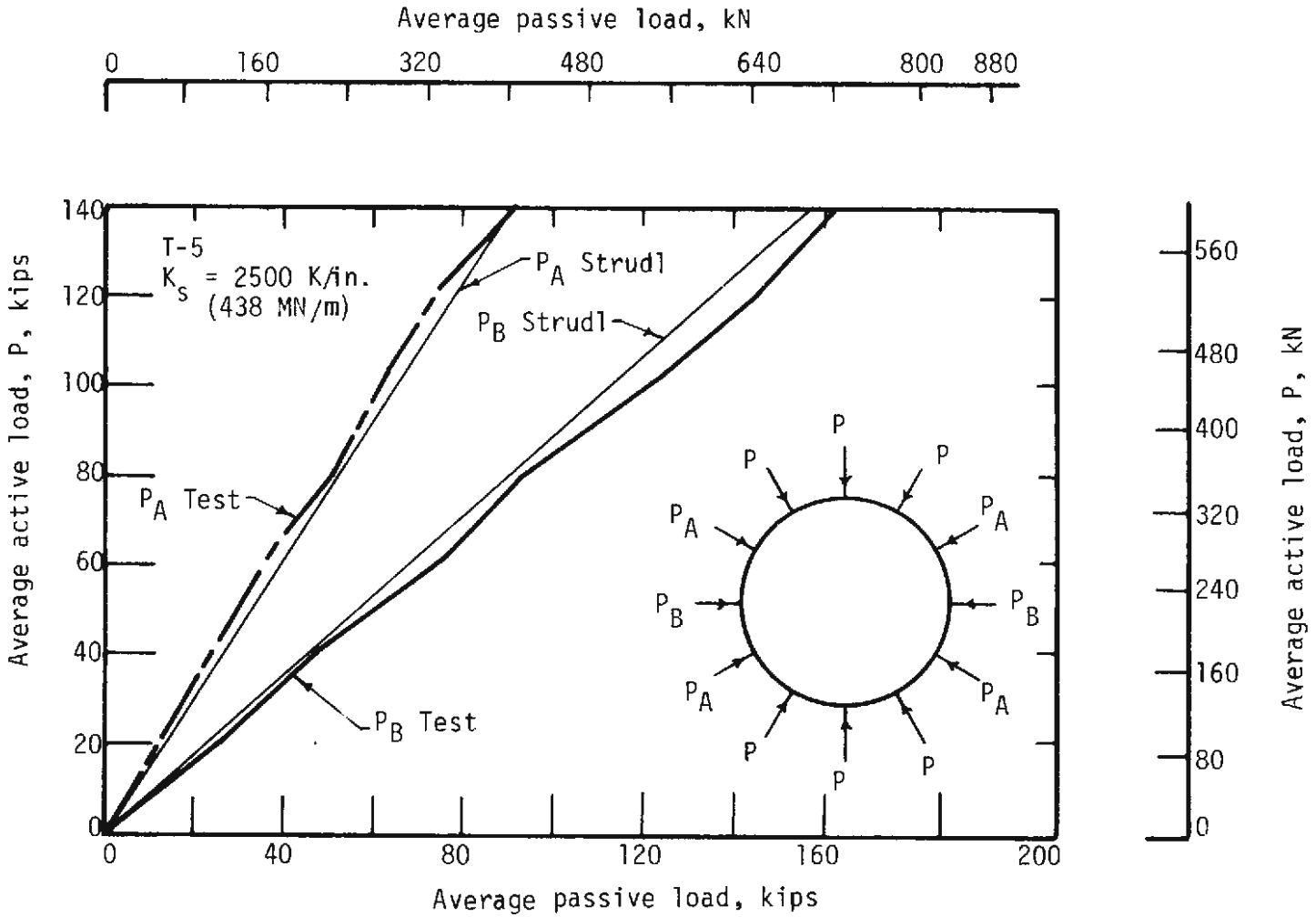

FIGURE 4.31 ACTIVE-PASSIVE LOADS FOR SPECIMEN C-2 TEST T-5

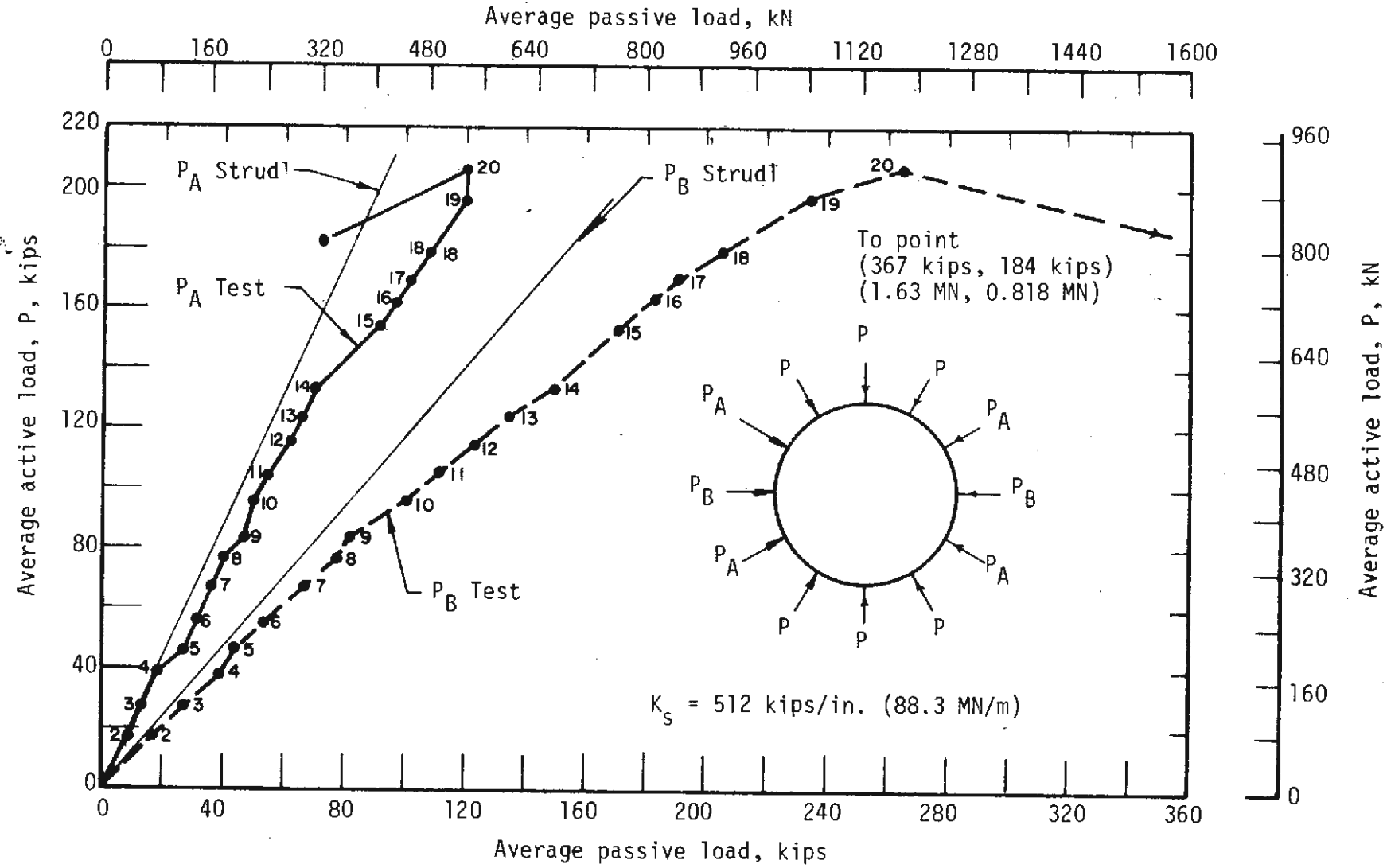

FIGURE 4.32 ACTIVE-PASSIVE LOADS FOR SPECIMEN C-2 TEST T-6

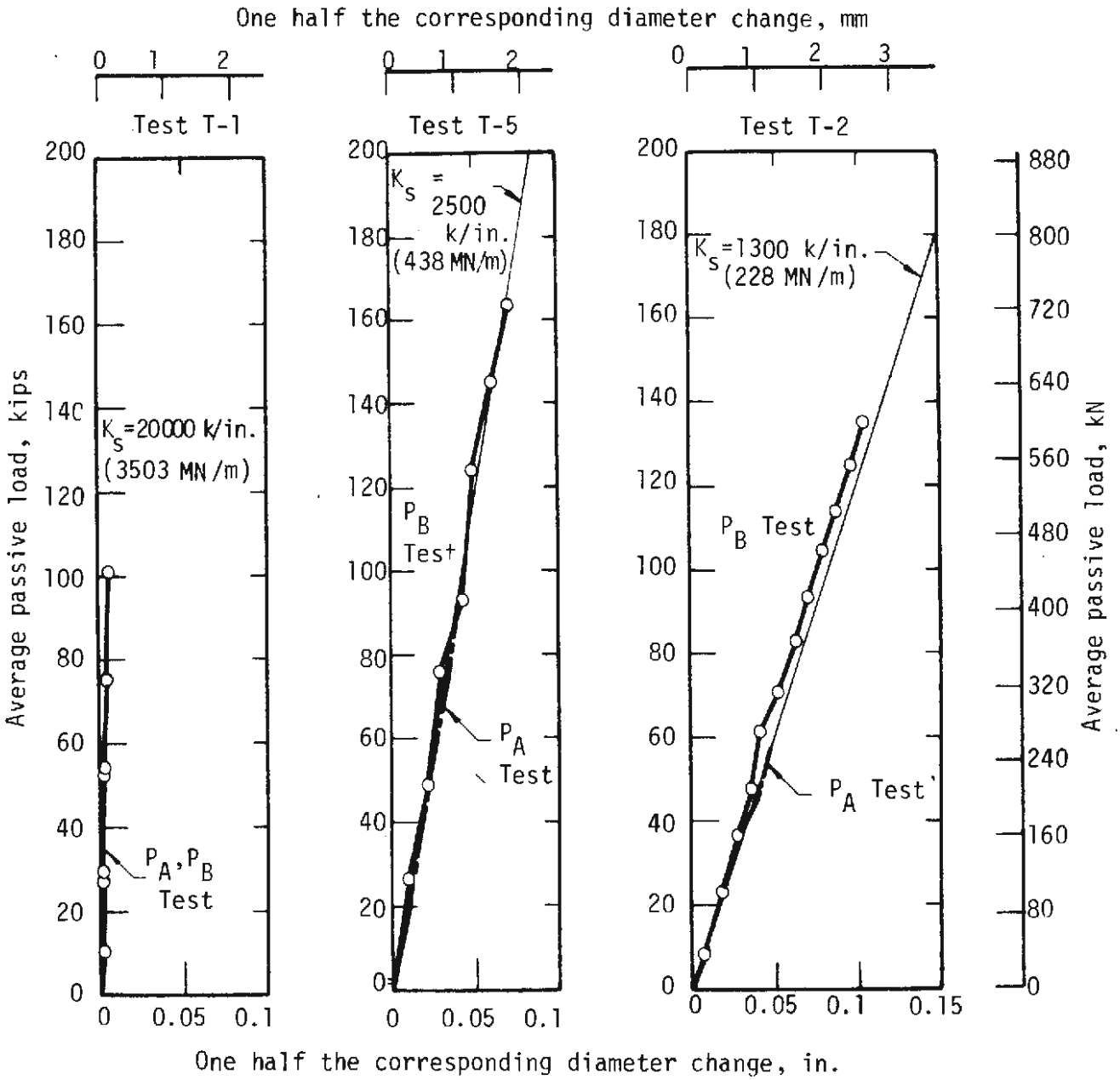

FIGURE 4.33 LOAD-DEFORMATION OF PASSIVE FORCES FOR SPECIMEN C-2 TESTS T-1, T-5 AND T-2

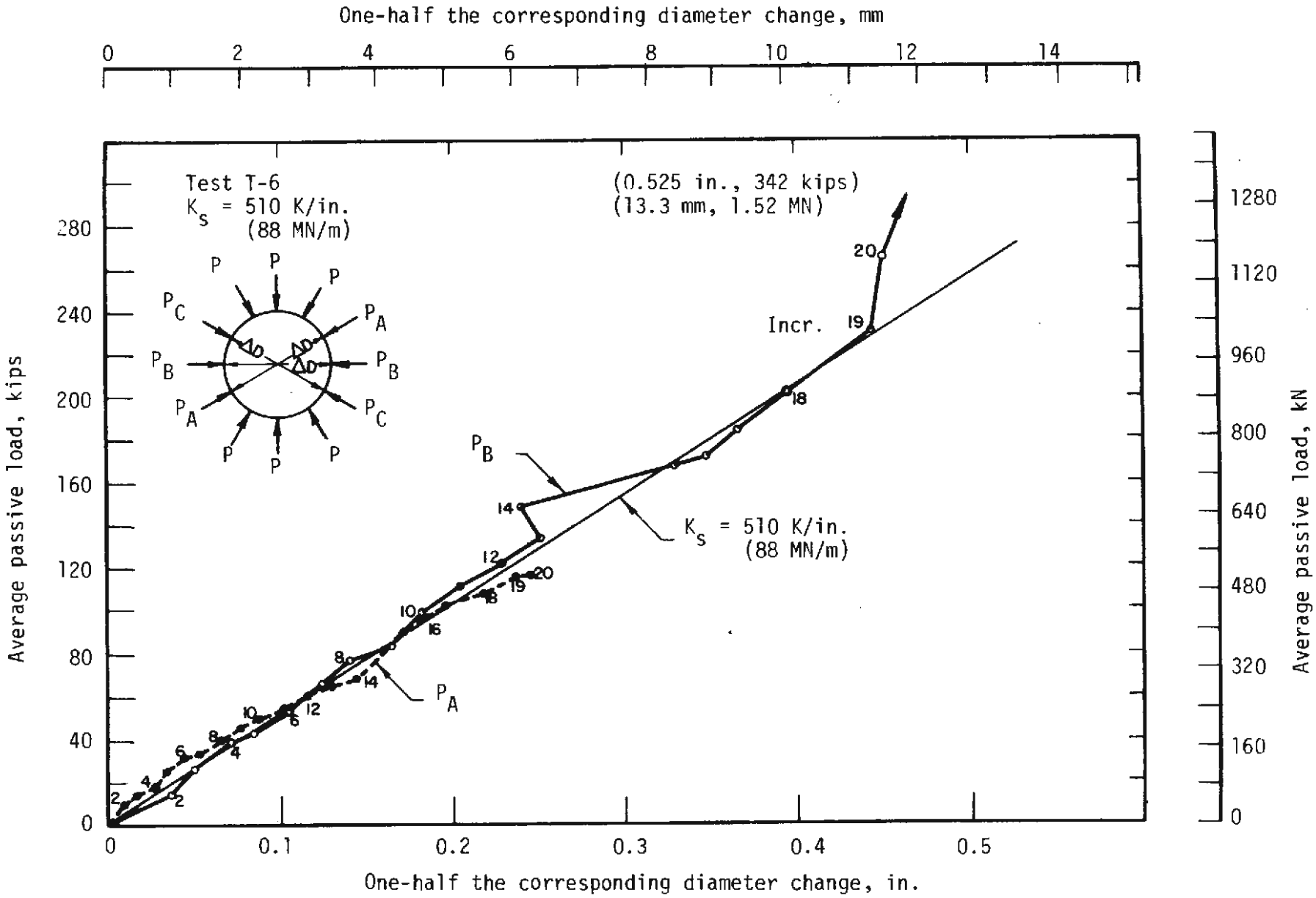

FIGURE 4.34 LOAD-DEFORMATION OF PASSIVE FORCES FOR SPECIMEN C-2 TEST T-6

in load after increment 20. Inspection of the passive loads shows that this cannot be attributed to structural failure with the intended loading, however. Figure 4.34 shows that P_B, the E and W passive loads, left the intended path and increased sharply after load increment 19. A different path is also shown on Fig. 4.29 for the moment-thrust after load increment 19. Thus it is concluded that structural failure did not occur with the intended passive loading, but resulted from high local moments due to very high passive loads P_B and very low passive loads P_A. This problem occurred because of a hydraulic jack failure in the P_A jacking system which allowed the pressure to fall. The loads in the P_A jacks were then transferred to the P_B jacks. Therefore, the behavior of specimen C-2 can be compared with other tests and with analyses only to load increment 19. Also, the maximum load on specimen C-2 can be considered in a general way only as a lower limit of the ultimate load that it could have resisted with the intended passive resistance.

Though the passive loading at failure was not the intended one, it is still informative to summarize the overall conditions at peak load as a lower limit of the loading, and as an indication of the type of failure to be expected. At failure the concrete opposite the major tension cracks crushed as shown in the photographs of Fig. 4.22. The overall behavior was ductile as shown by the load-deformation of Fig. 4.25. The maximum total active load on the N side (sum of all active jack loads on the N side) was 618 kips (2.75 MN) at a diameter change ΔD in the N-S direction of 0.010D while a maximum ΔD of 0.024D was reached with little loss of load.

4.6 DISCUSSION OF RESULTS

Structural stiffness is an important parameter in assessing the structure-medium interaction and the structural behavior of a tunnel liner. In these tests the load-deformation behavior of the liner and jacking system combined were measured at several values of passive jack stiffness. Figure 4.35 shows this combined stiffness in the linear range as the ratio of average load at each active load point divided by change in N-S diameter as a function of passive jack stiffness from the tests. Comparable curves are also shown on the figure for results obtained from a linear analysis which will be discussed later. At a particular passive jack stiffness the difference between the curves for specimens C-1 and C-2 is due to the difference in stiffness of the two specimens. In the range of passive jack stiffness between 500 kips/in (87.6 MN/m) and 1300 kips/in (228 MN/m), which is the range in which the curves overlap, there appears to be a difference in stiffness of less than 50 kips/in. (8.76 MN/m) attributable to difference in the two specimens. This seems to indicate that Young's modulus of the concrete, which is the major variable between the two specimens in the low load range, does not have a strong influence on the overall stiffness.

Distribution of passive loads depends on the stiffness of the resisting elements and the structural parameters which describe the liner. The distribution of loads around the liner for specimen C-2 test T-6 is compared in Fig. 4.36 for a load in the linear range of behavior and for a load near failure (increment 19, Fig. 4.23). The loads are normalized to the average active load. The E and W loads (load points 4 and 10, Fig. 4.7) change from values almost equal to the active jack loads in the linear range (Fig. 4.36a) to values that are about 18 percent larger near failure (Fig. 4.36b). In general the passive forces increase relative to the active forces beyond the

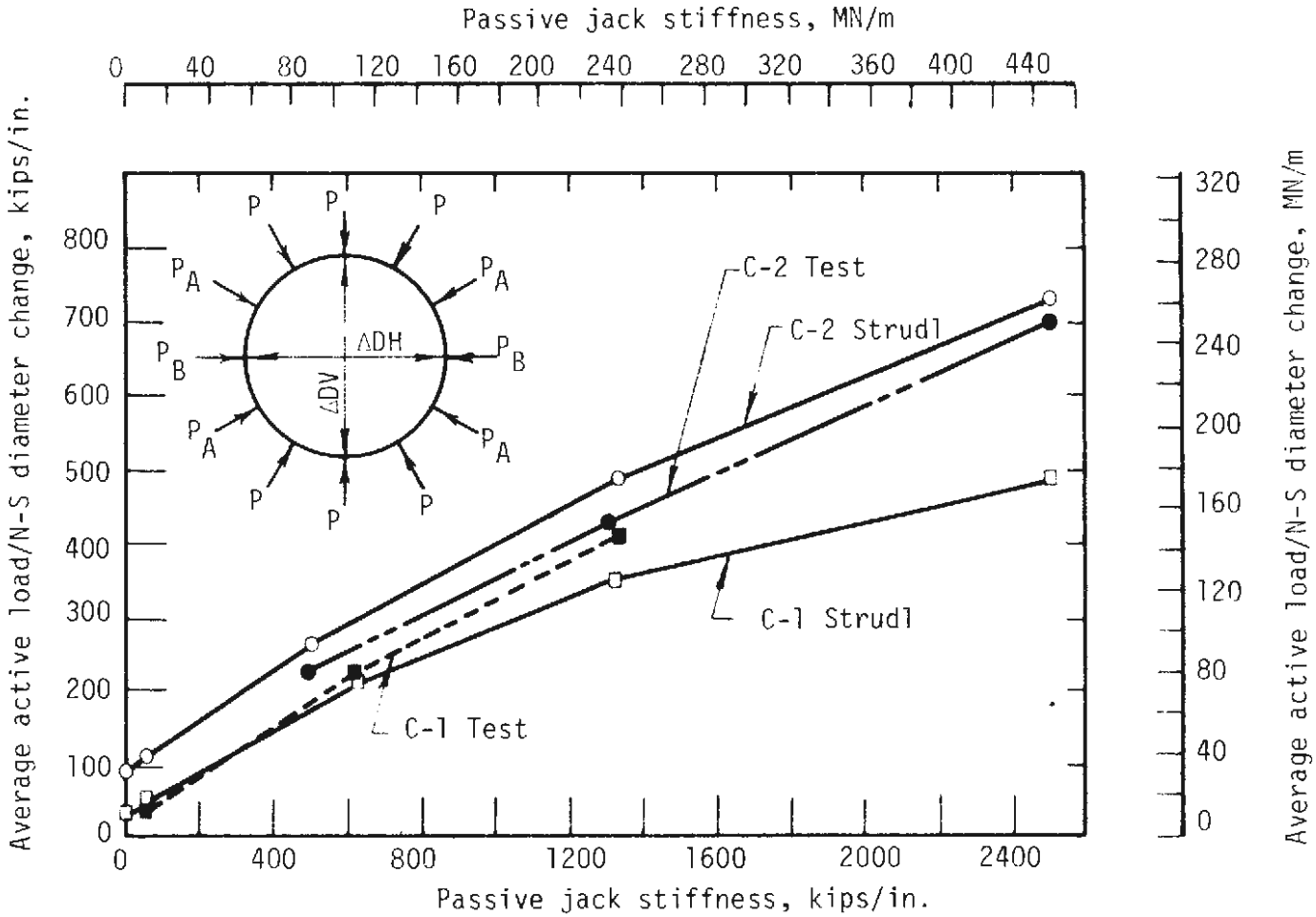

FIGURE 4.35 STIFFNESS OF LINER-JACK SYSTEM FOR THE LINEAR RANGE AS JACK STIFFNESS VARIED

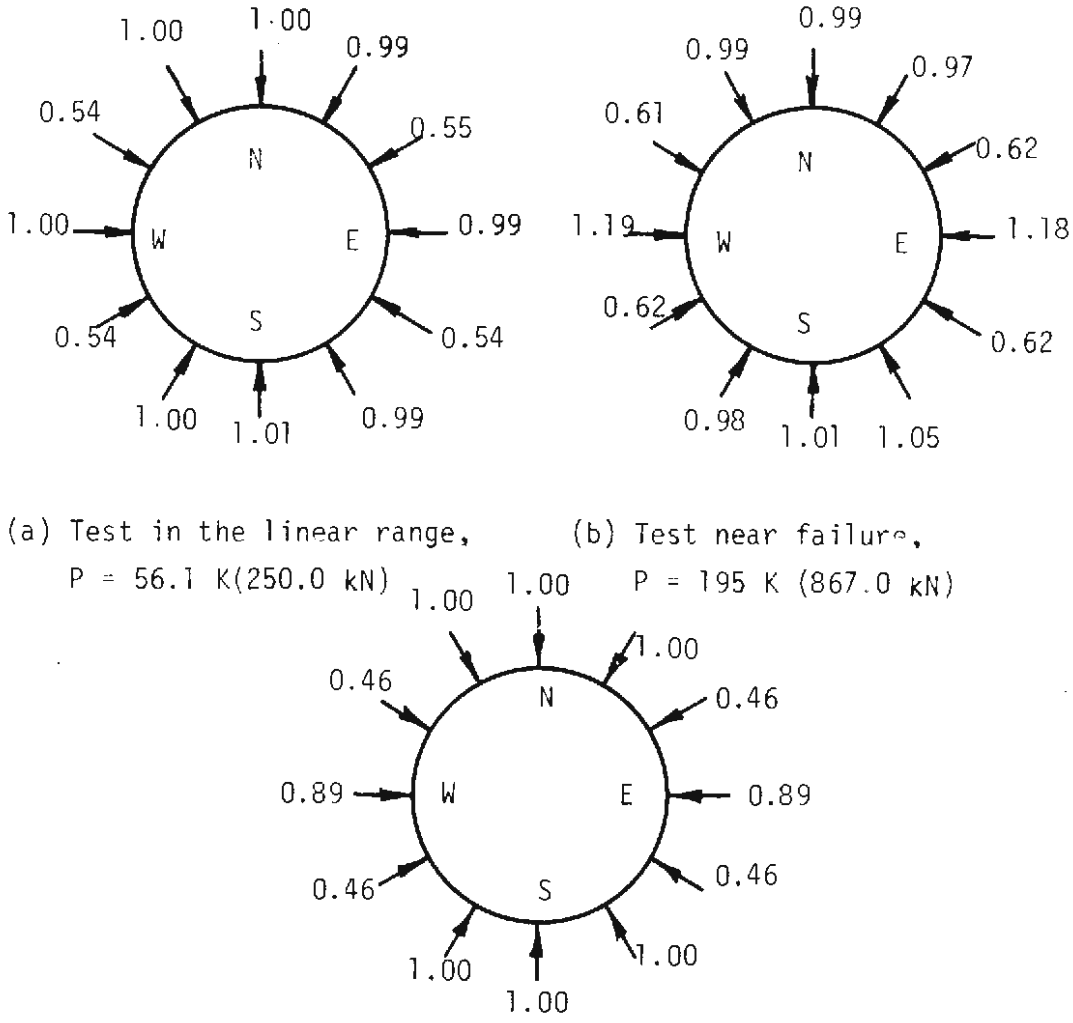

(a) Test in the linear range, P = 56.1 K(250.0 kN)

(b) Test near failure, P = 195 K (867.0 kN)

(c) Linear analysis

FIGURE 4.36 DISTRIBUTION OF LOADS FOR SPECIMEN C-2, TEST T-6

linear range. The linear analysis results shown in the figure will be discussed later.

The effect of passive jack stiffness on the load distribution in the linear range is shown in Fig. 4.37 for the two tests. From this figure, it is apparent that a passive stiffness is reached beyond which there is little change in load distribution; the test curves for specimen C-2 are relatively flat beyond a passive stiffness of about 1300 kips/in. (228 MN/m). Below this range there is an increase in passive loads relative to active loads as the stiffness increases. Comparing the curve for specimens C-1 and C-2, specimen C-1, the one with lower Young's modulus, has higher passive loads in the range of passive jack stiffness where the curves overlap; this demonstrates graphically that the less stiff liner transfers more load to the medium through thrust. Comparisons with the linear analysis will be discussed in the next section.

The curves of Fig. 4.37 show the changes in structure loading as it interacts with a passive resisting mechanism. The passive jacks may be thought of as representing, in a crude way, the geologic medium surrounding the liner. It has been recognized for a long time that the support loading depends on the relative stiffness of the support and the surrounding medium, and these curves show in a qualititave way how the liner loading changes as the relative stiffness changes. Also shown are the points which represent the loading distribution well beyond the linear range for specimen C-2 test T-6 (increment 19, Fig. 4.23), and it is apparent from the location of these points relative to the test curves for the linear range that the loading distribution changes as the mechanism of structural behavior changes even with the same passive resisting mechanism.

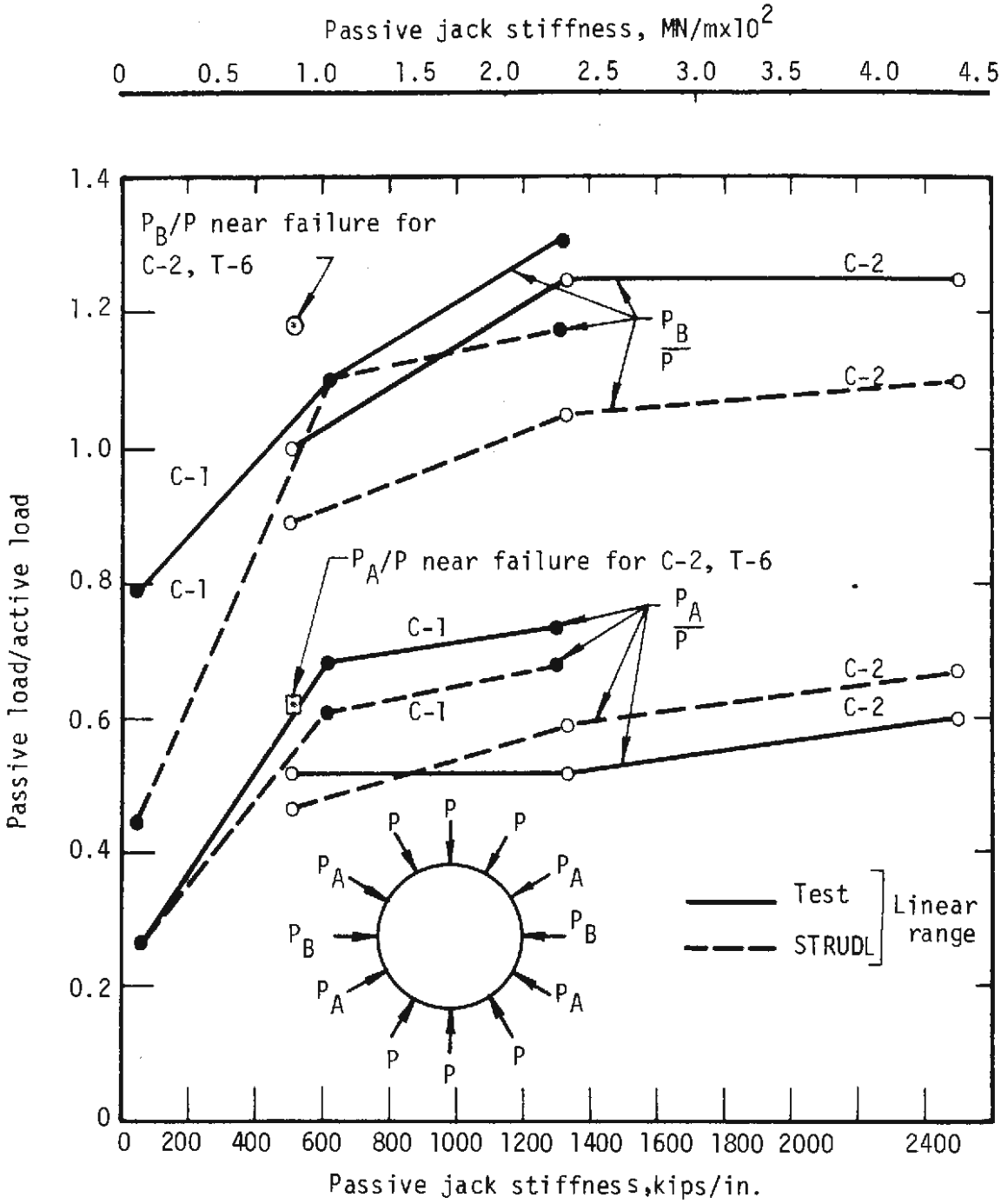

FIGURE 4.37 EFFECT OF PASSIVE JACK STIFFNESS ON THE PASSIVE LOAD DISTRIBUTION

The structural behavior of the liner and its relation to the changing load distribution will be discussed in the following paragraphs.

The thrust-moment relationship at selected sections in test T-6 of specimen C-2 (Fig. 4.29) indicates a relatively linear behavior at low loads. The load-deformation curves (Fig. 4.25) and the active-passive load relationships (Fig. 4.32) were also linear to about one-half the maximum load. The load increments are numbered on the curves of Fig. 4.29 for convenience in discussion and to permit comparison of thrust and moment at various sections at the same loading. The N section (Fig. 4.29) began to attract less moment at about load increment 9, and the thrust to moment ratio increased. There is a transition range between increments 8 and 11, and above 11 the thrust-moment ratio again became constant. The slope changes in the thrust-moment curve at the N section are accompanied by corresponding changes in slope for other sections shown in the figure. It appears that the N section was the first to reach its capacity, as indicated by its proximity to the moment-thrust failure envelope also shown on the figure, and therefore it triggered the change. A linear analysis of the loaded ring also shows that the N and S sections have the largest moment. When the N section began to resist less moment, an increase in moment occurred at the E section and 15 degrees S of E. The moment in the liner thus was redistributed to accommodate the reduction in moment capacity at the N (and S) sections, and it appears in Fig. 4.29 that the path of the moment and thrust at the N section follow the failure envelope.

The moment-thrust path along the failure envelope and the resulting redistribution of moments are an important part of the liner behavior and

influence its load capacity substantially. These points are discussed in more detail below. It is desirable to describe the failure envelope in more detail first.

The failure envelopes shown in the graphs of moment-thrust give the combination of moment and thrust for which an eccentrically loaded beam-column can resist the largest load. Thus the section which fails is loaded so that moment and thrust are proportional except for the effect of deflection due to bending of the beam-column. When a section is loaded so that its moment-thrust path reaches the envelope, it cannot go outside the envelope because the section cannot resist a larger moment at that thrust. An example of the general shape of the envelope is shown in Fig. 4.38. In the lower portion the load is limited by tension in the section and the envelope has a positive slope. An increase in thrust will then increase the moment that the section can resist. This is called positive interaction. In the upper region the load is limited by compression in the section and the envelope has a negative slope. An increase in thrust decreases the moment that the section can resist. This is described as negative interaction. The two regions of the envelope have in common a point which is called the balance point because the two modes of failure occur simultaneously. Determination of the envelope is discussed in Chapter 3 and example envelopes are shown in Figs. 3.20 to 3.22.

The mechanism that permits a moment-thrust path for a section to coincide with the failure envelope can be described by following the path on the qualitative moment-thrust-curvature graphs of Fig. 4.39. The numbered points on each graph correspond to the same conditions at the section. In Fig. 4.39(b) the section curvature is shown for each point on the moment-

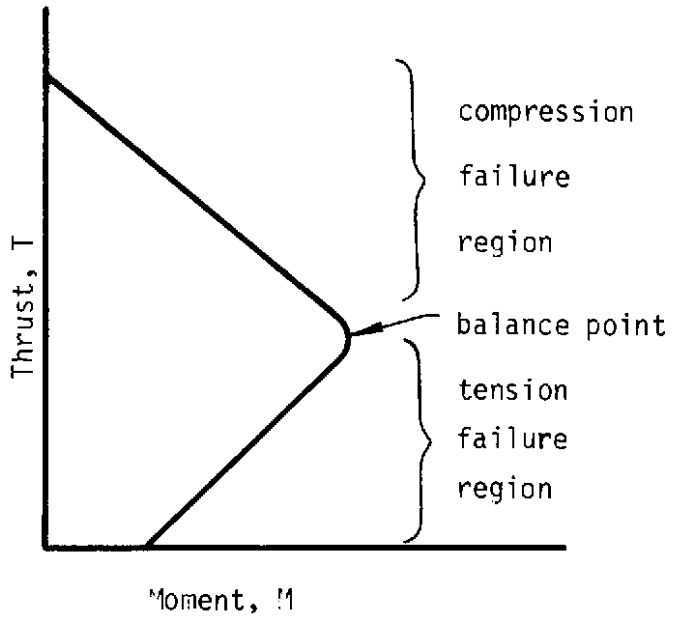

FIGURE 4.38 MOMENT-THRUST FAILURE ENVELOPE FOR THE SECTION

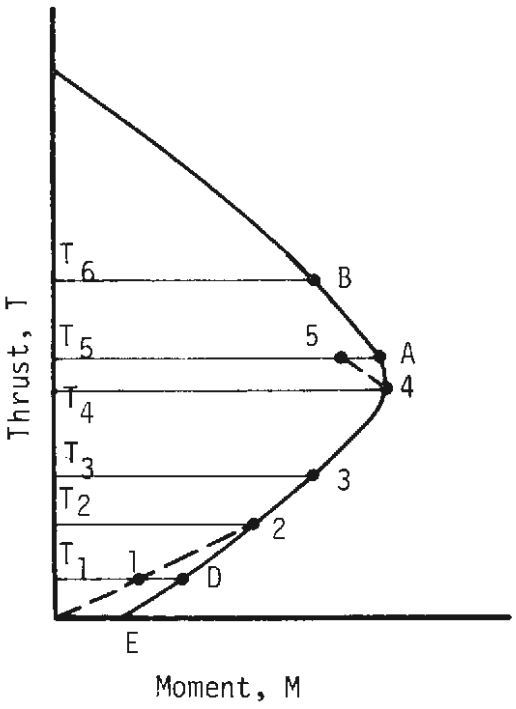

(a) Moment-thrust failure envelope

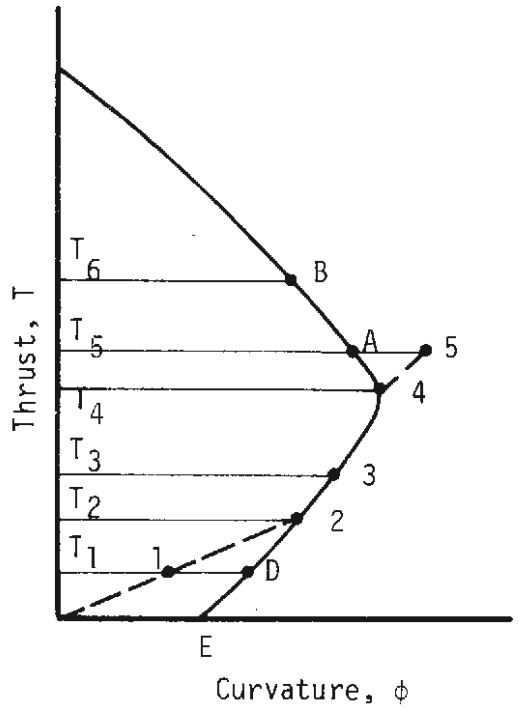

(b) Thrust-curvature envelope at failure

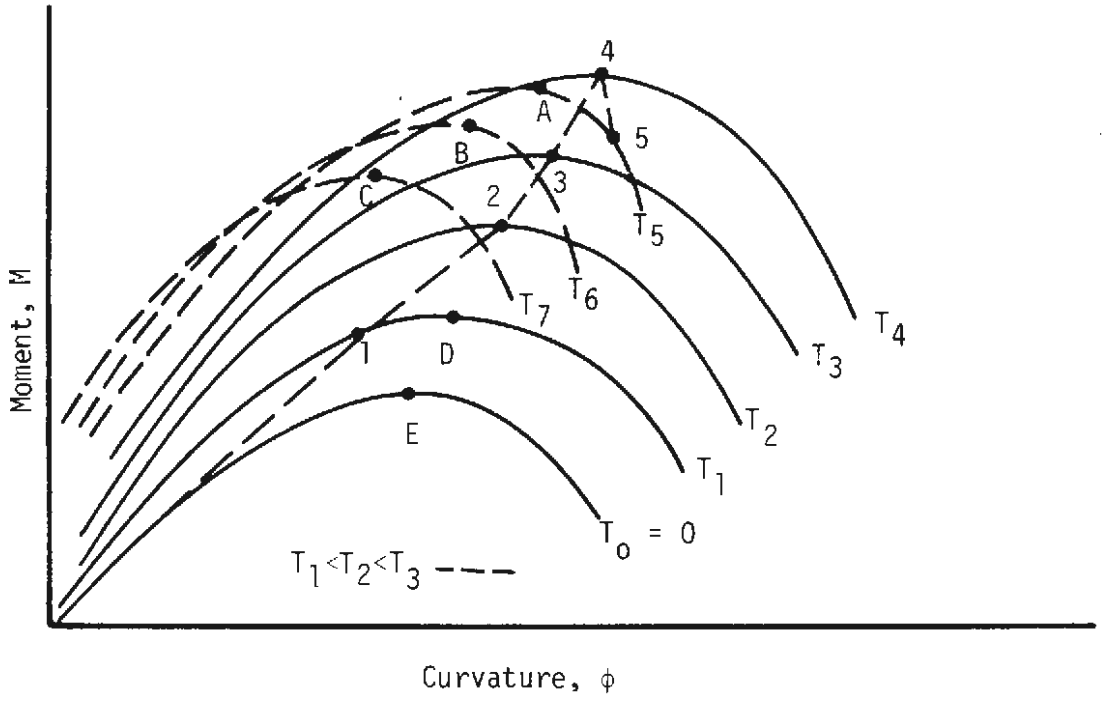

(c) Moment-curvature curves at constant thrust

FIGURE 4.39 IDEALIZED MOMENT-THRUST-CURVATURE RELATIONSHIPS FOR THE LINER SECTION

failure envelope of Fig. 4.39 (a). Moment-curvature relationships at constant thrust are shown for the section in Fig. 4.39(c). The relative positions and general shape of these curves are as shown. The peak (maximum moment) of each curve defines a point on the failure envelope. At point 2 the moment-thrust path has reached the envelope in Fig. 4.39(a) and the section has the curvature ϕ_2 shown in Fig. 4.39(b). This point also corresponds to the peak on the moment-curvature curve at a thrust T_2. If the thrust at the critical section is increased to T_3 the moment must lie on the failure envelope at point 3, which corresponds to the peak on the T_3 moment-curvature curve. The point cannot lie outside the envelope because a moment is then implied that the section cannot resist (above the T_3 curve in Fig. 4.39(c)). The reason why the path does not go inside the envelope is not nearly as clear. Mathematical arguments are difficult because of the extreme nonlinearity of the system, but it is clear that the structural behavior as well as the section behavior must be involved. Intuitively, the path of the critical section must follow the envelope because the section will be forced to resist the maximum moment possible at a given thrust because the curvature continues to increase at the section. The maximum moment occurs at the peak of the moment-curvature curve which is on the envelope. It is not completely clear when the path leaves the envelope and goes inside the enclosed region, but it cannot follow the envelope above the balance point. This can be seen by observing the curves of Fig. 4.39. Point 4 is the balance point. An increase in load will result in an increase in thrust say to T_5 and an increase in curvature. From Fig. 4.39(c), in order to get to the T_5 curve and have a curvature larger than that at point 4, point 5 must lie below the peak of the T_5 curve. Thus the moment must be less than the maximum.

There is some evidence that the moment-thrust path of the critical section should follow the failure envelope to the balance point if the liner remains monolithic. In the tests a crack formed at the N section which continued to open. Thus the increased curvature was concentrated at the crack and the section that must resist the internal forces became smaller because of the crack. Further tests are in progress to define the failure mechanism and make it possible to predict the ultimate load and cracking load of the liner.

Test C-2 confirms the proposed general structural response in which the section moment-thrust path follows the failure envelope, but the maximum load was not obtained in the test due to failure of the passive jack system. It will be shown in the next section that major features of the behavior discussed above can be simulated by a nonlinear finite element computer program.

The discussion thus far has concerned only the structural behavior of a circular liner, as the loading was never intended to represent a true ground loading. It is possible, however, to draw some very general conclusions about the liner-ground interaction. There are two distinct problems in evaluation of the real liner behavior. One is the behavior of the liner subjected to given loadings, and the other is the loading variation as the liner interacts with the ground. In these tests, the loading change due to change in stiffness of the structure has been demonstrated. Beyond the range of linear structural behavior, the loading changed as the structure cracked. These tests contained the interaction aspects of the real problem, that of the passive resistance of the ground on the sides of the liner.

Equivalent uniform loads in the active (N-S) and passive (E-W) directions can be obtained by dividing the total load components in these directions by the outside liner diameter. In this way the loading can be converted to more familiar terms by dividing the uniform passive load by the active load to obtain K, the earth-pressure ratio. When the liner began to crack and the moment at these sections became rather constant, K approached 1.0. The total maximum load in the N-S direction was 682 kips (3.03 MN) and in the E-W direction 679 kips (3.02 MN) for specimen C-2 increment 20. These loads represent an average load of 11.3 kips/ft^2 (541 KPa) and a hoop stress in the liner, assuming all the load to be resisted by hoop compression, of about 800 psi (5.52 MPa) or 9 percent of the concrete compressive strength. The maximum load reached on specimen C-1 corresponds to a hoop stress of 170 psi (1.18 MPa) or about 11 percent of the compressive strength.

Both specimens displayed considerable deformation which resulted primarily from deformation of the passive resisting mechanism while the specimen still resisted considerable load. This would be true of a ground loading also; as long as the ground provides sufficient passive force for the liner to resist active load by arch action even after its moment capacity is exceeded, it would continue to take load. Cracking began at loads of 20 to 30 percent of the maximum load reached in these tests.

Cracking is a function of the relative amounts of thrust and bending deformation, which depends on the passive jack stiffness. The material properties and amount of steel fiber present will also influence the initiation and propagation of cracks. Cracks were first detected at a ratio of diameter change divided by diameter of 0.0015 for specimen C-2 and 0.0028

for C-1, but the corresponding loads were a small percentage of the maximum load.

4.7 COMPUTER SIMULATION OF BEHAVIOR

4.7.1 LINEAR ANALYSIS

A linear frame analysis program (STRUDL) was used for planning the test program and later the results were compared with the initial behavior of the test specimens. Linear analyses are used for support-medium interaction studies and for structural design of supports. It is therefore useful to discuss these comparisons in order to place the linear analysis in perspective.

The full circular liner was represented by two straight beam elements between each load, with all joints lying on the circle representing the mid-depth of the liner. Concentrated loads were applied at the joints in the same locations as in the test, but all loads were perfectly radial and symmetrical in location and magnitude. A radial rod was used to represent the passive jacks; the axial stiffness of the rod was adjusted to match the average passive jack stiffness. Results of the analysis are shown on most of the graphs which portray the test results in Section 4.4.

If the geometric representation of the liner is adequate, and the initial slope representing the material behavior is used, the initial slope of the test and analysis curves should correspond reasonably well. This is particularly true since the passive jacks exhibited a linear behavior. There are several reasons, however, why agreement with the tests might be poor. The mathematical representation assumes that the liner material is homogeneous;

therefore, cracks in the concrete would cause poor agreement with the test. An important approximation used in this study was that the loads are symmetrical whereas in reality there were local variations from the ideal loading in both the active and passive forces. Because point loads are assumed the analysis results in a moment distribution around the liner which is a series of straight lines with peaks at the loads. The loads in the tests were distributed over about 8 in. and resulted in a curved moment diagram which rounds off the peaks under the loads.

The magnitude of disagreement between the initial slopes of relationships obtained in the test and in the analyses depends a great deal on what is compared. Those quantities which represent gross behavior, such as diameter change, are insensitive to minor variations in load as long as the overall loading is nearly correct, whereas local quantities, such as moment at a section, are very sensitive to small load variations in the vicinity. A part of the moment at a section results from the eccentricity of the thrust resulting from the curvature between loads, so the error resulting from geometric approximation depends on the magnitude of thrust and the accuracy of the geometric approximation.

Load-deformations computed by the linear analysis for specimen C-2 agree reasonably well with the test curves in their initial slopes as shown in Figs. 4.24 and 4.25. The passive jack stiffness used was the average of those measured in the tests, and the initial modulus of the liner was obtained from the control cylinder tests. Moment-thrust curves from the analysis in general do not agree nearly as well with the test curves as shown in Figs. 4.26-4.29, although the comparison is good for Test T-6. The poor comparison of moment-thrust initial slopes is

probably not due to inadequacies of the analysis, but results from not representing in every detail what occurred in the test.

The linear analysis moment-thrust path for the N section reached the predicted failure envelope at a thrust of 120 kips (534 kN) in Fig. 4.29 (specimen C-2, test T-6) which corresponds to an active load, P, of 83 kips (369 kN). By the linear analysis this represents the predicted failure of the section and thus of the liner. The liner actually resisted more than twice this load and might have resisted much more if the passive load system had not failed. Thus, for predicting ultimate load, the linear analysis is much too conservative.

It may be possible to use the linear analysis to predict cracking loads for the liner provided the correct cracking criterion is used. Reference to Fig. 4.29 shows that two visible cracks had formed near the S side of specimen C-2 in test T-4 before the linear analysis would have predicted failure at a thrust of 120 kips (534 kN). The first crack at increment 4 (Fig. 4.29) would have occurred at a tensile stress at the north section of 880 psi (6.07 MPa) according to the linear analysis. The modulus of rupture for the control specimens of specimen C-2 was 1590 psi (11.0 MPa). However, as mentioned in Section 4.2.2, specimens cut from the failed ring and tested in flexure showed a modulus of rupture of only 705 psi (4.86 MPa); consequently, the control specimens probably were not representative of the tensile strength of the specimen owing to differences in fiber orientation. Moreover, the modulus of rupture is not a good criterion for cracking of fiber reinforced concrete because of its post-crack resistance. The peak load on the flexure specimen is used to calculate the modulus of rupture using an assumed linear stress distribution. Actually,

the peak load occurs after a crack has formed and tensile stress at the extreme fiber has fallen off. Thus another means of finding the cracking stress is required since the conventional modulus of rupture is a measure of ultimate strength in tension which for fiber reinforced concrete, is larger than the cracking strength.

The stiffness of the system computed by the linear analysis is shown in Fig. 4.35 as a function of the passive jack stiffness. This analysis shows the trend in system stiffness reasonably well since the computed curves, especially that for specimen C-2, are parallel to the test curves. It would appear, however, that the analysis overestimated the stiffness for specimen C-2 since the computed curve is above the test curve. Also the analysis underestimated the stiffness of C-1 beyond a passive jack stiffness of 600 kips/in. (105 MN/m). The only difference in the two linear analyses is the Young's modulus of the liner material. The material properties obtained from the control specimens listed in Table 4.2 were used. The stiffness of the system when the passive jack stiffness is zero represents the liner stiffness with only the six active loads applied, and thus shows the influence of the passive jacks on the combined stiffness.

A nonlinear analysis is needed to describe adequately the progressive cracking and ultimate load; these descriptions are needed because cracking affects the serviceability and ultimate load determines the safety of the liner. A program which has a nonlinear capability was obtained and the initial results from its use are described in the following section.

4.7.2 NONLINEAR ANALYSIS

The structural analysis program developed by NASA called NASTRAN was used to represent the tunnel liner passive jack system. This program

has the capability to represent nonlinear behavior due to nonlinear material properties or due to geometry changes during loading. Only the first type of nonlinearity has been used, and only a few problems have been solved. This program will represent the features of the concrete liner and jacking system which allow it to behave much like the test specimen; that is, it will compute a nonlinear load deflection curve, and the moment-thrust path of the critical section in the liner will follow the failure envelope.

Two straight elements were used between loads with the dimensions shown in Fig. 4.40. Each element consisted of seven longitudinal rods connected at the ends by radial rods, and with shear panels between the longitudinal rods as shown also in Fig. 4.40. Shear is resisted only by the shear panels while bending is resisted by longitudinal forces in the rods. A piecewise linear stress-strain curve that is different in tension and compression can be described for the rods. The general shape of the curve used was that of the concrete up to maximum stress, but it remained flat beyond the peak because the program will not allow a descending branch.

Linear radial springs were used to represent the passive jacks and point loads were applied at the nodes between the elements. The model is the same as the one used in the linear analysis except for the details of the element itself, and the fact that only one quarter of the liner was actually represented with the boundary conditions based on assumed symmetry.

The load-deformation and moment-thrust curves for an example problem are presented in Figs. 4.41 and 4.42 to show the behavior of the model. The stress-strain curve used for the example is shown on Fig. 4.41. In Fig. 4.41 the N-S diameter change shows a decidedly nonlinear curve, while the

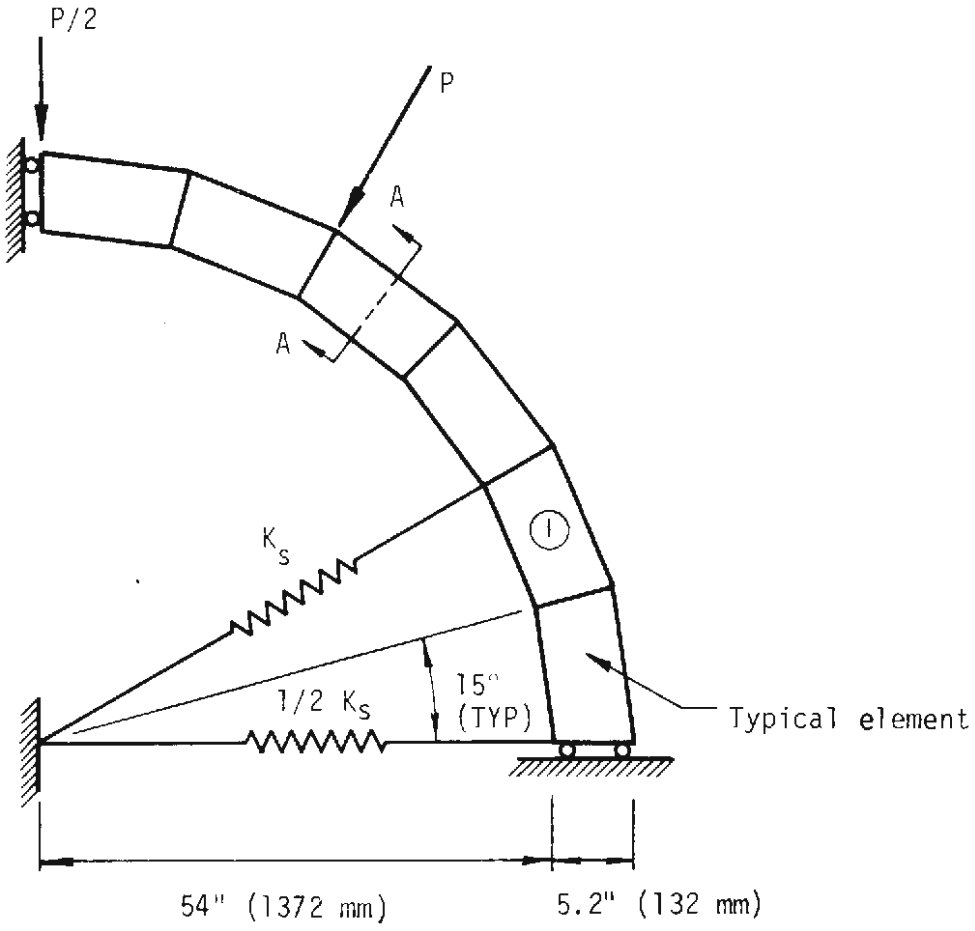

(a) Finite element assemblage

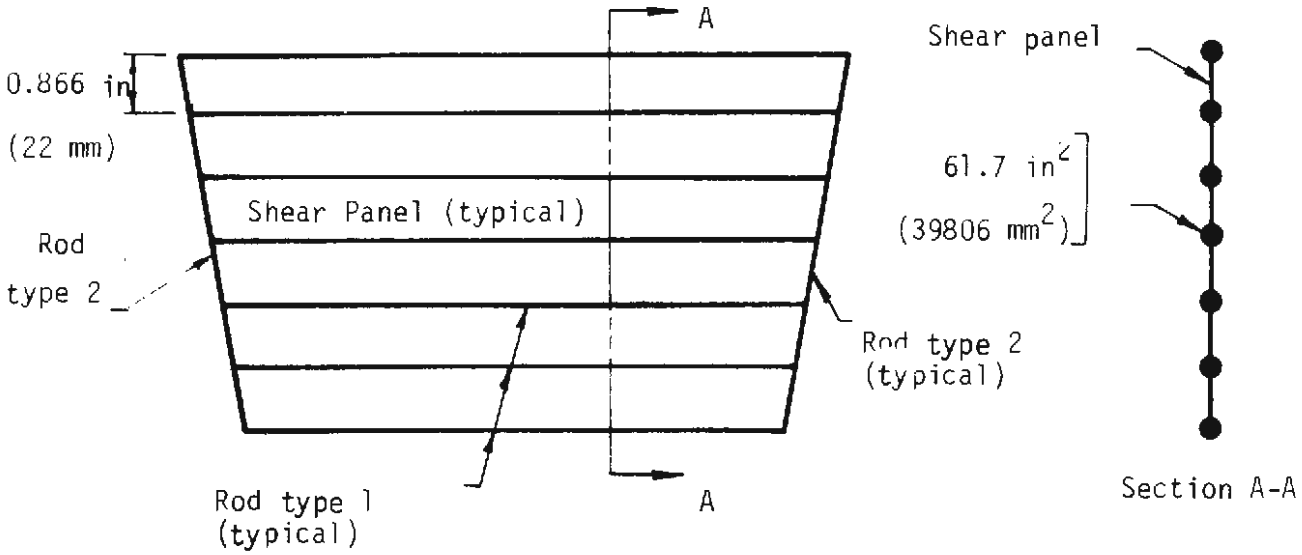

(b) Typical finite element composed of rods and shear panels

FIGURE 4.40 MODEL USED IN THE NONLINEAR ANALYSIS

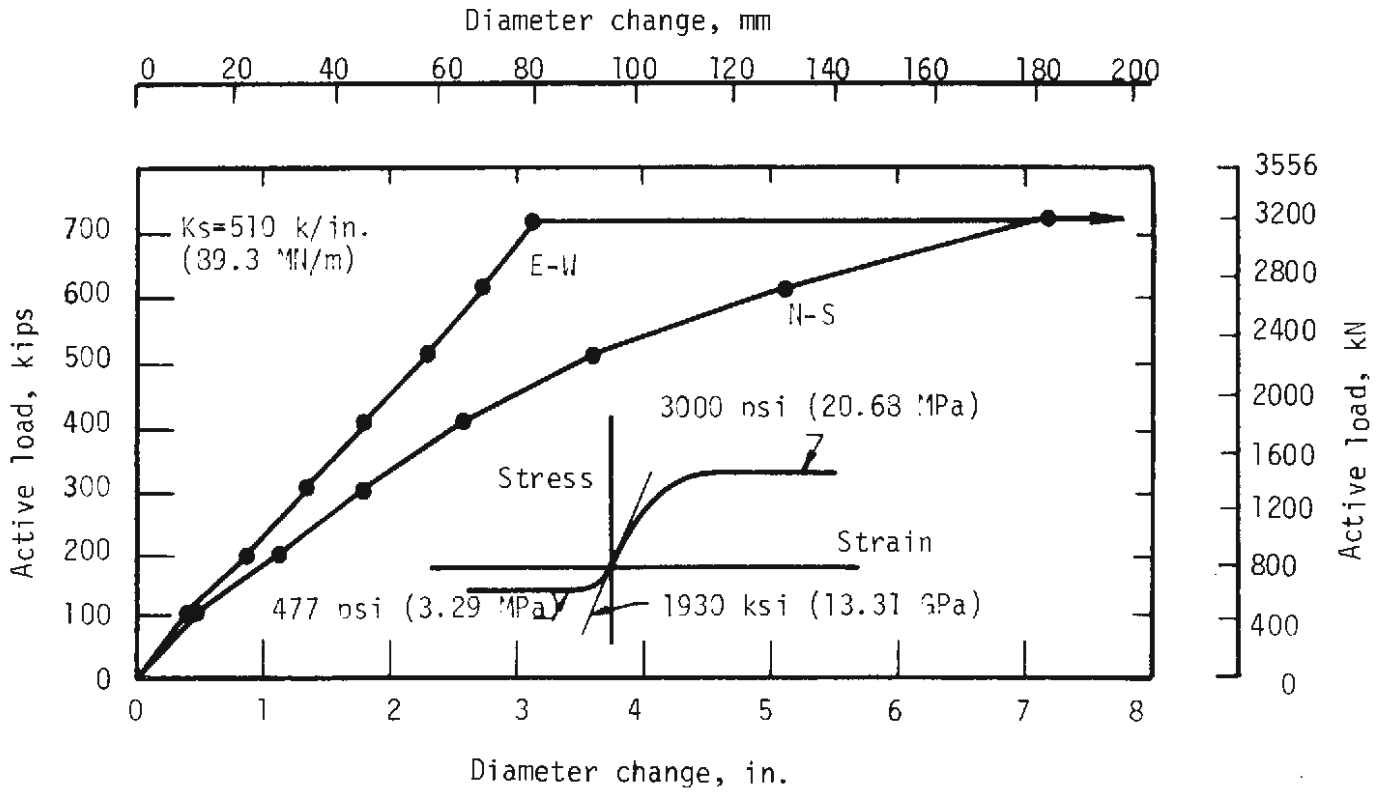

FIGURE 4.41 LOAD DEFORMATION FOR NONLINEAR ANALYSIS EXAMPLE PROBLEM

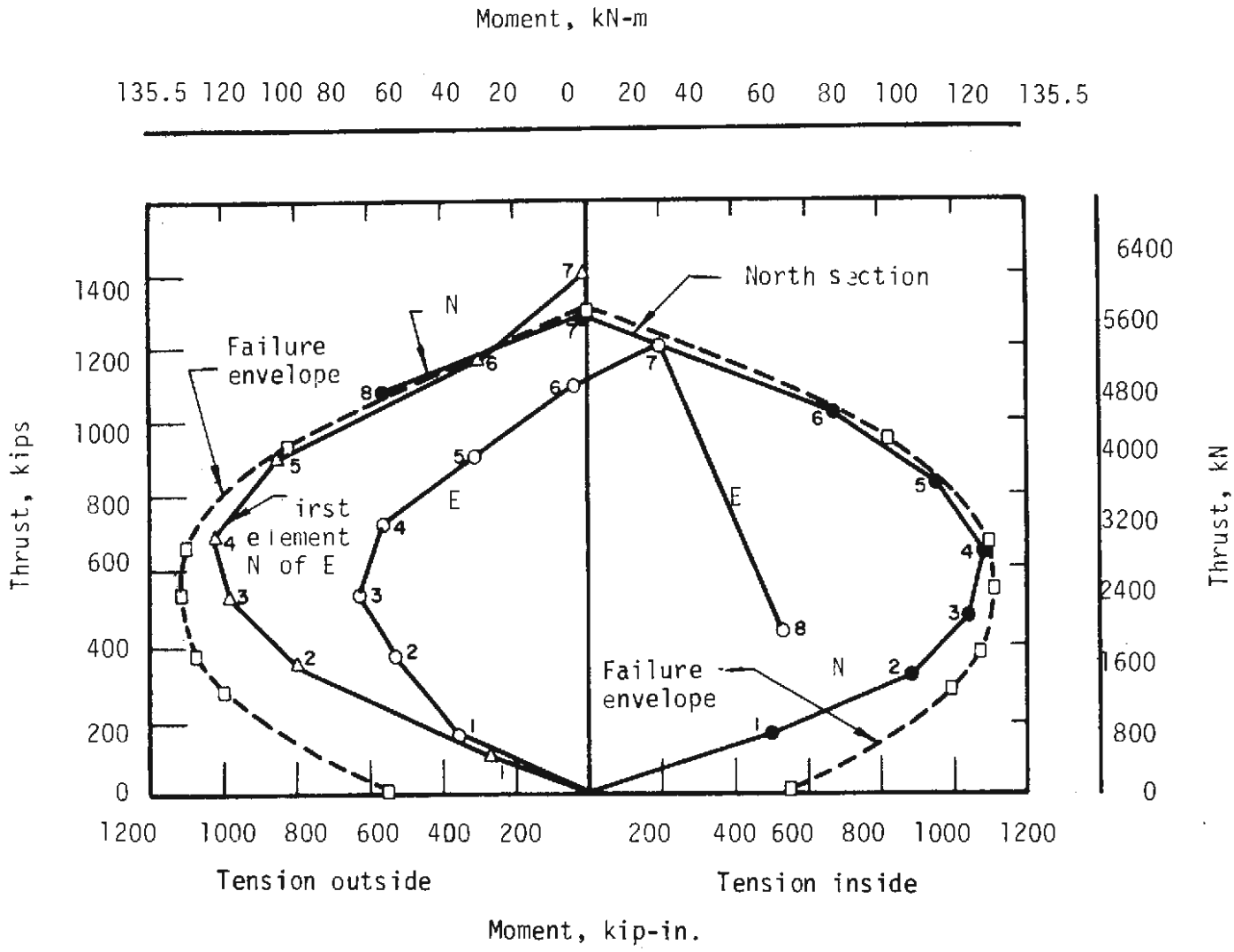

FIGURE 4.42 MOMENT-THRUSTS FOR NONLINEAR ANALYSIS EXAMPLE PROBLEM

E-W curve is almost linear to failure. The E-W diameter change depends heavily on the imposed passive jacks which have a linear load-deformation so it is reasonable for the E-W curve to be more linear.

The moment-thrust paths for sections at the N, E, and just N of E are shown in Fig. 4.42 and display shapes much like those of Fig. 4.29 for specimen C-2, test T-6. The stress distribution at the corresponding section for each load increment is shown in Fig. 4.43 where each curve is keyed to the corresponding point on the curve in Fig. 4.42 so the section behavior can be followed. The curves follow the trend described in Section 4.4 up to the balance point, and it is clear here that the compression strain grows rapidly and the tension strain becomes smaller after the failure envelope is reached. At the north section, the neutral axis moves first toward the compression face and then toward the tension face of the liner. Maximum thrust is reached when the entire section has maximum compression stress, but at this condition no moment can be resisted. Finally, the maximum load on the liner is reached when the maximum thrust is reached at several sections.

The failure envelope shown in Fig. 4.42 was obtained from the nonlinear analysis by applying load to a small beam-column consisting of the same elements used for the liner with the same stress-strain curve. An eccentric load was applied to the beam-column, and the moment and thrust plotted is that which occurred at maximum load just as if a series of experiments were performed as described in Section 3.3 to determine the envelope.

The moment-thrust paths of critical sections continue to follow the failure envelope above the balance point in the nonlinear analysis while it is argued in Section 4.4 that this cannot occur. The difference occurs be-

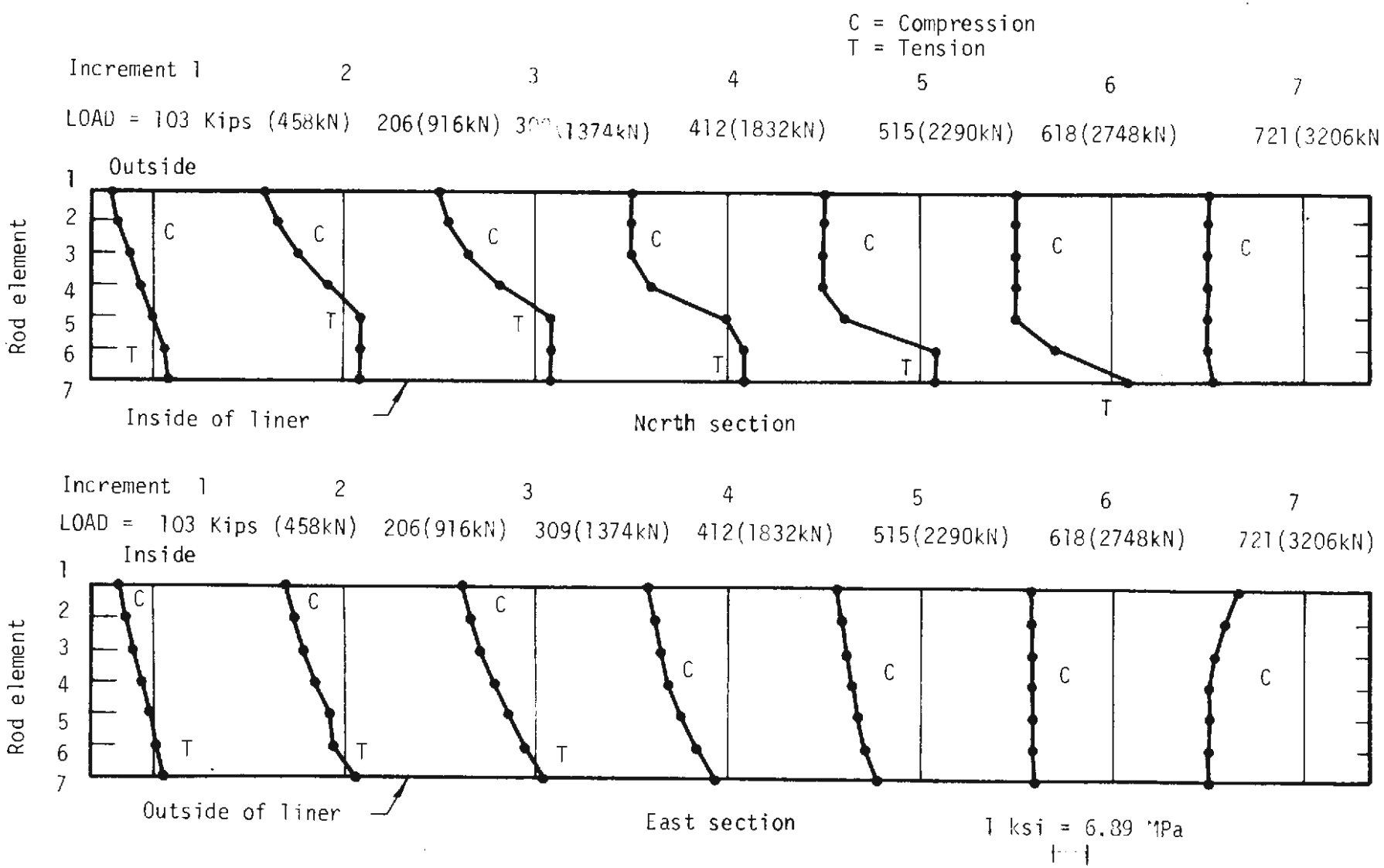

FIGURE 4.43 STRESS DISTRIBUTION AT EACH LOAD INCREMENT FOR THE NONLINEAR ANALYSIS EXAMPLE PROBLEM

cause, in the nonlinear analysis the stress-strain curve is not allowed to have a descending portion beyond the peak, and the resulting fully-plastic region of behavior allows the path to remain on the envelope.

A nonlinear analysis of Specimen C-2, test T-6, was made using the material properties obtained from the control specimens. However, comparison of the analysis with the test results indicated that the model was too stiff; thus all stresses on the stress-strain curve were reduced in the same proportions at each strain until the initial slope of the load-deformation curve of the liner matched the test curve as shown in Fig. 4.44(b). The resulting stress-strain curve is shown on Fig. 4.44(a). Above an average load at each active load point of 100 kips (445 kN) the model is still too stiff (Fig. 4.44(b)). It is also stronger than the specimen. This is shown by comparing the computed response to failure in Fig. 4.44(a) to the maximum load in the test from Fig. 4.44(b). The model is expected to be stronger because of the premature failure of the test specimen. Figure 4.45 compares the computed and measured moment-thrust paths for the N and E sections. The poor agreement for the E section probably results because there are not enough elements in the region just N of E in the Model to represent the sharp moment gradient which results there from the high load in the E passive jack. The analytical model will be refined in this region to investigate this problem.

Since a discrete model is being used to represent a generally continuous material, the model does not necessarily behave like the continuous structure. For this reason it is reasonable to expect that the material properties might need to be modified to account for this difference. The analysis is useful only if it is understood beforehand how to make the model behave like the real material. This can be done by studying the

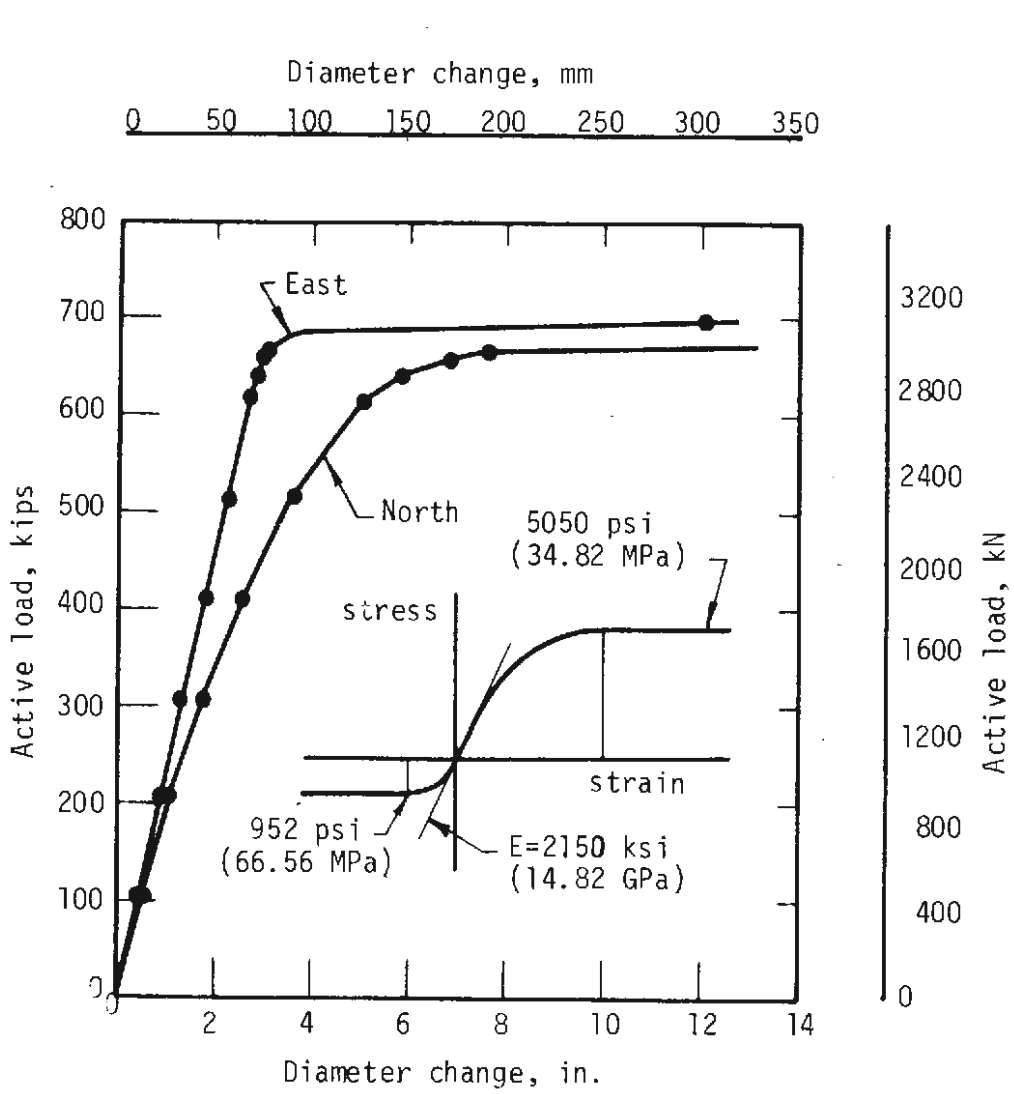

(a) Results of nonlinear analysis

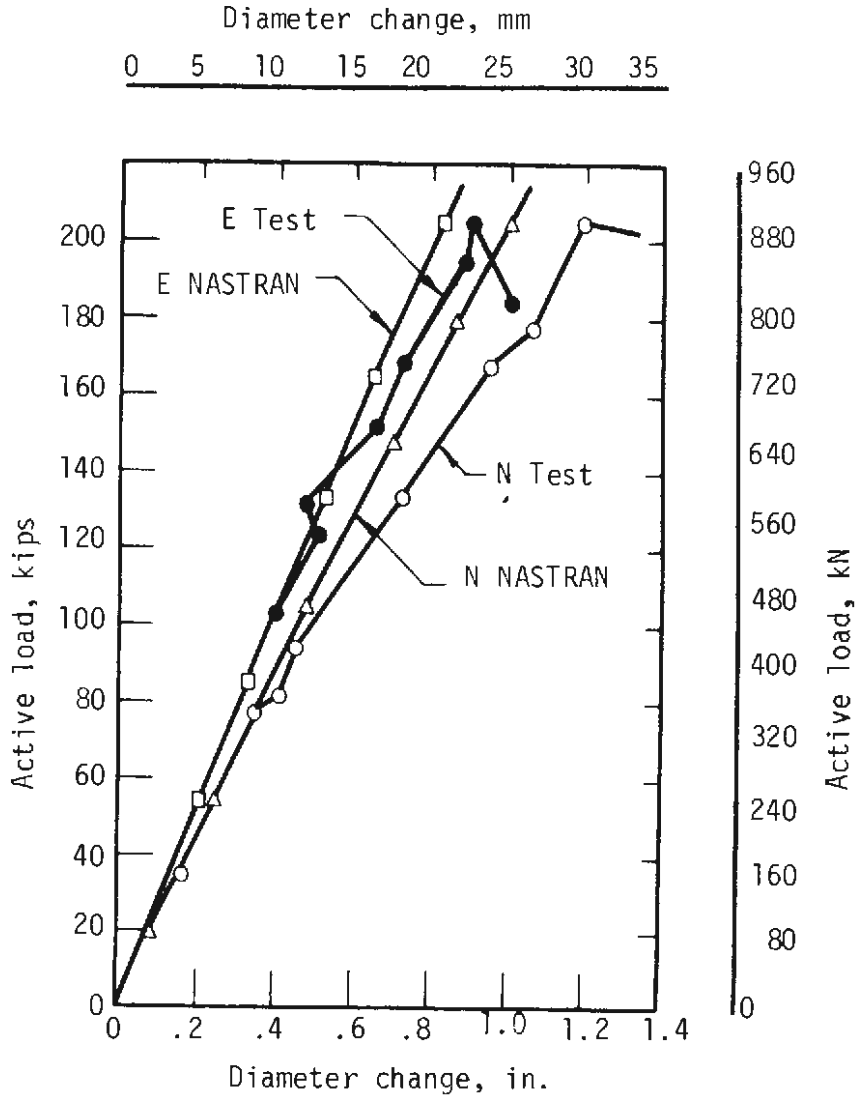

(b) Comparison of test with nonlinear analysis

FIGURE 4.44 LOAD-DEFORMATION CURVES FOR SPECIMEN C-2, TEST T-6 AND THE NONLINEAR ANALYSIS

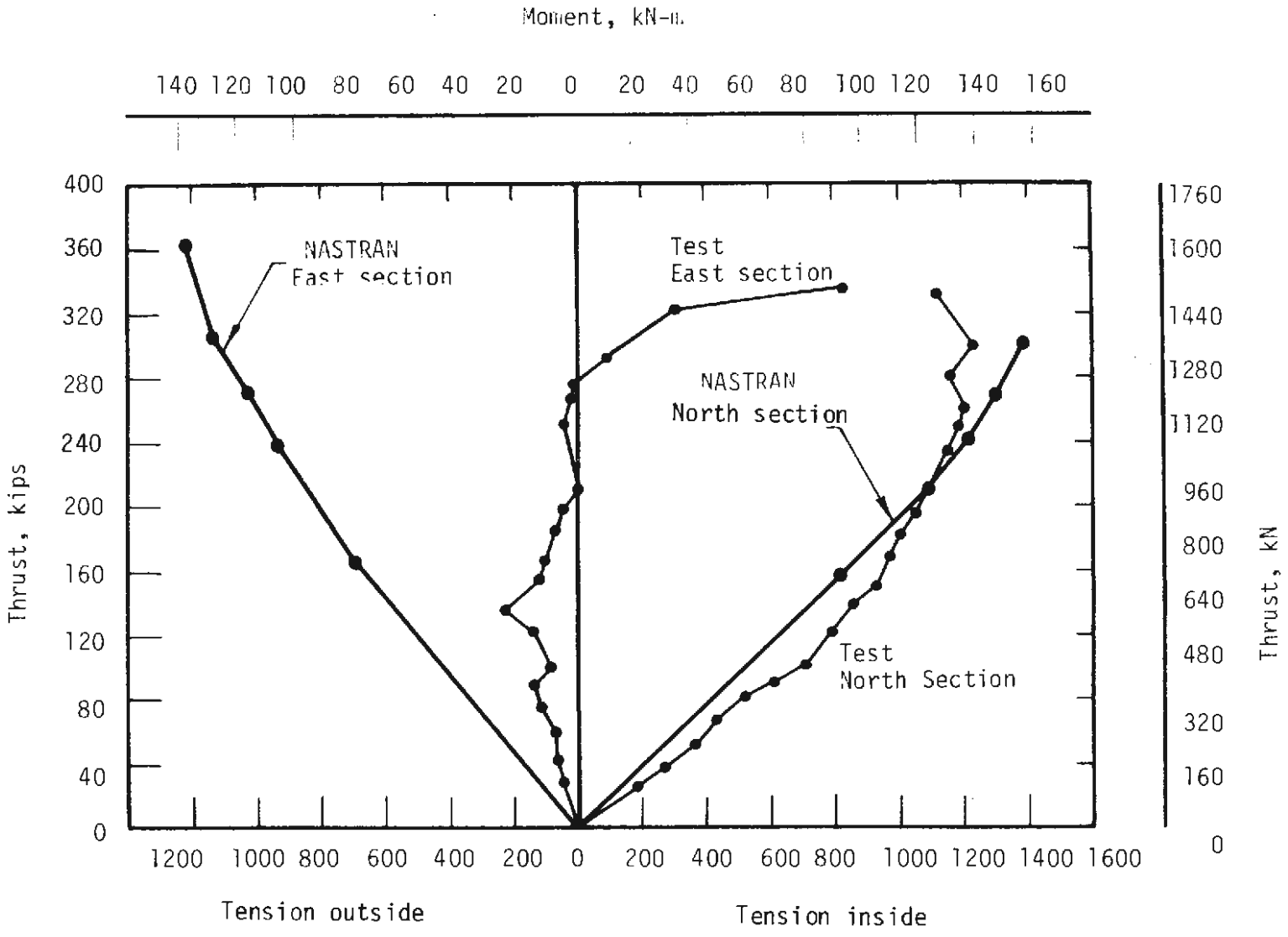

FIGURE 4.45 MOMENT-THRUST FOR SPECIMEN C-2 TEST T-6 AND THE NONLINEAR ANALYSIS

element alone and the representation of very simple structures like the beam-column tests described in Section 3.3, to obtain the correct material behavior of the basic element. These studies are in progress.

The weaker tensile strength of concrete is considered by this analysis, but the effect of tensile cracking and a descending portion of the stress-strain curve cannot be represented. Further work is planned to refine the behavior of the nonlinear model, and then to use it to study the effect of various structural, ground and loading parameters on the liner response.

4.8 SUMMARY

Two continuous steel-fiber-reinforced concrete tunnel liners were tested and their behavior was found to be quite ductile. Confinement of the liner by the passive forces and the unique properties of the steel fiber reinforced concrete result in a combination of section and structural behavior which allows the moment-thrust path to remain on the failure envelope. Classical plastic analysis predicts this type of behavior for ideal plastic structures, but a fiber reinforced concrete member is far from ideal plastic.

Prediction of ultimate load remains uncertain. The maximum loads in the tests are not representative of the capacity of the specimens because of problems with the test arrangements. A hypothesis is presented which predicts that the critical section moment-thrust path (the N or crown sections in this case) can remain on the failure envelope until the balance point is reached. The mechanism of moment redistribution changes when the path goes inside the region enclosed by the envelope and depends on the

structural behavior. Prediction of ultimate load requires a nonlinear analysis which will allow the moment-thrust paths of all critical sections to be predicted accurately until the active load reaches its maximum value. Future work will be directed toward prediction of behavior to the maximum load.

A nonlinear analysis is described which allows the moment-thrust paths of critical sections to follow the failure envelope as required, but this analysis in its present form will not predict departure from the envelope because it will not allow the material to fail or the stress to decrease with increasing strain as it does in the real material for both compression and tension. Work is continuing to develop criteria which, in conjunction with the analysis, will allow prediction of failure. It will then be possible to vary the liner thickness, material properties, loading, confining mechanism, etc. and know the behavior and capacity of the liner. With this information, structural design of continuous steel-fiber-reinforced liners can be placed on a more rational basis. The procedure can be extended to other types of liners as well.

A linear analysis is compared with test results and it is found that a way to determine when cracking of a control specimen occurs and some criterion for cracking are needed to apply to the structure. The cracking mechanism of steel fiber reinforced concrete is very complex. The stress-strain curve increases almost linearly to a peak and the stress then drops sharply to some value where it remains almost constant with increasing strain until eventually it starts to drop off slowly. Cracking is not detected visually until after the peak stress is passed. Calculation of the modulus of rupture based on the peak load on a beam overestimates

the cracking stress. It is certainly reasonably to expect, however, that a linear analysis can predict cracking of the structure, but it has been shown that ultimate load is underestimated by a considerable amount.

Work is continuing in the experimental and analytic areas. Several more steel-fiber-reinforced and conventionally-reinforced liners will be tested to determine differences in their behavior and their ultimate loads. The analysis technicques will be refined further so the entire behavior can be predicted through cracking to maximum load.

The objective of these studies is to develop a means for design which will provide the most economical liner which meets adequate serviceability and safety requirements. The requirements for serviceability concern those quantities which might affect satisfactory performance such as cracking, permeability, etc. while safety concerns structural integrity. The criteria to be applied to each of these failure conditions are quite different and the desired safety factor may also be different. Thus, a thorough understanding of the cracking mechanism as well as capacity is necessary for a balanced and economical design.

CHAPTER 5

IMPROVEMENTS TO STEEL TUNNEL SUPPORTS

5.1 INTRODUCTION

The use of steel sets for tunnel supports is discussed in this section to show why certain studies were made and how they can affect design of the supports.

Steel sets may be shaped like horseshoes, 180-degree (3.14 rad) circular arcs with straight legs, circles, etc. They are jointed in order to make the pieces small enough to handle easily in a tunnel and the section is usually a wide-flange shape. The joints have nominal moment resistance, usually much smaller than that of the steel section itself, and there are a minimum number of bolts for ease and speed of erection. Joints influence the moment distribution around the set and thus affect its behavior and strength. Therefore, connections are one of the variables considered in this report.

In transportation tunnels steel sets with lagging provide only temporary support because a more durable and watertight support is ultimately required. The final liner generally is of continuous reinforced concrete, and the temporary supports may or may not be removed. In most cases the resistance of the steel sets cannot be considered in the long-term design of the tunnel because of the possibility of rusting of the steel. The short-term usefulness of steel sets is an important consideration in their design.

Rock tunneling requires support of the opening as close behind the face as possible, and supports are placed as soon as the face moves forward a

short distance. It is not possible to mine the opening to the exact dimensions of the sets, and there is often considerable overbreak of the rock. Therefore, it is necessary to place wood blocking between the set and the rock. The blocking is tightened by driving wedges between it and the set. This method of load transfer results in point loading in rather random locations. The loading at these points depends on the ground conditions, and in general is not uniform. Because of bedding planes and fault zones the rock may tend to move inward in part of the opening, so that load is applied to some blocking points while the others serve as points of reaction. These resisting or passive load points may have substantial influence on the deformation of the set, and usually affect its strength, but to a lesser degree. The passive load-deformation characteristics of a load point depend on the amount of blocking, the type of wood, its moisture content, the care with which it was placed, and other factors. The effect of blocking stiffness on set behavior is investigated in this study.

Neither the active loads nor the passive resisting forces are likely to act in the plane of the set, because the rock movement which produces the active loads may not be in the plane of the set, and because the wedges used to tighten the blocking are usually driven from only one side so that the load tends to act at the tip of one flange. Inclination of load relative to the plane of the set is considered in this report. Eccentricity of load relative to the cross section centroid is to be studied in the next phase of the project.

Because of out-of-plane loads and the possibility of lateral buckling, lateral support of the set is important. Some lateral support is provided by friction between the blocking and the set, but the amount of this resistance is

uncertain. In most cases tie rods are placed between the sets in a fixed pattern around the set. These rods may be combined with collar braces. Loading conditions along the axis of the tunnel may vary a great deal, and inclined loads and lateral movement in one region may cause the ties to transfer loads to sets in an adjacent region. In these studies one typical lateral support condition is considered.

The shape of the section used for the set may influence its behavior. If there are large twisting moments or significant moments perpendicular to the plane of the set, a shape with torsional resistance and weak-axis bending resistance larger than that of a wide-flange may be desirable. Such sections must be considered in terms of their cost, availability, and ease of connection as well as their improved resisting capacity. In this investigation a set with a square tubular section of approximately the same moment capacity as the wide-flange in the strong direction was tested for comparison with the wide-flange. The increased strength that can be realized by filling the tubular section with concrete was also investigated. Sets fabricated from steel pipe have been used in Japan, with concrete fill reserved as a means of strengthening the set should the need arise after it has been erected.

The objectives of the studies described in this chapter are to develop a better understanding of the behavior of steel sets and to suggest ways in which present design practice may be improved. To accomplish the first objective, a particular set configuration was tested and the behavior compared with computer analyses. The results of these studies are described in the latter sections of this chapter. To accomplish the second objective

some of the variables which affect steel set behavior were investigated. In some cases this was done experimentally while in others it was done by varying parameters in computer analyses. These studies are also described in this chapter.

In order to evaluate improvements in steel sets it is necessary to determine what behavior is desirable and then determine how it is to be measured. The set strength can be measured in terms of total load, but distribution of the load affects the capacity. Thus, strength comparisons can be made only on the basis of a fixed loading configuration.

Behavior is usually discussed in terms of load-deformation characteristics. In general, a desirable behavior is one which allows considerable deformation before the set begins to lose resistance. This gives visual evidence of distress and allows remedial measures to be taken before a collapse occurs. Also, the deformation may allow the rock to mobilize some of its own resisting capabilities to help relieve the set. Thus it is the displacements at the load points which are of interest.

5.2 SECTION BEHAVIOR

5.2.1 DESCRIPTION OF TESTS

The two standard steel shapes that were used for the sets tested in this program were the wide flange M4 x 13 ordered to ASTM Specification A36 and structural tubing TS4 x 4 x 1/4 (12 lbs/ft) ordered to Specification ASTM A501. A501 is essentially equivalent to A36 in mechanical properties. Twelve tensile coupons were tested to obtain properties of the steel in the

straight legs and in the curved or arch segments of the sets. Eight-inch (203 mm) specimens were tested with a 2-in. (51 mm) gage length according to ASTM A370 Specifications. Coupons from the curved sections were machined from the outer and inner surfaces, and therefore were in a circular form with a radius of about 5 ft (1.5 m). The coupons were not straightened but were placed in a testing machine with grips that are operated hydraulically. The grips were tightened and the spherical seat in the grips left unlocked so that the grips could turn and come into alignment as load was applied and the specimen straightened.

Stub column tests were performed on each of the two types of cross section. The stub column test is a standard test described by the Column Research Council, 1967. In this test a length of member long enough to retain a representative residual stress distribution and short enough not to fail by primary buckling is subjected to uniform compression in a universal testing machine. The stub column tests were performed in a 600 kip (2670 kN) MTS universal testing machine using the "displacement control" mode of operation. The adjustment of the machine heads to obtain a uniform strain application made use of both mechanical and electrical resistance strain gages. The specimen geometry, preparation, tolerance and test procedure followed the procedures recommended by the Column Research Council. Table 5.1 summarizes the tests performed.

5.2.2 TEST RESULTS

Tension tests were carried to rupture while the load-strain curves

TABLE 5.1

SUMMARY OF TENSILE COUPON

Section	Description of section	No. of tensile tests	No. of stub column tests
Tube	4 x 4 x 1/4	2	1
Wide flange	M4 x 13	2	1
Curved tube	4 x 4 x 1/4	4*	0
Curved wide flange	M4 x 13	4*	0

*2 specimens from each flange

were plotted automatically. Figure 5.1 shows the stress-strain curves for the various tests. Yield stresses for curves 1 and 2 were determined by the offset method at 0.2 percent strain. The proportional limit σ_{PL}, yield stress σ_y, tensile strength σ_u and percent elongation Δ/L determined from these curves are given in Table 5.2, where the values reported are the averages of the results of tests noted in Table 5.1.

Stub-column stress-strain curves were reported in Parker, et. al., 1973 and are repeated here for convenience in comparing them with the results for the concrete-filled box section. The average yield strengths in stub column tests compare well with those obtained in the tensile coupon tests from the straight sections and the shapes of the stress-strain curves are similar. The M4 in Fig. 5.2 shows a nonlinear relationship above 32 ksi (221 MPa) and

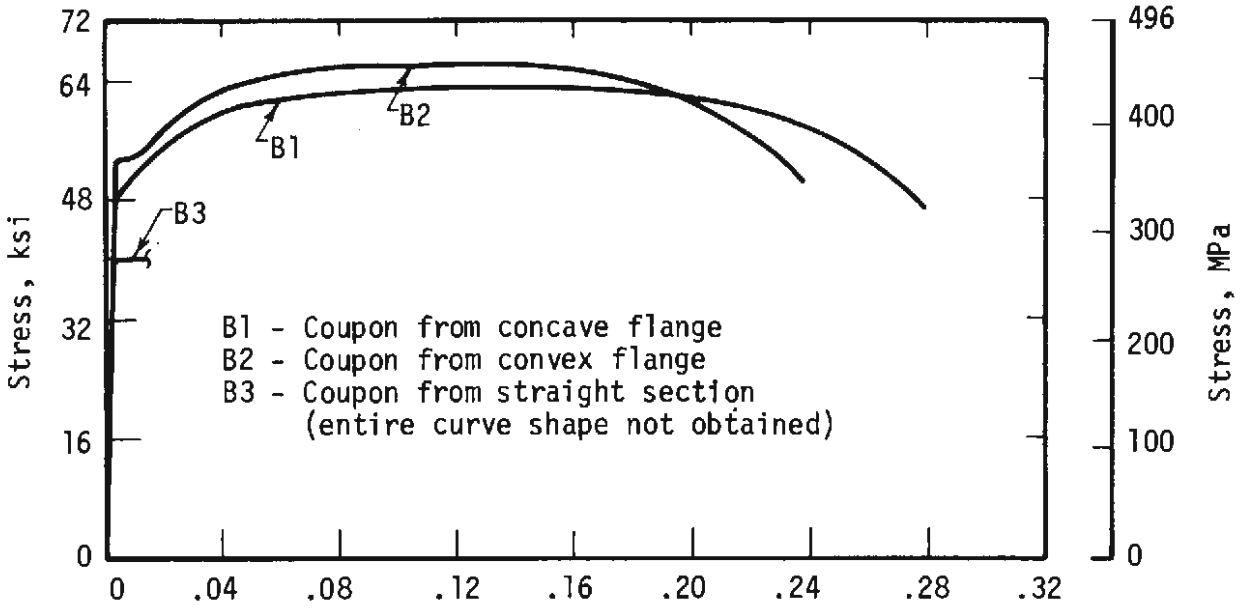

(a) Coupons from TS 4 x 4 x 1/4 in. section

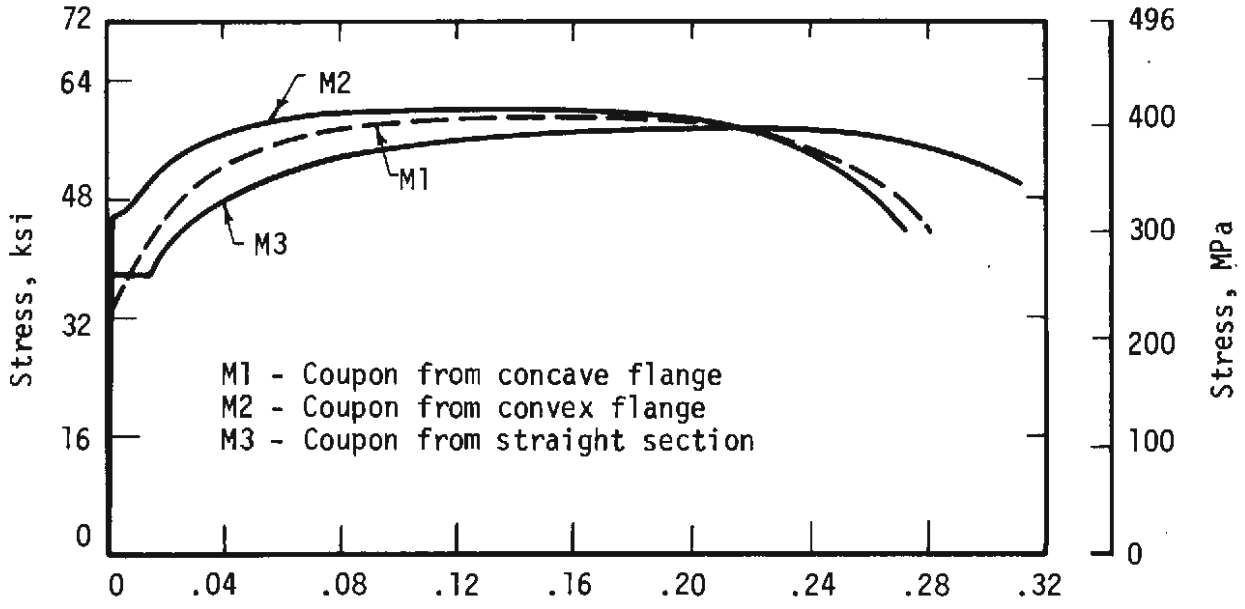

(b) Coupons from M4 x 13 section

FIG. 5.1 STRESS-STRAIN FOR TENSILE COUPON TESTS

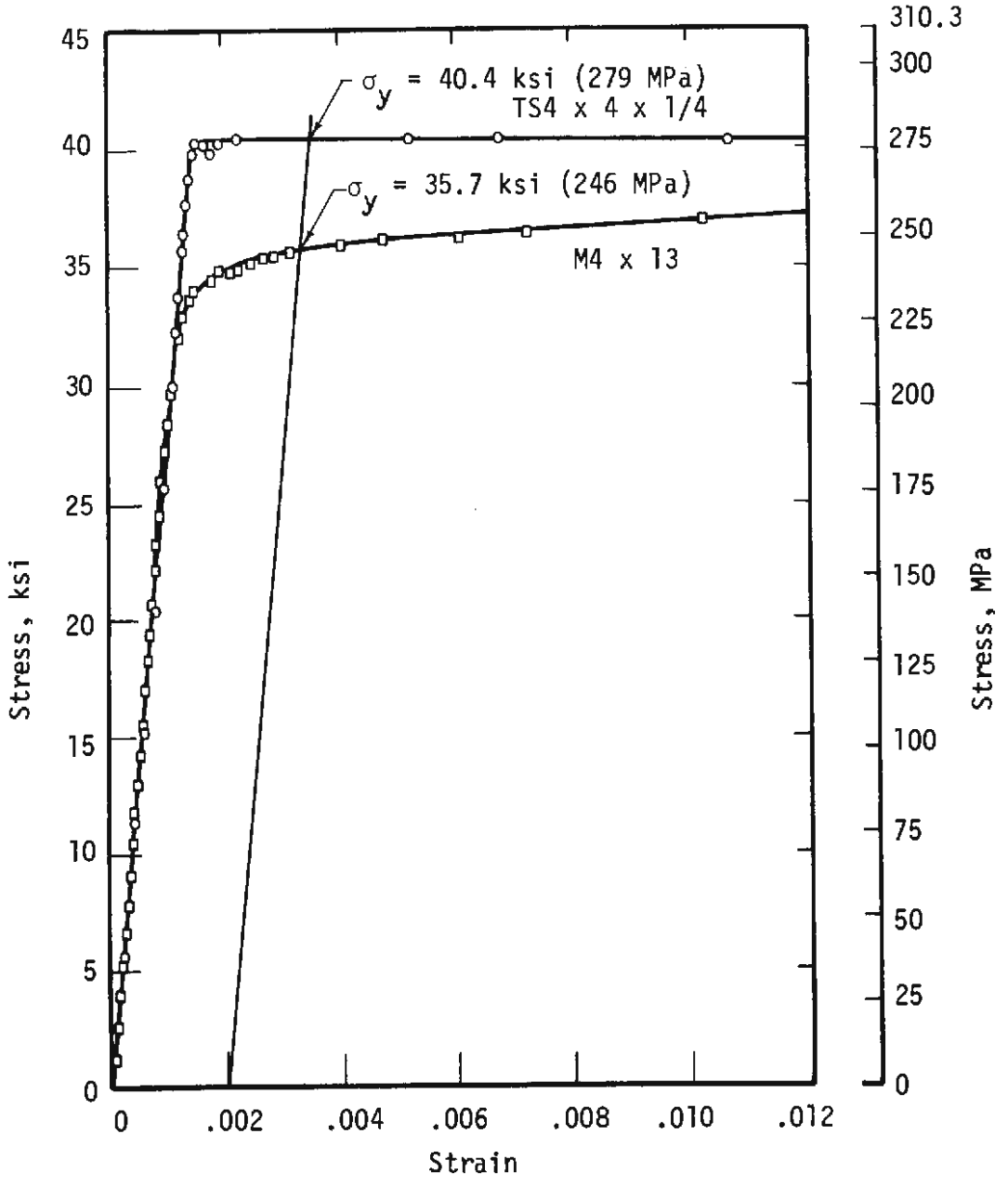

FIG. 5.2 STUB COLUMN TESTS FOR THE WIDE FLANGE AND STRUCTURAL TUBE SECTIONS

TABLE 5.2

COUPON TENSILE PROPERTIES

Test*	σ_{PL}, ksi (MPa)	σ_y, ksi (MPa)	σ_u, ksi (MPa)	Elongation, percent
B1	47.15 (325.1)	53.03 (365.6)	65.04 (448.4)	28
B2	50.00 (344.7)	54.00 (372.3)	67.20 (463.3)	24
B3	40.00 (275.8)	43.70 (301.3)	66.20 (456.4)	--
M1	33.06 (227.9)	34.68 (239.1)	60.08 (414.2)	28
M2	46.56 (321.0)	48.85 (336.8)	60.69 (418.4)	28
M3	37.66 (259.7)	37.66 (259.7)	58.06 (400.3)	28

*See Fig. 5.1 for description of test specimen

lacks a sharp knee, probably because of the residual stresses typical for hot-rolled wide flange shapes. On the other hand, the curve for the tubular stub columns is sharply yielding in character, which is indicative of a section that is essentially free of residual stresses.

The coupon properties of the cold-formed arch segments differ from those of the straight sections and depend on the location of the specimen in the section. This is because of cold working during bending and for the arch portion of the tube section, the curvature of the coupon, which was the same as that of the arch. Coupons taken from the arch portion and straight portion of the M4 section were machined straight. Cold working leaves residual stresses in the material which tend to round off the knee at the yield point of the stress-strain curve, possibly enough to eliminate the yield plateau. This is shown by the curves of Fig. 5.1 for the M4. Here the yield plateau is absent

in the cold-worked specimens and the ultimate stress is higher. The comparison is not so clear for the tube because the difference in the properties of the straight and curved sections results both from cold working and the curvature of the arch coupons. The concave face of an arch coupon is well into the yield range from straightening the coupon during testing, which alone would eliminate the yield plateau. However, the yield plateau would be absent also because of cold working in forming the arch, as shown for the M4. But the effect of the curvature of the coupon for the tube would not increase the tensile strength or change the stress-strain curve beyond the yield range, so any increased tensile strength can be attributed to cold working.

There appears to be a slight difference in the effect of cold working on the convex and concave faces of the arch segments. Coupons from the convex face of both the M4 and the tube show a slightly larger tensile strength than those from the concave face. There appears to be no significant difference between the tensile strengths of the coupons from the straight and the arched segments. In any case, the differences are so small that a general conclusion cannot be drawn from such a limited number of tests.

5.2.3 CONCRETE FILLED STRUCTURAL TUBE SECTION BEHAVIOR

STUB COLUMN TESTS

Six stub columns 18.5 in. (470 mm) long were tested, two for each of three strengths of concrete, in the 600 kip (2670 kN) MTS universal testing machine. Strains were measured at midheight on the exterior surface of two opposing sides of the steel tube. Lateral deflection at midheight was measured with dial gauges. The tests were conducted as prescribed by the Column Research Council. Figure 5.3a shows the load-strain curve for an unfilled section and

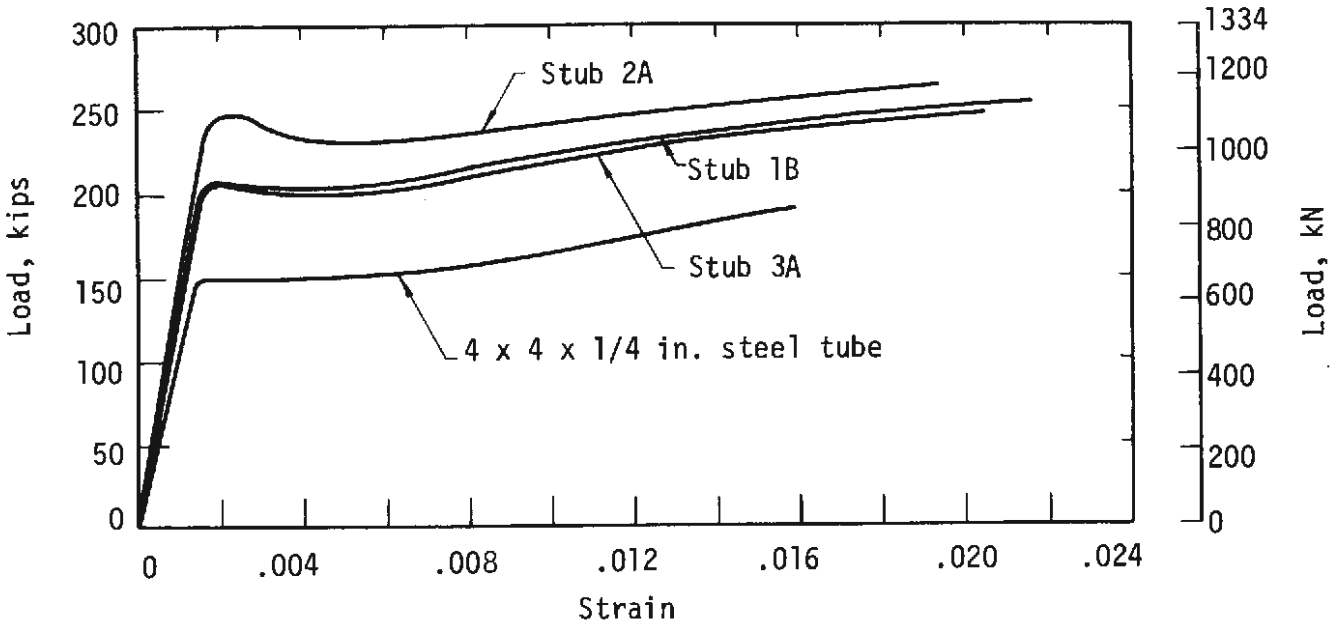

(a) Load-strain for filled and unfilled stub columns

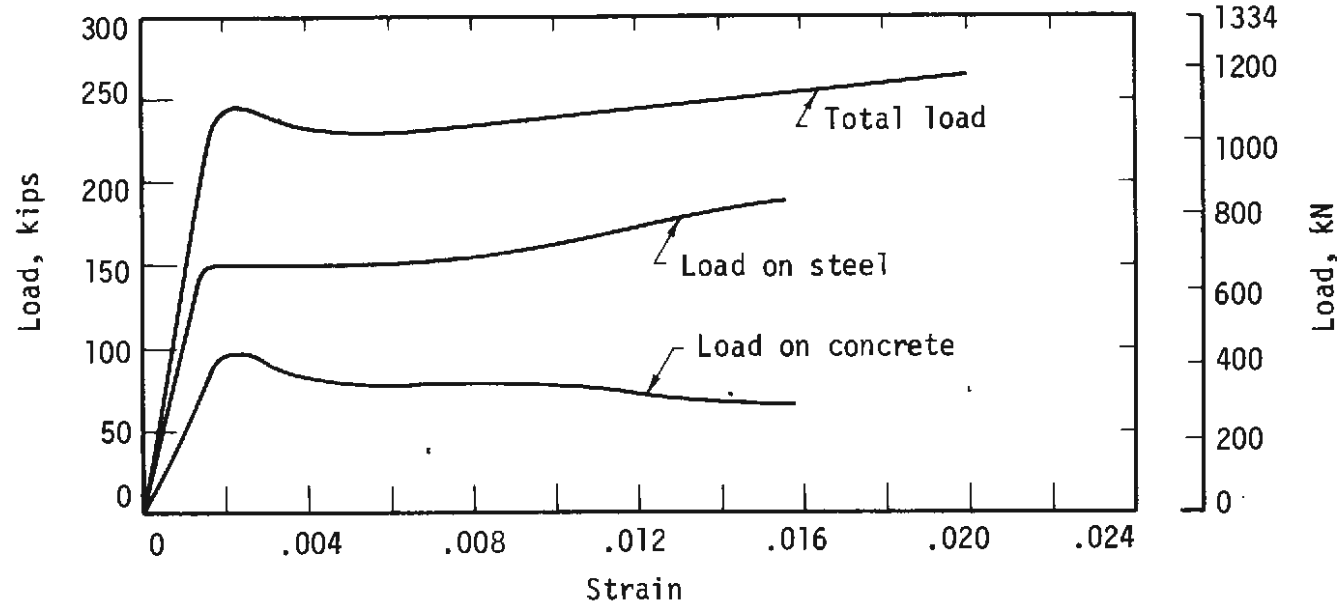

(b) Load-strain for components in structural tube and in concrete for test 2A

FIG. 5.3 LOAD-STRAIN FOR STUB COLUMN TESTS OF STRUCTURAL TUBES

three of the concrete-filled sections. Strains in this figure less than .0015 were determined from strain gage readings. Strains larger than .0015 were derived from the curves of applied load vs. machine-head deflection which were plotted continuously during the test.

The first peak that develops in the load-strain curve of the concrete-filled section is assumed to determine the yield load P_y. This is followed by a slight decrease in load, after which the load increases until the ultimate strength P_u is attained. Values of P_y and P_u for the six specimens are given in Table 5.3. Values of P_y were computed by adding the compressive strength ($f'_c A_c$) of the concrete core to the yield strength ($\sigma_y A_s$) of the steel tube from the stub column tests. Values of P_u were computed by adding $f'_c A_c$ to the ultimate strength ($\sigma_u A_s$) of the steel tube, where σ_u was obtained from tensile coupons. The computed yield loads are within 5 percent of the test values but the computed ultimate values are not consistent with the corresponding test results. It will be noted that the 87 percent increase in strength of the 7.26 ksi (50.1 MPa) concrete over the 3.89 ksi (26.8 MPa) concrete produces a 20 percent increase in yield strength P_y, but only 5 percent in P_u.

An estimate of the division of load between the steel and the concrete of the filled box stub 2A of Fig. 5.3a is shown in Fig. 5.3b. Ordinates to the curve labeled "load on concrete" were obtained by subtracting the test values of the steel tube curve of Fig. 5.3a from the ordinates to the stub 2A curve. The resulting concrete strength curve is typical.

TABLE 5.3

STUB COLUMN TEST RESULTS FOR
CONCRETE-FILLED STRUCTURAL STEEL TUBES

Test no.	Concrete strength, kips/in.^{2} (MPa)	Yield load, P_y, kips (kN)	Computed P_y, kips (kN)	Ultimate load, P_u, kips (kN)	Computed P_u, kips (kN)
Stub 3A	3.89 (26.8)	206.1 (916.7)	196.9 (875.9)	247.3 (1100.)	254.5 (1132.)
Stub 3B	3.89 (26.8)	207.4 (922.5)	196.9 (875.9)	249.5 (1110.)	254.5 (1132.)
Stub 1A	4.93 (34.0)	199.9 (889.2)	209.6 (932.3)	250.9 (1116.)	267.2 (1189.)
Stub 1B	4.93 (34.0)	207.4 (922.5)	209.6 (932.3)	252.7 (1124.)	267.2 (1189.)
Stub 2A	7.26 (50.1)	247.6 (1101.)	238.1 (1059.)	263.1 (1170.)	295.6 (1315.)
Stub 2B	7.26 (50.1)	247.6 (1101.)	238.1 (1059.)	256.9 (1143.)	295.6 (1315.)

Specimen data:
1. 4" x 4" x 1/4" structural steel tube 18.5 in. (470 mm) long.
2. Steel area = 3.70 in.^{2} (23.9 cm^2).
3. Concrete area = 12.2 in.^{2} (78.7 cm^2).
4. Yield stress of steel = 40.4 ksi (279 MPa), from stub column test of tube alone.
5. Ultimate strength of steel = 55.9 ksi (385 MPa).

BEAM TESTS

Two simply supported beams filled with concrete were tested for each of the three different strengths of concrete shown in Table 5.4. The beams were 78 in. (1.98 m) long, with 6 in. (152 mm) extending beyond each of two end supports. Loads monitored with load cells were applied at the third points by a hydraulic jack. Plates were welded on the ends of the tubes to prevent the possibility of concrete movement to the outside. Surface strains on the steel were measured at midspan, while deflections were measured with dial gauges at midspan and under each of the two loads. Results are shown in Table 5.4 and Fig. 5.4.

An arbitrary definition of the moment capacities, M_u, given in Table 5.4 is taken as that moment which occurs at a midspan deflection of L/100 where L is equal to the span length. For these tests this value was 0.66 in. (16.8 mm). A definition of this type was required for these tests since near and beyond the yield point the strain and deflection readings became highly time dependent; that is, a reading taken immediately after a particular load was applied was substantially different from one taken 30 seconds later. In all tests this deflection occurred just beyond the linear range.

As can be seen from the three moment-curvature curves of Fig. 5.4 the correlation between beam strength and concrete strength is poor. There is practically no increase in moment capacity due to filling the tube with concrete. Since the concrete can take very little tension the only source of increased moment capacity comes from the upward movement of the neutral axis because of compression in the concrete. This allows a slightly larger amount of steel to develop tension to balance the resultant compression, which gives

TABLE 5.4

BEAM TEST RESULTS FOR
CONCRETE-FILLED STRUCTURAL STEEL TUBES

Test no.	Concrete strength, kips/in.^{2} (MPa)	Moment capacity, M_u, k-in. (kN-m)
SCB 3A	3.89 (26.8)	216.0 (24.40)
SCB 3B	3.89 (26.8)	227.2 (25.67)
SCB 1A	4.93 (34.0)	201.6 (22.78)
SCB 1B	4.93 (34.0)	191.6 (21.65)
SCB 2A	7.26 (50.1)	218.6 (24.70)
SCB 2B	7.26 (50.1)	219.3 (24.78)

Specimen data: 1. Overall length = 78 in. (1.98 m), span = 66 in. (1.68 m).
2. Other data, same as in Table 5.3.

a slight increase in moment. Strain measurements made during the tests did show a continuous, small upward movement of the neutral axis.

BEAM-COLUMN TESTS

Beam-column tests were conducted on six concrete-filled box sections, two for each concrete strength, and on one unfilled section. The beam-column effect was obtained by eccentric loading in a universal testing machine. Lateral deflections were measured along the length of the specimen with dial gages and strain readings taken at midspan. The specimen length was 34 in. (.86 m) with 19 in. (.48 m) clear between connections. The initial eccentricity was 4 in. (102 mm) for all specimens.

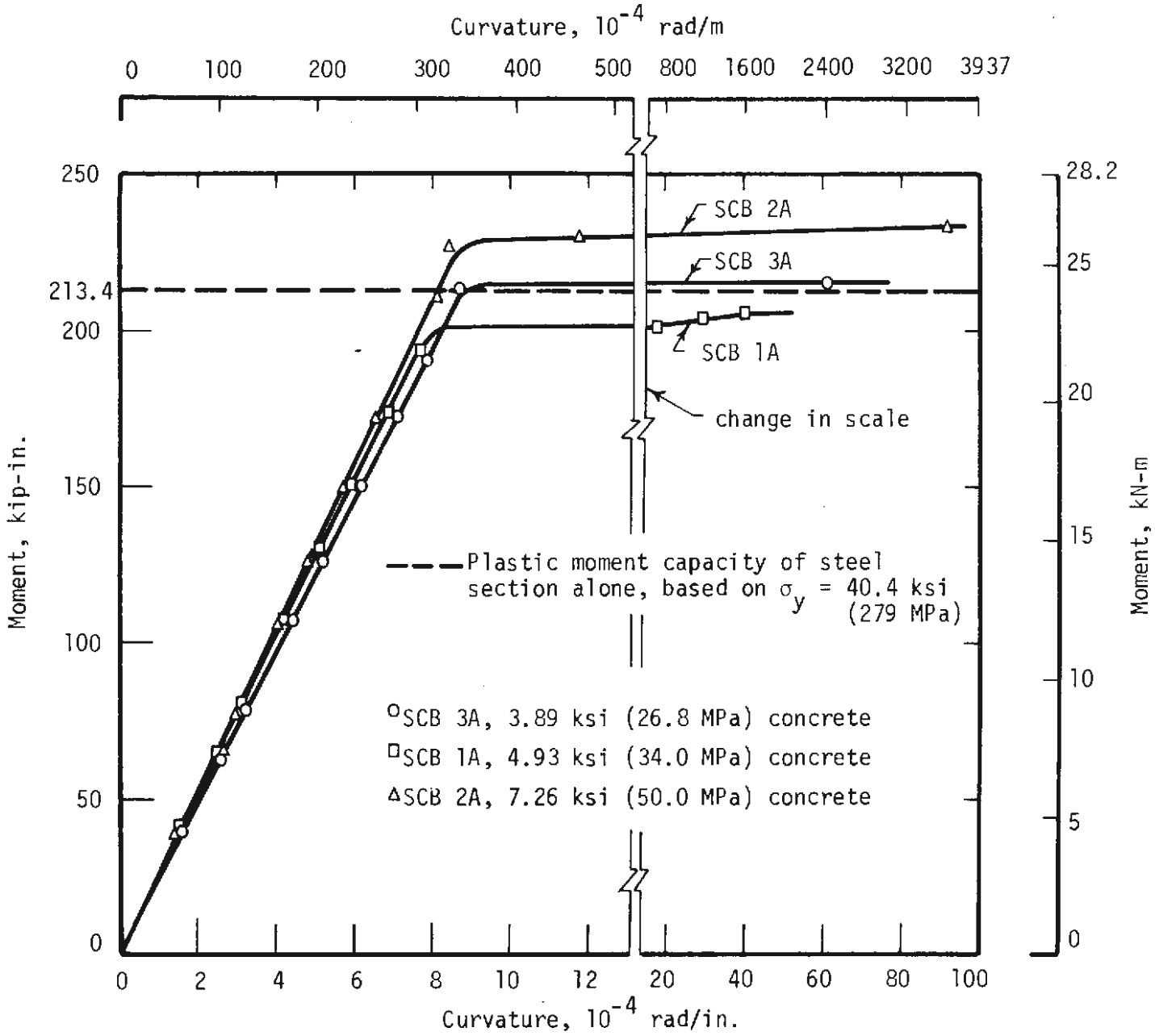

FIG. 5.4 MOMENT-CURVATURE FOR CONCRETE FILLED STRUCTURAL STEEL TUBE BEAMS

Moment-curvature plots are shown in Fig. 5.5. The moment capacity, M_u, given in Table 5.5 is taken to be the value from these curves at a curvature of 18×10^{-4} rad/in. (710×10^{-4} rad/m). Also shown are the increases in moment capacity attributed to the concrete. These are determined by subtracting the test value 200 in.-kips (22.6 kN-m) for the unfilled tube. It will be noted that the bending strength of the concrete-filled tube is not significantly larger than that of the unfilled tube except where high-strength concrete was used.

TABLE 5.5

BEAM-COLUMN TEST RESULTS FOR
CONCRETE-FILLED STRUCTURAL STEEL TUBES

Test no.	Concrete strength, kips/in.^{2} (MPa)	Moment capacity, M_u, k-in. (kN-m)	Increase in M_u due to concrete, percent
BCF 3A	3.89 (26.8)	217 (24.5)	8.5
BCF 3B	3.89 (26.8)	223 (25.2)	11.5
BCF 1A	4.93 (34.0)	223 (25.2)	11.5
BCF 1B	4.93 (34.0)	225 (25.4)	12.5
BCF 2A	7.26 (50.1)	249 (28.1)	24.5
BCF 2B	7.26 (50.1)	225 (25.4)	12.5

MOMENT-THRUST INTERACTION BEHAVIOR

Theoretical moment-thrust interaction curves for the concrete-filled sections and the unfilled steel tube are shown in Fig. 5.6. The concrete-filled sections are analyzed as composite sections. Development of the interaction

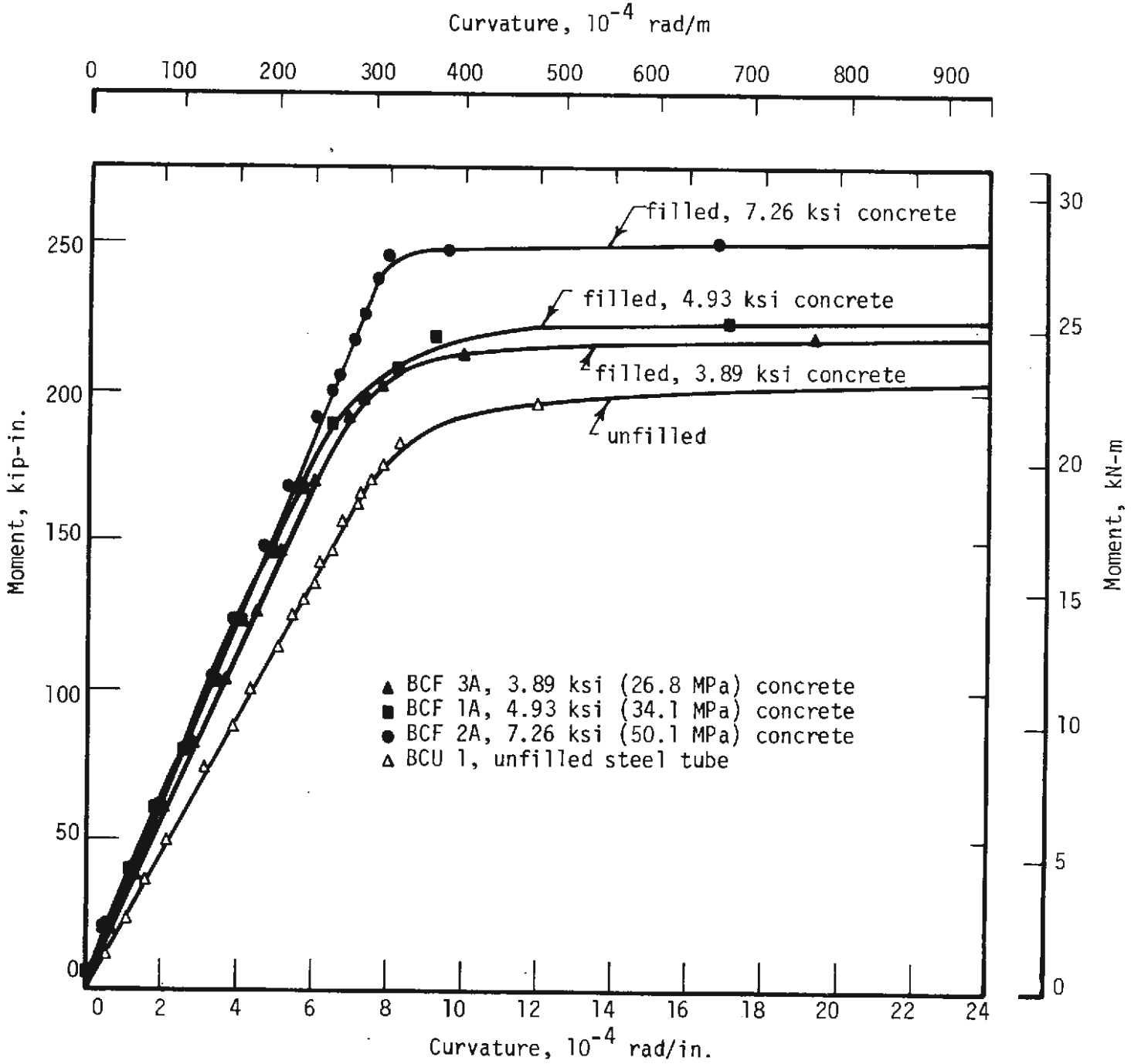

FIG. 5.5 MOMENT-CURVATURE FOR CONCRETE FILLED STRUCTURAL STEEL TUBE BEAM-COLUMNS

curves is based on the assumptions stated in Section 1503 (g) of the ACI Building Code, 1971, except that a limiting concrete strain of .004 was used instead of .003. For the unfilled tube the interaction curve is based on the fully plastic condition as described by Furlong, 1967. Results of the tests on the concrete-filled stub columns, beams, and beam-columns are plotted in the figure. All the experimental values are within 10 percent of the theoretical values and are usually on the conservative side.

The potential usefulness of concrete-filled sections in tunnel supports depends on the types of loads that must be resisted at critical sections of the set. Figure 5.6 shows that the concrete provides an increase in strength which ranges from very little at zero thrust to fairly significant amounts at small eccentricities. For example, the tube with 7.26 ksi (50.1 MPa) concrete can be expected to be about 26 percent stronger than the unfilled tube if e = 3 in. (76 mm) and about 32 percent stronger if e = 2 in. (51 mm). In general, the critical points for the sets in this investigation fall in the upper half of the envelope of Fig. 5.6. Thus, the concrete-filled box may have possibilities in tunnel construction. However, the same extra strength can be achieved by using a heavier unfilled section, the extra cost of which would probably be less than the material and labor cost of the concrete fill. Therefore, the concrete-filled tube must offer benefits in addition to the extra strength in order to pay out in tunnel construction. It should also be noted that the relative increase in strength of the concrete-filled section depends on the steel area, and might be significant for a thin-walled box.

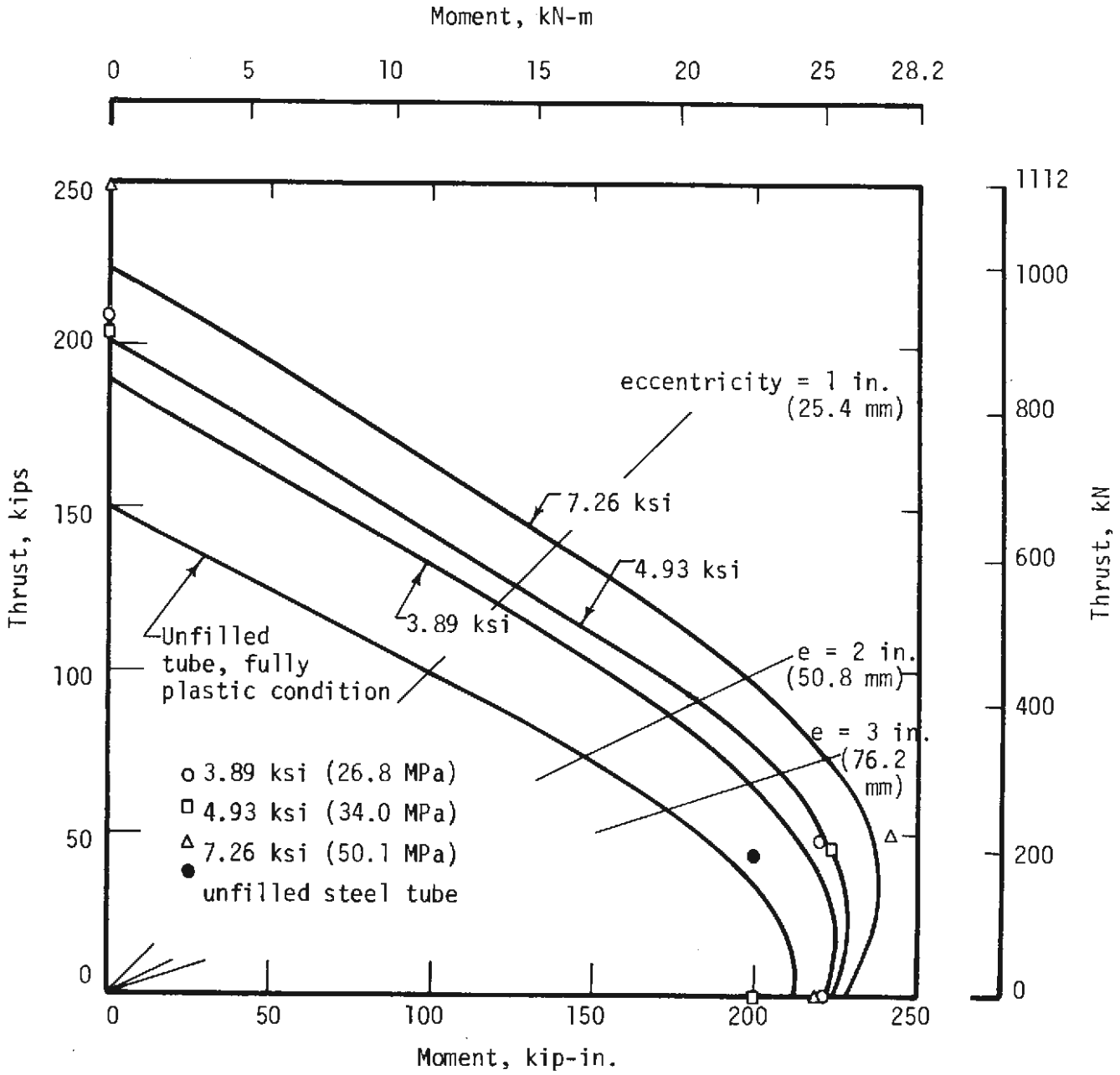

FIG. 5.6 MOMENT-THRUST INTERACTION BEHAVIOR FOR FILLED AND UNFILLED STRUCTURAL STEEL TUBE

5.3 CONNECTION TESTS

Two types of connection were investigated: (a) a standard connection of the type usually used on wide-flange sets and (b) a moment resistant connection. Details of the connections are shown in Fig. 5.7 and Table 5.6. The standard connection was made with 3/4-in. (19 mm) fit-up bolts of the type commonly used in practice or A325 high strength bolts. The moment resistant connection was made with 3/4-in. (19 mm) A325 bolts torqued to specifications of The Research Council on Riveted and Bolted Structural Joints, 1969, by the turn-of-the-nut method.

TABLE 5.6

SUMMARY OF CONNECTION TESTS
FOR STEEL SUPPORTS

Specimen no.	Connection type	Section	Bolts	Butt plate thickness, in. (mm)	Initial eccentricity, in. (mm)	Moment capacity, k-in. (kN-m)
1	Standard	M4 X 13	2-A325	3/8 (10)	8 (203)	93 (10.5)
2	Standard	M4 X 13	2-A325	3/8 (10)	4 (102)	100 (11.3)
3	Standard	4 X 4 X 1/4 tube	2-fit-up bolts	3/8 (10)	4 (102)	89 (10.1)
4	Moment resistant	M4 X 13	4-A325	1/2 (13)	4 (102)	167 (18.9)
5	Moment resistant	M4 X 13	4-A325	1/2 (13)	8 (203)	174 (19.7)
6	Moment resistant	M4 X 13	4-A325	5/8 (16)	8 (203)	202 (22.8)

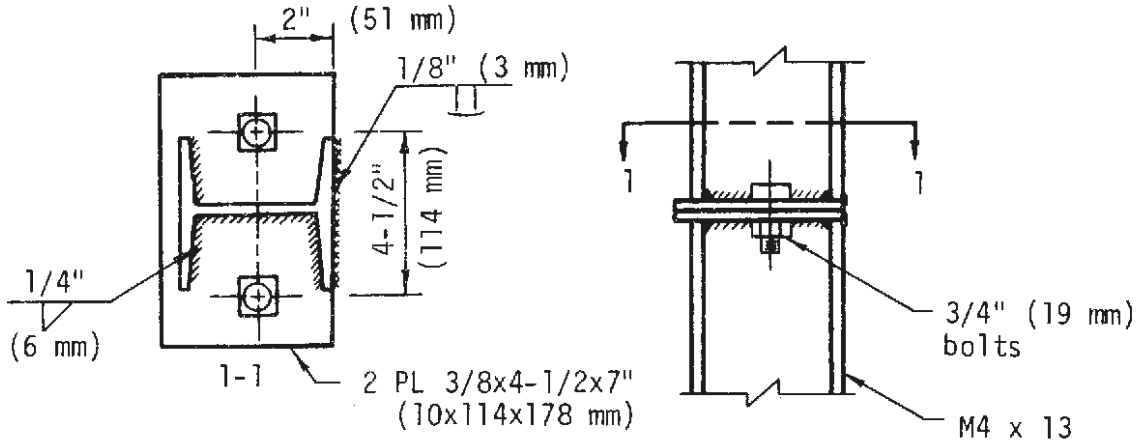

(a) Standard connection for the M4 x 13

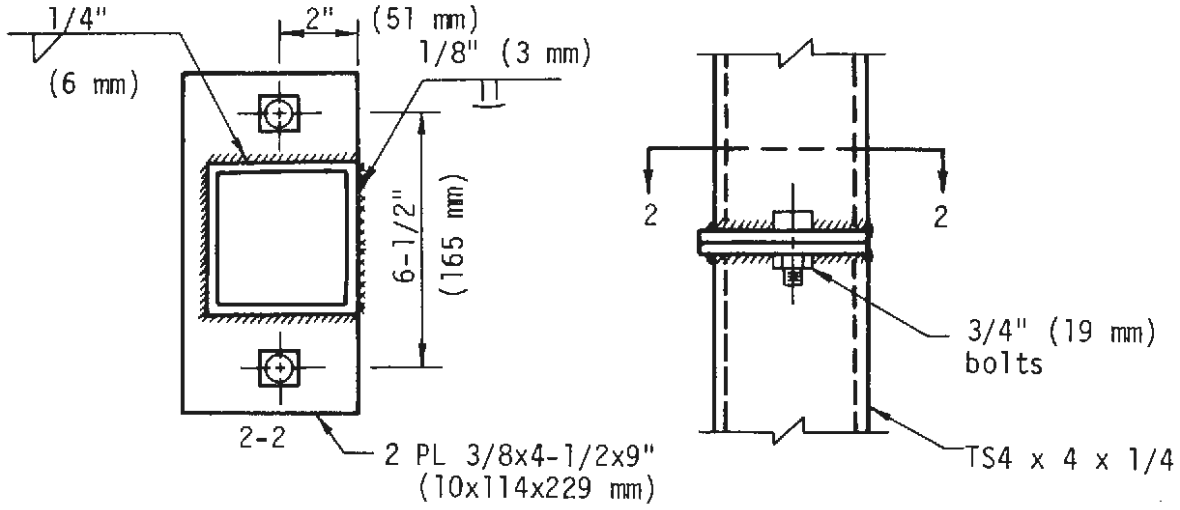

(b) Standard connection for the TS4 x 4 x 1/4

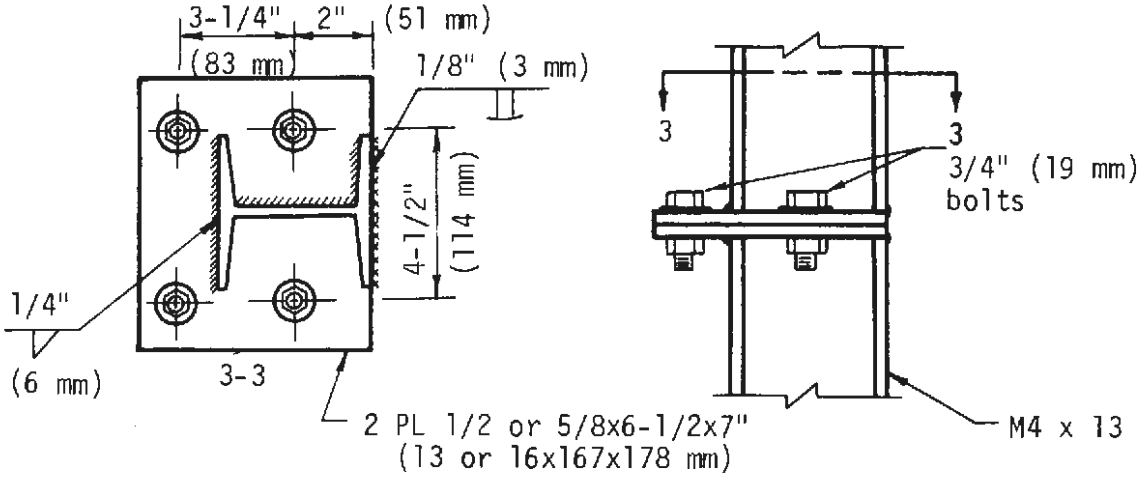

(c) Moment resistant connection for the M4 x 13

FIG. 5.7 STANDARD AND MOMENT RESISTANT CONNECTIONS

An eccentric load was applied to the connection in the test arrangement shown in Fig. 5.8 in a testing machine. Rotation was measured by bars attached 4.5 in. (114 mm) on each side of the connection. Midheight lateral deflection was also measured. This deflection was added to the end eccentricity to obtain the moment at the connection. Bolt elongations were monitored with an extensometer. The test procedure is described in detail by Parker, et. al., 1973.

The test results are shown in Fig. 5.9. The fully plastic moment of the M4X13 and the theoretical moment-rotation curve for an 9-in. (229 mm) length of the section are also shown. Deformation of the standard connection occurred primarily by bending deformation of the butt plates with no visible deformation of the wide flange or box and no visible distress of the welds. Initial deformation of the moment resistant connections was in the butt plates, but some yielding of the welds became visible as loading continued. A photograph of a failed standard connection is shown in Fig. 5.10.

The 3/8-in. (10 mm) butt plates of the standard connection yielded at a low moment, about 10 percent of the moment capacity of the M4, with essentially no increase in bolt tension. The moment-rotation curves for this connection are nonlinear almost from the beginning of loading. The moment-rotation curves for the moment resistant connections are linear up to 70 or 80 percent of the peak values, and tests 5 and 6 (Fig. 5.9) show that the moment capacity is influenced by the butt-plate thickness. The connection with 5/8-in. (16 mm) butt plates attained a peak moment of 96 percent of the M4X13 plastic moment. There was no measurable elongation of the bolts at the peak moments.

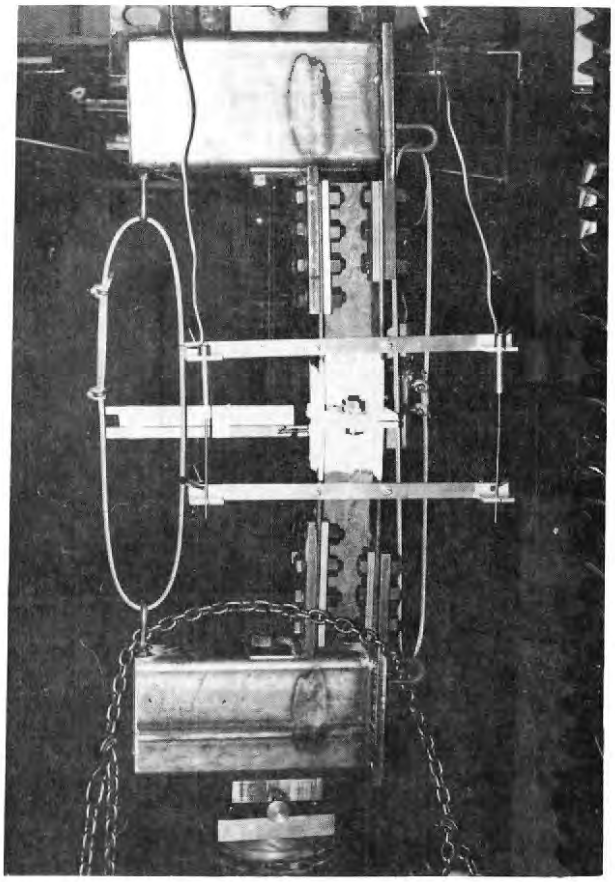

FIG. 5.8 TEST ARRANGEMENT FOR CONNECTION TESTS

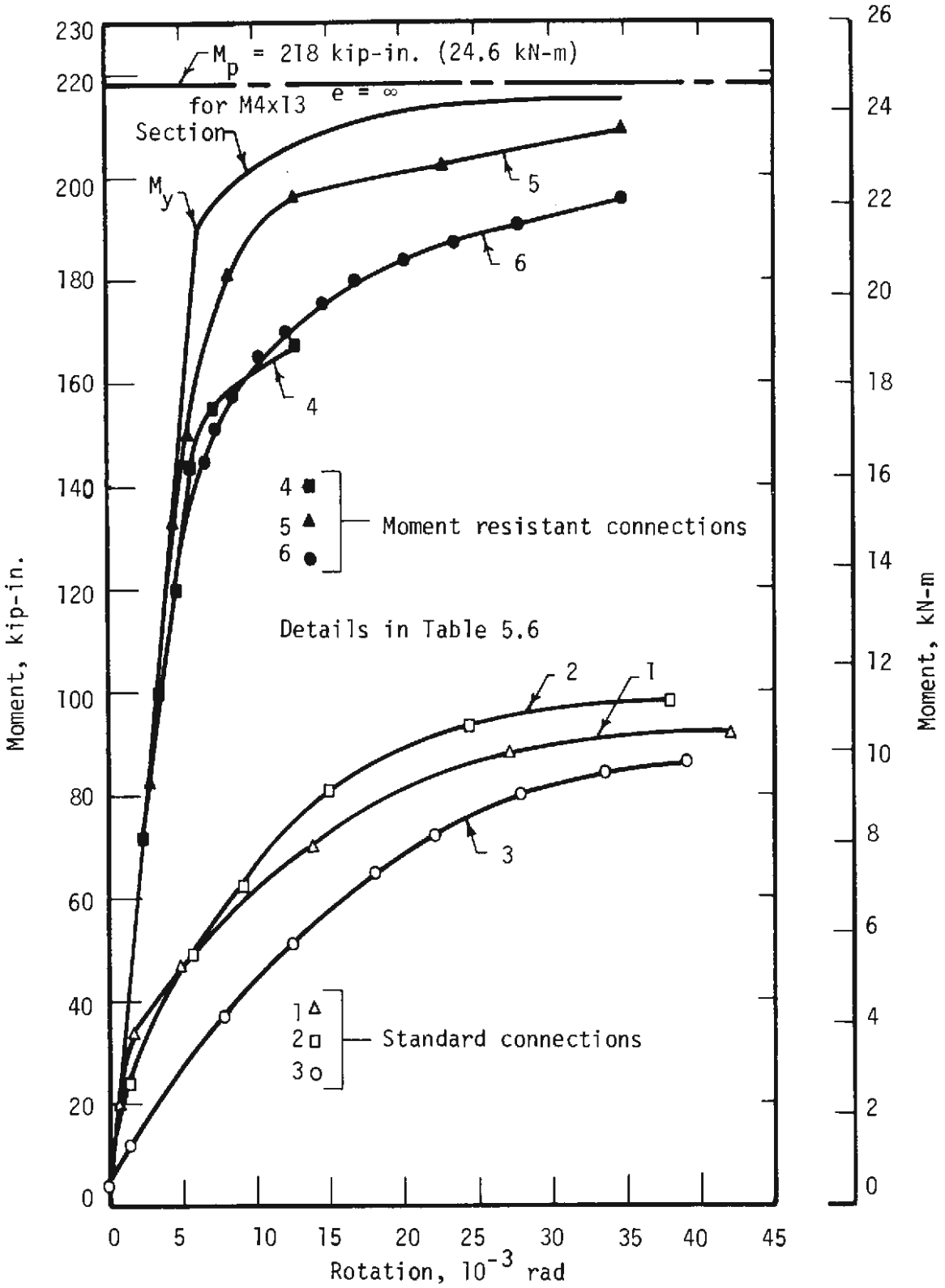

FIG. 5.9 MOMENT-ROTATION FOR CONNECTION TESTS

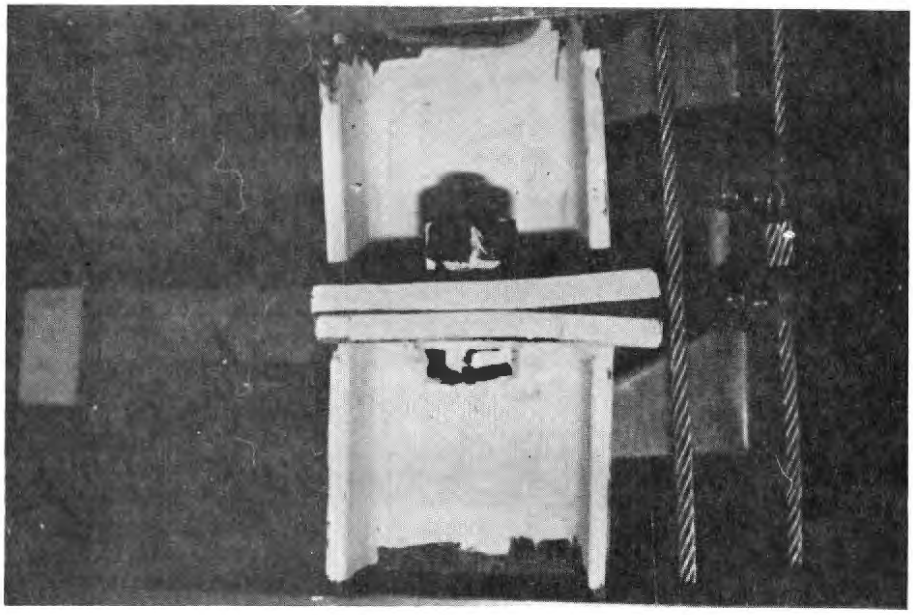

FIG. 5.10 STANDARD CONNECTION AFTER FAILURE

The moment-rotation curves of Fig. 5.9 were used to determine an average connection stiffness to be used in the analytical studies to duplicate the set test results. An equivalent moment of inertia I was computed from the formula $\theta = ML/EI$, where θ is the rotation in the 8-in. (203 mm) length, L, over which the rotation was measured. Young's modulus E was taken as 29,000 ksi (200.0 GPa), the value for the M4 X 13. The resulting equivalent moments of inertia averaged approximately 1 $in.^4$ (42 cm^4) for the standard connection and 10 $in.^4$ (416 cm^4) for the moment resistant connection.

5.4 STEEL SET TESTS

5.4.1 INTRODUCTION

Results of 11 tests on steel sets are presented in this section. The test facility and the instrumentation and test procedures are discussed by Parker, et. al., 1973. Two of the tests were conducted in that program. Figure 5.11 shows the test set and the numbering system for nodes, strain gage locations, etc.

The following variables were chosen for study:

1. Cross-sectional shape: 9 tests with M4 X 13, 2 with box section.
2. Connections: 5 tests with standard, 6 with moment resistant.
3. Blocking: 8 tests with hard blocking, 3 with soft.
4. Loading: 5 tests with in-plane loads, 6 with out-of-plane loads.

With only 11 tests, it was not possible to compare all the combinations of the above variables. Furthermore, only 5 tests were carried to failure; loading of

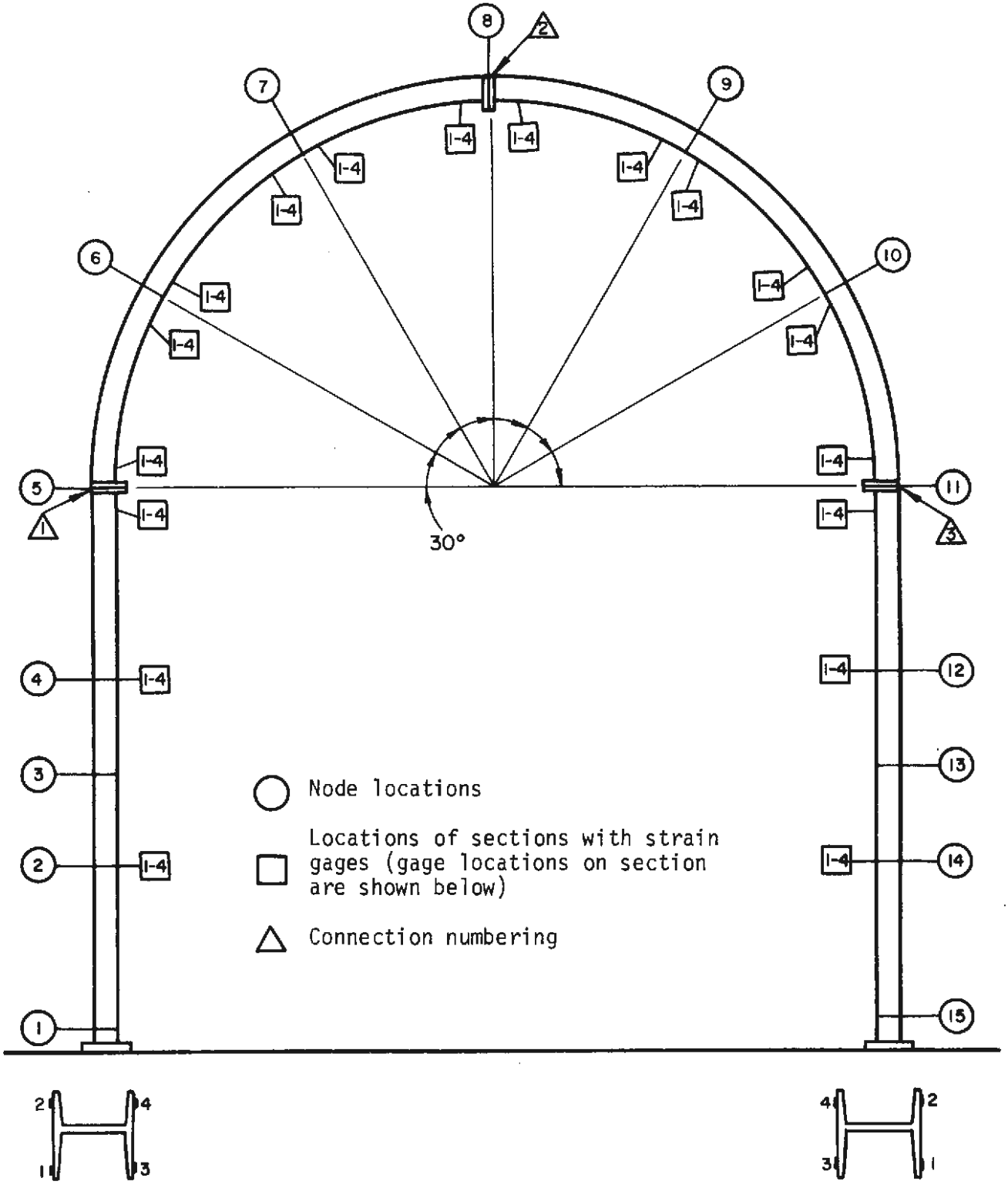

FIG. 5.11 STRAIN GAGE LOCATIONS AND NUMBERING FOR LOADS AND CONNECTIONS FOR THE STEEL SET

the other six was stopped before yielding so that they could be reused. The tests are summarized in Table 5.7.

Comparisons of experimental results with linear analysis by the STRUDL model described in Section 5.6 were made and the sensitivity of the analysis to some of the simplifying assumptions that were required to model the test sets was investigated. Calculated bending moments at strain-gaged sections are compared with analytically determined moment diagrams and measured deflections are compared with analytically determined deflection diagrams.

The bending moments M and the axial force P are computed from the strain gage readings at the four flange-tip locations shown in Fig. 5.11 by the following equations:

$$M_x = \frac{1}{4} (\sigma_1 + \sigma_2 - \sigma_3 - \sigma_4) S_x$$

$$M_y = \frac{1}{4} (\sigma_1 + \sigma_3 - \sigma_2 - \sigma_4) S_y \qquad (5.1)$$

$$P = \frac{1}{4} (\sigma_1 + \sigma_2 + \sigma_3 + \sigma_4) A$$

The strain gage readings and the formulas above are valid only for linearly elastic behavior.

5.4.2 ASSUMPTIONS FOR ANALYSIS OF TEST SET

CONNECTION STIFFNESS

Connection stiffness is discussed in Section 5.3 and its simulation for the STRUDL analysis in Section 5.6.1. For the analysis in this section,

TABLE 5.7

SUMMARY OF STEEL SET TESTS

Test	Loading	In or out of plane	Shape	Connection	Blocking Stiffness	Extent of load	Loading at failure kips (kN)
M1a	S	in	M4	std.[7]	hard	elastic	--
M1b	U	in	M4	std.	hard	failure	21.7 (96.5)[1] 99.3 (442.0)[2]
M2a	U	out (active)	M4	std.	hard	failure	21.1 (94.0)[1] 92.8 (413.0)[2] 21.8 (97.0)[3]
B1a	U	out (active)	box	std.	hard	failure	21.5 (95.5)[1] 100.2 (446.0)[2] 22.1 (98.0)[3]
M3a	S	in	M4	m.r.[8]	hard	elastic	--
M3b	S	in	M4	m.r.	soft	elastic	--
M3c	U	in	M4	m.r.	soft	elastic	--
M3d	U	out (active)	M4	m.r.	hard	elastic[4]	--
M3e	U	out (active)	M4	m.r.	hard	elastic	--
M3f	U	out (active)	M4	m.r.	soft	failure[5]	21.2 (94.0)[1] 98.5 (438.0)[2] 22.0 (98.0)[3]
M3g	U	out (active)	M4	m.r.	soft	elastic[6]	--

[1] Average active jack load (in plane)
[2] Total base reaction (in plane)
[3] Average active jack load (out of plane)
[4] Passive jack at crown not seated prior to test. This jack was seated at an active jack load of 7 kips (31 kN). Test halted at 10.5 kips (47 kN).
[5] Failure in right leg. Right leg replaced for tests M3g and M3h.
[6] Attempted local failure of flange in right arch. This did not occur so test stopped at average active jack load of 12 kips (53 kN).
[7] Standard connection
[8] Moment resistant connection

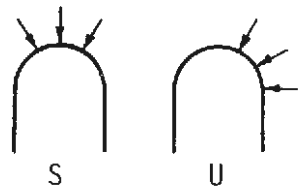

connection moments of inertia are assumed to be 1-in.^{4} (42 cm^4) for the standard connection and 10-in.^{4} (416 cm^4) for the moment-resistant connection.

BLOCKING STIFFNESS

Simulated blocking stiffness in the large-scale set tests are defined by the load-deflection behavior of the passive jacks. They are categorized as either hard or soft. Hard stiffnesses were functions of the passive jack system--the individual jack, the length of hydraulic hose, and the 1/4 in. (6 mm) thick plywood load application block. Soft stiffnesses were individually controlled by adjusting the passive jack so that the load-deflection behavior at that location followed a predetermined curve.

Figure 5.12 shows the results of two load-deformation tests of hardwood blocking made in a standard testing machine. In one test (curve 1), a stack of 4 blocks, totaling 9-3/4 in. (248 mm) in height, was loaded through a steel block. In the other test (curve 2), a stack of blocks was arranged in a cribbed configuration, totaling about 10-1/2 in. (267 mm) in height. Passive jack stiffnesses representing the hard blocking are at least as stiff as the cribbed blocking test, and generally range between curves 1 and 2. This would normally be the case for the best blocking conditions. Curve 3 in Fig. 5.12 was obtained by doubling the deflections of the cribbed blocking test. It represents an extreme blocking condition, such as might occur if the wood were wet, and is the curve to which the passive jacks were regulated to represent the soft blocking.

The stiffness of the passive jacks used to simulate blocking was nonlinear. The assumptions made in the analysis are discussed in Section 5.6.1.

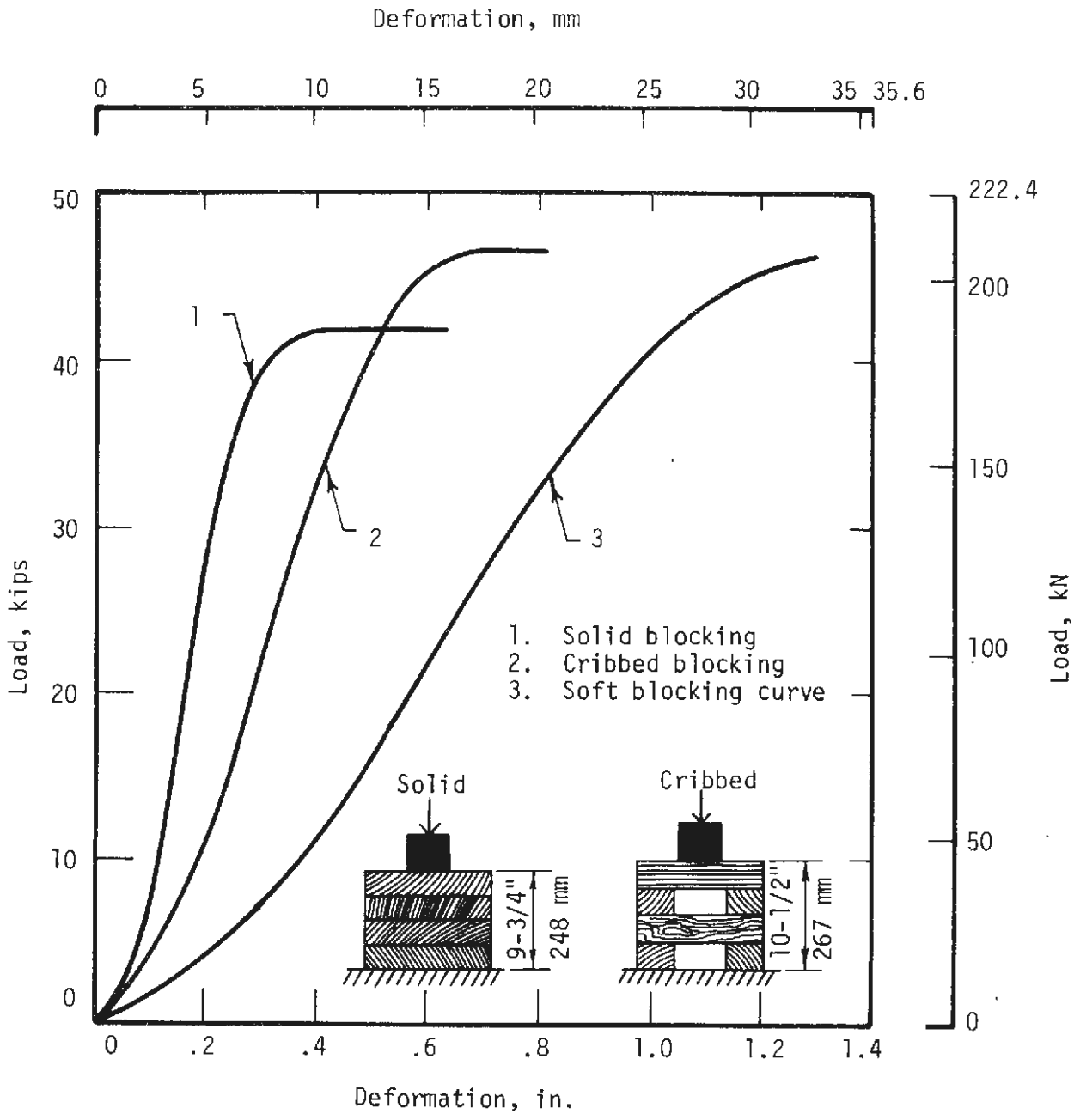

FIG. 5.12 LOAD-DEFORMATION FOR WOOD BLOCKING TESTS

BASE CONNECTION

The base connections are neither fixed nor hinged. They are restrained against lateral displacement and twist about the axis of the legs but are permitted to rotate about an axis perpendicular to the plane of the set. The base can rotate about the edge of the base plate, which gives an eccentricity of the reaction relative to the centerline of the set that varies as rotation progresses. The effect of this eccentricity was investigated by analysis. Moment diagrams for base reaction eccentricities of zero and 2 in. (51 mm) are compared with the experimental results in Fig. 5.13. It will be noted that the major effect of the eccentricity is in the leg of the set. The change in moment in the arch is only 4 percent. Therefore, analytical moment diagrams and deflection diagrams for comparison with set tests are computed for base connections with no eccentricity.

POINT LOAD VS. FINITELY DISTRIBUTED LOAD

The loads on the test set are applied through 4 x 4 in. (102 x 102 mm) distributing plates but are assumed to be point loads in the analysis. The effect of this idealization was investigated for set M3f by an analysis with the load distributed over the 4-in. (102 mm) length. The results are shown in Fig. 5.14. It will be noted that the error in assuming point loads is very small and confined to the immediate vicinity of the load. The maximum error is about 4 percent. Therefore, analytical moment diagrams and deflection diagrams for comparison with set tests are computed for point loads.

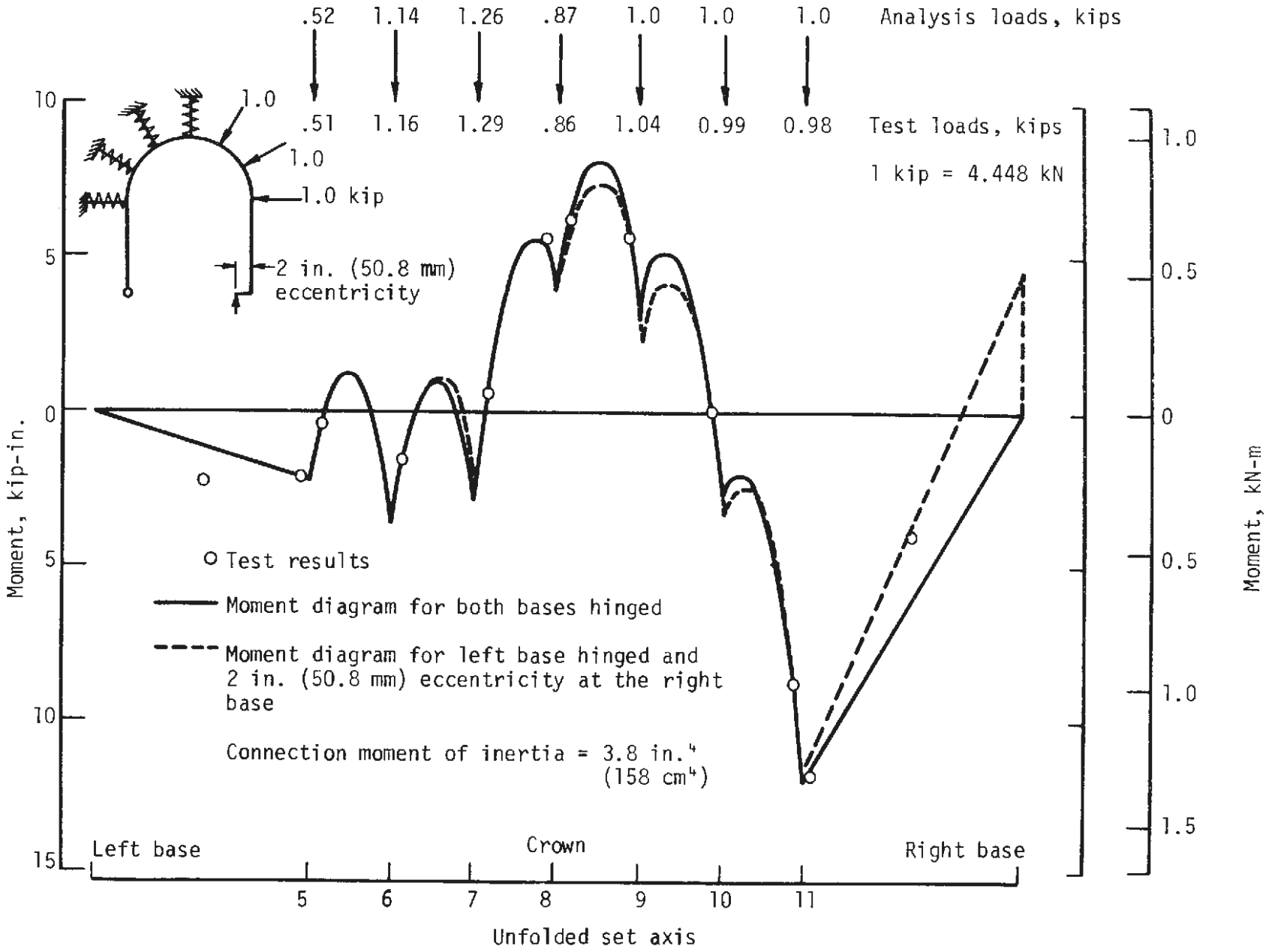

FIG. 5.13 COMPARISON OF MOMENT DIAGRAMS FOR DIFFERENT BASE CONDITIONS

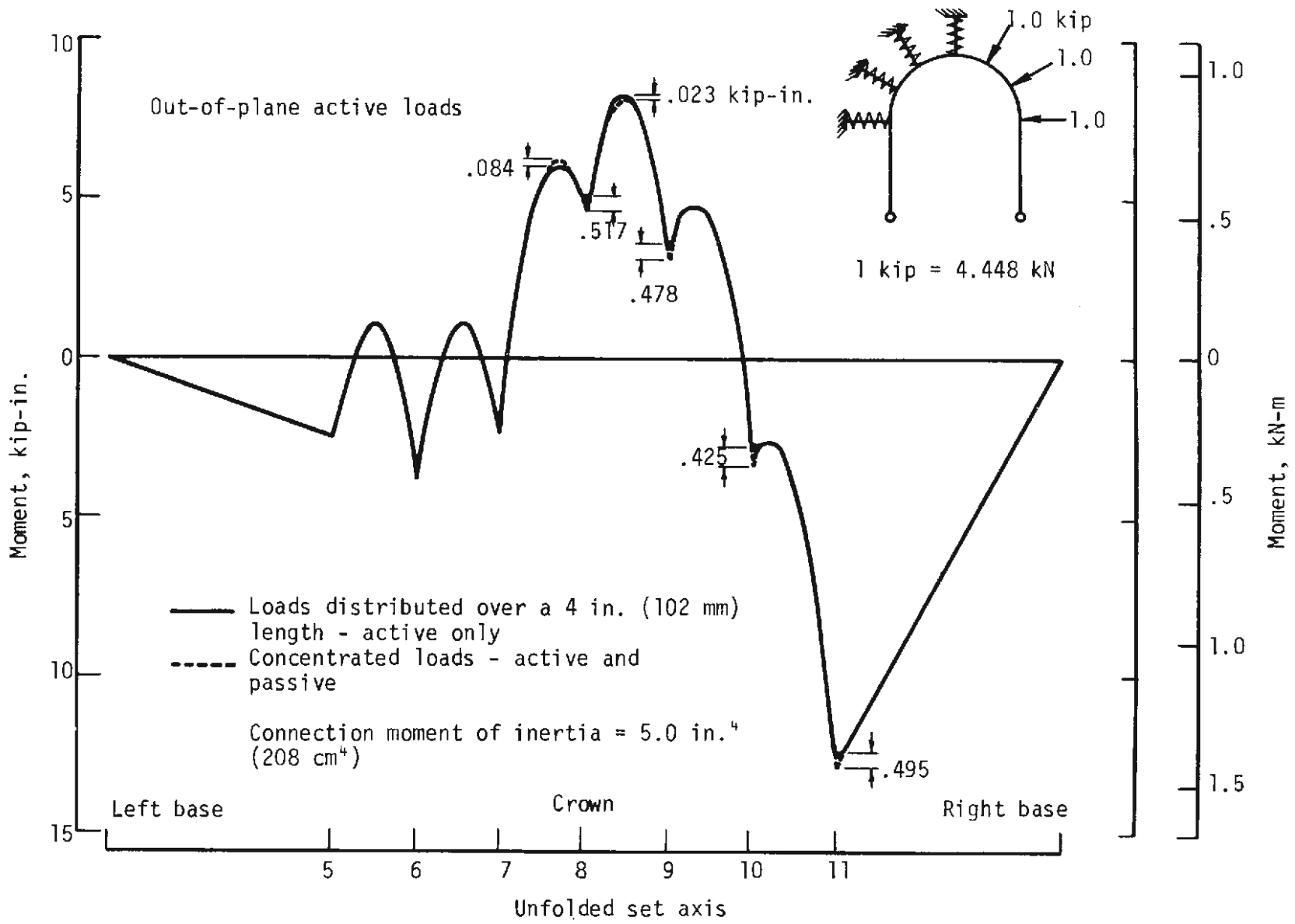

FIG. 5.14 COMPARISON OF MOMENTS ALONG THE SET FOR CONCENTRATED LOADS AND DISTRIBUTED ACTIVE LOADS

5.4.3 COMPARISON OF TESTS WITH ANALYSIS

Moment diagrams and deflected shapes obtained from the linear analysis were compared with results of all the tests described in Section 5.4.1. Results for tests B1a and M3f are discussed here.

B1a has standard connections and was tested with hard blocking; M3f has moment-resistant connections and was tested with soft blocking. Both were side-loaded 17 deg (.30 rad) out-of-plane and both were tested to failure. Figures 5.15 and 5.16 compare the elastic moments computed from Eqs. 5.1, and Figs. 5.17 and 5.18 compare the deflected shapes. It will be noted that experimental results compare favorably with predictions in all four figures. It is also of interest to note that the two sets failed at almost identical active loads even though the moment diagrams from the linear analysis show considerably larger unit-load maximum moments for M3f. This suggests that the load at initial yield is not indicative of the ultimate load.

5.4.4 COMPARISON OF STANDARD AND MOMENT RESISTANT CONNECTIONS

Connection stiffness affects the load-displacement behavior of the sets, but the effect is much larger for the side-loaded case than for the crown-loaded case since the moments are larger for a given active load. Tests M1a and M3a, with standard and moment resistant connections respectively, are crown loaded and tested in the elastic range. Radial displacement at the crown is plotted in Fig. 5.19 for these tests. At an average active load of 9 kips (40 kN)

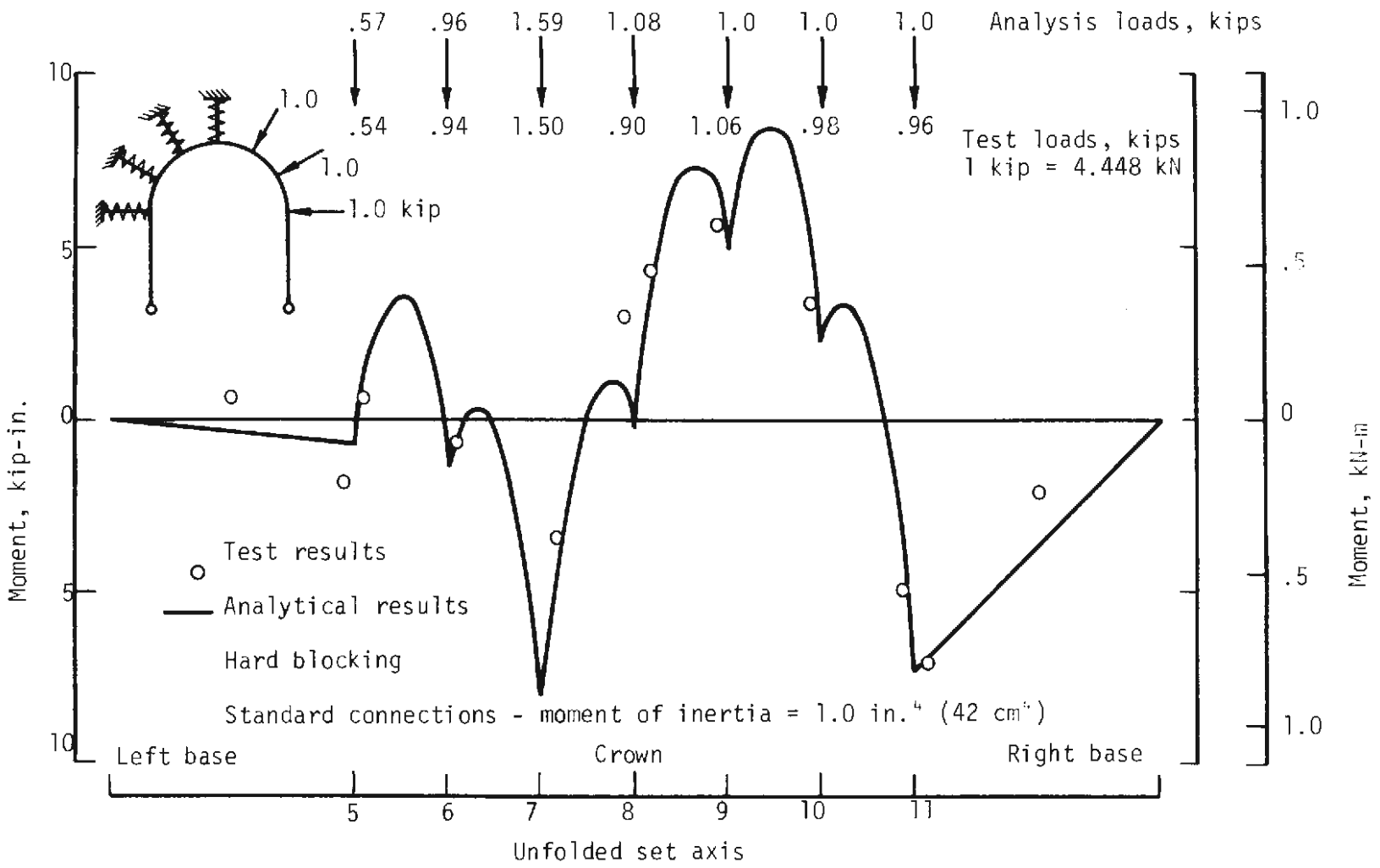

FIG. 5.15 COMPARISON OF ANALYTICAL MOMENT DIAGRAM AND TEST MOMENTS FOR B1A IN THE LINEAR RANGE

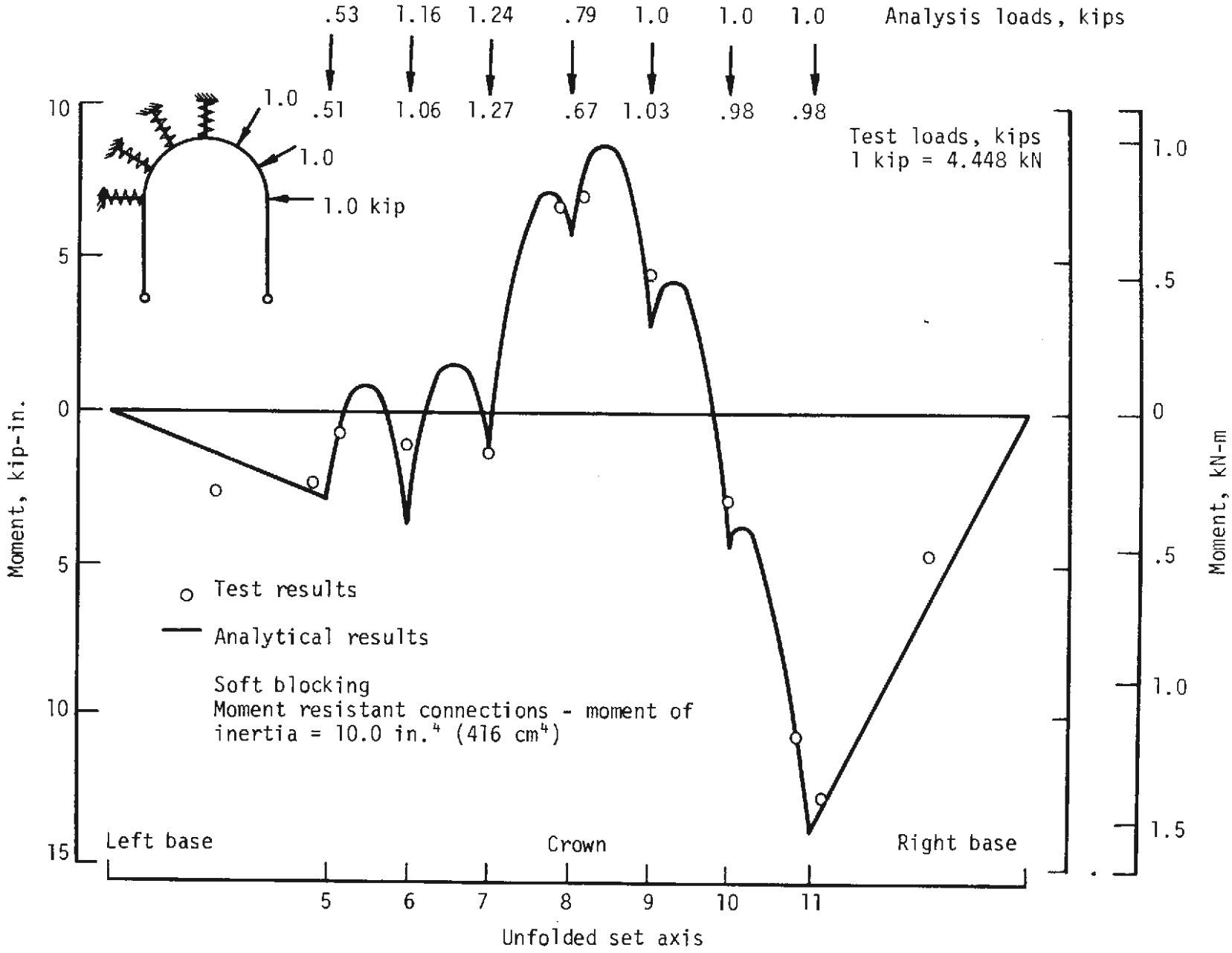

FIG. 5.16 COMPARISON OF ANALYTICAL MOMENT DIAGRAM AND TEST MOMENTS FOR M3F IN THE LINEAR RANGE

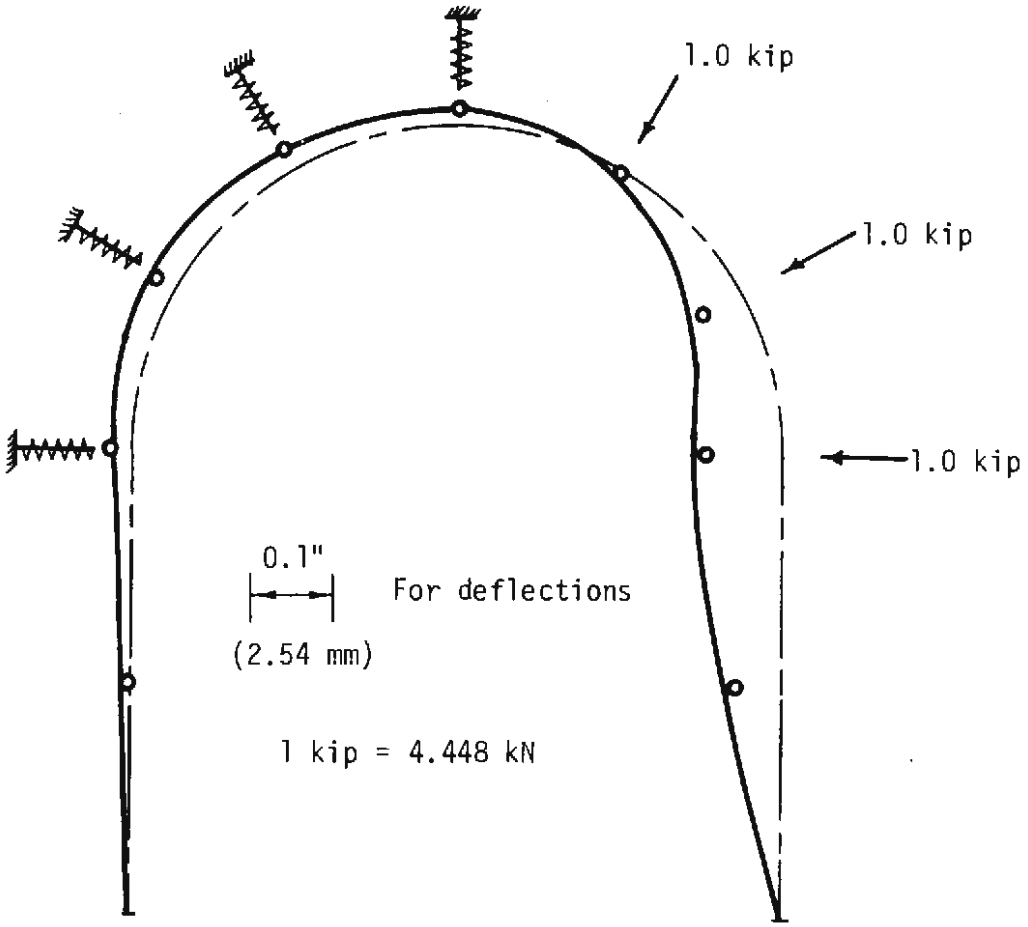

FIG. 5.17 COMPARISON OF DEFLECTIONS FROM LINEAR ANALYSIS AND TEST B1A

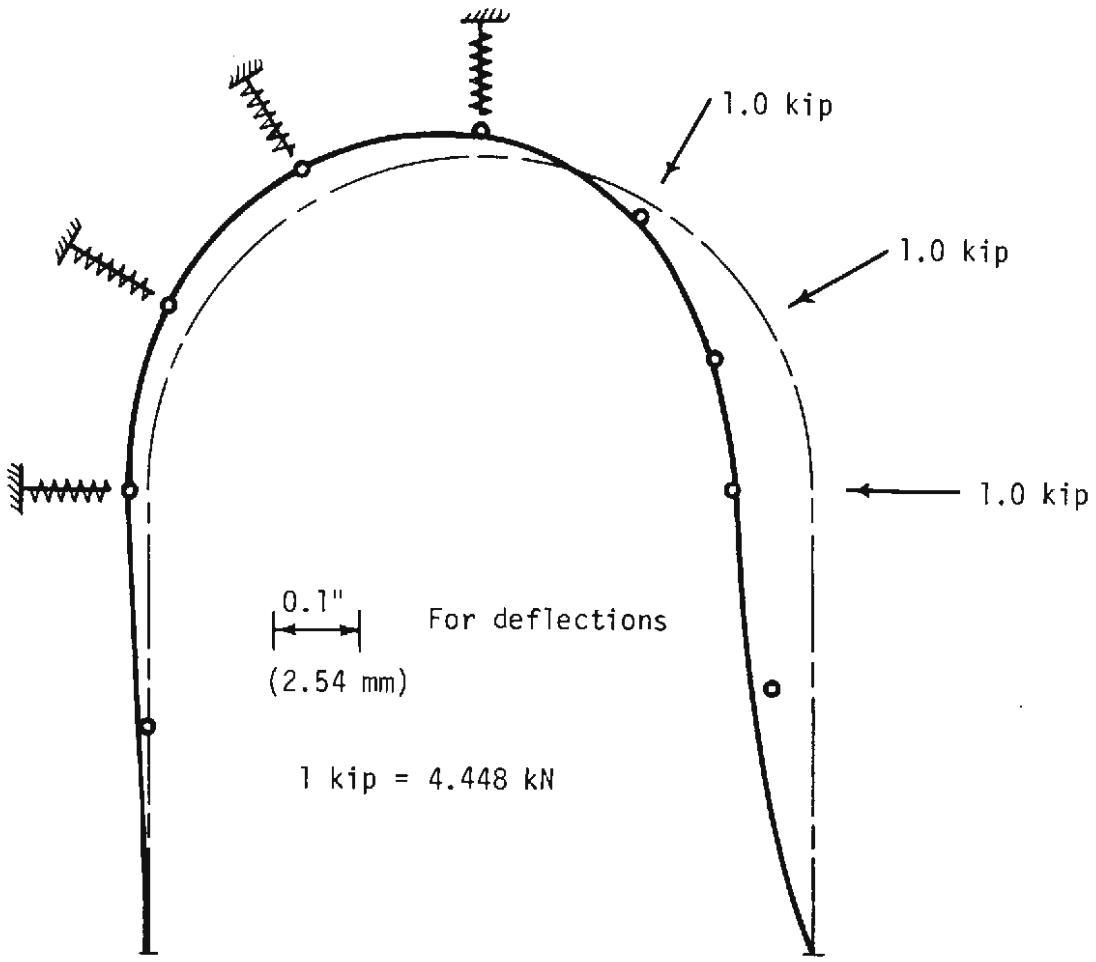

FIG. 5.18 COMPARISONS OF DEFLECTIONS FROM LINEAR ANALYSIS AND TEST M3F

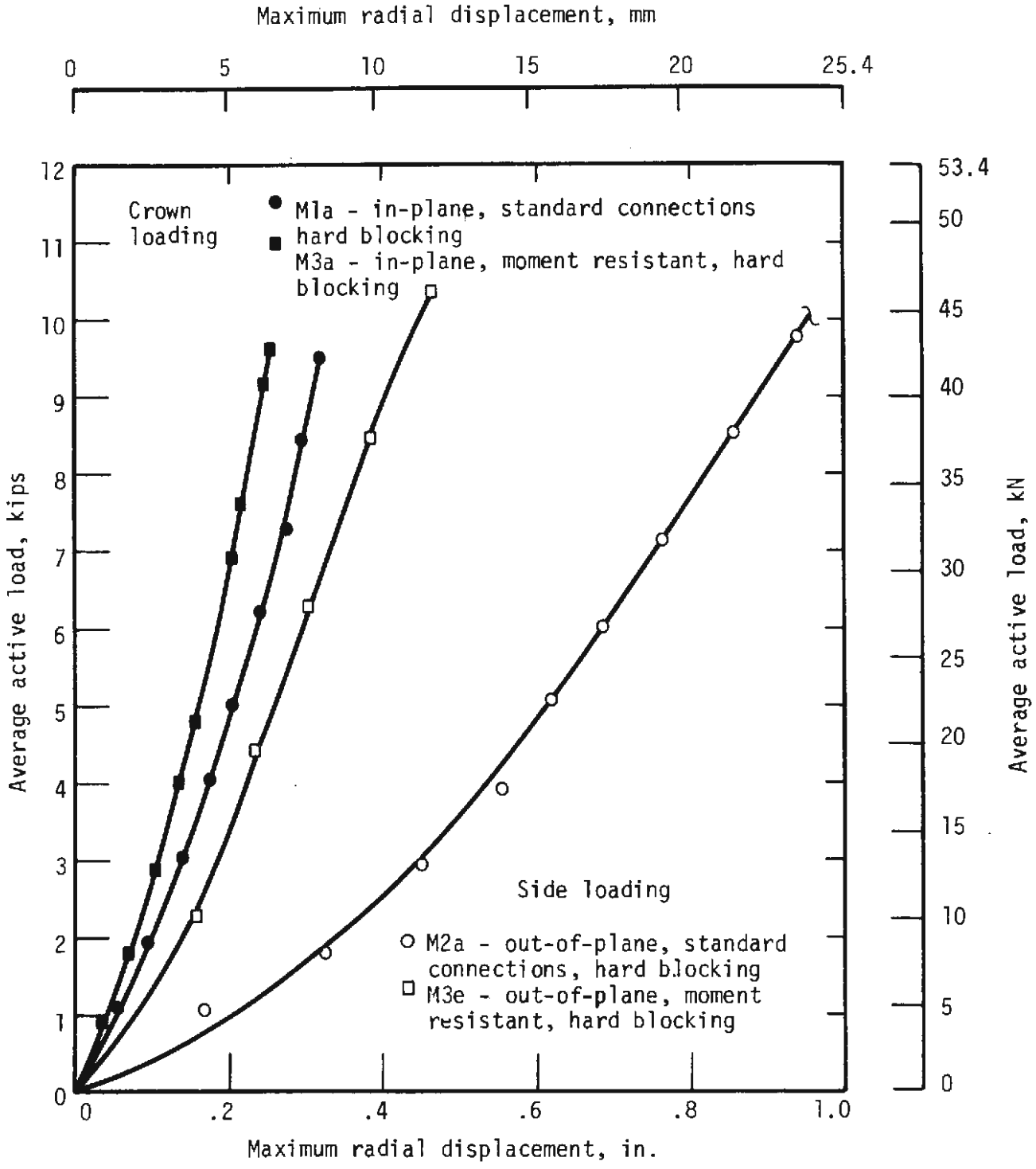

FIG. 5.19 LOAD-DISPLACEMENT FOR COMPARING THE EFFECTS OF STANDARD AND MOMENT RESISTANT CONNECTIONS

the set with standard connections has a radial displacement about 30 percent larger than that of the set with moment resistant connections. For side-loaded tests M2a and M3e, with standard and moment resistant connections respectively, the difference is much larger (Fig. 5.19). At the right springline the radial displacement of the set with standard connections is about 120 percent larger than for the set with moment resistant connections at the 9-kip (40 kN) load. Thus, when the loading is one that produces large moments the standard connection results in much larger displacements.

The generally lower structural stiffness due to standard connections is not necessarily an indication of lower strength. Although there were no tests to failure with connection stiffness the only variable, a general overview of the tests to failure (all of which were side loaded) indicates that the ultimate strength may not be greatly affected by connection stiffness. In the three sets with standard connections tested to failure (M1b, M2a, B1a) the right side connection began to open first as the load increased, after which, near the ultimate load, yielding occurred midway between the right side connection and the crown, accompanied by opening of the crown connection. In the one test to failure with moment resistant connections (M3f), the behavior was considerably different. First yielding occurred at the top of the right leg, next to the connection. Then yielding occurred on both sides of the crown connection as well as near the passive jack to the left of the crown, but at no time did the connections open. In all four tests the ultimate active jack load was 21 to 22 kips (93 to 98 kN), so that the connection stiffness appears to make less difference than might be expected. However, additional tests to failure would be needed before this observation could be taken to be generally true.

Only set M1b mentioned above was loaded in the plane of the set; load was inclined 17 degrees (.30 rad) to the plane in the other four. However, the in-plane component is 96 percent of the inclined active jack load, so that all five sets carried essentially the same in-plane load at failure (Table 5.7). It is of interest to note that the component of the inclined load normal to the plane of the set is 29 percent of the active jack load, but appears to have had little effect on the strength of the set. This question is discussed further in Sections 5.4.5 and 5.4.6.

5.4.5 COMPARISON OF IN-PLANE AND OUT-OF-PLANE LOADING

Two sets, M1b and M2a, were loaded to failure to compare the effects of in-plane loading and 17-degree out-of-plane loading. Both sets had M4 X 13 sections with standard connections and were tested with hard blocking. The loads were applied to the flanges with the line of action passing through the centroid of the section. Both tests progressed in similar fashion. The first notable deformation was the opening of the connection at the right springline at an average active load of about 4 kips (18 kN). Local yielding at the right springline (node 11), which is the point of maximum elastic moment, began at an active load of 8-10 kips (36-45 kN). The next region of yielding was between nodes 9 and 10 at an active load of 18-19 kips (80-85 kN). Maximum jack loads in the two tests are shown in Fig. 5.20. The average of the three active maximum loads was 22.7 kips (101 kN) for in-plane loading and 21.8 kips (97 kN) for the inclined loading. A difference of this magnitude could be attributed to slight structural variations or variations in the test procedure as well as to the differing load inclinations.

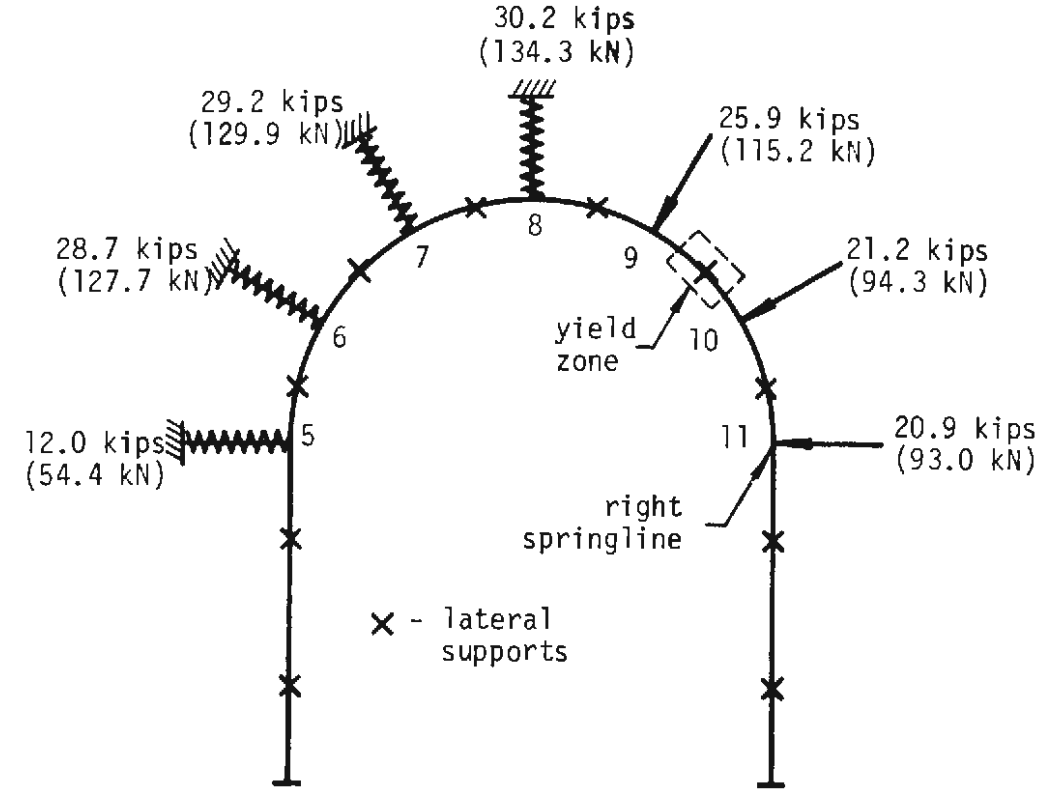

(a) M1b - in-plane loading

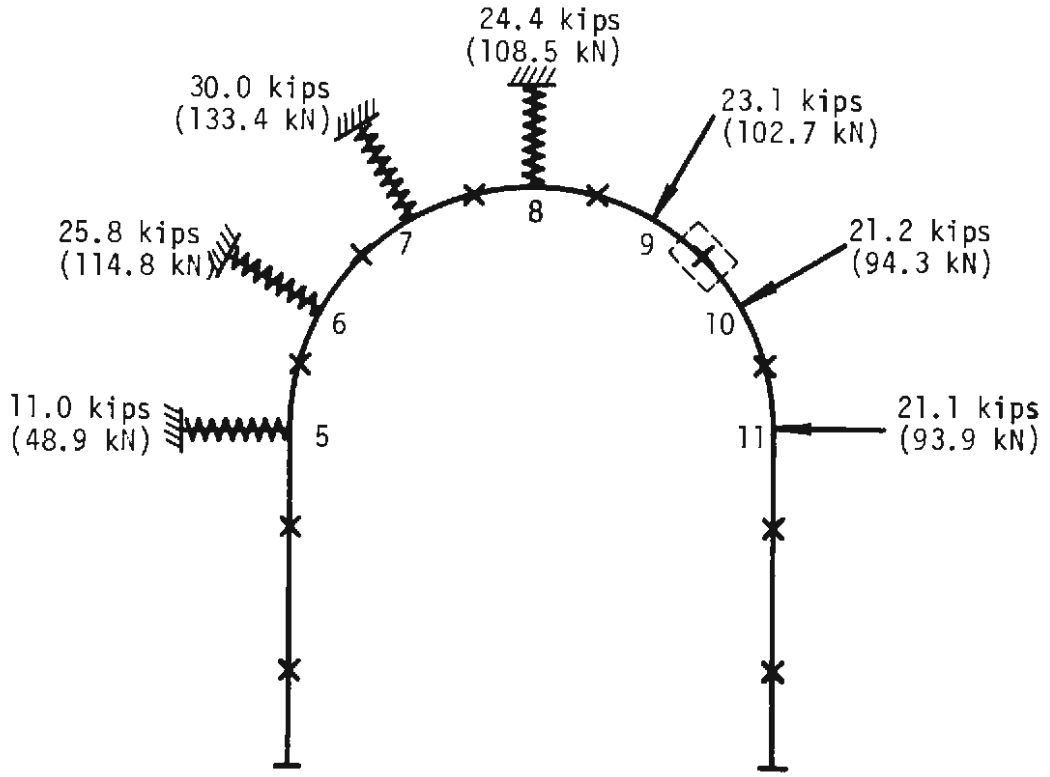

(b) M2a - out-of-plane active loading

FIG. 5.20 COMPARISON OF MAXIMUM LOADS WITH IN-PLANE AND OUT-OF-PLANE LOADING

Figure 5.21 shows the similarity in the behavior of the sets. The average active load is plotted against maximum radial displacement, which is at the right springline. Tests M3c and M3g, which were loaded only in the elastic range, are also shown. Since the sets in M1b and M2a have standard connections and hard blocking, they should not be compared directly with M3c and M3g, which have moment resistant connections and soft blocking. It will be noted that there are no significant differences between the effects of in-plane and 17-degree (.30 rad) out-of-plane loading.

5.4.6 COMPARISON OF WIDE FLANGE AND STRUCTURAL TUBE

Tests M2a and B1a were loaded to failure to compare the behavior of an M4 X 13 set with one made with the TS4 X 4 X 1/4 structural steel tube. Both sets were side loaded with out-of-plane active jacks, standard connections, and hard blocking stiffnesses. The line of action of each load passed through the section centroid so that there was no applied twisting moment. However, the component of the load perpendicular to the plane of the set at a given location induces an internal twisting moment elsewhere along the set. The linear analysis shows this twisting moment to be not more than 8 percent, and usually less than 5 percent, of the strong-axis bending moment for both the tube and the M4 X 13 in the locations where yielding occurs, assuming the torsional properties of the connection to be equal to those of the section. This ratio of twisting moment to strong-axis bending moment remains constant with increase in load, except for second-order effects such as changes in the shape of the set due to deformation. These effects are minor, however. Another

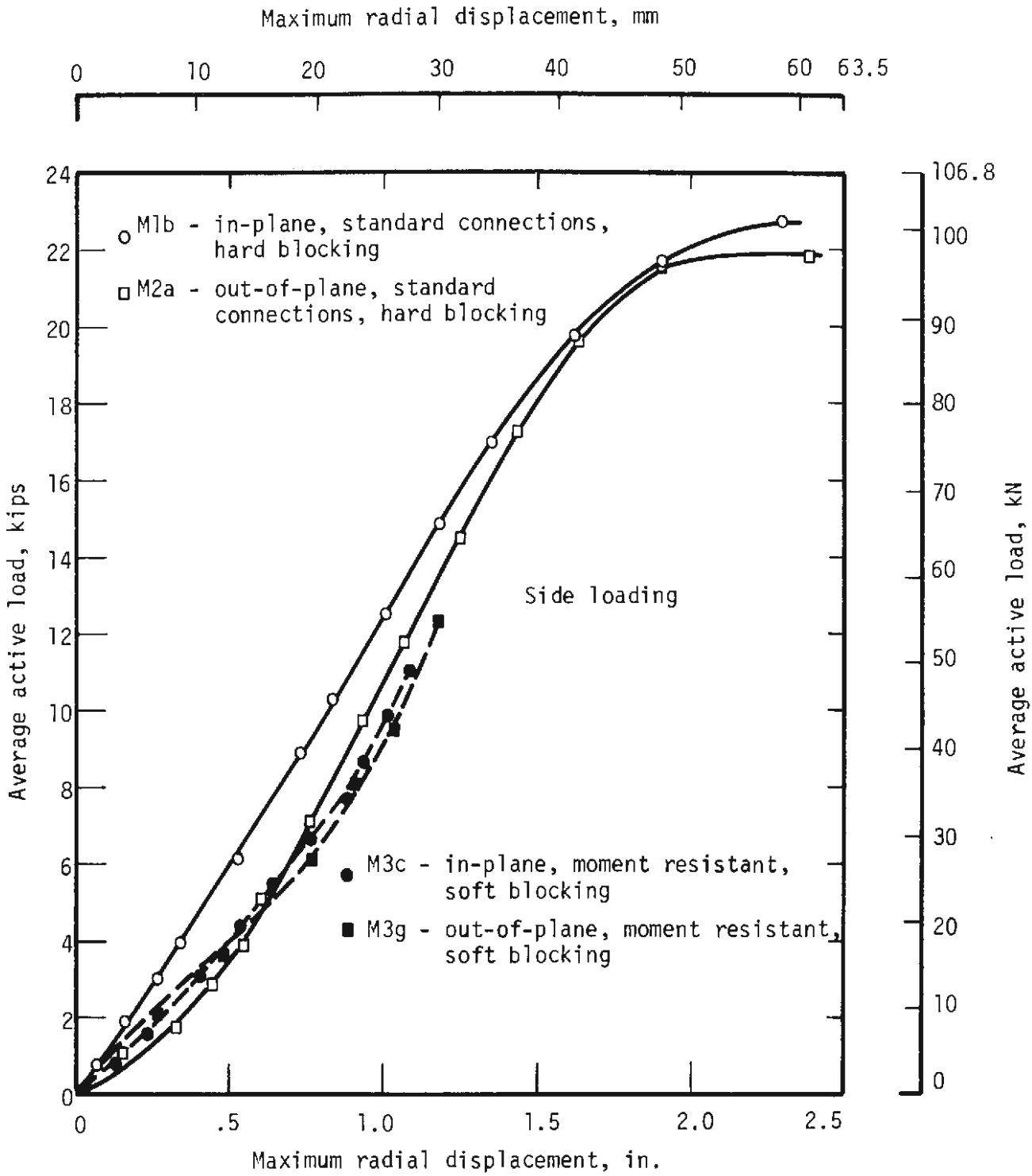

FIG. 5.21 LOAD-DISPLACEMENT FOR COMPARING IN-PLANE AND OUT-OF-PLANE LOADING

factor, which is potentially more important, is the manner in which plastic hinge formation may affect this ratio. When a plastic hinge occurs the distribution of strong-axis moment changes, and at a given location it may decrease or even change sign. On the other hand, twisting moments are not affected in the same way since a plastic hinge may continue to carry increased torsion. Therefore, as the load is increased, twisting resistance at plastic hinges may contribute significantly to the strength.

Weak-axis bending moment must also be considered in analyzing the ultimate behavior of the steel sets. For 17-degree (.30 rad) out-of-plane loading the component of a load, P, perpendicular to the set is 0.29P and that in the plane of the set is 0.96P. Because both the elastic section modulus S and the plastic section modulus Z of the square tube are considerably higher than those of the M4 X 13 about the weak axis (Table 5.8), the ultimate strength of the tube set might be expected to be somewhat higher than that of the M4 X 13 set for out-of-plane loading. But this was not the case for the 17-degree (.30 rad) inclination of load. For both sets the maximum measured moment about the weak axis, up to the point of maximum active load, was less than 40 percent of yield moment about the weak axis for that section. Although the weak axis moment contributes to the stress level in the cross section, it was not large enough in this case to appreciably affect the strong-axis failure mode. However, it should be noted that the lateral bracing inhibits deflections perpendicular to the set, so that weak-axis moments are better distributed than they would be if there were no bracing. This results in a smaller (in this case negligible) contribution of weak-axis moment to failure of the section.

Figure 5.22 shows the average active load versus radial displacement for the point of maximum displacement, which is at the right side connection in this case. Aside from a small difference in the elastic range, the curves for the tube and the M4 X 13 are essentially the same. It is evident that for this loading the strong-axis section properties control the type of failure, so that the tube has no advantage over the M4 X 13.

TABLE 5.8

SECTION MODULI FOR M4 X 13 AND TS4 X 4 X 1/4

Property	M4 X 13	TS4 X 4 X 1/4
Elastic section modulus, S, in.^{3} (cm^3)		
Strong axis	5.24 (85.9)	4.00 (65.5)
Weak axis	1.71 (28.0)	4.00 (65.5)
Plastic section modulus, Z, in.^{3} (cm^3)		
Strong axis	6.06 (99.3)	5.28 (86.5)
Weak axis	2.74 (44.9)	5.28 (86.5)

5.4.7 EFFECT OF BLOCKING STIFFNESS

The effect of blocking stiffness on behavior of the structure can be assessed by comparing points of maximum displacement. For the symmetrically loaded set maximum displacement is at the crown connection, while for side loading it is at the connection on the loaded side. Figure 5.23 shows the differences in displacement at these points for the soft and hard blocking. These

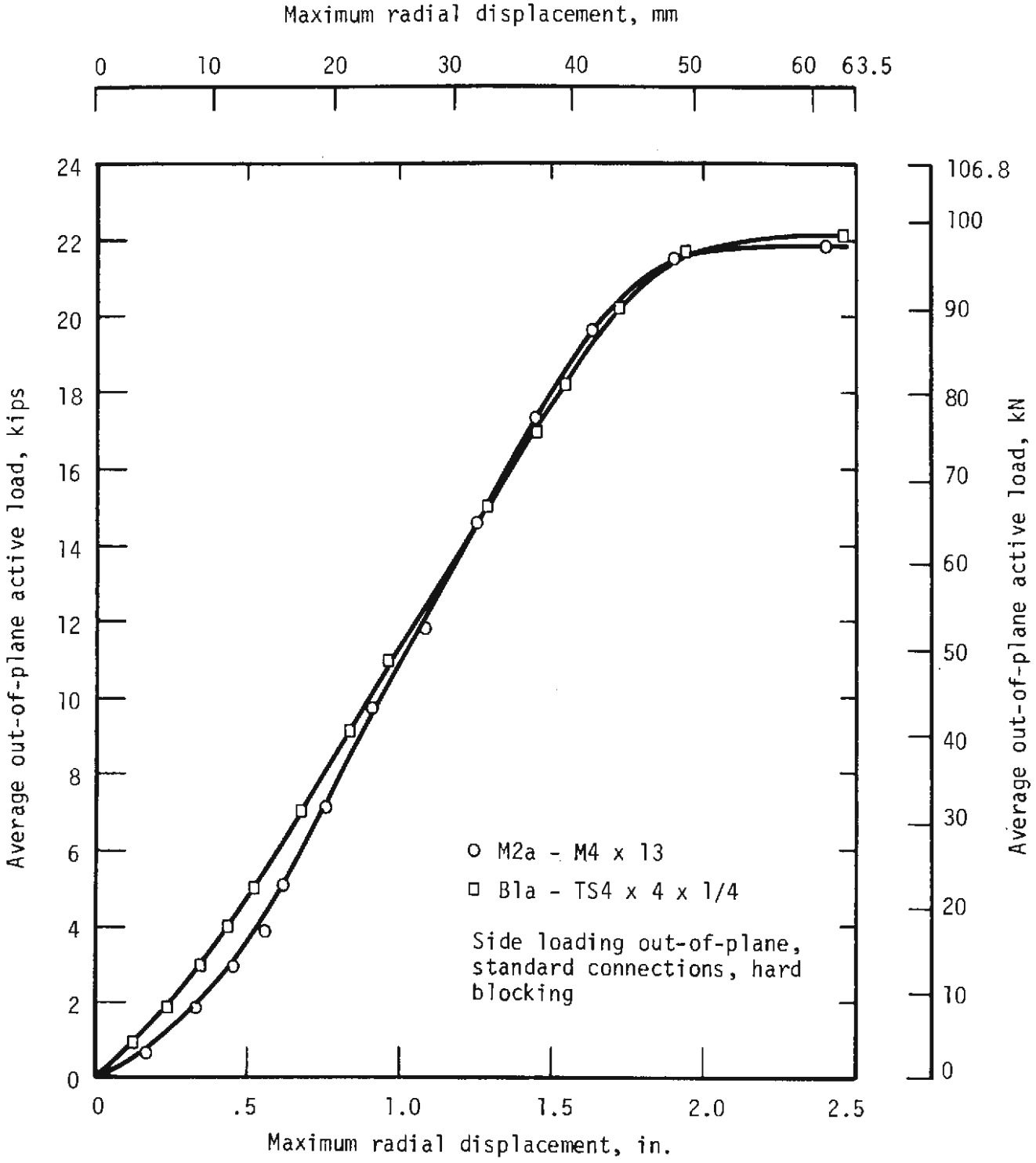

FIG. 5.22 LOAD-DISPLACEMENT FOR COMPARING WIDE FLANGE AND STRUCTURAL TUBE SECTIONS

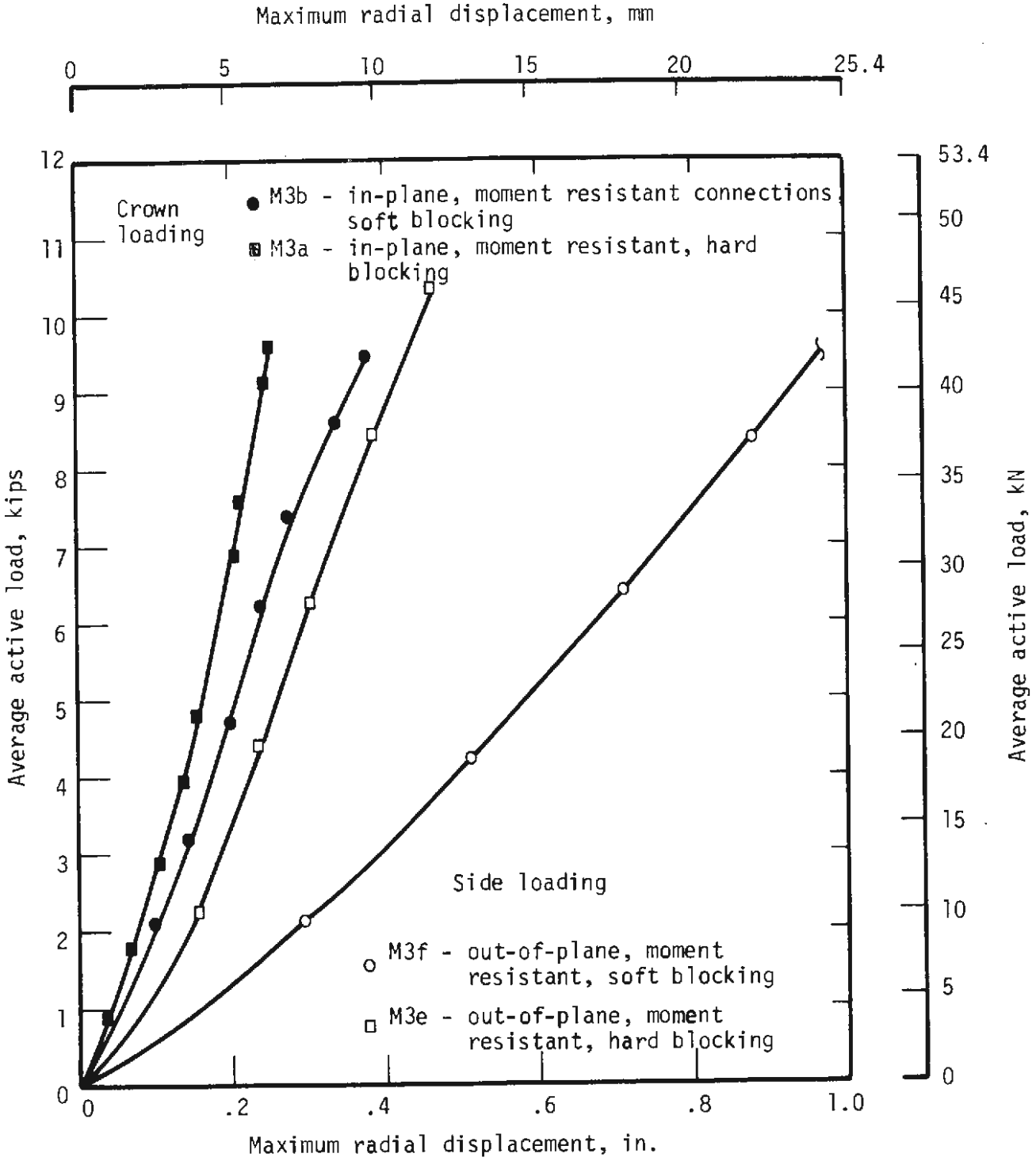

FIG. 5.23 LOAD-DISPLACEMENT FOR COMPARING HARD AND SOFT BLOCKING

curves are only for the elastic range of behavior of the structure. At an average active load of 9 kips (40 kN) per jack for the symmetrical loading (approximately 40 percent of the failure load), the soft blocking results in a crown displacement about 45 percent larger than with the hard blocking. The difference is even more pronounced for side loading. Here the soft-blocking displacement at the side connection is 127 percent greater than the hard blocking displacement for an average active load of 9 kips (40 kN). It is clear that displacements are larger if the active loading is from the side. In the elastic range, greater displacements are accompanied by higher bending stresses, so stiffer blocking tends to allow higher loads before yielding. However, this does not necessarily mean that the ultimate capacity of the structure is affected by blocking stiffness, because of the redistribution of moments after yielding. Results of the four tests to failure show that the ultimate average active jack load, in the plane of the set, was between 21 and 22 kips (93-98 kN) in all cases. This suggests that blocking stiffness may not appreciably affect the ultimate capacity of the structure. However, if displacements in the tunnel are minimized immediately after excavation, large movements of the soil or rock mass, accompanied by excessive loads on the structure, are less likely to occur. Stiff and well-placed blocking will help keep initial displacements small, thereby mobilizing the strength of the supported material and lessening the load which the structure is required to carry.

The spacing of blocking on the structure may be of greater importance than the blocking stiffness. Closer, more uniform spacing will distribute

load more evenly around the structure, thereby decreasing bending stresses for a given active load. A computer analysis in the nonlinear range, such as the piecewise linear analysis of NASTRAN, is better suited than laboratory tests for an investigation of the effects of blocking spacing. Such an analysis to investigate blocking spacing is being considered for the future.

5.5 ANALYTICAL STUDY OF SET PARAMETERS

5.5.1 INTRODUCTION

In this section an analytical investigation of the effects of various parameters on the elastic behavior of steel sets is made. The structure is modeled for STRUDL, details of which are discussed in Section 5.6.1. The parameters considered are load configuration, connection stiffness, passive jack stiffness, and inclination of load with respect to the plane of the set. The set assumed is of M4 X 13 cross section and has hinged bases.

The tests described in Section 5.3 show that connection behavior is nonlinear for the standard connection almost from the beginning of loading and for the moment resistant connection after reaching 70 to 80 percent of its peak moment. However, since STRUDL is a linearly elastic analysis it was necessary to hold the connection stiffness constant for each stiffness that was investigated. The stiffnesses are assumed to be 1 $in.^4$ (42 cm^4) for the standard connection and 10 $in.^4$ (416 cm^4) for the moment resistant one. These are approximations of the test results described in Section 5.3. The section modulus and the equivalent cross sectional area are assumed to be the same as for

the M4 X 13, i.e., S = 5.24 in.^{3} (85.9 cm^3) and A = 3.81 in.^{2} (24.6 cm^2), for both connections. Passive jack stiffness was also nonlinear but was assumed to be linear.

5.5.2 LOAD CONFIGURATION

The load configurations considered are symmetrical crown loading and side loading. Figure 5.24 shows the position of the active loads and passive loads. Soft blocking and standard connections are assumed. The analysis is made for unit in-plane loads. The yield load is defined as the active load that produced first yielding of the extreme fiber, with the stress computed by N/A + M/S, where N is the normal force and M the bending moment acting on a cross section.

The yield load was 24 kips (107 kN) per active jack for crown loading and 13.7 kips (61 kN) for side loading. Maximum moment was at the crown for crown loading and at the springline connection for side loading. It will be noted that the yield load for the side loading case is about 60 percent of the failure load (Table 5.7). There were no tests to failure under crown loading.

It is of interest to note that the failure load was the same for sets with standard connections and the one set with moment resistant connections, even though moments were maximum at the connections. The difference in behavior for these two cases is discussed in Section 5.4.4.

5.5.3 EFFECT OF CONNECTION STIFFNESS

Analyses are made for M4 X 13 sets with hinged bases and side loading both in-plane and out-of-plane. The passive jack stiffness is held at 30 kips

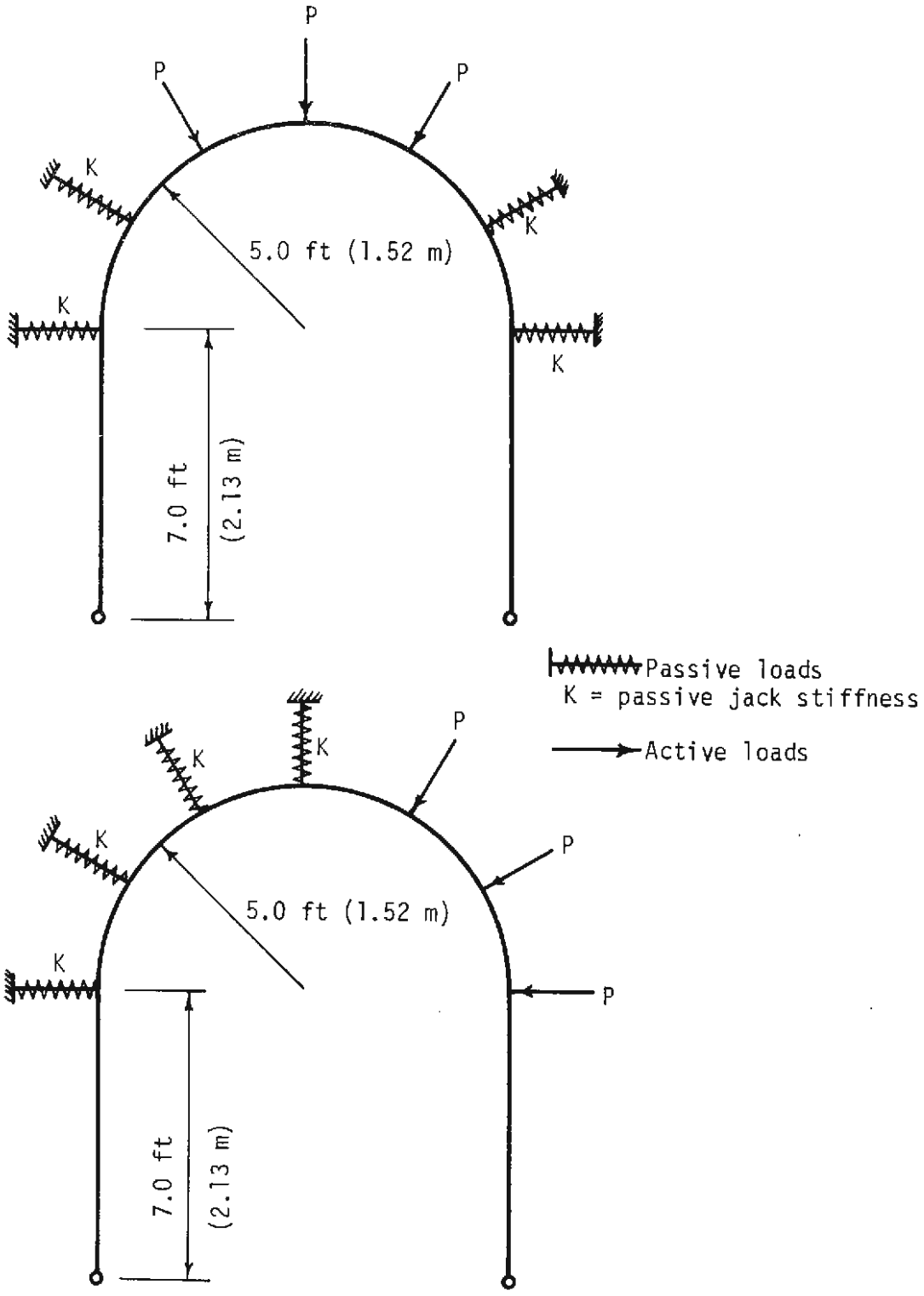

FIG. 5.24 POSITION OF ACTIVE AND PASSIVE LOADS IN STRUDL

per inch (5.3 MN/m) (soft blocking). Figure 5.25 shows maximum radial displacement, which is at connection 3, versus connection moments of inertia ranging from 0 to 15 in.^{4} (624 cm^4). These curves show that the effect of connection stiffness on deflection is small if the moment of inertia is larger than about 1 in.^{4} (42 cm^4), that of a standard connection.

Figure 5.26 is a plot of maximum moment for in-plane loads versus connection moment of inertia. The point of maximum moment is at connection 3 if the moment of inertia exceeds about 0.5 in.^{4} (21 cm^4), while for smaller moments of inertia it shifts to point A, about midway between active loads 9 and 10. The solid-line portions of the curves give the envelope of maximum moment for I varying from 0 to 15 in.^{4} (624 cm^4). The maximum moment for values of I larger than 5 in.^{4} (208 cm^4) does not increase significantly with increase in I. For I smaller than 1 in.^{4} (42 cm^4) the maximum moment increases until it reaches about 16 in.-kips (1.8 kN-m) for a hinged connection.

5.5.4 EFFECT OF PASSIVE JACK STIFFNESS

The range of blocking stiffness assumed in this analysis is from 0 to 100 kips/in. (17.5 MN/m), and all blocking locations are assumed to have the same stiffness. The set has hinged bases and is side-loaded in plane. Analyses are made for standard connections and moment-resistant connections.

Figure 5.27 is a plot of average active load at first yield versus passive jack stiffness for two values of connection stiffness. The curves show that strength, measured by the load at first yield, does not increase significantly for large passive jack stiffnesses.

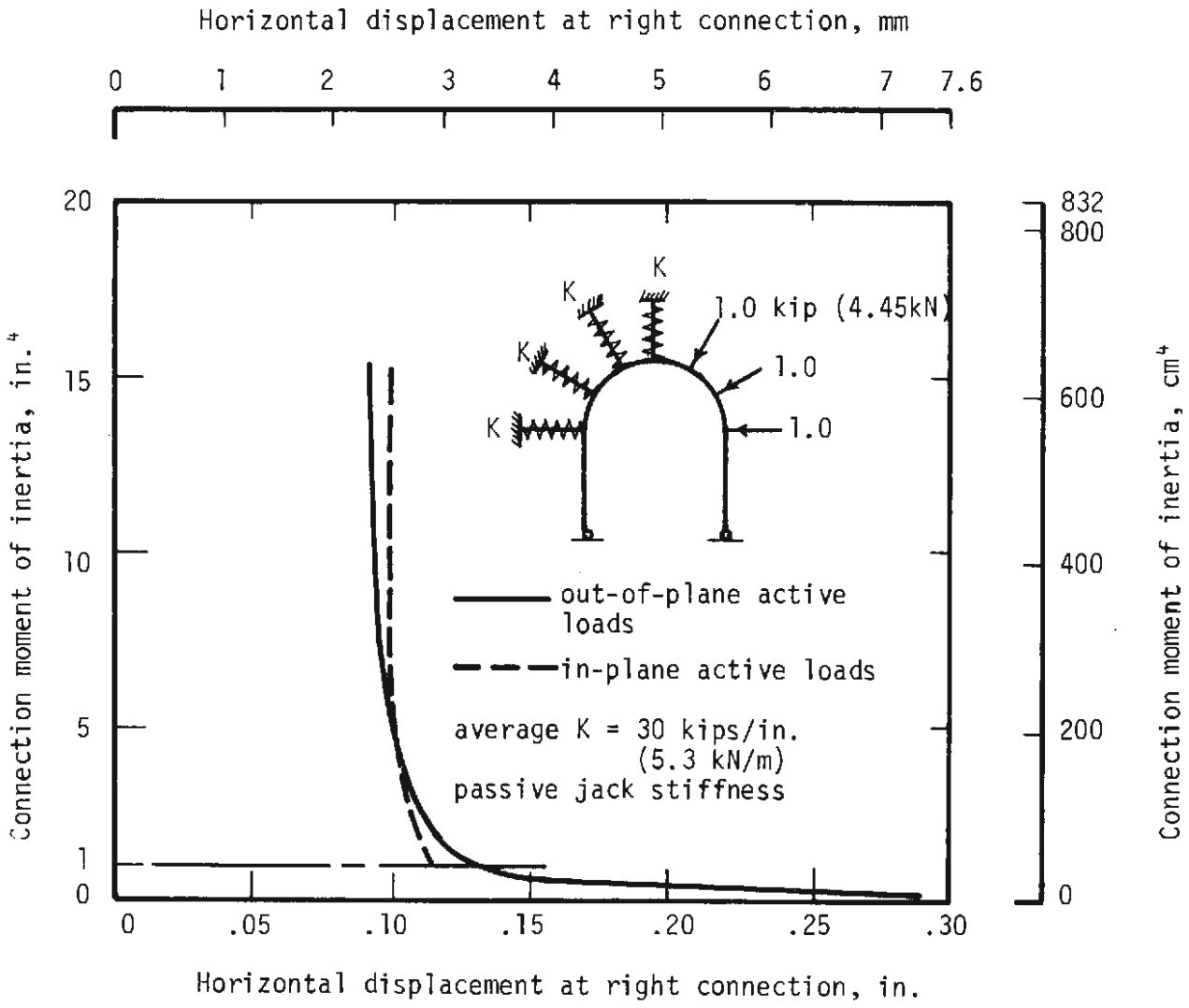

FIG. 5.25 EFFECT OF CONNECTION STIFFNESS ON SET DEFLECTION FROM THE LINEAR ANALYSIS

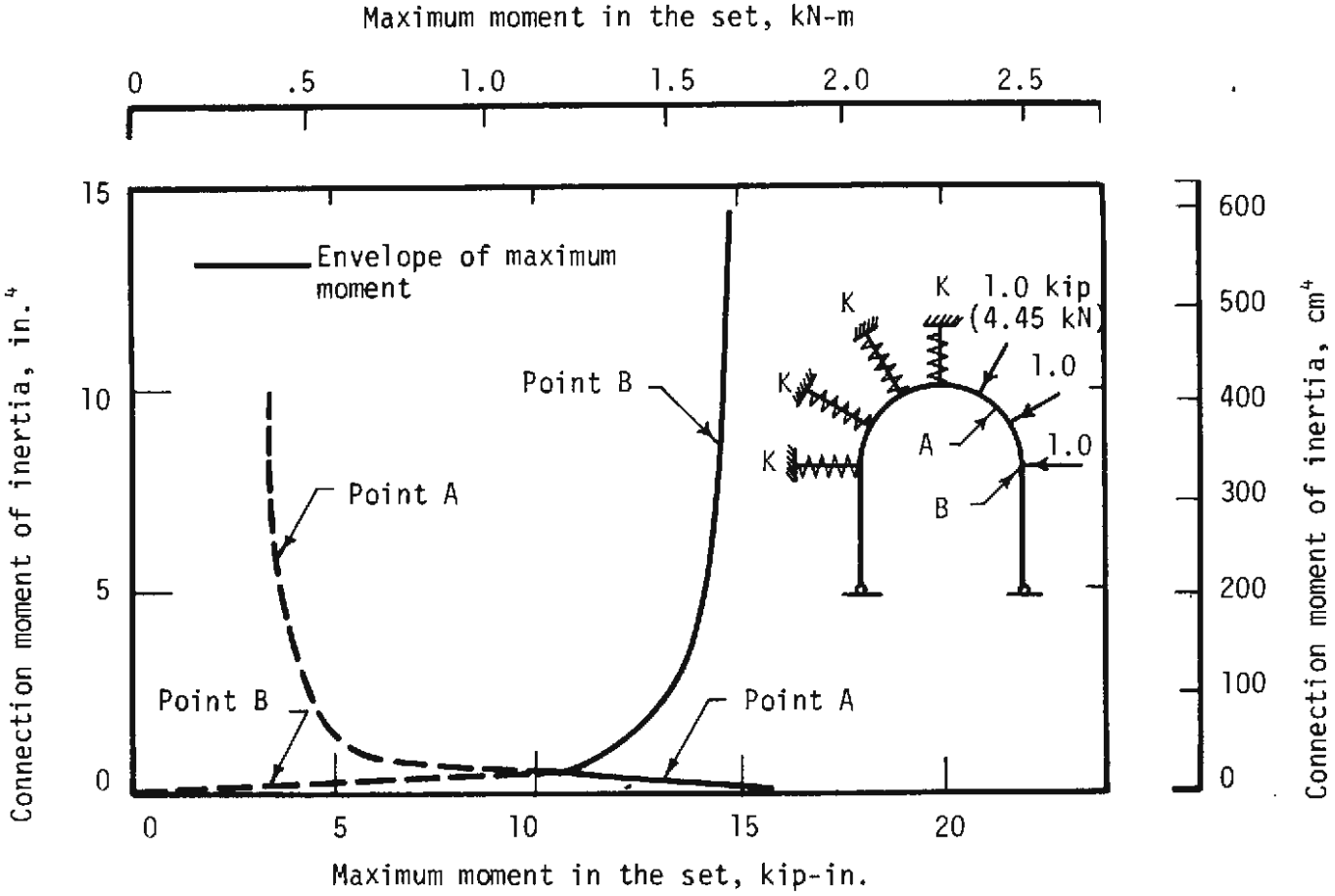

FIG. 5.26 EFFECT OF CONNECTION STIFFNESS ON MAXIMUM MOMENT IN THE SET FROM THE LINEAR ANALYSIS

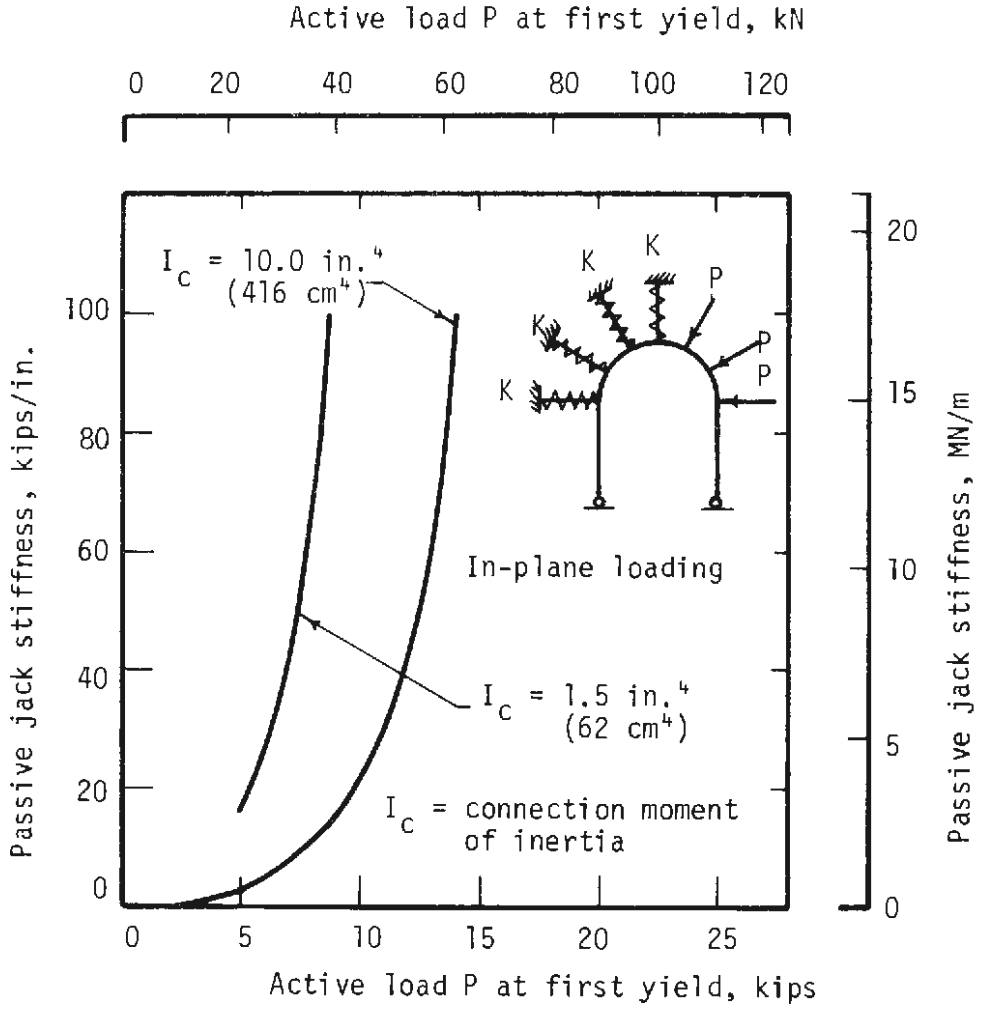

FIG. 5.27 EFFECT OF PASSIVE JACK STIFFNESS ON YIELD LOAD OF THE SET FROM THE LINEAR ANALYSIS

Figure 5.28 is a plot of passive jack stiffness versus horizontal displacement at connection 3. The displacement is seen to be affected only slightly by passive jack (blocking) stiffness above a stiffness of about 20 kips/in. (3.5 MN/m).

The manner in which maximum moment for a given active load configuration varies with blocking stiffness can be observed in Fig. 5.29. Increasing the blocking stiffness reduces the maximum moment, but the effect is much less pronounced at high stiffnesses. Stiffnesses above 100 kips/in. (17.5 MN/m) appear to have no effect on the maximum moment. The maximum-moment curves for the two connection stiffnesses are parallel, indicating that a change in passive jack stiffness has the same effect for sets with standard or moment resistant connections. The curves are similar in shape to those of Fig. 5.28 for deflection, as would be expected.

5.5.5 EFFECT OF OUT-OF-PLANE LOADS

The variable for analysis in this section is the angle of inclination of load relative to the plane of the set. Connection stiffness is assumed to be 10 in.^{4} (416 cm^4) (moment resistant connection) and passive jack stiffness 30 kips/in. (5.3 MN/m) (soft blocking).

The average inclined active load to produce first yield is plotted as a function of inclination in Fig. 5.30. The yield load reduces from 11.1 kips (49 kN) at no inclination to 8.0 kips (36 kN) for a 30 deg (.52 rad) inclination. It then begins to increase and attains a value of about 13.5 kips

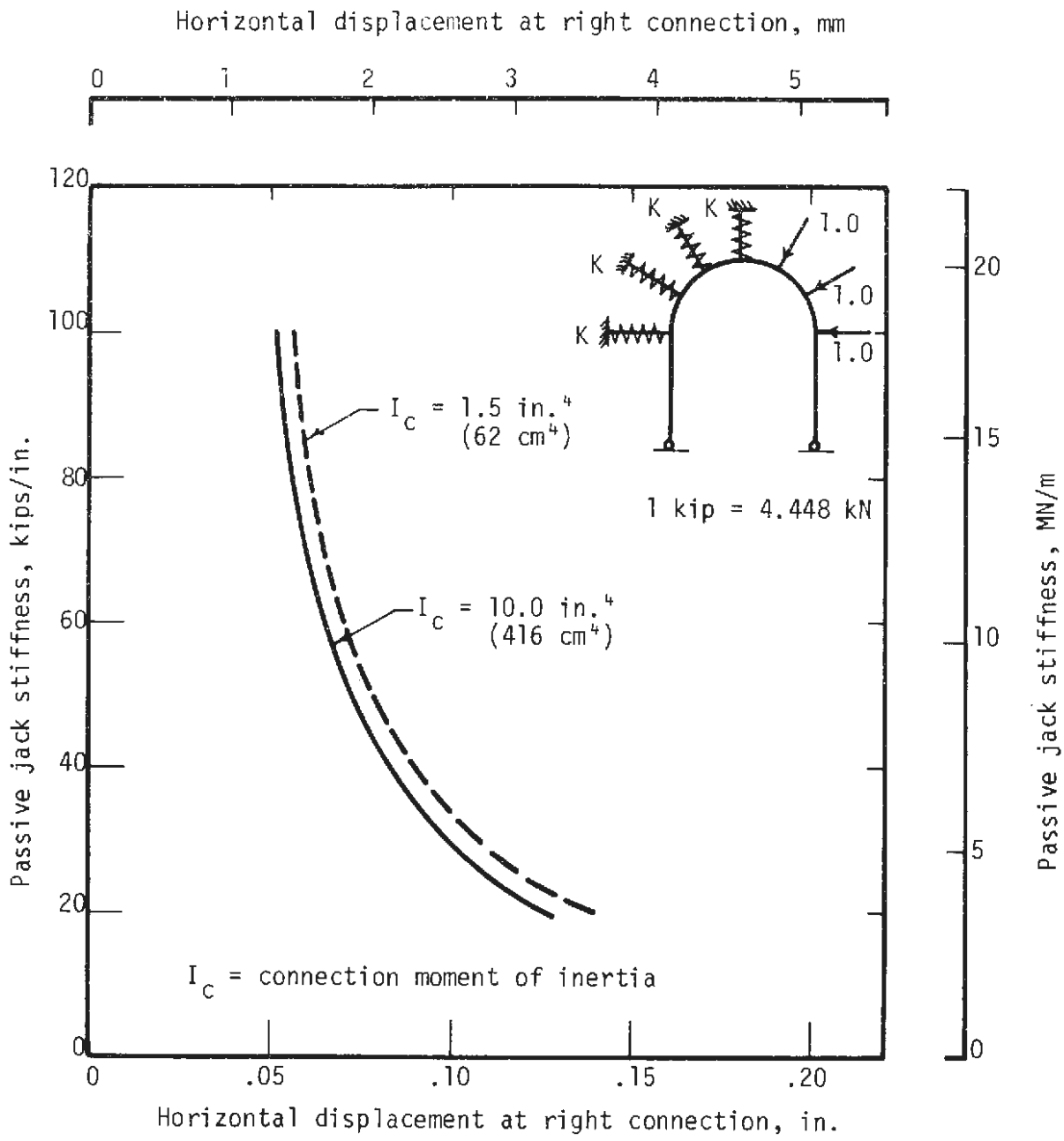

FIG. 5.28 EFFECT OF PASSIVE JACK STIFFNESS ON MAXIMUM DEFLECTION OF THE SET FROM THE LINEAR ANALYSIS

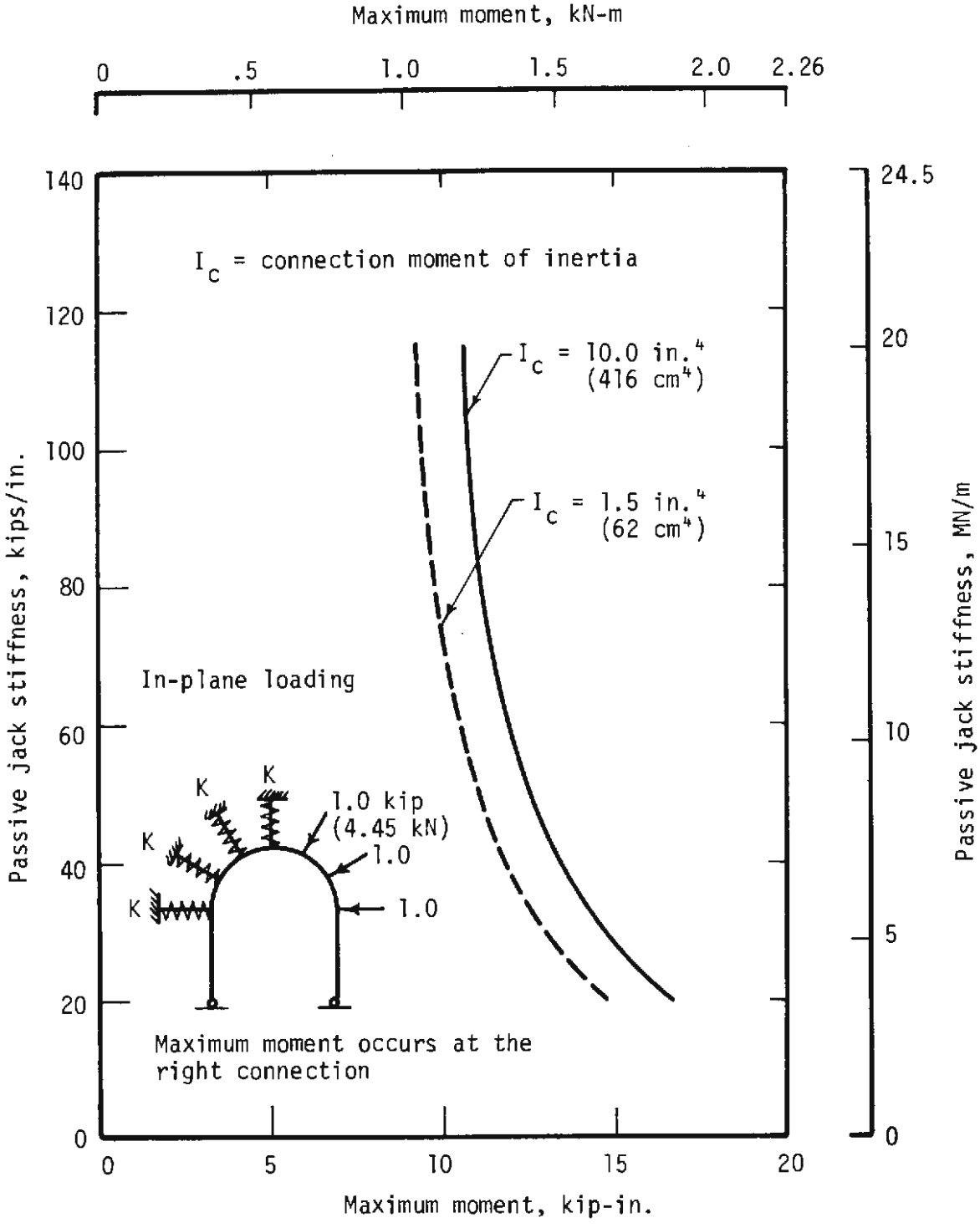

FIG. 5.29 EFFECT OF PASSIVE JACK STIFFNESS ON MAXIMUM MOMENT IN THE SET FROM THE LINEAR ANALYSIS

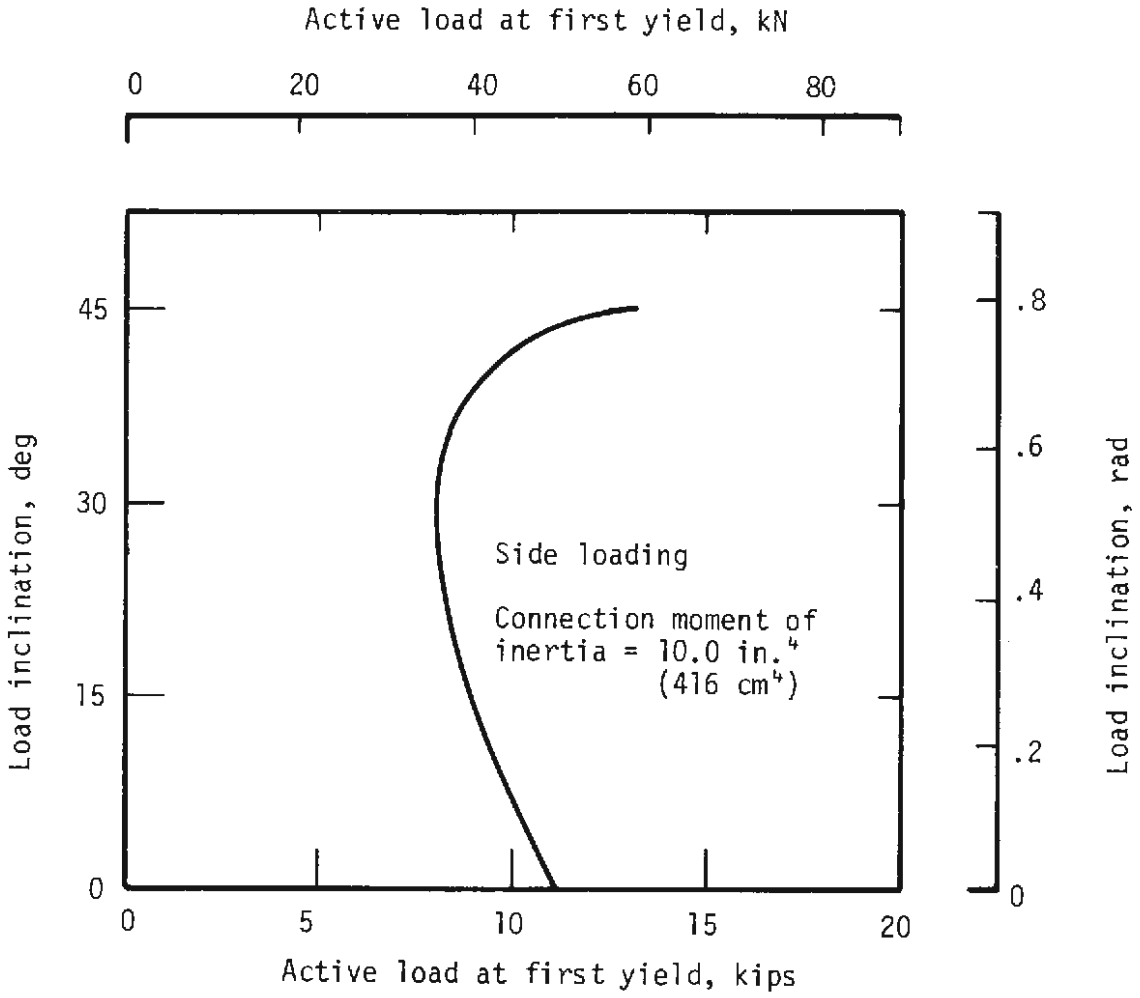

FIG. 5.30 EFFECT ON YIELD LOAD OF THE INCLINATION OF ACTIVE LOADS ON THE SET, FROM THE LINEAR ANALYSIS

(60 kN) for a 45 deg (.79 rad) inclination. The analysis shows that maximum moments are about the strong axis for inclinations less than 30 deg (.52 rad) and about the weak axis for inclinations greater than 30 deg (.52 rad). The increase in load with larger inclinations is due to the lateral support of the set at the brace points.

5.6 ANALYSES BASED ON A LINEARLY ELASTIC PROGRAM

5.6.1 LINEARLY ELASTIC ANALYSIS

The linearly elastic behavior of the set was estimated before each test by the ICES-STRUDL frame analysis. After the tests the estimates were revised to reflect the actual test conditions as closely as possible. Also, several analyses were performed to study the effect of various parameters as discussed in the previous section. ICES-STRUDL assumes that displacements are small and that each member behaves in a linearly elastic manner. The circular arch in the model consisted of a series of 24 straight members, not including the connection members. Straight members do not affect the results significantly if they are sufficiently short. Figure 5.31 shows the model for a typical test (M1b). The set was considered to be a space frame, so the out-of-plane load components and their effect on the structure were included.

The center line of the structure is used to define the geometry of the frame. Loads are applied on the center line. In the tests the loads were applied at the outer flange, with the line of application passing through the centroid of the section.

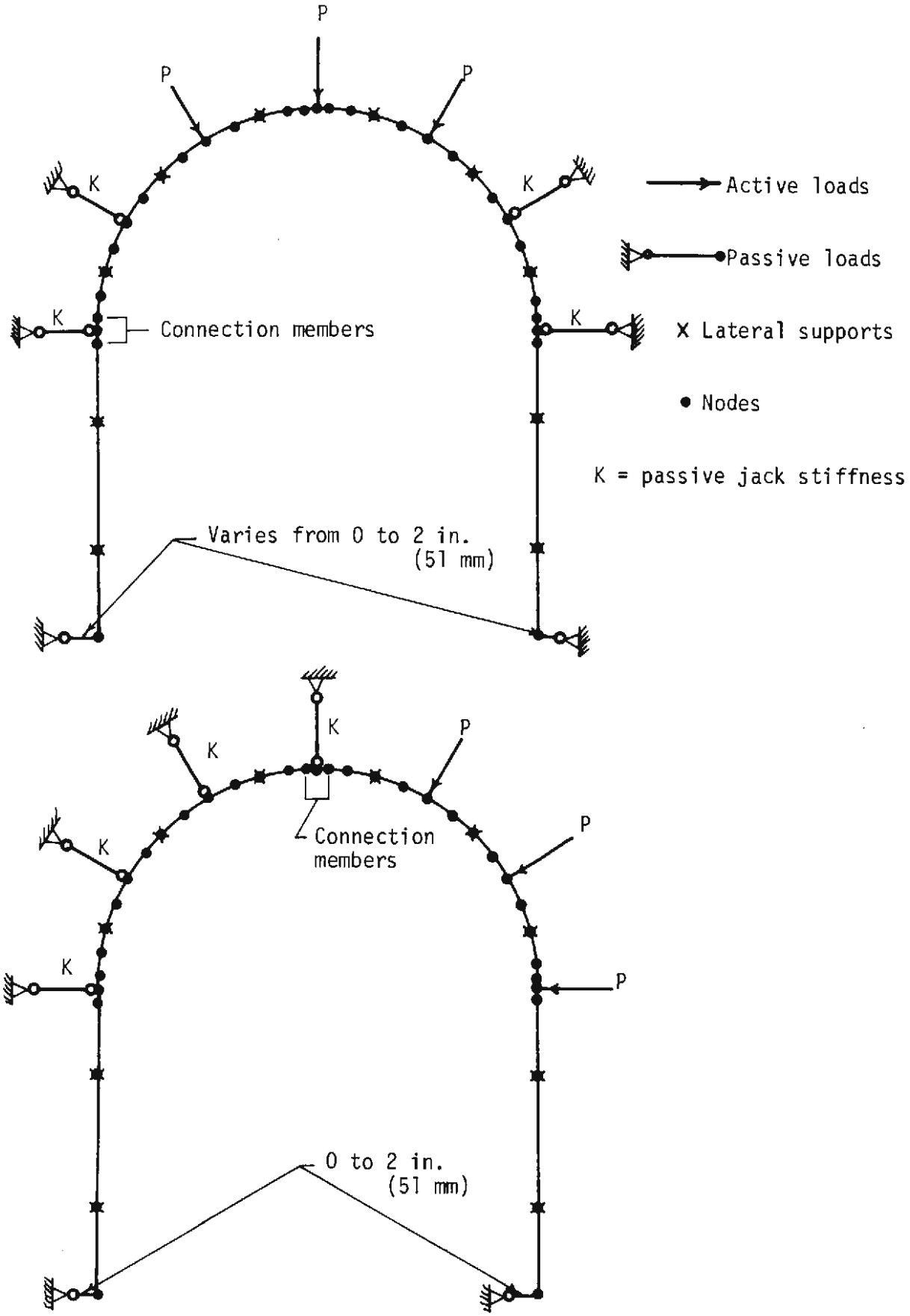

FIG. 5.31 MODEL USED FOR LINEAR ANALYSIS OF THE STEEL SETS

The three active loads were represented by three equal point loads. The two load configurations were the same as those used in the tests. Straight members perpendicular to the plane of the set and simply connected to it were used to simulate the lateral support furnished by ties and collar bracing. The properties of these members remained constant. Each connection was represented by two adjoining beam members each 5 in. (130 mm) long. The equivalent moments of inertia of these members were determined approximately from Fig. 5.9. In some cases members were added perpendicular to the base of the column to simulate the eccentricity of the reaction that occurred in the tests. This is shown in Fig. 5.31.

The stiffness of the passive jacks used in the set tests was nonlinear. In those problems that were designed to model the set tests, these jacks were simulated by simply connected straight members with linear properties. The point on the jack load-displacement curve corresponding to the load for which the analysis is made is used to determine an idealized linear jack stiffness, and may differ for each of the three passive jacks. The jack stiffness is defined by $P/\Delta = AE/L$, where P is the load in the jack, Δ the deflection under load P, A the area of the member, L the length of the member and E the modulus of elasticity. E and L were held constant in the analysis while A was chosen to conform with the jack stiffness corresponding to the particular point on the test load-displacement curve.

5.6.2 INCREMENTAL STRUDL ANALYSIS

Since analysis by the STRUDL program is based upon linearly elastic

behavior of a structure the ultimate load capacity generally cannot be directly predicted. However, by using the principle of superposition it is not difficult to obtain a reasonable value for the ultimate load capacity of some simple structures.

If the effects of residual stresses and strain hardening are neglected, a flat-topped stress-strain curve may be assumed for most common structural steels. With this idealization, a limiting value of moment resistance (plastic moment) of a section may be determined. When the plastic moment develops at a cross section in a member, a plastic hinge is said to have formed. For any loading tending to cause a higher moment this point acts as a hinge, but continues to carry the plastic moment.

A nonlinear analysis may be obtained with the STRUDL analysis by superimposing load increments, one for each plastic hinge. Unit loads are applied, corresponding to the location of the active loads in the test, and the first plastic hinge location is found. A second analysis is then made with a hinge in the structure at the location of the first plastic hinge, and an increment of load sufficient to cause a second plastic hinge is determined. This procedure continues step by step until a collapse mechanism is formed, and thus the ultimate load is reached.

The following continuous-beam example illustrates the procedure. Figure 5.32 shows a continuous beam of two equal spans simply supported at A, C and E. The plastic moment is taken to be that of an M4 X 13 in A36 steel, i.e., 18.2 ft-kips (24.7 kN-m). Unit loads are applied to the structure at points B and D, with P_B equal to P_D. The resulting moment diagram is shown in

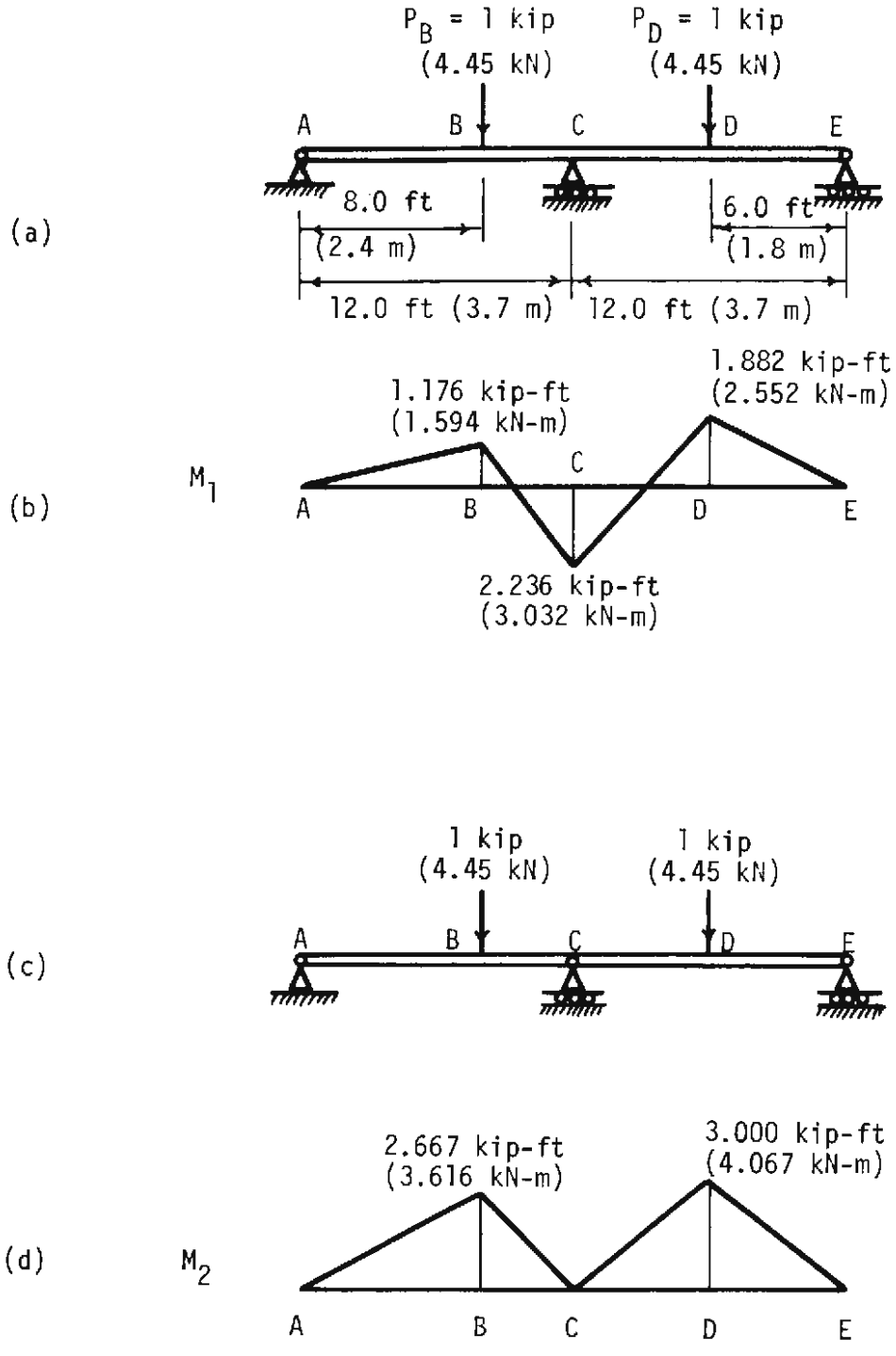

FIG. 5.32 EXAMPLE OF NONLINEAR ANALYSIS BY INCREMENTAL APPLICATION OF THE LINEAR ANALYSIS

Fig. 5.32b. This corresponds to the first linear analysis. It can be seen that the first plastic hinge will occur at the center support, point C. For a plastic moment of 18.2 ft-kips (24.7 kN-m), the loads at the time the first hinge occurs are $P_B = P_D = 18.2/2.236 = 8.14$ kips (36.2 kN).

With a hinge at point C unit loads are applied to the structure shown in Fig. 5.32c. The corresponding moment diagram is shown in Fig. 5.32d. This step in the procedure corresponds to the second linear analysis. To locate the position of the second hinge, it is necessary to proceed along the structure, using the following formula:

$$P_1 M_1 + (P_2 - P_1) M_2 = M_P$$

where M_1 = moment at a particular location determined from the M_1 diagram, M_2 = moment at the same location determined from the M_2 diagram, P_1 = load at which the first plastic hinge forms, P_2 = load at which the second plastic hinge forms. For simple structures, as in this example, the procedure is not lengthy. It is only necessary to find the section for which the values of M_1 and M_2 give the smallest value of P_2. In this structure, points B and D are the obvious ones to check.

$$P_2 = \frac{M_P - P_1 M_1}{M_2} + P_1$$

$$= \frac{18.2 - 8.14 \times 1.176}{2.667} + 8.14 = 11.37 \text{ for point B,}$$

$$= \frac{18.2 - 8.14 \times 1.882}{3.000} + 8.14 = 9.10 \text{ for point D.}$$

Therefore, when P_2 = 9.10 kips (40.5 kN) span CE will collapse.

In the analysis of the steel sets, the third hinge is found in a similar manner, using the formula:

$$P_1M_1 + (P_2 - P_1)\, M_2 + (P_3 - P_2)\, M_3 = M_P$$

and finding the location which gives the smallest value of P_3. For each succeeding hinge, the formula takes on an additional term. Each term P_1, $P_2 - P_1$, $P_3 - P_2$ and so on, represents an increment in the total load on the structure. This method for determining the ultimate load is easily used when the number of load increments is small and the loading is not complicated. One substantial difficulty arises when the interaction among strong-axis moment, weak-axis moment, and axial force is significant. The principle involved is the same, but the number of calculations and the bookkeeping problems increase greatly.

In the incremental analyses performed thus far the resulting ultimate loads have been conservative, but they are much more realistic than those given by a single application of the linear analysis. Further study may enable the development of an analysis that will give more accurate results.

5.7 NONLINEAR ANALYSIS OF STEEL SETS

5.7.1 INTRODUCTION

This portion of the computer-aided analysis was undertaken to predict the ultimate strength and nonlinear behavior of a steel set. For this purpose the general structural analysis computer program developed by NASA for

support of the space program was used. The program, called NASTRAN, contains elements which can be given a piecewise linear stress-strain relationship. Details of the model used to represent the steel sets are given in Appendix A.

5.7.2 NASTRAN MODEL

To represent the nonlinear behavior of a wide-flange section the element must be constructed of two-force members (rods) for the flange and shear panels for the web. The flanges of a wide-flange section resist most of the axial force and bending moment while the web resists most of the shear. By using the combination of rods and shear panel shown in Fig. 5.33 the element can be made to duplicate the behavior of the wide-flange section for axial force, shear, and bending moment. The built-up section must have the same cross-sectional properties as the wide-flange section. Therefore, each rod flange must have an area of one-half the cross-sectional area of the section and the distance h of the rods from the centerline must be computed to furnish a moment of inertia of 10.5 in.^{4} (437 cm^4). The shear panel has a modulus of elasticity E = 30,000 ksi (207 GPa) to simulate the steel in the web. The thickness of the web of the M4 X 13 is 0.256 in. (6.5 mm) but since the flanges resist some shear this was increased to 0.306 in. (7.8 mm) in the model.

The program must be given the desired stress-strain curve for the nonlinear element, in this case the rod. With the stress-strain curve for the grade of steel used, the moment-curvature relationship of the cross section can be determined, from which the stress-strain curve for the model cross section can be found as follows:

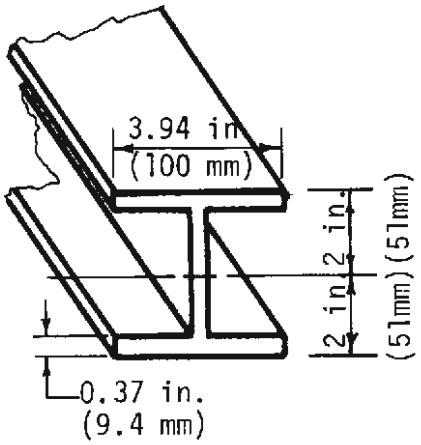

(a) M4 x 13 section

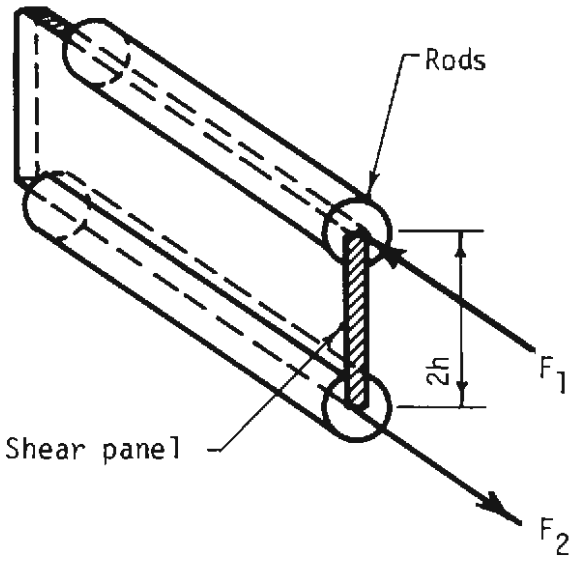

(b) Built up section

Rod areas for 36 ksi (248 MPa) yield point steel, flat top stress-strain curve:

A_1 = 1.005 in.^{2} (6.484 cm^2)
A_2 = 0.813 in.^{2} (5.245 cm^2)
A_3 = 0.087 in.^{2} (0.561 cm^2)

Rod areas for 60 ksi (414 MPa) yield point steel, flat top stress-strain curve:

A_1 = 1.076 in.^{2} (6.942 cm^2)
A_2 = 0.803 in.^{2} (5.181 cm^2)
A_3 = 0.026 in.^{2} (0.168 cm^2)

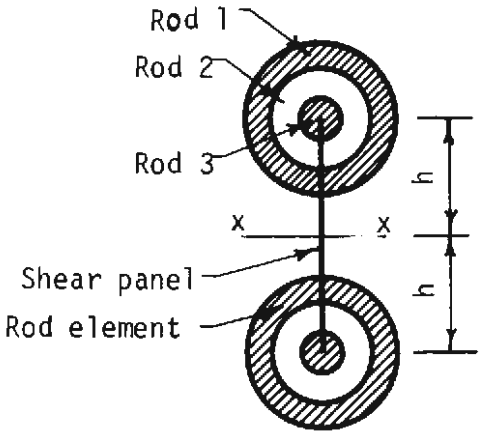

(c) Rod configuration

h = 1.66 in. (42.2 mm)

I_{xx} = 10.5 in.^{4} (437 cm^4)

Area = 3.81 in.^{2} (24.6 cm^2)

FIG. 5.33 IDEALIZED REPRESENTATION OF THE M4 x 13 SECTION IN THE NASTRAN NONLINEAR ANALYSIS

1. Idealized steel stress-strain curves are shown in Fig. 5.34 for steels with yield stresses of 36 and 60 ksi (248 and 414 MPa). It is conservative practice to neglect strain hardening. The modulus of elasticity is assumed to be 30,000 ksi (207 GPa). The corresponding yield strains are ε_y = .0012 and .002 for σ_y = 36 and 60, respectively.

2. Moment-curvature curves are computed from the stress-strain curve assuming plane cross sections remain plane. These curves are shown in Fig. 5.35. For 60 ksi (414 MPa) steel the cross section has a fully plastic moment capacity of 355 kip-in. (40.1 kN-m) while the 36 ksi (248 MPa) cross section has a capacity of 215 kip-in. (24.3 kN-m).

3. Since the moment curvature curves can be represented by three straight segments, the rod which models each flange was divided into three parts. Each part is assumed to have linear stress-strain properties until yield, when it becomes perfectly plastic and the three parts become plastic at different stresses. With this arrangement each rod is ideally elasto-plastic, but the interaction simulates a nonlinear element. The yield stresses are determined from the moment-curvature curves by using the intersections of the straight segments as failure moments. These cusps are marked M_1, M_2, M_3 on Fig. 5.35. The yield strains are calculated from the curvatures and the yield stresses from the moments at M_1, M_2, and M_3. Figure 5.36 shows the results of these calculations for the two steels. The yield stresses and corresponding yield strains for each of the three rod elements are shown on the figure.

4. Because material properties differ for the three rods of each flange, the areas must be computed to maintain the desired moment curvature

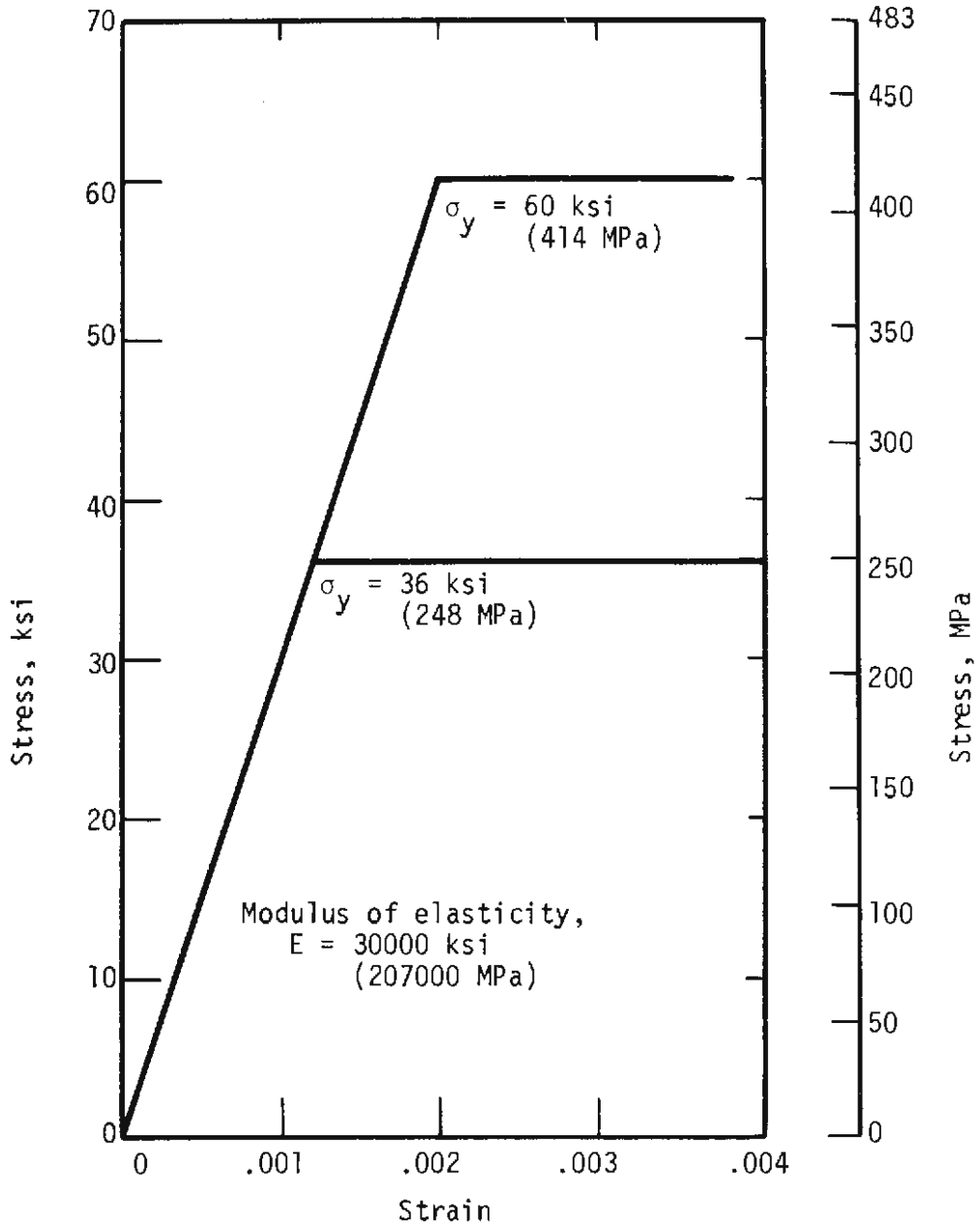

FIG. 5.34 IDEALIZED STRESS-STRAIN FOR THE STEELS

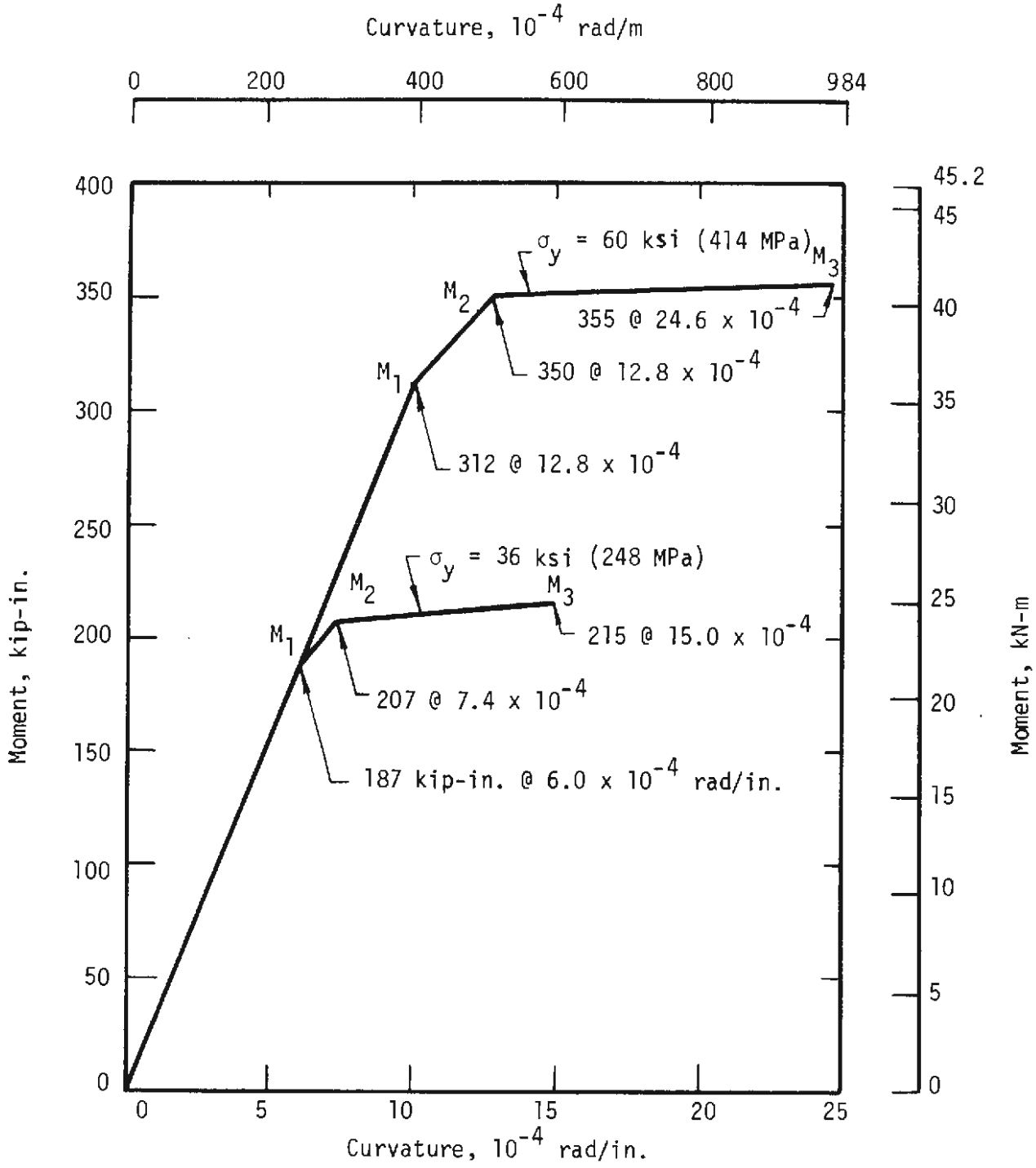

FIG. 5.35 CALCULATED MOMENT-CURVATURE FOR THE M4 x 13 SECTION

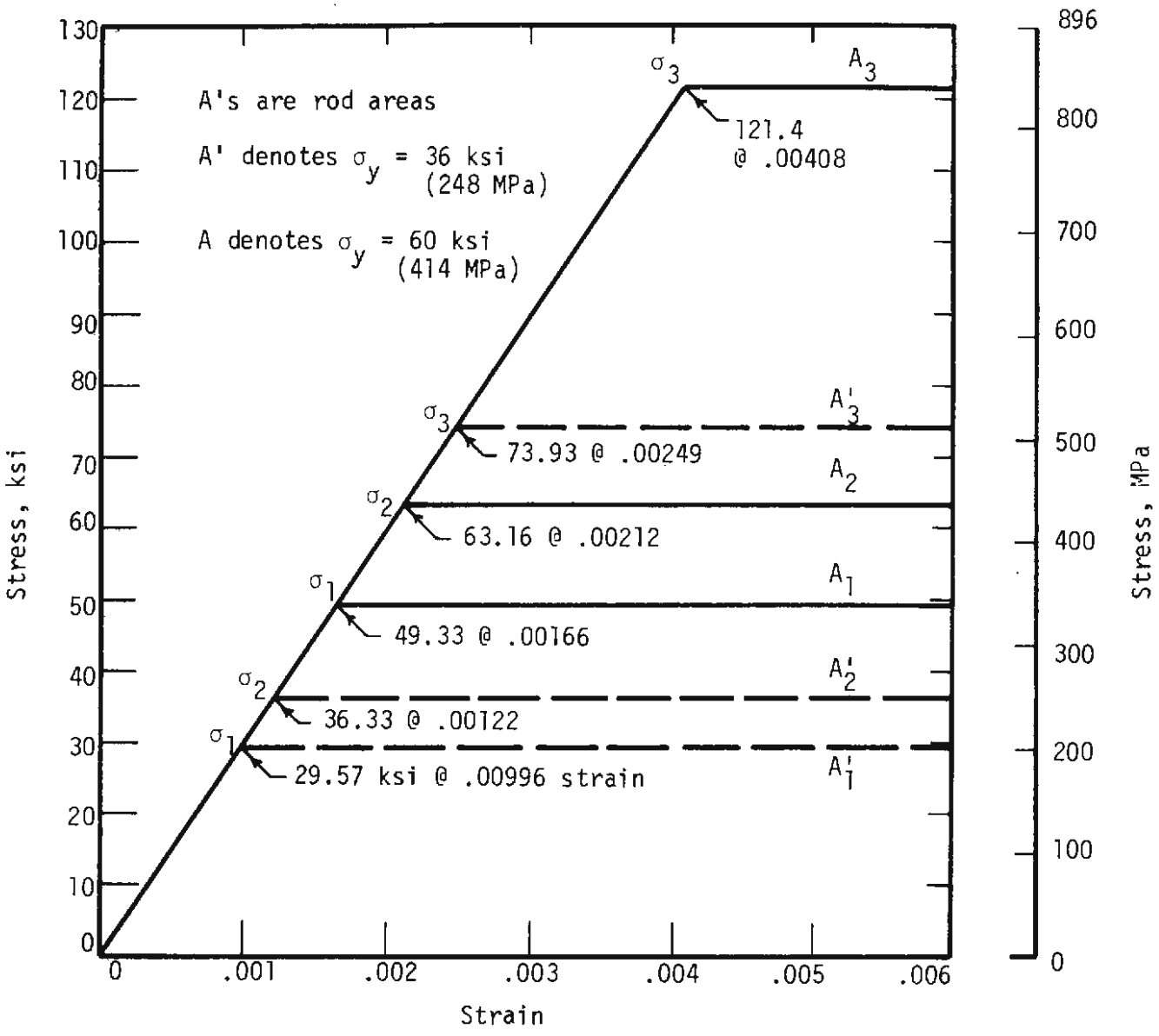

FIG. 5.36 ADJUSTED STRESS-STRAIN FOR THE NASTRAN REPRESENTATION OF THE M4 x 13 SECTION

curve for the model. The final model section is shown in Figure 5.33c.

The accuracy of the assumptions and the accuracy of the model were tested by simulating and analyzing a simple beam in the elastic and inelastic ranges. A beam 120 in. (0.75 m) long was divided into 30 equal rod/shear panel segments and a concentrated load was applied at midspan. The computed deflection at midspan for a load of 10 kips, which is in the linear range, and a material with E = 29.7 x 10^6 psi (205 GPa) and σ_y = 60 ksi (414 MPa) is 1.15 in. (29.2 mm). The NASTRAN program computes a midspan deflection of 1.18 in. (30.0 mm) for 10.0 kips (44.5 kN) load. This is an error of approximately 3 percent in the elastic range. The actual yield load, P_y, and ultimate load, P_p, are computed to be:

$$P_y = \frac{4M_y}{L} \qquad P_p = \frac{4M_p}{L}$$

where $M_y = \sigma_y S_x$ and $M_p = \sigma_y Z_x$

$$P_y = \frac{(4)(60)(5.24)}{120} \qquad P_p = \frac{(4)(60)(6.06)}{120}$$

$$= 10.48 \text{ kips (46.6 kN)} \qquad = 12.12 \text{ kips (53.9 kN)}$$

These values and two NASTRAN analyses are shown in Fig. 5.37. The initial difference in slope between the NASTRAN and the elastic ($PL^3/48EI$) curve is due to the slight 3 percent error of modeling. The NASTRAN model has an initial yield at a value slightly below 10.7 kips (47.6 kN) which is within 3 percent of the computed P_y of 10.48 kips (46.6 kN).

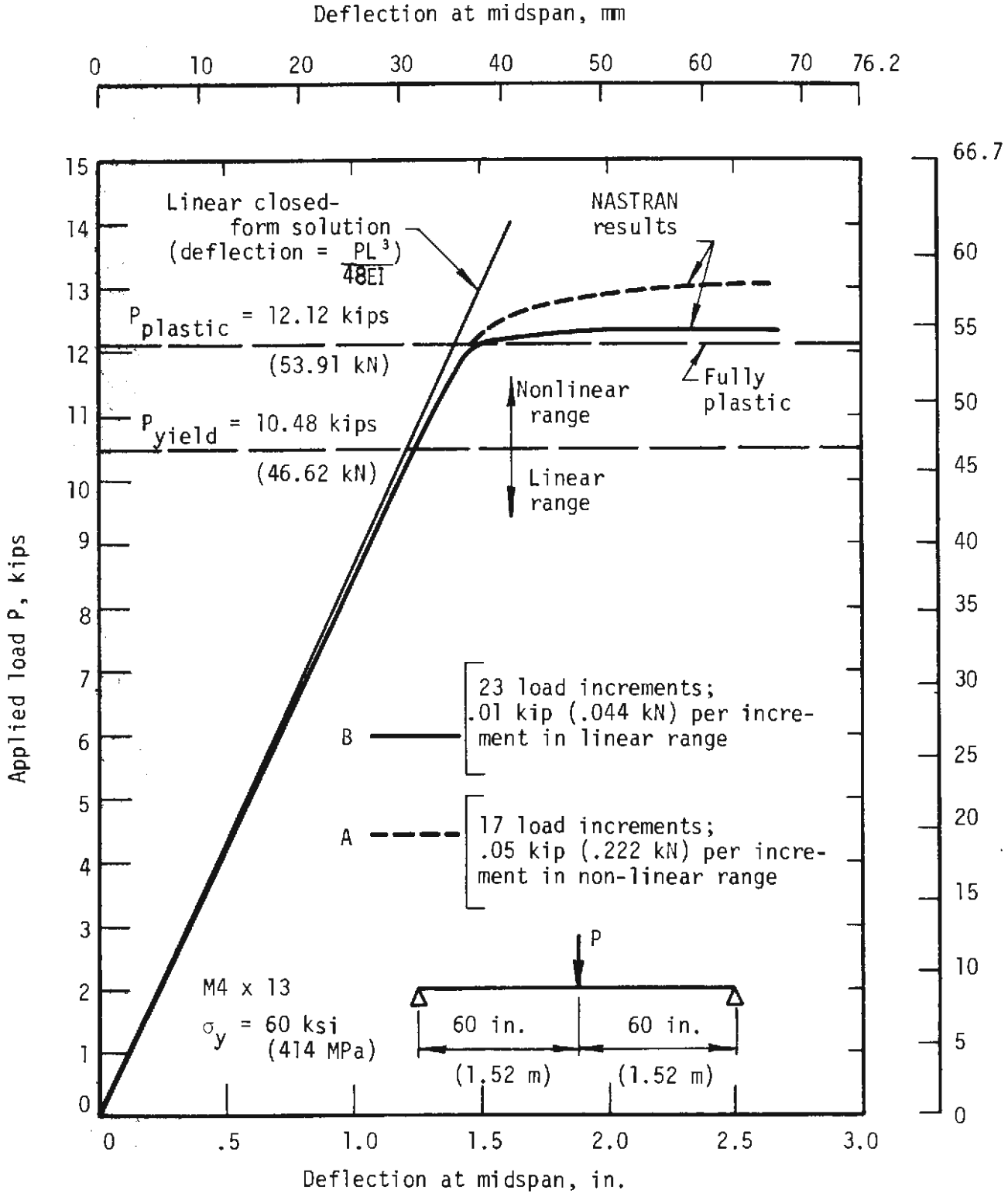

FIG. 5.37 LOAD-DEFLECTION FOR A SIMPLE BEAM ANALYZED WITH THE NASTRAN PROGRAM

Because NASTRAN is a finite element program, the results obtained are approximate. The degree of accuracy of the inelastic analysis is a function of the model and of the load increments used. With large load increments and rapidly changing material properties, the results may be grossly inaccurate. This is illustrated in Fig. 5.37. Curve A is from an analysis using 17 load increments at a load increment of 0.05 kips (0.22 kN) in the inelastic range. This analysis predicted an ultimate load P_p of slightly more than 13 kips (57.8 kN), or 7 percent above the actual P_p of 12.12 kips (53.9 kN). The second analysis (curve B) used 23 load increments at a load increment of 0.01 kips (0.04 kN) in the inelastic range. Here the ultimate load was determined to be 12.3 kips (54.7 kN), an error of 2 percent. Thus, with care in incrementing, the NASTRAN section model is quite accurate in both the elastic and inelastic ranges.

NASTRAN assumes the rod elements to be straight. Figure 5.38 shows the structure centerline of the steel set as modeled. The frame was divided into 44 segments. There are 90 grid points and some 350 rod and shear panel elements. As in the STRUDL analysis, there are three active point loads at varying locations which depend on the test being simulated. The blocking stiffnesses (represented by the passive jacks) and the lateral supports are simulated by straight members which are simply connected to the steel set. The accuracy of this frame model was tested by comparing results in the elastic range to those of STRUDL. The effect of reduced bending resistance at the joints and the base fixity were ignored. The set was assumed to have a uniform

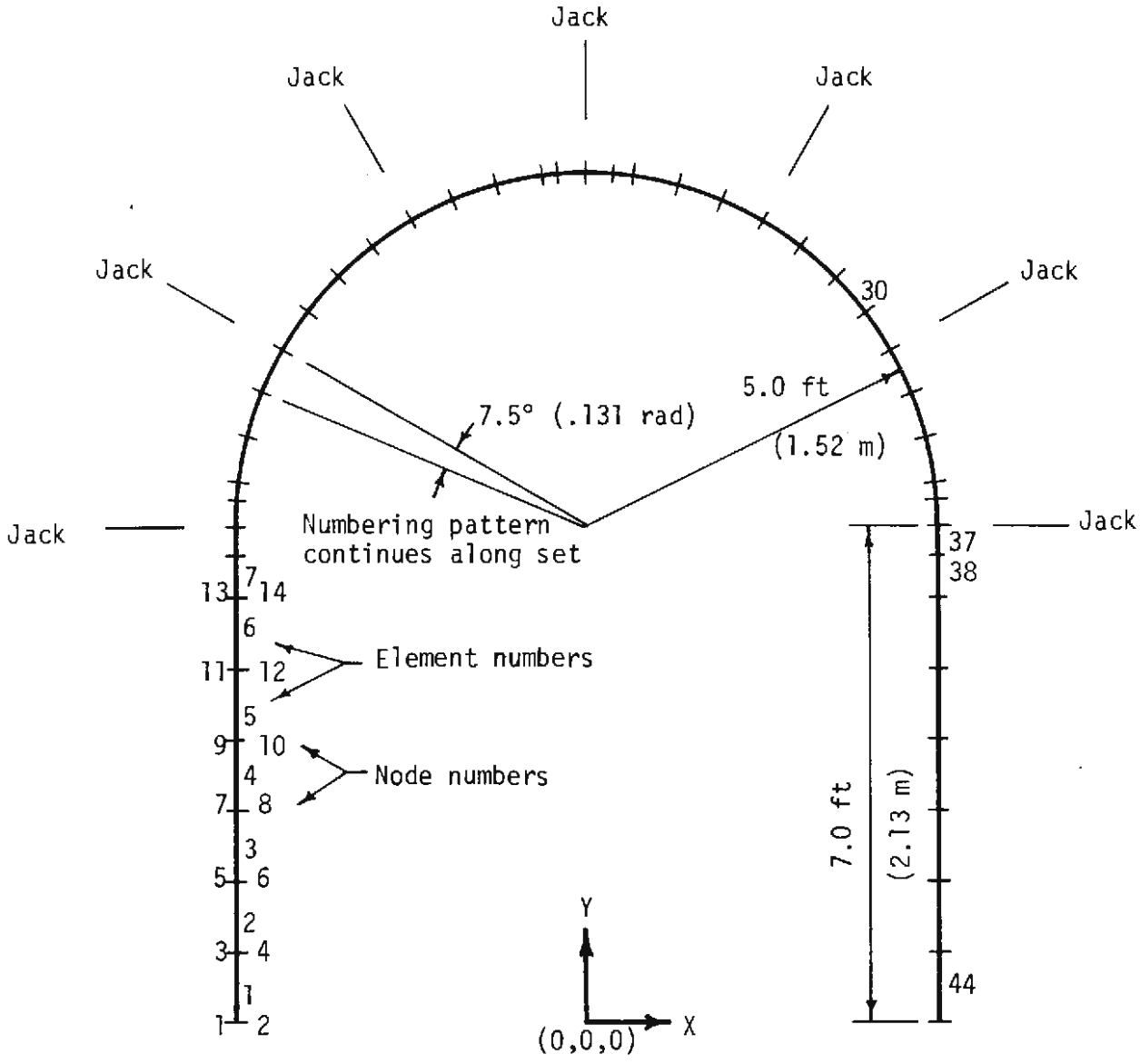

FIG. 5.38 IDEALIZED STRUCTURE IN THE NASTRAN PROGRAM

moment of inertia of 10.5 in.^{4} (437 cm^4) and fixed bases. The difference in computed displacements ranged from 0.3 percent to 3 percent depending on which portion of the frame was examined. Thus the NASTRAN section and frame models are very accurate in the elastic range.

It was also necessary to determine the most accurate method of representing a connection (standard and moment resistant) in NASTRAN. To reduce the moment of inertia at a particular section in an attempt to simulate a joint, it is necessary to decrease the distance between the rod flanges. This may be accomplished in two ways. For example, to simulate a moment of inertia of I = 1.0 in.^{4} (42 cm^4) at a joint, the distance between the rod elements, d, at that section must be:

$$d = 2\sqrt{I/A} = A\sqrt{1.0/3.81} = 1.024 \text{ in. } (26.01 \text{ mm})$$

where A is the total section area. The distance between the rods at the end grid points may be reduced to the value d, as in Fig. 5.39, so that the minimum value of I = 1.0 in.^{4} (42 cm^4), or by decreasing the distance between the rods for that element to the value d', which is less than d, as shown by the dashed lines so that the average I = 1.0 in.^{4} (42 cm^4). These two methods were compared in the elastic range. For this comparison, the joint moments of inertia were reduced to 3.81 in.^{4} (159 cm^4) and the bases were fixed. It was found that the first method produced displacements with only 2 percent difference between NASTRAN and STRUDL. The second method was slightly less accurate.

To simulate the reduced fixity of the bases, the moment of inertia at the base of both legs was reduced to 1.0 in.^{4} (42 cm^4); the corresponding maximum resisting moment is 67.3 in.-kips (7.60 kN-m). For the standard

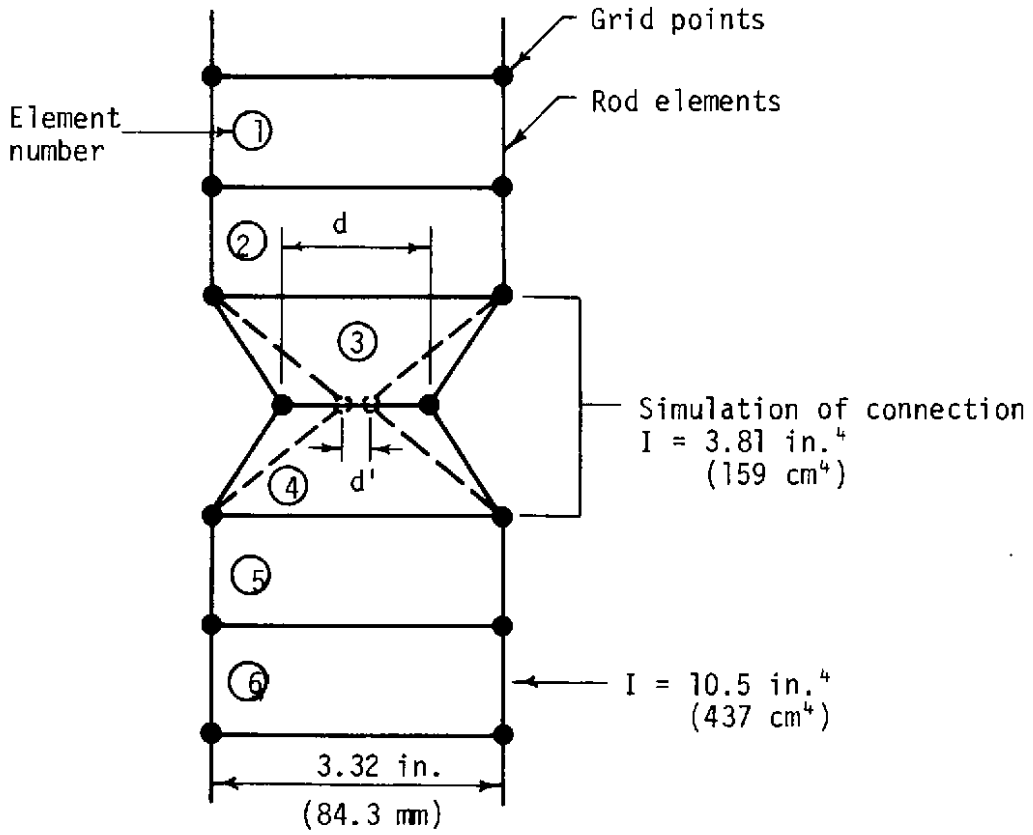

FIG. 5.39 SIMULATION OF CONNECTIONS IN THE NASTRAN PROGRAM

connection, the moment of inertia was reduced to 1.5 in.^{4} (62 cm^4), yielding a maximum moment resisting capacity of 82.43 in.-kips (9.31 kN-m), while for the moment resistant connection it was increased to 12.0 in.^{4} (499 cm^4) with a moment resistance of 233.14 in.-kips (26.34 kN-m). These are summarized in Table 5.9 for A36 steel.

TABLE 5.9

SUMMARY OF ELEMENT PROPERTIES USED IN THE NASTRAN MODEL

Section	I, in.^{4} (cm^4)	Plastic moment, in.-kips (kN-m)
M4 X 13	10.5 (437)	218 (24.6)
Base	1.0 (42)	67.3 (7.60)
Standard Connection	1.5 (62)	82.43 (9.31)
Moment Resistant Connection	12.0 (499)	233.14 (26.34)

In determining the passive jack stiffness to be used in the nonlinear analysis, the set tests were consulted. Although a single load-deflection curve was used in the tests, due to testing methods the load-deflection curves varied somewhat from jack to jack and from test to test. The STRUDL analysis attempted to model the tests. Each passive jack model was given a resisting capacity which was computed from the load-deflection curve measured in the test for that particular jack at that particular loading. Since the piecewise linear analysis loads the structure from zero load to the failure load, the complete curve for

each passive jack would have to be included as an element stress-strain curve. This was not done in these studies.

In the NASTRAN analysis, the load-deflection curves for the passive loads were only approximated. This assumption was tested for accuracy in the elastic range using STRUDL. One run was made using values computed from the actual passive jack load-deflection curves. Another run was made using a one decimal place approximation of the value for each jack. A final run was made using one value which was an average for all four jacks. It was found that the latter two runs gave results within 2 percent of the value obtained from the STRUDL analysis. Therefore, the approximation using an average jack stiffness was adopted.

Figure 5.40 shows preliminary NASTRAN results for the analysis of the M1b test in terms of a load-displacement plot. The M1b set was a wide-flange section with standard connections and in-plane side loading. The average blocking stiffness was calculated to be approximately 21 kips (93 kN) for the A36 steel and 30 kips (133 kN) for the grade 60 steel is predicted. Also shown is a curve for the grade 60 steel with the base completely fixed, which increases the ultimate load by only 3 kips (13 kN). The first yield occurred at approximately 12 kips (53 kN) and the first hinges were observed in elements 37 and 38 (Fig. 5.38) at approximately 17 kips (76 kN). Second and third hinges formed in elements 30 and 44, respectively, before complete failure.

Although the ultimate load found for the A36 steel correlated very well with the set tests, it should be noted that the loading increments are relatively large. As shown before, the accuracy of the results is a function

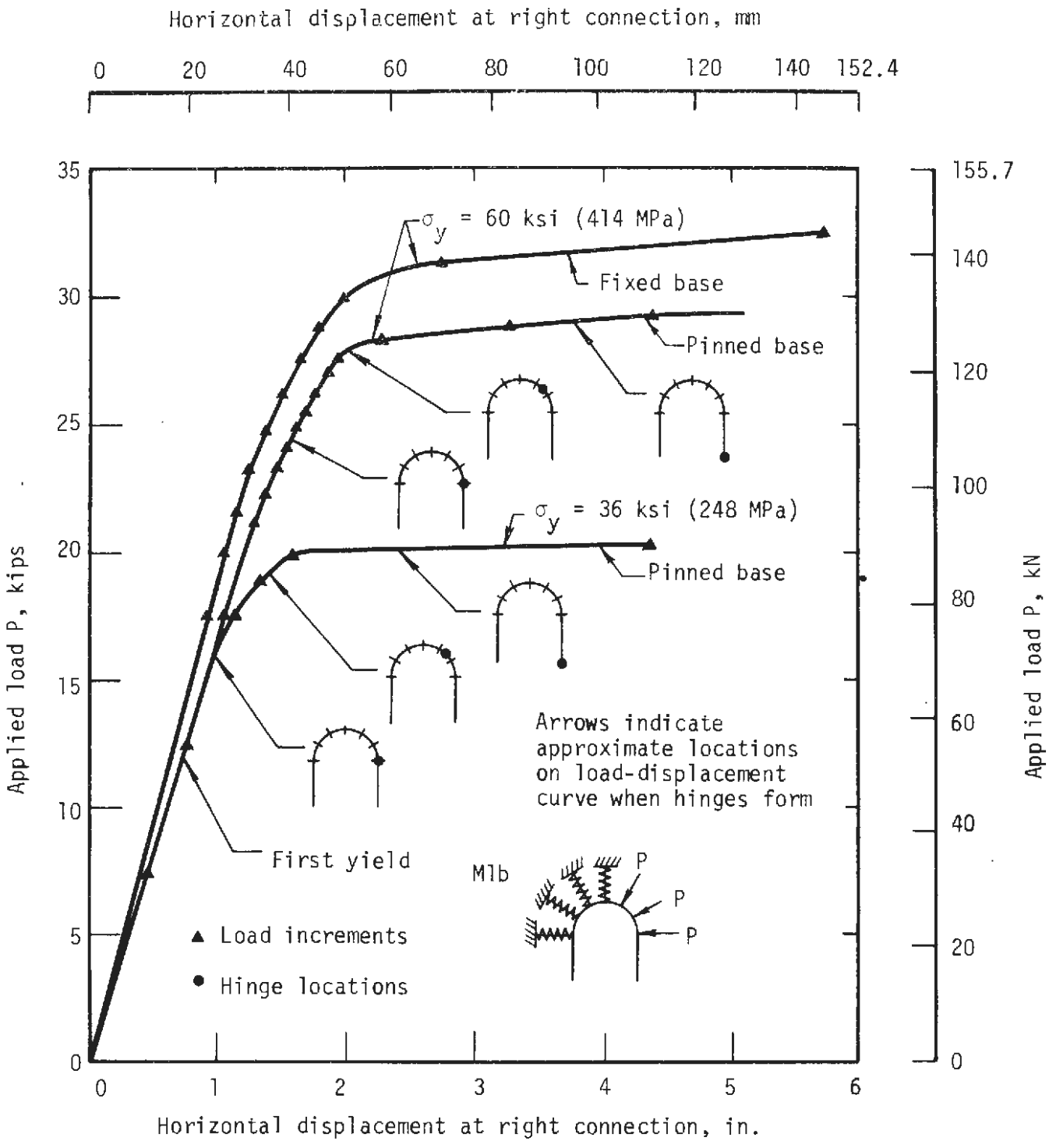

FIG. 5.40 ANALYSIS OF TEST M1B WITH THE NASTRAN PROGRAM

of the load increments. For this reason, additional investigations were undertaken using more load increments while all other parameters were held constant. These results are shown in Fig. 5.41. In these runs, the ultimate load was approximately 18 kips (80 kN), 3 kips (13 kN) less than for the larger load increments. This result is more accurate than the previous one because of the increased number of increments, but it does not correlate as well with the tests. With even more load increments, the NASTRAN ultimate load would underestimate the test results by 5 to 6 kips (22 to 27 kN). These differences may be due to strain hardening since the accuracy of the section and frame model have been tested. The stress-strain curve for the steel used in the sets tested suggest that the strain-hardening effect could be considerable. Therefore, the NASTRAN analysis of the steel set is being modified to incorporate this added strength. Studies will be performed with the actual stress-strain curve to determine the strength of the tested sets. Other parameter studies will also be performed with the NASTRAN analysis.

5.8 SUMMARY

Mechanical properties of the test specimens were investigated for both wide-flange and structural tube sections. Small differences in stress-strain properties were noted between the straight and curved portions of the arch due to cold working. In general, the yield plateau is absent and the ultimate strength is slightly higher in coupons from the cold worked portion. However, ductility is about the same for the straight and curved portions.

The section properties of a structural tube filled with concrete were investigated experimentally. Moment-thrust failure could be calculated

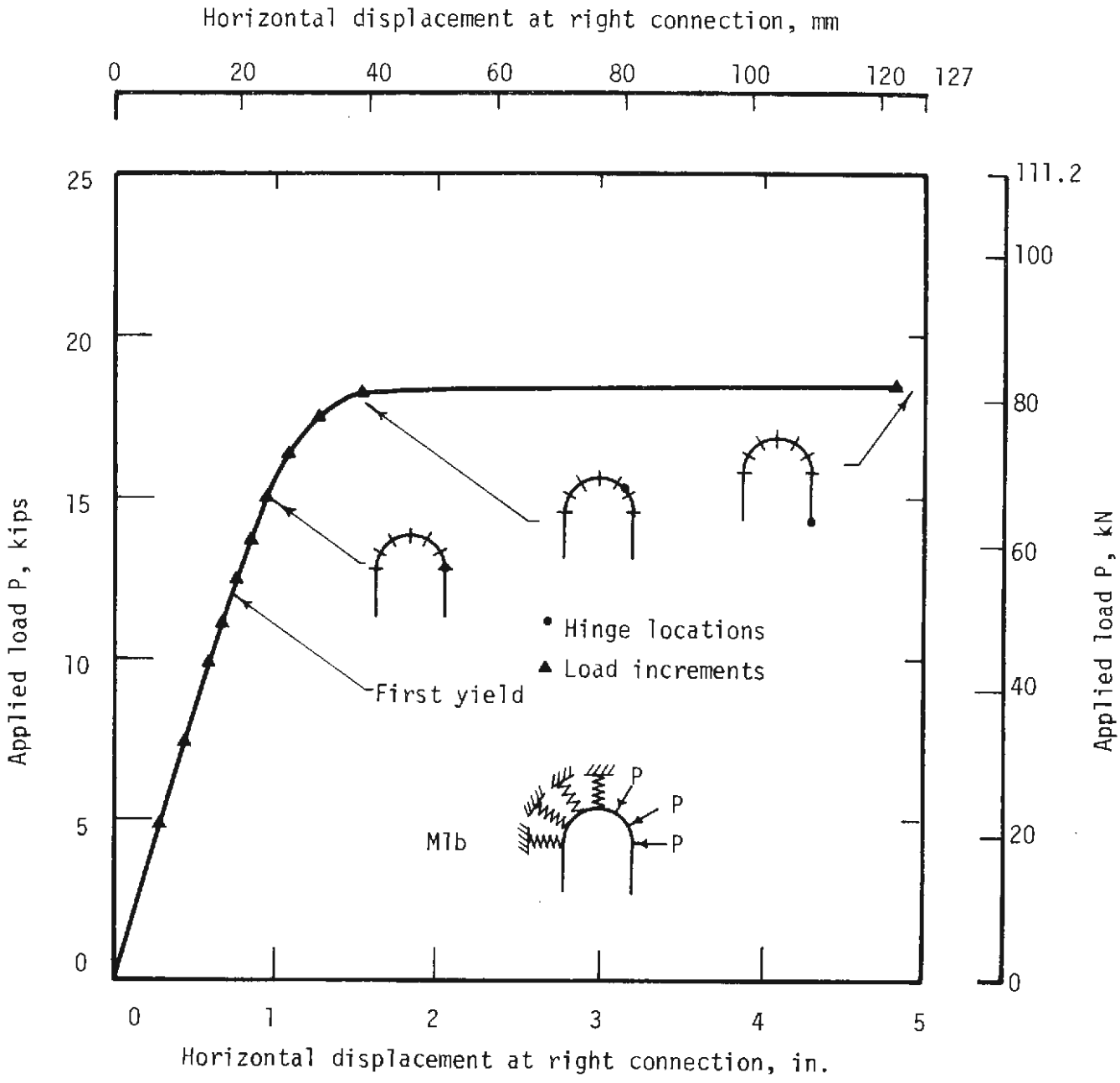

FIG. 5.41 ANALYSIS OF TEST M1B WITH THE NASTRAN PROGRAM USING ADDITIONAL LOAD INCREMENTS

within 10 percent. The additional strength provided by concrete fill depends on the relative amounts of thrust and moment, and is considerable when thrust is large and moment small but reduces to almost zero for pure moment.

Concrete fill may be most advantageous as a backup to increase the strength of sets which experience distress as loads increase with time. In other words, the tubes would not be filled when placed, but only when excessive deformation or yielding of the set is noted. Filling would then not slow down the operations at the face or add to the congestion there and might, in most cases, eliminate the necessity for remining.

The stiffness and strength of several connection configurations were determined experimentally for use in the analytic investigation. A connection with a configuration similar to that usually used in steel sets had a moment capacity of about 10 percent of the plastic moment of the set section and therefore would act much like a hinge. Deformation of these connections occurred by bending of the butt plates, and the bolts did not elongate or the welds yield. A greater stiffness can be obtained by increasing the butt plate thickness.

Several moment-resistant connections were tested, and it was found that the use of thicker butt plates and high strength bolts raised the moment capacity of the connection to as high as 96 percent of the plastic moment of the section. In these connections the butt plate deformed first, but as loading progressed the section and the welds yielded.

The results of 11 tests on steel sets are reported, four of which were loaded to failure. In the linear range of behavior the test results are compared

with a linear analysis and the effect of connection stiffness, blocking stiffness and base conditions on behavior are discussed. The linear analysis predicts the behavior of the set very well in the low-load range. It is shown that the load at initial yield of the set is not a good index of strength of the set. Also, the load at initial yield is affected appreciably by the blocking stiffness and connection stiffness, while the ultimate load is not.

The set deflection at a given load level was considerably larger with standard connections than with moment resistant connections. The load configuration also affects this comparison as the difference is much larger with unsymmetrical loading than with symmetrical loading.

When loaded 17 deg (.30 rad) out-of-the-plane of the set, the structural tube and wide-flange sets had the same load-deflection behavior and the same ultimate load. This comparison is influenced strongly by the inclination of the load and the spacing of the lateral supports and for larger values of these variables the comparison may not be so close.

With a crown loading of 45 percent of capacity deflections were 45 percent larger with soft blocking than with hard blocking, while for a side loading of 45 percent of capacity they were 127 percent larger. However, there was no significant difference in ultimate strength.

A linear analysis was used to investigate the same variables that were considered in the tests. It was found that connection stiffness larger than 50 percent of that of the set section has very little effect on deflection or maximum moment in the set. For smaller stiffnesses the effect increases, but is not marked down to 20 percent of the set section stiffness. The effect

of blocking stiffness on yield load, deflection and maximum moment is similar in that these quantities are not sensitive to change in stiffness at high values of blocking stiffness. It appears that above a stiffness of 30 or 40 kips/in. (7.0 MN/m) the effect is negligible but increases rapidly for smaller stiffnesses. The reduction in yield load with inclination of the plane of the active loads increases up to 30 deg (0.52 rad) inclination, reaching a maximum of 28 percent. Inclination above 30 deg (0.52 rad) results in an increase in yield load due to the large load component that is resisted by the lateral bracing. The maximum reduction in yield load and the inclination at which it occurs depend on the lateral support spacing and relative stiffness of the section about the strong and weak axes.

A procedure for a nonlinear analysis by successive applications of the linear analysis is described. The superposition of separate solutions, one for each hinge that forms, is required, so the bookkeeping becomes tedious for complex structures that develop several hinges before maximum load is reached. Use of the procedure thus far has provided conservative maximum loads, but they are much more realistic than those given by a single application of the analysis. It has the advantage that a more realistic analysis for set capacity can be obtained with a tool that is readily available.

The nonlinear structural analysis program developed by NASA for design of space structures was used to model the steel sets. It provides a means to predict the entire behavior accurately. A beam was analyzed to study the accuracy of the model and the results for a steel set test were then obtained. The model will be developed further. This program will allow the investigation of a greater number of variables over a wider range than would be possible in a test program.

REFERENCES

Burns, J. Q. and R. M. Richards (1964), "Attenuation of Stresses for Buried Cylinders," *Proceedings*, Symposium on Soil-Structure Interaction, Tucson, pp. 378-92.

Column Research Council (1967). *Guide to Design Criteria for Metal Compression Members*, Column Research Council, New York, 217 pp.

Furlong, R. W. (1967). "Strength of Steel-Encased Concrete Beam Columns," *Journal of the Structural Division*, ASCE, Vol. 93, No. ST5, October, pp. 113-24.

Höeg, K. (1968). "Stresses Against Underground Structural Cylinders," *Journal of the Soil Mechanics and Foundation Division*, ASCE, Vol. 94, No. SM4, pp. 833-58.

Krizek, R. J. and J. N. Kay (1972). "Material Properties Affecting Soil Structure Interaction of Underground Openings," Soil Structure Interaction - A Symposium, Highway Research Record No. 413, pp. 13-29.

Mindlin, R. D. (1940). "Stress Distribution Around a Tunnel," *Transactions*, ASCE, Vol. 105, pp. 1117-53.

Naoman, A. E., F. Moavenzadeh, F. J. McGarry (1974). "Probabilistic Analysis of Fiber-Reinforced Concrete," *Journal of the Engineering Mechanics Division*, ASCE, Vol. 100, No. EM2, April, pp. 397-413.

"NASTRAN User's Manual (Level 15)," (1972). Edited by C. W. McCormick, National Aeronautics and Space Administration, Washington, D. C., June.

Parker, H. W., R. M. Semple, A. Rokhsar, E. Febres-Cordero, D. U. Deere and R. B. Peck (1971a). *Innovations in Tunnel Support Systems*, Report No. FRA-RT-72-17, Office of High Speed Ground Transportation, Federal Railroad Administration (Order No. PB-204-437 from NTIS, Springfield, VA 22151).

Parker, H. W., D. U. Deere, R. B. Peck, R. M. Semple and E. Febres-Cordero (1971b). *Program for Large-Scale Tests on Prototype Tunnel Supports*, Report No. FRA-RT-72-26, Office of High Speed Ground Transportation, Federal Railroad Administration (Order No. PB-212-843/7 from NTIS, Springfield, VA 22151).

Parker, H. W., D. U. Deere, R. B. Peck, P. C. Birkemoe, R. M. Semple (1973). *Testing and Evaluation of Prototype Tunnel Support Systems*, Report No. FRA-ORDD 74-11, Federal Railroad Administration, Department of Transportation (Order No. PB-231-912/AS from NTIS).

Peck, R. B. (1969). "Deep Excavations and Tunneling in Soft Ground," *Proceedings*, 7th International Conference on Soil Mechanics and Foundation Engineering, State of the Art Volume, pp. 225-90.

Peck, R. B., A. J. Hendron, B. Mohraz (1972). "State of the Art of Soft-Ground Tunneling," *Proceedings*, North American Rapid Excavation and Tunneling Conference, American Institute of Mining, Metallurgical, and Petroleum Engineers, New York, Vol. 1, Chapter 19, pp. 259-86.

Research Council on Riveted and Bolted Structural Joints of the Engineering Foundation (1972). *Specifications for Structural Joints Using ASTM A325 or A490 Bolts*, New York.

Romualdi, J. P., J. A. Mandel (1964). "Tensile Strength of Concrete Affected by Uniformly Distributed and Closely Spaced Short Lengths of Wire Reinforcement," *Journal of the American Concrete Institute*, Vol. 61, No. 6, Part 1, June, pp. 657-71.

Semple, R. M., A. J. Hendron, G. Mesri (1973). "The Effect of Time-Dependent Properties of Altered Rock on Tunnel Support Requirements," University of Illinois at Urbana-Champaign, Report No. FRA-ORD&D 74-30, For Federal Railroad Administration, Department of Transportation, December.

APPENDIX A

DESCRIPTION OF THE NASTRAN PROGRAM

The Piecewise Linear option in the NASTRAN Program is used to solve structural problems with material nonlinearity. The load is applied in increments with the stiffness properties assumed to be constant during each increment. The stiffness matrix for each increment is dependent on the current state of stress in the element. The increments in displacements and stresses are accumulated to produce the final results. Since the algorithm assumes linearity between sequential loads, the results depend on the size of the load increments. When the user selects large load increments and the material properties are changing rapidly, the results may be inaccurate. On the other hand, if small load increments are used when the structure is nearly linear, the solution will be unnecessarily precise and costly.

A summary flow diagram is given in Fig. A.1. The various steps are numbered corresponding to the explanations below:

1. The normal static analysis "front end" is used to generate the grid point, element, and loading tables. The stiffness matrix is generated in the normal manner using the initial moduli of elasticity given with the materials.
2. The element tables are separated into linear and nonlinear elements. The program recognizes a nonlinear element as one with a stress-strain table referred to by its material.
3. The load vector for the structure $\{P_g\}$, is generated by normal methods.

Static analysis by the displacement method

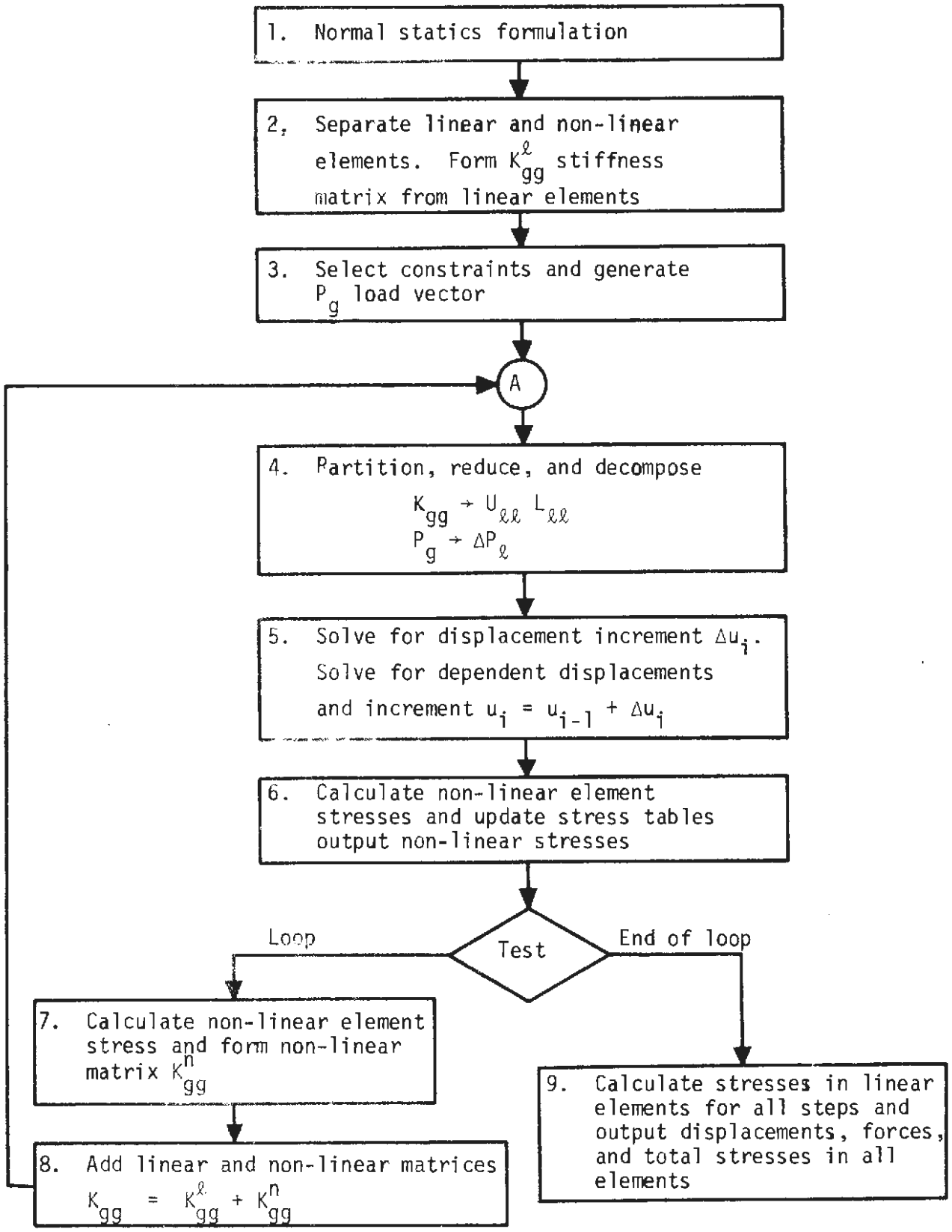

FIG. A.1 PIECEWISE LINEAR FLOW DIAGRAM

4. The current stiffness matrix is initially the linear elastic matrix; for subsequent load increments the matrix is changed as shown in step 8. The constraints are applied to the matrix in the normal sequence. The initial stiffness matrix $[K_{\ell\ell}]$ is decomposed to produce the triangular matrices $[u_{\ell\ell}]$ and $[L_{\ell\ell}]$. In a similar manner, the applied loads, including enforced displacements at grid points are modified by the constraints to produce a load vector for the independent coordinates $\{P_\ell\}$. The current load increment is:

$$\{\Delta P_\ell^i\} = (\alpha_i - \alpha_{i-1})\{P_\ell\} = \Delta\alpha_i\{P_\ell\}, \qquad i = 1,2,\ldots$$

where $\alpha_1, \alpha_2, \ldots n$ are a set of load level factors provided by the user.

5. The incremental displacements are generated using the current load vector increment. The dependent displacements are recovered in the normal manner to produce the increments for all degrees of freedom, $\{\Delta u_g^i\}$. The incremental forces of single point constraint, $\{\Delta q_s^i\}$, are also recovered. The increments are added to the previous vectors to produce the current vectors:

$$\{u_g^i\} = \{u_g^{i-1}\} + \{\Delta u_g^i\} \quad ,$$

$$\{q_s^i\} = \{q_s^{i-1}\} + \{\Delta q_s^i\}$$

6. Total nonlinear element stresses are calculated and output within the loop.
7. The stiffness matrix for the nonlinear elements $[K^n_{gg}]$, is generated six columns at a time for all nonlinear elements connected to a grid point. The table of element connections and properties is appended to include the current stress and strain values. The modulus of elasticity is calculated from the slope of the stress-strain curve.
8. The nonlinear element stiffness matrix (step 7) is added to the linear element stiffness matrix (step 2) to produce a new stiffness matrix. The next pass through the loop will reflect the new stress state of the structure.
9. Stresses for the linear elements are calculated directly from the total displacement vector.

The nonlinearity of a structural element is defined by the material of the element. Any isotropic material may be made nonlinear by including a stress-strain table defining its extensional characteristics. The stress-strain table must define a nondecreasing sequence of both stresses and strains. Because the stiffness matrix for the first load increment uses the elastic material coefficients, the initial slope should be Young's modulus E. Linear elements may be used in any combination with the nonlinear elements.

To simplify input to the program, a single type of plastic material table is used. A stress-strain tabular function is input for each nonlinear material. Only certain types of elements may use the nonlinear tables.

In calculating the current modulus of elasticity of an inelastic element, an approximation of the slope of the stress-strain function is used. Because this modulus is to be used for the interval between the present load and the next one, an extrapolation of current information is required. A linear extrapolation is used to estimate the strain due to the next load increment (Fig. A.2). The current strain increment, $\Delta\varepsilon_i$, is computed from the current displacement increment, Δu_g^i, by separate subroutines for each type of element and the next strain increment, $\Delta\varepsilon_{i+1} = \varepsilon_{i+1} - \varepsilon_i$, estimated by linear extrapolation. The corresponding moduli are

$$E_{i+1} = \frac{\sigma_{i+1} - \sigma_i}{\varepsilon_{i+1} - \varepsilon_i} \tag{A.1}$$

$$G_{i+1} = \frac{G_o}{E_o} E_{i+1} \tag{A.2}$$

where σ_i and σ_{i+1} are obtained from points on the stress-strain curve corresponding to ε_i and ε_{i+1} (Fig. A.3), and G_o and E_o are the elastic shear and extensional moduli. The estimated next extensional strain is:

$$\varepsilon_{i+1} = \varepsilon_i + \gamma\Delta\varepsilon_i \tag{A.3}$$

where the coefficient γ_i is the ratio of load increments.

$$\gamma_i = \frac{\alpha_{i+1} - \alpha_i}{\alpha_i - \alpha_{i-1}} = \frac{\Delta\alpha_{i+1}}{\Delta\alpha_i} \tag{A.4}$$

Plastic properties may be assigned only to the following element types: the bar, the rod, the tube, and the plate. In the static, elastic

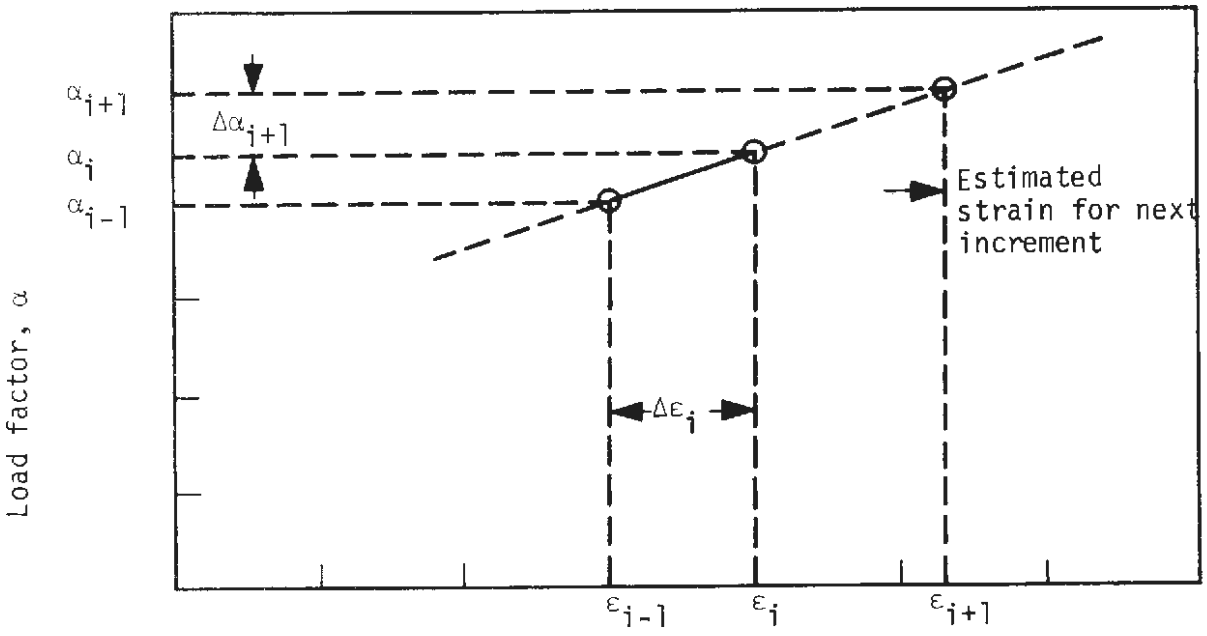

FIG. A.2 METHOD OF EXTRAPOLATING PREVIOUS STRAINS TO PRODUCE ESTIMATE OF NEXT STRAIN

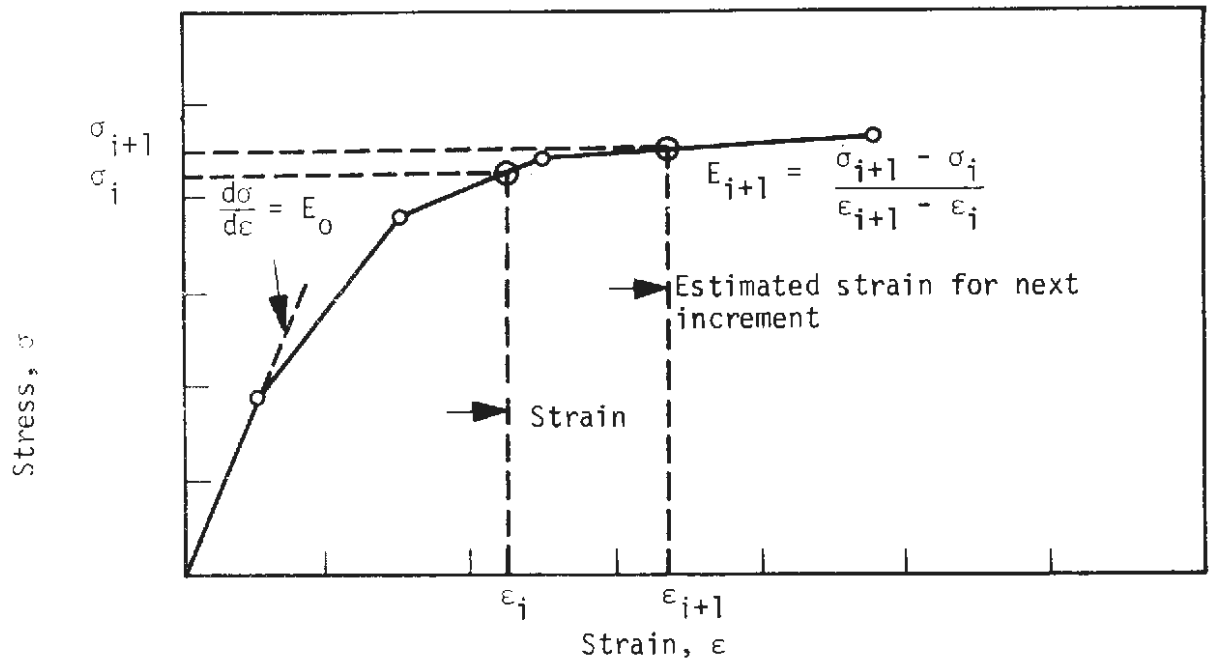

FIG. A.3 DETERMINATION OF ELASTIC MODULUS FROM TABULAR STRESS-STRAIN CURVE DEFINED BY USER

analysis, the bar takes into account extension, torsion, and bending properties while the rod includes only extension and torsion. The only restrictive assumptions are that the elements be straight, unloaded except at their ends, and have uniform properties from end to end. The plasticity of these elements, however, is assumed to depend only on the state of extensional stress, i.e., bending and twisting stresses are ignored. Therefore, if bending stresses are important, the bar must be represented as a built up structure composed of rods, shear panels, and/or plates.

A shear panel in NASTRAN is a two-dimensional structural element that resists the action of tangential forces applied to its edges but does not resist the action of normal forces. Consider the flat quadrilateral panel shown in Fig. A.4. The panel is in equilibrium under the action of tangential edge forces, F_1, F_2, F_3, and F_4. The forces on elements are applied only at their corners, i.e., at grid points. The equivalent corner forces f_A, f_B, f_C, and f_D are made colinear with the diagonals. Only one of the edge forces is independent, the others taking values to satisfy equilibrium. The auxiliary quadrilateral BEFC is a force polygon that may be used to evaluate the ratios of the edge forces. BF is drawn parallel to AC and EF is drawn parallel to AD. Since the resultant of F_1 and F_4 must lie along AC in order to balance the resultant of F_2 and F_3, the triangle BEF expresses the relationship among F_1, F_4, and their resultant. It is assumed (arbitrarily) that one-half of each adjacent edge force is reached at each corner. Thus, if q_1 is the average shear flow along edge AB,

$$f_A = f_C = \frac{1}{2} q_1 \frac{AB \cdot BF}{BE} \qquad (A.5)$$

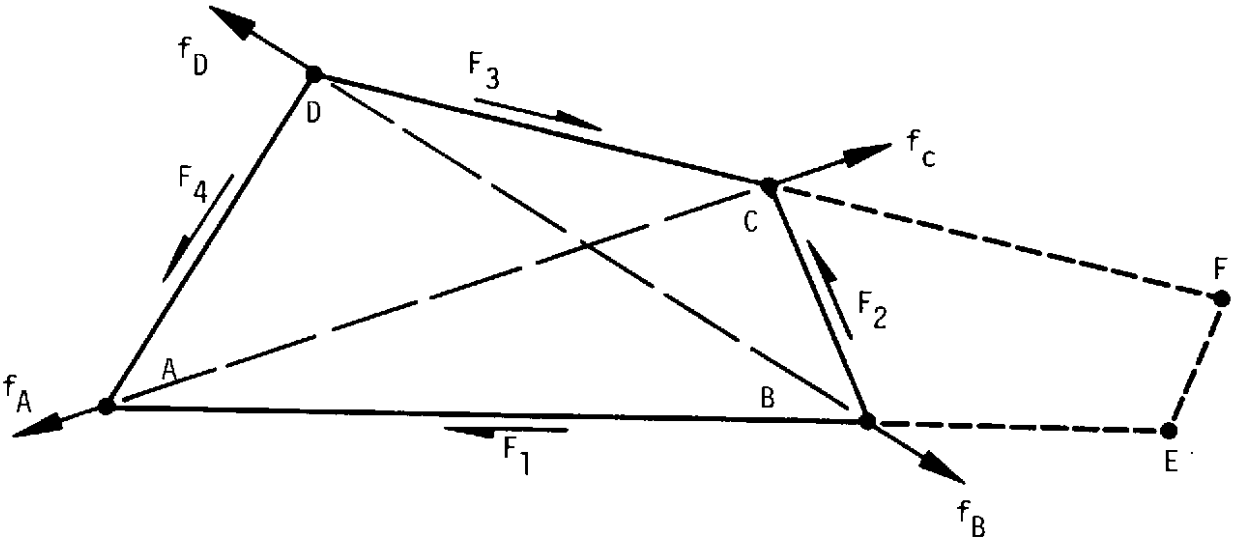

FIG. A.4 SHEAR PANEL FORCE POLYGON

$$f_B = f_D = \frac{1}{2} q_1 \frac{AB \cdot CE}{BE} \tag{A.6}$$

If the strain energy E is expressed as a quadratic function of q_1,

$$E = 1/2\ Z\ q_1^2 \tag{A.7}$$

then the stiffness matrix referring to motions at the corners is derived from Eqs. A.5, A.6, and A.7 as follows.

Let the element stiffness matrix $[K_{ee}]$ be defined by $[K_{ee}]\{u_e\} = \{f_e\}$, where $\{f_e\} = [f_A, f_B, f_C, f_D]^T$ and the elements of $\{u_e\}$ are components of corner motion colinear with the elements of $\{f_e\}$. Equations A.5 and A.6 may be written in matrix form as:

$$\{f_e\} = \{C\}q_1$$

The strain energy is related to corner motions by:

$$E = \frac{1}{2} \{u_e\}^T [K_{ee}] \{u_e\}$$

It is convenient to define a generalized displacement, δ, conjugate to q_1, such that $\delta = zq_1$ and

$$E = \frac{1}{2} \delta q_1 = \frac{1}{2Z} \delta^2$$

Alternatively, the strain energy may be expressed in the forms

$$E = \frac{1}{2} \{u_e\}^T \{f_e\}$$

$$E = \frac{1}{2} \{u_e\}^T \{C\}q_1$$

Then

$$\delta = \{u_e\}^T \{C\} = \{C\}^T \{u_e\}$$

so that

$$E = \frac{1}{2Z} \{u_e\}^T \{C\} \{C\}^T \{u_e\}$$

Finally, the stiffness matrix is obtained

$$[K_{ee}] = \frac{1}{Z} \{C\} \{C\}^T$$

Let $\{u_g\}$ be the degrees of freedom at adjacent grid points in the global coordinate system, to which the element coordinates, $\{u_e\}$, are related by

$$\{u_e\} = [T] \{u_g\}$$

The stiffness matrix of the shear panel referred to grid points coordinates is:

$$[K_{gg}] = [T]^T [K_{ee}] [T]$$

For a rectangular panel, the shear flow is constant over the surface and $Z = A/Gt$ where Z relates strain energy to average shear flow on side 1 of the panel, A is the area, t is the thickness, and G is the shear modulus of the panel.

62852